

RICE UNIVERSITY

Bilayer Approaches for Nanoparticle Phase Transfer

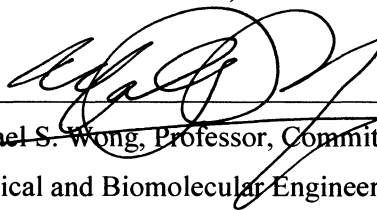
by

Gautam Chandrakanth Kini

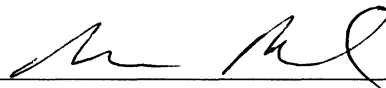
A THESIS SUBMITTED
IN PARTIAL FULFILLMENT OF THE
REQUIREMENTS FOR THE DEGREE

Doctor of Philosophy

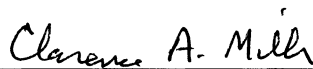
APPROVED, THESIS COMMITTEE:



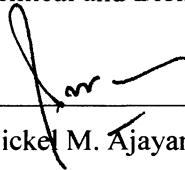
Michael S. Wong, Professor, Committee Chair
Chemical and Biomolecular Engineering, Chemistry



Sibani Lisa Biswal, Assistant Professor, Co Chair
Chemical and Biomolecular Engineering



Clarence A. Miller, Professor Emeritus
Chemical and Biomolecular Engineering



Pulickel M. Ajayan, Professor
Mechanical Engineering and Materials Science

HOUSTON, TEXAS

NOVEMBER 2011

Bilayer Approaches for Nanoparticle Phase-Transfer

by

Gautam Chandrakanth Kini

Department of Chemical and Biomolecular Engineering

Rice University, Houston TX

ABSTRACT

Nanoparticles (NPs) are often synthesized in organic solvents due to advantages of superior size and shape control obtainable in a non-polar environment. However, many applications featuring NPs require them to be in aqueous media. To transfer NPs from oil to water, surfactants with amphiphilic (hydrophobic and hydrophilic) groups have been widely used. A popular phase-transfer approach involves formation of oil-in-water emulsions upon which the oil storing the NPs is boiled off. In the process, surfactants form bilayers with hydrophobic groups on the NPs rendering them water-dispersible. This transfer route however is limited in that NPs aggregate to form clusters which results in poor colloidal stability and for the specific case of quantum dots (QDs), adversely impacts optical properties. It has ever since remained a challenge to devise approaches that transfer NPs from oil to water as single particles without compromising NP stability and properties.

We have discovered that by simple addition of salt to water during the step of emulsion formation, NP transfer efficiency can be greatly enhanced in "salty-micelles" of surfactants. The strength of this approach lies in its simplicity and generic nature in that the transfer scheme is valid for different NP, surfactant and salt types. Using a model

system with cadmium selenide (CdSe) QDs as NPs, Aerosol-OT (AOT) as the surfactant and NaCl as the salt in water, we found >90% of CdSe QDs transferred in salty-micelles of AOT which was significantly higher than the 45-55% QDs that transferred in deionized-water (DI-water) micelles of AOT. In the salty-micelle environment, QDs were found to exist predominantly as single NPs with narrow size distribution, as established by light scattering, analytical ultracentrifugation and electron microscopy. The effects of salt were in lowering aqueous solubility of AOT through "salting-out" action and in screening repulsions between like-charged head groups of AOT molecules. Electrophoresis, thermogravimetric analysis and photoluminescence measurements using a solvatochromic dye established higher surfactant coverage with greater lateral compaction for QDs in salty-micelles over the DI-micelle counterpart. Single NP characteristics along with a hydrophobic environment in laterally compact salty-micelles resulted in better retention of optical properties of QDs.

Observations of a secondary effect by salt in inducing spontaneous emulsification of a hydrocarbon (octane)/AOT/brine system were systematically investigated by tracking time-variant octane droplet size and charge. Salinity levels that determine the spontaneous curvature and phase behavior of AOT were seen to influence the initial nucleation of octane droplets and their subsequent growth. The smallest octane drops (sub 50 nm) were nucleated at the optimum cross-over salinity and emergence of the liquid crystalline phase of AOT resulted in slowest growth rates. These factors contributed towards higher transfer efficiency of NPs in salty-micelles.

Two applications from formulating aqueous NP suspensions by the new phase-transfer approach are described. In the first, QD and carbon-dot (C-Dot) "nanoreporters"

ACKNOWLEDGMENTS

There are many people who have contributed to my doctoral experience at Rice University and I take this opportunity to express to them, my sincere gratitude. Foremost, I express my sincere gratitude and appreciation to my graduate research advisors, Professor Michael S. Wong and Professor Sibani Lisa Biswal. They have always believed in my abilities and provided me with an environment of independence, free thinking, abundant resources, opportunities for many project collaborations and a free hand at research. I remain grateful to them for their support in helping me get through some very trying personal problems and initial difficulties I had concerning the department qualifiers. Their encouragement, advice and guidance helped me transition to a better, stronger and more productive engineer and independent researcher.

I also take this opportunity to thank Professor Clarence A. Miller for the many fruitful discussions we had related to colloids and interfacial phenomena and more specifically, on spontaneous emulsification of microemulsions. I have benefited immensely from his knowledge, wisdom and experience and attribute much of my research progress to his guidance. I also thank Professor P. M. Ajayan for his guidance, the many lectures on materials science and biomimetics, and for the opportunity he provided me to pursue an independent research project on dynamic self-assembly and reaction-diffusion systems.

Outside of my research committee, I thank my many collaborators with whom I had the opportunity to work on interdisciplinary projects. Many thanks to my friend and colleague Dr. Hitesh Bagaria, who helped me in rationalizing initial observations on salt-mediated nanoparticle transfer enhancement. He spent several hours discussing,

educating and training me in the fascinating area of nanoparticle research; many thanks for the high standards you set in research, professionalism and integrity and I wish you the best in realizing your career goals. I also acknowledge Dr. Wen-Yin Ko for starting this project and for the many fun times we had together in the lab - your hard work and systematic efforts sure did pave the way in developing a novel nanoparticle transfer method and became the basis of my thesis.

Many thanks to the AEC nanoreporters team - Professors James M. Tour and Mason B. Tomson, Dr. Amy T. Kan, Dr. Jie Yu, Lu Wang, Wei Lu and Garry - we did make nanoreporters a serious contender as future reservoir illuminators. I also thank Charles Conn, Justin Lai and Nicholas Hoefft for their sincere and enthusiastic efforts in carrying out several exciting studies in lithography and the microfluidic assembly of polymer/salt/nanoparticles as gels and capsules. I look forward to our publications together in the near future.

Many thanks to Jose Lopez-Salina and Maura Puerto for their help with spinning drop tensiometry and phase behavior analysis. To Natnael Behabtu for his help with cross-polarizing microscopy that established beyond doubt the location of the liquid crystal. In you I find one of the most outstanding chemical engineers I have ever met - your genuine and fearless curiosity, the joy you derive in discovery and discussions - be it science, philosophy, culture or wine and the countless people you have helped with no ulterior motives and expectations of return are all commendable qualities.

My sincere thanks to the post-doctoral fellows, visiting scholars, graduate and undergraduate students of Wong and Biswal laboratories. Your friendly, supportive, caring and ever-helpful nature has helped me cherish the good times and get through the

hard times. To Juan Carlos Velazquez, Quang Nguyen, Hyun Song, Joni Arentz, Shujin Li, Dr. Sukit Leekumjorn, Dr. Yu-Lun Fang, Dr. Benny Kadali, Dr. Nurgul Akcin, Zhun Zhao, Varun Shenoy, Dr. Madhuri Thakur, Dr. Dichuan Li, Dr. Kai-Wei Liu, Kung-Po Chao, Julie Byrom, Kun Ma, Jinghui Wang and Daniel Du, thank you for the wonderful times we have spent together.

To Nikos "Papa" Soultanidis, we were the bad boys of the batch of 2011 who initially flirted with danger, but through our constant support of each other and reminders that our hard work and long nights would eventually pay off - look at what we achieved - reforms we brought to the departmental qualifier systems, jobs in Exxon, SABIC, Intel, Unilever and Shell that we obtained in a challenging economy and most important, the doctoral degree we achieved which now makes us licensed philosophers. I thank you for the many lessons in the Greek language you gave me (particularly our secret admiration for mavro vuvali me kudunia) but still fail to understand how you differentiate between your text and symbols in an already abstract thermo lesson! To Lori Pretzer, a feisty but genius chemist who always fought and (successfully) bullied the chemical engineers she was surrounded by - what would I have done without you? Your drive, fantastic attitude towards research and genuinely altruistic and helpful nature continues to amaze me. Many thanks to you and Sravani Gullapalli for help with proof-reading this thesis and improving my defense presentation a thousand-fold through honest and constructive criticism.

Thanks to Dr. Tracy Volz and Dr. Jan Hewitt for their guidance and constructive criticism of my presentations and thesis writing - I owe much of my success in the job interviews and timely completion of my thesis to them.

I also thank the ever-helpful staff of Rice SEA - Dr. Angelo Benedetto and Dr. Wenhua Guo for training me on the SEM and TEM instruments. Thanks are also due to my many friends on campus: Shyla, Sukesh, Saumyakanti, Sergio, Clementina, Avani, Vandana and Priyank Jaiswal, Karishma and Arshad Sayyad, Richa and Sayantan, Vijetha, Shruthi, Aparna, Neeraj, Michael, Achal, Chinmay, Deepti, Arjun, Pragya and Vivek Anand, Neha and Sushant Datta, Lily and Paco Vergaz, Vishnu Mohan, Debshila, Neelam, Leela Mohan, Akshay, Sanketh and Hemtej.

Lastly, my thanks to my family and friends in the United States who have always been there for me - to my first family in Houston - Anil, Sunitha, Dhruv and Sitara for their warmth, hospitality and unconditional love. Anil anna, I look up to your courageous entrepreneurship skills and to what you have singularly achieved while still remaining a grounded, caring, generous and objective person; Sunitha vanni - thank you for the abundance of love and pampering you have showered on me through the years. To my aunt and uncle Gayathri and Rajaram Baliga, who have been wonderful role models with their altruistic, caring and highly principled nature. To my late uncle Dr. Vivek Kusumakar and my aunt Shalini Kusumakar whose mentorship and advice will be a guiding force through my life and career. To my dear friends Rita and Surendra Talwar, Vishnu, Vijeth, Santosh, Kishore, Vivek and the Baliga and Shenoy families. To my loving fiancée Anubha and my family back home in India - mom, dad, Ashu, Girish, Aditi. Mamama, Pallavi, Renu, Dayanand, Shashikala, Naveen, Prathima and the Manimarans - thank you for being there and making the many hard days seem not so bad after all. It is to my parents I attribute much of whom I am today. They have taught me to reach for my goals through hard work and fair means. To them I dedicate this thesis.

To my dear and loving mother Lalitha C. Kini who wonders why I study so much and to my loving dad K. Chandrakanth Kini who remains highly amused with my mother's doting and anxious nature.

Table of Contents

Abstract	i
List of Figures	xvi
List of Tables	xxxiv

Chapter 1: Background and Research Motivation

1.1	Nanotechnology: Arrival of a New Research Theme.....	1
1.2	Critical Impact Area of Nanotechnology: Energy.....	3
1.3	The Need for Stable Aqueous NP Suspensions.....	5
1.4	Research Motivation and Layout of the Thesis.....	6
1.5	References.....	15

Chapter 2: Electrolytes Improve Nanoparticle Transfer from Oil to Water

2.1	Nanoparticles Phase-Transfer Strategies.....	21
	2.1.1 Ligand Exchange Methods.....	22
	2.1.2 Bilayer Formation Methods.....	27
2.2	New Nanoparticle Phase-Transfer Concept: “Salty-Micelles”.....	34
	2.2.1 Introduction.....	34
	2.2.2 Materials and Methods.....	36
	2.2.2.1 Synthesis of Nanoparticles.....	36
	2.2.2.2 Phase-Transfer of Nanoparticles.....	38
	2.2.2.3 Nile Red Fluorescence Study.....	42
	2.2.2.4 Colloidal Stability Study.....	42

2.2.2.5	Characterization.....	43
2.2.3	New Phase-Transfer Scheme.....	49
2.2.4	Results and Discussions.....	53
2.2.5	Conclusions.....	64
2.3	References.....	65

Chapter 3: Spontaneous Emulsification of Hydrocarbon/Aerosol-OT/Brine Systems

3.1	Introduction.....	78
3.2	Materials and Methods.....	84
3.2.1	Preparation of Microemulsions.....	84
3.2.2	Preparation of Nanoemulsions.....	85
3.2.3	Characterization of Emulsions.....	85
3.2.3.1	Phase Behavior Studies.....	85
3.2.3.2	Polarized Light Screening System.....	85
3.2.3.3	Interfacial-Tension Measurements.....	86
3.2.3.4	Dynamic Light Scattering.....	87
3.2.3.5	Zeta Potential Measurements.....	87
3.2.3.6	Optical Microscopy.....	88
3.3	Results and Discussions.....	88
3.3.1	Phase Behavior and Interfacial Tensions of Octane-AOT-Brine Systems.....	88
3.3.2	Droplet Size Evolution upon Diluting W/O Microemulsions and B/O Microemulsions in Different Winsor Salinities.....	94

3.3.3	Zeta Potential of Octane Droplets in Different Winsor Regimes.....	97
3.4	Mechanism of Octane Droplet Growth in Nanoemulsions.....	100
3.4.1	Nanoemulsion Droplet Growth in Water ($\% \varepsilon = 0$).....	100
3.4.2	Droplet Growth in Brine ($\% \varepsilon = 0.2$ and 0.3).....	108
3.4.3	Nanoemulsions formed in Brine ($\% \varepsilon = 0.4$).....	116
3.5	Conclusions.....	118
3.6	References.....	120

Chapter 4: Colloidal and Flow Behavior of Brine-Stable Quantum Dot Nanoparticles

4.1	Introduction.....	128
4.2	Colloidal Stability of Nanoparticles: The Role of Intermolecular Forces.....	129
4.2.1	Nanoparticles Stabilized by Electrostatics.....	130
4.2.2	Nanoparticles Stabilized by Steric Hindrance.....	136
4.3	Materials and Methods.....	138
4.3.1	Synthesis and Phase Transfer of Quantum Dots.....	138
4.3.2	Characterization.....	140
4.3.2.1	Dynamic Light Scattering.....	140
4.3.2.2	Zeta Potential.....	142
4.3.2.3	UV-vis Spectroscopy.....	143
4.3.2.4	Transmission Emission Microscopy.....	143
4.3.3	Breakthrough Studies.....	143
4.3.3.1	Scintillation Counter.....	146
4.4	Results and Discussions.....	147

4.4.1	Colloidal Properties of QDs/Neodol.....	147
4.4.2	Transport and Breakthrough of QD/Neodol through Packed Calcite Column.....	151
4.4.3	Modeling Transport and Breakthrough of QD/Neodol through Packed Calcite Column.....	156
4.5	Conclusions.....	161
4.6	References.....	162

Chapter 5: Colloidal and Flow Behavior of Brine and Temperature-Stable C-Dot Nanoreporters

5.1	Introduction.....	171
5.2	Materials and Methods.....	173
5.2.1	Synthesis and Phase-Transfer of C-Dots in Bilayers of Avanel.....	173
5.2.2	Characterization.....	176
5.2.2.1	Dynamic Light Scattering.....	176
5.2.2.2	Zeta Potential.....	177
5.2.2.3	UV-vis Spectroscopy.....	177
5.2.3	Breakthrough Studies.....	177
5.3	Results and Discussions.....	179
5.3.1	Colloidal Properties of C-Dolt/Avanel.....	179
5.3.2	Transport and Breakthrough of C-Dot/Avanel through Crushed-Calcite and Quartz Sand Columns.....	181
5.4	Conclusions.....	182
5.5	References.....	184

Chapter 6: Microfluidic Formation of Ionically Crosslinked Polyamine Gels

6.1	Introduction.....	186
6.1.1	Microfluidics and its Unique Environment.....	187
6.1.2	Reynolds Number.....	189
6.1.3	Péclet Number.....	191
6.1.4	Capillary Number.....	194
6.2	Microfluidic Formation of Ionically Cross-Linked Gels and Nanoparticle Assembled Capsules.....	194
6.2.1	Background.....	194
6.2.2	Gel Formation Strategies in Microfluidic Devices and their Applications.....	199
6.2.3	Materials and Methods.....	205
6.2.3.1	Materials.....	205
6.2.3.2	Microfluidic Master Template and Device Formation.....	206
6.2.3.3	Monitoring Gel Formation.....	207
6.2.4	Results and Discussion.....	209
6.2.4.1	Nature of Structures formed in Microfluidic Channels.....	209
6.2.4.2	Structural Changes in Microfluidic Channels.....	215
6.2.4.3	Effects of R ratio and Flow Rates.....	217
6.2.4.4	Effect of Laminar Flow Conditions.....	219
6.2.4.5	Manipulating Electrostatic Interactions via pH.....	221

6.2.5	Conclusions.....	225
6.3	References.....	228

Chapter 7: Summary and Recommendations for Future Work

7.1	Thesis Summary.....	237
7.2	Recommendations for Future Work.....	240
7.2.1	Electrostatic Self-Assembly of Nanoparticles to form Superlattices.....	240
7.2.2	Nanoreporters with Oil-Detection Capabilities.....	242
7.2.2.1	Nanoreporters where NPs function as Signaling or Contrast Agents.....	242
7.2.2.2	Nanoreporters where NPs function as Delivery Agents of Signaling Molecules.....	244
7.2.3	Polyamine Gels for Flow Control and Actuation.....	246
7.2.4	Hybrid Polyamine/Glutaraldehyde Gels for Flow of Organic Solvents.....	247
7.2.5	Flow Focusing Approaches for Microfluidic Synthesis of NACs.....	248
7.3	References.....	250

Appendix A:

Section A1	Photoluminescence Studies.....	253
Section A2	Thermogravimetric Analysis (TGA).....	254
Section A3	Nile Red Studies.....	255

Section A4	Phase-Transfer of CdSe QDs using CTAB.....	256
Section A5	Phase-Transfer of CdSe QDs in Na ₂ SO ₄	256
Section A6	Phase-Transfer of CdSe QDs in CaCl ₂	257

Appendix B:

Section B1	Time-dependent Droplet Size of Nanoemulsions formed by diluting 60/30/10 and 80/10/10 W/O Microemulsions in Excess Brine.....	258
Section B2	Time-dependent Droplet Size of Nanoemulsions formed by diluting 70/20/10 B/O Microemulsions with Different Internal Salinities in Excess Brine.....	259
Section B3	Time-dependent Zeta Potential on Octane Drops of Nanoemulsions formed by diluting 60/30/10 and 80/10/10 W/O Microemulsions in Excess Brine.....	260
Section B4	Plots of R ³ vs. t of Nanoemulsion Drops formed by diluting B/O Microemulsions in Winsor I (%ε = 0).....	261

Appendix C:

Section C1	Details of Curve Fitting by the CXTFIT Routine.....	262
Section C2	Breakthrough Profile of Tracer through Calcite.....	264
Section C3	Transport and Breakthrough of QD/Neodol through Quartz Sand.....	264
Section C4	Sensitivity Analysis of 1D Advection-Dispersion Equation.....	267

List of Figures

Figure 1.1:	Current and forecasted global funding for nanotechnology research projects.....	2
Figure 1.2:	Number of nanotechnology patents published by the USPTO, EPO and JPO in the past 3 decades.....	2
Figure 1.3:	Number of patents issued for nanotechnology-based inventions vs. microtechnology-based inventions.....	3
Figure 1.4:	(Left) Schematic of flow of a nanoreporter with signaling molecules, through oil-saturated porous media. (Right) Flow of QDs as model nanoreporters through oil-free crushed calcite in a background of seawater. Excitation under a UV-Lamp shows illumination of the reservoir column from photoluminescence of QDs.....	5
Figure 1.5:	CdSe QDs transfer to salty-water within laterally compact bilayers of Aerosol-OT and to deionized water within loose bilayers of Aerosol-OT.....	7
Figure 1.6:	Upper inset shows a) birefringence from liquid crystal coating of AOT on octane droplets in Winsor 1 observed using cross-polarized microscopy, b) a visual image of octane in water nanoemulsions prepared at the cross-over salinity (Winsor III) under cross-polarizers, and c) multiple W/O/W emulsions observed using fluorescence microscopy. The middle inset (d) provides a visual comparison of the various octane/brine nanoemulsions formed in different Winsor domains after 28 days and the lower inset (e) shows the time-dependent droplet diameters of octane/brine nanoemulsions formed in different Winsor domains.....	9
Figure 1.7:	QD suspensions prepared in high salinity water (1M NaCl and 0.55M Seawater).....	11
Figure 1.8:	a) Schematic of process used to phase-transfer carbon dots from chloroform to saline water. b) Change in C-Dot diameters as a function of temperature in different salt solutions. c) Visual comparison of C-dot suspensions prepared in high salinity water (1M NaCl, 1M KCl and 0.55M Seawater) at 100 °C.....	12
Figure 1.9:	Ionic cross-linking of polyamine gels of PAH-citrate in a microfluidic channel.....	14

- Figure 2.1:** Nanoparticle (NP) dispersed in a non-polar solvent (oil) by surface ligand/surfactant molecules such as (a) oleic acid or (b) dodecanethiol. The hydrophilic (-COOH or -SH) groups of the ligands are chemically bound to the NP surface and the hydrophobic groups render oil-dispersibility to the NP..... 21
- Figure 2.2:** Schematic of two approaches to transfer nanoparticles (NPs) from oil to water by surface modification of NP surface. (a) Top Panel: NP phase-transfer through ligand or place exchange of native ligands on NP surface (in black) with ligands containing hydrophilic head groups (black and brown) at both ends of a hydrocarbon chain (in green), making NPs water-dispersible. An example of a commonly used ligand is 11-mercaptoundecanoic acid (MUA) with -SH and -OH hydrophilic head groups on either ends of an eleven carbon-chain hydrocarbon (b) Bottom Panel: NP phase-transfer through formation of bilayers wherein, the native ligands on the NP surface are retained but phase-transfer is done using amphiphilic ligands, constituted of a hydrophobic tail group (in green) and hydrophilic head group (in brown). The hydrophobic group (in green) of the amphiphile associates with the hydrophobic end of the native ligand (in black) and the hydrophilic end (in brown) of the amphiphile makes the NP water-dispersible..... 23
- Figure 2.3:** Phase-transfer of NPs from toluene to water by ligand-exchange with 11-mercaptoundecanoic acid (MUA). For each image pair, the left image corresponds to NPs in toluene before phase-transfer and the right image to NPs in water upon phase-transfer. (A, B: silver. C, D: gold. E, F: platinum. G, H: gold. I, J: palladium). For cases (A-H), phase-transfer efficiency was ~ 100%, for case (I-J), phase-transfer efficiency was > 90%. Note: Differences between gold NPs in pairs (C-D) and (G-H) are in the synthesis methods..... 25
- Figure 2.4:** CdSe-ZnS core-shell QDs, transferred from chloroform to phosphate buffer saline (PBS) solution, upon ligand-exchange with mercaptoacetic acid. Conjugation of the mercaptoacetic acid with protein (transferrin) translated to receptor-mediated endocytosis in cultured HeLa cells..... 25

- Figure 2.5:** (A) Schematic representing phase-transfer of CdSe/ZnS QDs from chloroform to water using a mixture of phospholipids (n-poly (ethylene glycol) phosphatidylethanolamine (PEG-PE) and phosphatidylcholine (PC)). (B) TEM images of QDs without staining and (C) TEM Images of QDs with staining dye, reveal transfer as single QDs encapsulated in a phospholipid block-polymer micelle..... 29
- Figure 2.6:** Transfer of oleic-acid stabilized iron-oxide NPs from hexane to water through bilayer formation with (A) IGEPAL®CO 630 (octylphenyl-polyethylene glycol: nonionic surfactant) and (B) oleic acid. Iron-oxide was phase-transferred as clusters of 2-3 NPs in IGEPAL®CO 630, as determined by dynamic light scattering (DLS) and as single NPs in oleic acid, as determined by DLS and small-angle X-Ray scattering (SAXS)..... 29
- Figure 2.7:** Transfer of Au NPs from chloroform to water by microemulsion formation. Aqueous surfactant solution of cetyltrimethylammonium bromide (CTAB) was added to the oil phase that contained nanoparticles (NPs), and stirred to form an oil/water microemulsion. The microemulsion was heated to a temperature above the boiling point of oil but below that of water to boil off oil, resulting in phase-transfer to water. NPs with native ligands (a) transferred to water by encapsulation in bilayers of surfactant/phospholipids. (b) These NPs can self-assemble into ordered nanocrystal-micelle superlattices with (c) hexagonal close packed (hcp) or (d) face cubic closed (fcc) structures. (e) Thermodynamically defined interdigitated bilayers..... 32
- Figure 2.8:** (a) Nanoparticle (NP) phase-transfer using plain/deionized (DI)-water micelles: Hexane containing CdSe QDs and Aerosol-OT (AOT) is added to DI water and mixed gently to form an emulsion. The concentration of AOT is 1.5 g/L. The emulsion is heated at 85 °C for 30 minutes to boil off the hexane, resulting in QDs encapsulated in DI water-micelles of AOT. DI-water micelles have a loosely packed structure, resulting in quenched photoluminescence (PL) in water and a quantum yield (QY) at 3%. (b) NP phase-transfer using salty-micelles: Hexane containing CdSe QDs and Aerosol-OT (AOT) is added to salt-containing water (NaCl at 3 g/L) and mixed gently to form an emulsion. The concentration of AOT is also maintained at 1.5 g/L. The emulsion is heated at 85 °C for 30 minutes to boil off the hexane, resulting in QDs encapsulated in salty-micelles of AOT. Salty-micelles have laterally compact structure, resulting in strong retention of PL in water and a higher QY at 7%..... 51

- Figure 2.9:** Solubility trends for ionic surfactants. The Krafft point or Krafft temperature is the point at which surfactant solubility equals the critical micelle concentration. Above this temperature, surfactants form a dispersed phase with a steep increase in solubility as micelles. Below the Krafft temperature, surfactants crystallize out of solution as hydrated crystals..... 52
- Figure 2.10:** (a) Photographs of "salty" (3 g-NaCl/L = 51 mM; 0.6 μ mol-QD/L) and "no-salt" aqueous suspensions of 3.0-nm oleate-coated CdSe QDs (0.6 μ mol-QD/L) under ambient and UV lighting (365 nm); phase-transfer agent = AOT. (b) UV-vis absorbance and photoluminescence (PL) spectra of oleate-coated CdSe QDs suspended in hexane, salty water, and no-salt water. (c) Percentage PL decrease of QD suspensions stored under ambient conditions as a function of time..... 54
- Figure 2.11:** Phase-transfer yield of CdSe QDs transferred from hexane to salty-water and no-salt water with AOT at AOT: CdSe ratios of 285:1 (equivalent of 1 monolayer coverage of AOT on 3 nm CdSe QDs) and 2850:1 (equivalent of 10 monolayers coverage of AOT on 3 nm CdSe QDs)..... 55
- Figure 2.12:** (a) Schematic showing AOT-oleate bilayer structure surrounding a NP under salty and no-salt conditions. (b) Emission spectra of Nile Red (i) in hexane; phase transferred with AOT into (ii) 0, (iii) 1, (iv) 3 and (v) 5 g-NaCl/L; and phase transferred with AOT and ZnO NPs into (vi) 0, (vii) 1, (viii) 3 and (ix) 5 g-NaCl/L. Excitation wavelength = 480 nm. (c) Plot of polarity fraction, $PF=I_{605}/(I_{605}+I_{650})$, as a function of NaCl concentration for samples phase transferred with and without ZnO NPs, where I_{605} and I_{650} are the average Nile Red PL intensities in the 10 nm band centered at 605 nm and 650 nm, respectively..... 57
- Figure 2.13:** (a) TEM images of CdSe QDs drop-cast from hexane, salty, and no-salt suspensions. (b) Sedimentation coefficient distributions and (c) hydrodynamic diameter distributions of CdSe QDs in salty and no-salt water suspensions calculated from analytical ultracentrifugation measurements. 1 Svedberg = 10-13sec..... 59
- Figure 2.14:** Emulsions of hexane in (a) salty-water (3 g-NaCl/L) and no-salt water 5 minutes upon formation. The hexane phase contains CdSe QDs with AOT as the emulsifier..... 60

- Figure 2.15:** Colloidal stability of salty and no-salt suspensions of CdSe QDs at higher NaCl concentrations. pH = 6..... 61
- Figure 2.16:** UV-vis absorbance spectra of (a) alkylthiol-coated Au NPs suspended in hexane, (b) C₆₀ suspended in benzene, and (c) oleate-coated ZnO NPs in hexane, and the corresponding salty (3 g/L NaCl) and no-salt water suspensions; phase-transfer agent = AOT (for Au and ZnO NPs) or CTAB (for C₆₀). Inset: photographs of NP suspensions..... 62
- Figure 3.1:** Transitions between Winsor I ↔ Winsor III ↔ Winsor II domains of ternary Oil/Surfactant/Water systems. Surfactant solubility altering variables such as temperature, salt, and co-surfactants change the spontaneous curvature of the surfactant from what favors an Oil-in-Water configuration (Winsor I) to a Water-in-Oil configuration (Winsor II)..... 81
- Figure 3.2:** Spontaneous emulsification of hexadecane produced by a diffusion-based mechanism from mass transfer of octanol out of and mass transfer of water into an oil droplet comprising of hexadecane/C₈OH/C₁₂E₆ droplet..... 81
- Figure 3.3:** Phase diagram of n-Octane/AOT/Water ternary system. The three blue dots represent (from bottom to top) 60/30/10, 70/20/10, and 80/10/10 weight ratios of Octane/AOT/Water corresponding to an L₂ phase or W/O microemulsion phase. The red arrow corresponds to the dilution levels (but not dilution path) from the L₂ domains to O/W emulsion domains where AOT concentration levels are 1.5 g/L..... 89
- Figure 3.4:** Time-based phase-behavior of nanoemulsions prepared by diluting W/O microemulsions of Octane/AOT/Water (70/20/10) in different levels of excess brine. In each panel, bulk NaCl-brine salinities correspond to %ε = 0, 0.2, 0.3, and 0.4. Final AOT concentration in all solutions was 1.5 g/L..... 91
- Figure 3.5:** Time-based phase-behavior of nanoemulsions prepared by diluting W/O microemulsions of Octane/AOT/Water (70/20/10) in different levels of excess brine. In each panel, bulk NaCl-brine salinities correspond to %ε = 0, 0.2, 0.3, and 0.4. Final AOT concentration in all solutions was 15 g/L..... 91

- Figure 3.6:** Temperature vs. surfactant concentration (γ) phase behavior plots for different NaCl concentrations (ϵ) of iso-Octane/AOT/Brine systems. The red dots correspond to room temperature (25 °C) and AOT concentration of 1.5 g/L at which Octane/Brine emulsions for this study were formulated. Cross over salinity is seen to be at $\epsilon = 0.3$ 92
- Figure 3.7:** Nanoemulsions formed by W/O microemulsions of Octane/AOT/Water (70/20/10) in different levels of excess brine, as seen through cross-polarizers on day 4 with a polarized light screening system. In the image, bulk NaCl-brine salinities correspond to $\epsilon = 0, 0.2, 0.3,$ and 0.4 . Final AOT concentration in all solutions was at 15 g/L. Birefringence is observed in nanoemulsion formed at $\epsilon = 0.3$, indicating the lamellar liquid crystalline phase of AOT..... 92
- Figure 3.8:** Interfacial tensions of octane with nanoemulsions prepared by diluting various W/O microemulsions of Octane: AOT: Water (60/30/10, 70/20/10, and 80/10/10) in different levels of excess brine (AOT = 1.5 g/L)..... 93
- Figure 3.9:** Octane drop size study with respect to time in Octane/Brine nanoemulsions obtained by diluting 70/20/10 Octane/AOT/Water microemulsions in different levels of excess brine (AOT = 1.5g/L)..... 95
- Figure 3.10:** Octane drop size study with respect to time in octane/brine nanoemulsions obtained by diluting 70/20/10 Octane/AOT/Brine ($\epsilon = 0.3$) microemulsions in different levels of excess brine (AOT = 1.5 g/L)..... 97
- Figure 3.11:** Zeta potential of Octane/Brine nanoemulsions obtained by diluting 70/20/10 Octane/AOT/Water microemulsions in different concentrations of excess brine (AOT = 1.5 g/L)..... 98
- Figure 3.12:** Octane droplet size evolution of nanoemulsions formed by diluting W/O microemulsion compositions (Octane-AOT-Water: 60/30/10, 70/20/10, 80/10/10) in excess water (Winsor I) (AOT = 1.5 g/L)..... 101
- Figure 3.13:** Plot of R^3 vs. t for nanoemulsions prepared by diluting 60/30/10, 70/20/10, and 80/10/10 Octane/AOT/Water microemulsions in excess water (Winsor I domain, AOT = 1.5 g/L)..... 104

- Figure 3.14:** Optical micrographs of nanoemulsions (upon diluting 70/20/10 Octane/AOT/Water microemulsion) in excess water, $\% \epsilon = 0$, AOT = 1.5 g/L. (a) Top panel, image under fluorescence mode, 24 hour upon forming nanoemulsions (Scale bar: 10 μm). (b) Bottom panel. Images taken in bright field and under cross-polarizers after 4 weeks (all scale bars: 50 μm). Prominent birefringence patterns observed around large octane droplets (25-50 μm) and at the octane/water interface for (i) Central image: polarizer set at 0° and analyzer set orthogonal at 90° . (ii) Right corner image: polarizer set at -45° and analyzer set orthogonal at $+45^\circ$ 106
- Figure 3.15:** Octane droplet size study with respect to time in Octane/Brine nanoemulsions obtained by diluting 70/20/10 Octane/AOT/Brine microemulsions with different levels of internal salinity ($\% \epsilon = 0, 0.2, 0.3, \text{ and } 0.4$) in excess water ($\% \epsilon = 0$, Winsor I) (AOT = 1.5 g/L). The presence of internal salinity slows down droplet growth rate..... 107
- Figure 3.16:** Octane droplet size study with respect to time in Octane/Brine nanoemulsions obtained by diluting 70/20/10 Octane/AOT/Brine microemulsions with different levels of internal salinity ($\% \epsilon = 0, 0.2, 0.3, \text{ and } 0.4$) in excess brine ($\% \epsilon = 0.2$, Winsor I) (AOT = 1.5 g/L). The presence of internal salinity slows down droplet growth rate due to emergence of the lamellar phase of AOT. Overall growth rates in brine ($\% \epsilon = 0.2$) are slower when compared to emulsions formed in excess water ($\% \epsilon = 0$)..... 111
- Figure 3.17:** Octane droplet size study with respect to time in Octane/Brine nanoemulsions obtained by diluting 70/20/10 Octane/AOT/Brine microemulsions having different levels of internal salinity ($\% \epsilon = 0, 0.2, 0.3, \text{ and } 0.4$) in excess brine ($\% \epsilon = 0.3$, Winsor III), (AOT = 1.5 g/L). At the cross-over, the presence of internal salinity slowed down droplet growth rate due to emergence of the lamellar phase of AOT such that perceptible difference was seen in growth rates of nanoemulsions derived from microemulsion compositions with internal brine vs. that with internal water. Overall growth rates in brine ($\% \epsilon = 0.3$) are slower when compared to emulsions formed in excess water ($\% \epsilon = 0$) and lower brine salinity ($\% \epsilon = 0.2$)..... 112

- Figure 3.18:** Optical micrographs of nanoemulsions (upon diluting 70/20/10 Octane/AOT/Water microemulsion) in brine with salinity, $\% \epsilon = 0.2$ (AOT = 1.5 g/L). (a) Top panel: Image under fluorescence mode 24 hour upon forming nanoemulsions (Scale bar: 10 μm) (b) Bottom panel. Images taken in bright field and under cross-polarizers after 4 weeks. Prominent birefringence patterns observed for around large octane droplets (30-50 μm) and at the octane/water interface for (i) Central image: polarizer set at 0° and analyzer set orthogonal at 90° . (ii) Right corner image: polarizer set at -45° and analyzer set orthogonal at $+45^\circ$ (all scale bars: 100 μm)..... 113
- Figure 3.19:** (Left) Multiple emulsions of water/octane/water, observed under fluorescence mode (Texas Red Filter, Nile-Red dye), 4 hours upon diluting 70/20/10 Octane/AOT/Water microemulsions in brine at $\% \epsilon = 0.4$ (AOT = 1.5 g/L). (Right) Multiple emulsions with internally coalesced droplets observed at 12 hours. White color corresponds to octane domains; black color corresponds to water/brine domains. All scale bars = 10 μm 118
- Figure 4.1:** Net DLVO Interaction Energy for QDs stabilized by AOT at varying levels of NaCl concentrations (Inset figure - Magnified regions of energy-distance profile for QDs stabilized by AOT in different concentrations of NaCl)..... 133
- Figure 4.2:** Net DLVO Interaction Energy for QDs stabilized by AOT at varying levels of CaCl_2 concentrations (Inset figure - Magnified regions of energy-distance profile for QDs stabilized by AOT in different concentrations of CaCl_2)..... 135
- Figure 4.3:** Net Interaction Energy for NPs stabilized by a nonionic surfactant as a function of surface coverage..... 138
- Figure 4.4:** Schematic to formulate nanoparticle dispersions of QDs/Neodol 91-7 in saline water..... 139
- Figure 4.5:** Experimental set-up of QD breakthrough studies through crushed calcite column..... 146
- Figure 4.6:** Phase-transfer of QDs from chloroform to water and different salt environments using bilayers of oleic acid and Neodol..... 148
- Figure 4.7:** UV-vis spectra and TEM micrographs of QDs in chloroform and following phase-transfer to DI water and in various salt solutions. (All scale bars in TEM micrographs = 20 nm)..... 148

Figure 4.8:	Hydrodynamic diameter of QD/Neodol as a function of temperature in water and in different salt environments. QD concentration in all DLS measurements was 4.5 μM and the Neodol concentration was 0.75 g/L.....	149
Figure 4.9:	Breakthrough profiles of QD/Neodol in (a) 0.55M synthetic seawater and (b) 1M NaCl. A salt solution, passing through the column, is switched to the QD/Neodol suspension in the same salt solution at $PV = 0$. At $PV \sim 3.0-3.5$ (marked by a dashed vertical line), the QD/Neodol suspension is replaced by the same salt solution. (c) Breakthrough profiles of QD/Neodol at 70 $^{\circ}\text{C}$ in 1M NaCl background solution after calcite is pre-saturated by solutions of 1M NaCl and 0.75 g/L Neodol/1M NaCl. The error bars on C_{exit}/C_0 were $\pm 2\%$	155
Figure 4.10:	Experimental and fitted results for transport of QD/Neodol through crushed calcite in synthetic seawater background at (a) 25 $^{\circ}\text{C}$ (b) 50 $^{\circ}\text{C}$ (c) 70 $^{\circ}\text{C}$	160
Figure 4.11:	Experimental and fitted results for transport of QD/Neodol through crushed calcite in: (a) 1M NaCl background at 25 $^{\circ}\text{C}$ (b) 1M NaCl background at 70 $^{\circ}\text{C}$ upon pre-saturation with Neodol..	160
Figure 5.1:	Synthesis procedure of C-Dots from hydroxylation of carbon black and functionalization with oleic acid.....	174
Figure 5.2:	Transfer of C-Dots into bilayers of Avanel in various saline environments. The concentration of C-Dots in 1M NaCl and 1M KCl is 15 ppm and in 0.55M seawater is 80 ppm.....	175
Figure 5.3:	Transfer of C-Dots into bilayers of Avanel in API brine. Concentration of C-Dots in API brine is 100 ppm.....	176
Figure 5.4:	Hydrodynamic diameters of C-Dot/Avanel as a function of temperature in saline backgrounds of 1M NaCl, 1M KCl and 0.55M seawater.....	180
Figure 5.5:	Hydrodynamic diameters of C-Dot/Avanel as a function of temperature in 1.77M API Brine.....	180
Figure 5.6:	Breakthrough profiles of C-Dot/Avanel in 1.77M API brine background through crushed-calcite columns at 25 $^{\circ}\text{C}$ and 70 $^{\circ}\text{C}$. The calcite-columns were pre-saturated with 0.75 g/L Avanel before C-Dot/Avanel was introduced into the column.....	181

- Figure 5.7:** Breakthrough profiles of C-Dot/Avanel in 1.77M API brine background through quartz sand columns at 25 °C and 70 °C..... 182
- Figure 6.1:** (i) A simple microchannel comprising three inlet channels merging to form a main central channel. (ii) A highly miniaturized “Lab on a Chip” type of microfluidic device – Microfluidic Chemostat. This device is used to study growth of microbial populations. The human finger and the United States dime coin gives a sense of scale and the dramatic extent of miniaturization going from (i) to (ii)..... 188
- Figure 6.2:** Illustrations of laminar flow behavior in microfluidic devices (i) Inlet channels with different colored dyes flow into the main channel at different points but remain exactly parallel to each other. (ii) Color gradient generator: Inlet streams (top to bottom) with colors varying from red to green and its intermediate mixtures, are introduced into the main channel. It can be seen that the color gradient is maintained even in the main channel due to laminar flow conditions. (iii) Effects of valve shut on and off: (A) Colored dye solutions flow through six inlet pipes to the main channel. The dyes flow as parallel streams in the main channel due to laminar conditions. Images (B – F) correspond to those wherein inlet streams are shut (one at a time, and counter clockwise for images B through F). Fluid is occupied by the stream entering at a higher pressure and mixing is still seen to be absent..... 190
- Figure 6.3:** A microfluidic channel with T-junction geometry where two fluids A and B mix purely by diffusion. The Péclet number captures the time (and consequently channel length) required for complete mixing to take place..... 192
- Figure 6.4:** Rotary pumps have been utilized to rapidly mix solutions in microchannels (here DNA and cells). (i) DNA (green stream) and cells (yellow stream) before mixing. (ii) DNA and cell streams upon mixing..... 193

- Figure 6.5:** Schematic depicting tandem self-assembly of microcapsules. (a) Two-step formation of nanoparticle assembled capsules (NACs): In the first step, a positively charged linear cationic polymer (poly (L-lysine) (PLL) is reacted with a multivalent anion, tetrasodium ethylenediamine tetraacetate (EDTA) to form EDTA-bridged PLL aggregates. (b) Confocal microscopy image of EDTA-bridged PLL aggregates, where PLL is partially conjugated by FITC fluorophores. (c) Bright field (top), confocal (bottom), and combined confocal/bright-field images (inset) of three different silica structures suspended in water. (f) SEM images of NACs. (g) TEM images of NACs (Scale Bars: 5 μm).. 196
- Figure 6.6:** Preliminary schematic of forming nanoparticle assembled capsules (NACs) on a continuous mode basis and the possibility of forming new NAC types..... 198
- Figure 6.7:** Polyallylamine hydrochloride (PAH) and citrate interactions in a bulk vortexing environment (top) gives rise to citrate-bridged PAH aggregates (fluorescence mode). In a microfluidic environment (bottom), new structures such as gels and droplets form, in addition to previously reported aggregates, when PAH and citrate flow under conditions of shear..... 199
- Figure 6.8:** Rapid *in situ* formation of hydrogels in microchannels by direct photo patterning. (a) The fabrication procedure utilizes an online ultraviolet (UV) source and a photomask that transfers designs to the liquid phase with different shapes and patterns (b-f). Note: The photomask containing respective designs are listed at the top right corner of each photograph in (b-e). (b) Triangle shape (c) Convex shaped pattern (d) Concave shaped pattern (e) High aspect ratio design shaped in the English alphabet “C” (f) Simultaneous polymerization of multiple structures with a single exposure of UV light. Scale bars: (b-e): 250 μm ; (f): 500 μm 201
- Figure 6.9:** Prefabricated posts in a microchannel to provide structural support for hydrogels. (a) Diagram depicting hydrogel jackets around posts (b) Actual device after polymerization of hydrogels. (c) Hydrogel jackets block side channel branch in expanded states. (d) Contracted hydrogels allow fluid to flow down the side branch. (e) Improvement in time response of hydrogel jacket design (curve depicted by circles) versus alternate design using larger cylindrical structure but without hydrogel jacket (curve depicted by squares). f_D is the fractional change in diameter (scale bars: 300 μm)..... 202

- Figure 6.10:** (i) Photoreaction injection molding procedure to incorporate hydrogel channels within PDMS microchannels (ii) Arrays of hydrogel microstructures containing different fluorophores. (Top Left or (a)) Six channels filled with precursor solutions containing Fluorescein Isothiocyanate (FITC) and Tetramethylrhodamine isothiocyanate (TRITC) alternatively. (Bottom Left or (b)) Hydrogel microstructures inside microchannels upon photopolymerization. (Top Right or (c)) Array of hydrogel microstructures obtained after removal of PDMS microchannels. (Bottom Right or (d)) Scanning electron microscope image of the hydrogel array..... 203
- Figure 6.11:** (i) (a) Schematic of microfluidic device used to prepare calcium alginate gels by cross-linking reactions of sodium alginate with calcium chloride, utilizing either one (b, c) or two (d, e) flow-focusing step schemes. (b) One-flow focusing channel to generate sodium alginate droplets. (c) Another flow-focusing channel to generate CaCl_2 droplets. (d, e) Fusion channels with two circular expansion chambers where calcium alginate particles are formed, corresponding to two different conditions of volumetric flow rates. (ii) Optical microscopy images of calcium alginate particles (mean size of particle corresponds to $30\ \mu\text{m}$)..... 203
- Figure 6.12:** Schematic depicting experimental set-up of the microfluidic device and flow control systems used to study PAH-citrate interactions..... 208
- Figure 6.13:** Nonequilibrium state diagram summarizing changes in state of PAH from PAH-citrate interactions. (Diagram constructed from changes observed in PAH stream within the first five minutes of reacting flow. Initial inlet PAH concentration was fixed at $1\ \text{mg/mL}$ for all cases). Regions west and south of dotted line demark the space where aggregates could be resolved under fluorescence microscopy and regions north and east of dashed line demark the space where droplets appeared..... 209

Figure 6.14: Optical and fluorescence microscopy images of structures formed in microfluidic channels from PAH-citrate interactions. (1) PAH-citrate aggregates (formation conditions: $R = 10$, PAH = 1 mg/mL, flow rate = 25 $\mu\text{L/h}$): (a) bright field and (b) fluorescence images and (c) schematic of region where aggregates formed in the microfluidic channel (scale bars - a, b: 10 μm). (2) PAH cross-linked incompletely to form noncontinuous gels (formation conditions: $R = 0.1$, PAH = 1 mg/mL, flow rate = 25 mL/h): (d) bright field and (e) fluorescent images and (f) schematic of the region in the microfluidic channel where discrete gels formed (scale bars-d, e: 10 μm). (3) PAH cross-linked completely to form continuous gels (formation conditions: $R = 50$, PAH = 1mg/mL, flow rate = 25 mL/h): (g) bright field and (h) fluorescent images and (i) schematic of the region in the microfluidic channel where continuous gels formed (scale bars - g, h: 50 μm). (4) Droplets rich in citrate ions (formation conditions: $R = 50$, PAH = 1mg/mL, flow rate = 25mL/min): (j) bright field and (k) fluorescent images of citrate droplets within the continuous gel stream of the microfluidic channel. (l) Schematic depicting droplet formation in the microfluidic channel. Droplets emanate from the junction of the microfluidic channel after reactant streams first interact and form continuous gels. The droplets that formed flowed along the length of the channel. (scale bars - j, k: 25 μm)..... 213

Figure 6.15: (a) Schematic to elucidate the nature of droplets. A neutral dye (dextran-tetramethylrhodamine) was added to the citrate stream and reacted with PAH-FITC under conditions of $R = 10$, PAH = 1 mg/mL, and flow rate = 25 mL/h. Upon droplet formation, the flow was stopped and the reactant streams were observed in fluorescence mode of a confocal microscope. (b) Confocal images of droplets observed under a FITC filter. (c) Confocal images of droplets observed under a rhodamine filter. (d) Differential interference contrast (DIC) image of droplets corresponding to images b and c). (e) Magnified region of a droplet observed through a FITC filter that corresponds to the circled region in image b. (f) Magnified region of a droplet observed through a rhodamine filter that corresponds to the circled region in image c. (g) DIC image of droplets corresponding to images e and f. (h) Intensity profiles of droplets in images e and f along regions marked with a white line establishes the absence of PAH in droplet and the diffusion of dextran dye into the interior of the droplet. (All scale bars are 20 μm)..... 214

- Figure 6.16:** Negative control experiment to ascertain the requirement of citrate in forming droplets. Schematics (a, b) describe experiments that establish requirement of citrate to form droplets (Refer Figs. 6.12 and 6.14). Image (c) reveals that no new droplet formed when the citrate stream containing neutral dextran dye was replaced with an aqueous solution of neutral dextran dye. Images (d) and (e) are corresponding images under Rhodamine filter and in DIC mode respectively. (All scale bars: 20 μm)..... 215
- Figure 6.17:** Schematic depicting the coexistence of structures in a microfluidic channel using confocal microscopy (conditions: $R = 10$, PAH = 1 mg/mL, and flow rate = 25 mL/h) when viewed under (a) a FITC filter and (b) a rhodamine filter. (c) Predominant existence of PAH-citrate aggregates (green spots) and gel (continuous green region). (d) PAH-citrate aggregates, gels, and citrate droplets (dark spots). (e) Citrate droplets present within the cross-linked polymer gel. (f) Complementary region to image d as viewed through a rhodamine filter. PAH-citrate aggregates appear as dark spots. (g) Complementary region to image e as viewed through a rhodamine filter. The PAH gel appears dark, and droplets of citrate appear red because of the presence of dextran-Rh. (All scale bars are 20 μm)..... 216
- Figure 6.18:** Schematic of structures from R ratio and flow dependent PAH-interactions in microchannels..... 218

- Figure 6.19:** Gel profiles that emerge from interactions of PAH with citric acid. The pH of PAH was 4.38 and the pH of citric acid was varied to span its 3 pK_a values. R ratios of reactants were fixed at 50 and flow rate was maintained at 25 mL/hr. Bright Field (a) and Fluorescence images (b) when pH of citric acid stream was 8.38 (where it is predominantly in the trivalent (Cit^{3-}) state). Bright field (c) and Fluorescence (d) images when pH of citric acid stream was 6.39 (corresponds to pK_a value of citric acid where it co-exists as Cit^{3-} and HCit^{2-} in a 1:1 ratio). Bright field (e) and Fluorescence (f) images when pH of citric acid stream was 5.56 (where HCit^{2-} was at its highest theoretical level (77%)). Bright field (g) and Fluorescence (h) images when pH of citric acid stream was 4.77 (corresponds to pK_a value of citric acid where it coexists as HCit^{2-} and H_2Cit^- in a 1:1 ratio). Bright field (i) and Fluorescence (j) images when pH of citric acid stream was 4.0 (where H_2Cit^- is at its highest theoretical level (77%)). Bright field (k) and Fluorescence (l) images when pH of citric acid stream was 3.14 (pK_a value of citric acid where it coexists as $\text{H}_2\text{Cit}^{1-}$ and H_3Cit^0 in a 1:1 ratio). Bright field (m) Fluorescence (n) images when pH of citric acid stream was 1.38 (where citric acid exists predominantly in monovalent (H_3Cit^0 : > 97%) state). (All Scale Bars: 50 μm)..... 223
- Figure 6.20:** Fluorescence image when pH of PAH stream was adjusted to 10.25 (where it is uncharged: pK_a of PAH = 8.5) and the pH of citric acid was 8.38 (where it exists predominantly as Cit^{3-}). R ratios of reactants were fixed at 50 and flow rate was maintained at 25 mL/hr. No reaction occurred of PAH and citrate under these conditions (Scale bar: 50 μm)..... 224
- Figure 6.21:** Experiment to show the formation of nanoparticle assembled capsules (NACs) in a microfluidic device. (i) PAH-RITC and citrate flowed based on conditions in state diagram (Fig. 6.12) ($R = 10$, PAH = 1 mg/mL, flow rate = 25 $\mu\text{L/hr}$) to form aggregate-like structures. (ii) All flow streams replaced by 20 wt.%, SiO_2 NP stream. If aggregates had indeed formed in schematic (i), reaction configuration in schematic (ii) should result in NAC formation. (iii) Fluorescence images of NAC-like structures formed in microfluidic environment. (iv) Bright field image of NAC-like structures analyzed outside of the microfluidic on a glass-slide. Characteristic NAC-like behavior observed in that, the structures were in Brownian motion (v) Scanning electron microscope (SEM) images of structures formed from schematic (ii) confirm formation of NACs. Hence, structures formed from schematic (i) were indeed aggregates of PAH-citrate..... 226

Figure 7.1:	Electrostatic self-assembly (ESA) scheme to assemble oppositely charged nanoparticles into superlattices with open-pack diamond-like structure	240
Figure 7.2:	Electrostatic self-assembly (ESA) scheme to assemble oppositely charged nanoparticles using commercial surfactants (NP = CdSe QDs).....	241
Figure 7.3:	Irreversible migration of QDs (top panel) and C-Dots (bottom panel) from seawater to isooctane when the system is heated to 90 °C (above the cloud point of the surfactant Neodol 91-7) and cooled back to room temperature.....	243
Figure 7.4:	Schematic for delivery of signaling molecules loaded on a NP into oil domains within a reservoir.....	245
Figure 7.5:	(i) Increase-decrease pH cycle – gel thickness profile and (ii) Decrease-increase pH cycle – gel thickness profile for PAH-citrate gels formed, under conditions of R ratio = 50 (PAH = 1 mg/mL) and flow rate of 25 mL/hr.....	246
Figure 7.6:	(i) Schematic of the aldol condensation reaction (ii) Schematic for forming hybrid polyamine-glutaraldehyde gels.....	247
Figure 7.7:	Stability of PAH-Citrate-Glutaraldehyde Gels (i) in environments of (ii) water and mineral oil (iii). All scale bars are 50 μm	248
Figure 7.8:	Nanoparticle assembled capsules (NACs) of PAH, citrate and silica NPs formed in a microchannel with flow-focusing geometry with varying levels of NP coverage.....	249
Figure A1:	Dark-field digital images of CdSe QD fluorescence in three different environments upon excitation by a UV-lamp source. In each set comprising a triad, the left sample is QDs in hexane, the middle sample is QDs in plain/deionized (DI)-water micelles of AOT and the right sample is QDs in salty-water micelles of AOT. CdSe QD Types: Clockwise from Left – Red dots (5.79 nm), Green dots (2.68 nm), Yellow-Green dots (2.85 nm) and Yellow dots (3.26 nm). The measured quantum yields for the yellow-green dots (from left to right) are 14%, 3% and 5% respectively.....	253

Figure A2:	Results from thermogravimetric analysis of (a) CdSe+OA from hexane (b) CdSe+OA+AOT from 'no-salt' water, (c) CdSe+OA+AOT from 'salty' water and (d) AOT only. ('OA' refers to oleic acid).....	254
Figure A3:	Nile red PL spectra at various stages of the phase transfer process (up to 60 minutes).....	255
Figure A4:	(a) UV-vis spectra and (b) photograph of CdSe QDs phase transferred in DI water and 3 g/L NaCl solution with CTAB as the phase transfer agent.....	256
Figure A5:	(a) UV-vis spectra and (b) photograph of CdSe QDs phase transferred in DI water and (b) 0.38 g/L Na ₂ SO ₄ solution with AOT as the phase transfer agent.....	256
Figure A6:	(a) UV-vis spectra and (b) photograph of CdSe QDs phase transferred in DI water and (b) 0.05 g/L CaCl ₂ solution with AOT as the phase transfer agent.....	257
Figure B1:	Octane drop size study with respect to time in Octane/Brine nanoemulsions obtained by diluting 60/30/10 (top) and 80/10/10 (bottom) Octane/AOT/Water microemulsions in different levels of excess brine (AOT = 1.5 g/L).....	258
Figure B2:	Octane drop size study with respect to time in Octane/Brine nanoemulsions obtained by diluting 70/20/10 Octane/AOT/Brine (%ε = 0.2) (top) and 70/20/10 Octane/AOT/Brine (%ε = 0.4) (bottom) microemulsions in different levels of excess brine (AOT = 1.5 g/L).....	259
Figure B3:	Zeta potential of Octane/Brine nanoemulsions obtained by diluting 60/30/10 (top) and 80/10/10 (bottom) Octane/AOT/Water microemulsions in different levels of excess brine (AOT = 1.5 g/L).....	260
Figure B4:	Plots of R ³ vs. t for nanoemulsions prepared by diluting 70/20/10 Octane/AOT/Brine microemulsions with different levels of internal salinity (%ε = 0, 0.2, 0.3 and 0.4) in excess water (%ε = 0, Winsor I). AOT = 1.5 g/L).....	261
Figure C1:	Experimental and fitted results for ³ H ₂ O transport through calcite, 0.55M Synthetic seawater background, 25 °C. R and D values were estimated at 1 and 0.012 cm ² min ⁻¹ respectively.....	264

Figure C2:	Breakthrough profiles of QD/Neodol in (a) 0.54M synthetic seawater (b) 1M NaCl. At PV ~ 3.0-3.5, the inlet QD/Neodol formulations were replaced by solutions with respective background salinities. The error bar on C_{exit}/C_0 was $\pm 2\%$	266
Figure C3:	Sensitivity analysis of 1D advection-dispersion equation by varying R while keeping D and γ constant.....	268
Figure C4:	Sensitivity analysis of 1D advection-dispersion equation by varying D while keeping R and γ constant.....	268
Figure C5:	Sensitivity analysis of 1D advection-dispersion equation by varying γ while keeping R and D constant.....	269

List of Tables

Table 2.1:	Hydrodynamic diameter, zeta potential measurements and charge density estimations for different NPs phase transferred in no-salt and salt water (3 g-NaCl/L).....	63
Table 3.1:	Population distribution of octane nanoemulsions at select time points showing unimodal distribution when 70/20/10 Octane/AOT/Water microemulsions were diluted in excess water ($\% \varepsilon = 0$, AOT = 1.5 g/L).....	102
Table 3.2:	Comparison of experimentally measured and theoretically calculated Ostwald Ripening Rates of octane/water nanoemulsions when excess brine is zero ($\% \varepsilon = 0$, AOT = 1.5 g/L).....	105
Table 3.3:	Population distribution of octane nanoemulsions at select time points showing bimodal distribution when 70/20/10 Octane/AOT/Water microemulsions were diluted in excess brine ($\% \varepsilon = 0.2$, AOT = 1.5 g/L).....	110
Table 3.4:	Population distribution of octane droplets at select time points showing unimodal and bimodal distributions when 70/20/10 Octane/AOT/Water microemulsions were diluted in excess brine ($\% \varepsilon = 0.3$, AOT = 1.5 g/L).....	115
Table 4.1:	Parameters used for QD/Neodol breakthrough experiments.....	153
Table 4.2:	Percent recovery of QDs from calcite packed columns at different temperatures.....	154
Table 4.3:	Transport coefficients of QD/Neodol flow through calcite packed columns.....	159
Table 6.1:	Characteristics of PAH gelation upon varying pH of citric acid (The pH of PAH was fixed at 4.38).....	222
Table C1:	Parameters used for QD/Neodol breakthrough experiments in quartz sand.....	265
Table C2:	Percent recovery of QDs from quartz packed columns at different temperatures.....	267

Chapter 1

Background and Research Motivation

1.1 Nanotechnology: Arrival of a New Research Theme

The field of nanotechnology focuses on investigations and applications of size-dependent properties demonstrated by nanomaterials at length scales of 100 nm and below (1 nm = 10^{-9} m).¹⁻⁴ It was arguably Feynman's seminal lecture in 1959, "There's plenty of room at the bottom" that laid the foundation to concepts such as miniaturization and molecular machines.¹ This galvanized a movement that resulted in rapid scientific advances and the discovery of size-dependent optical,⁵⁻⁸ magnetic,⁹⁻¹² electrical,¹³⁻¹⁵ thermal¹⁶ and catalytic^{13, 17, 18} properties of nanoscale materials. Importantly, properties demonstrated by nanoparticles (NPs) at length scales of 100 nm and below were found to differ significantly from their bulk counterparts.

Understanding nanoscale properties and utilizing them for useful and commercial applications has made nanotechnology the most prominent research theme of the past three decades across global academia and industry. This is reflected in the systematic increase of global funding towards the nanotechnology research initiative (Fig. 1.1).¹⁹ In addition, the number of nanotechnology-based patents issued by various patent and trademark offices worldwide (United States PTO, Europe PO and Japan PO) has seen a significant increase indicating the rise in nanotechnology-related research (Fig. 1.2). This has been most dramatic in the recently concluded decade of 2000-2009, where nanotechnology-based patents that were granted increased from practically non-existent numbers in 1970-2000 to around two thousand, marking a 20-fold rise (Fig. 1.3).²⁰ It is therefore apparent that nanotechnology will be a key factor for every academic and corporate institution's survival and growth strategy in the decades to follow.

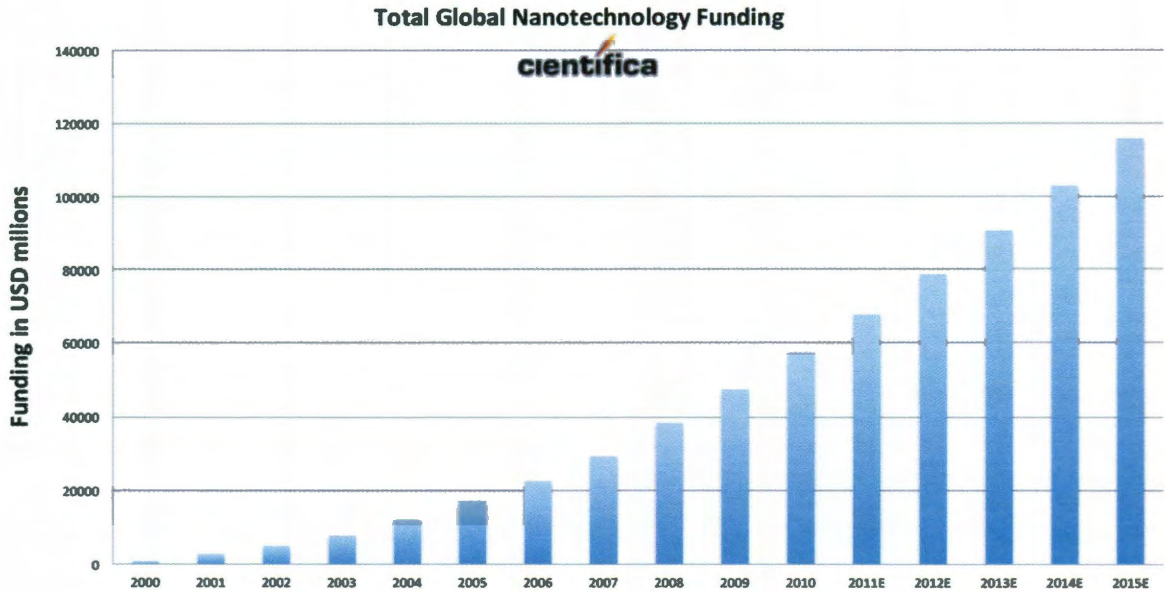


Figure 1.1: Current and forecasted global funding for nanotechnology research projects (Figure adapted from www.Cientifica.com).

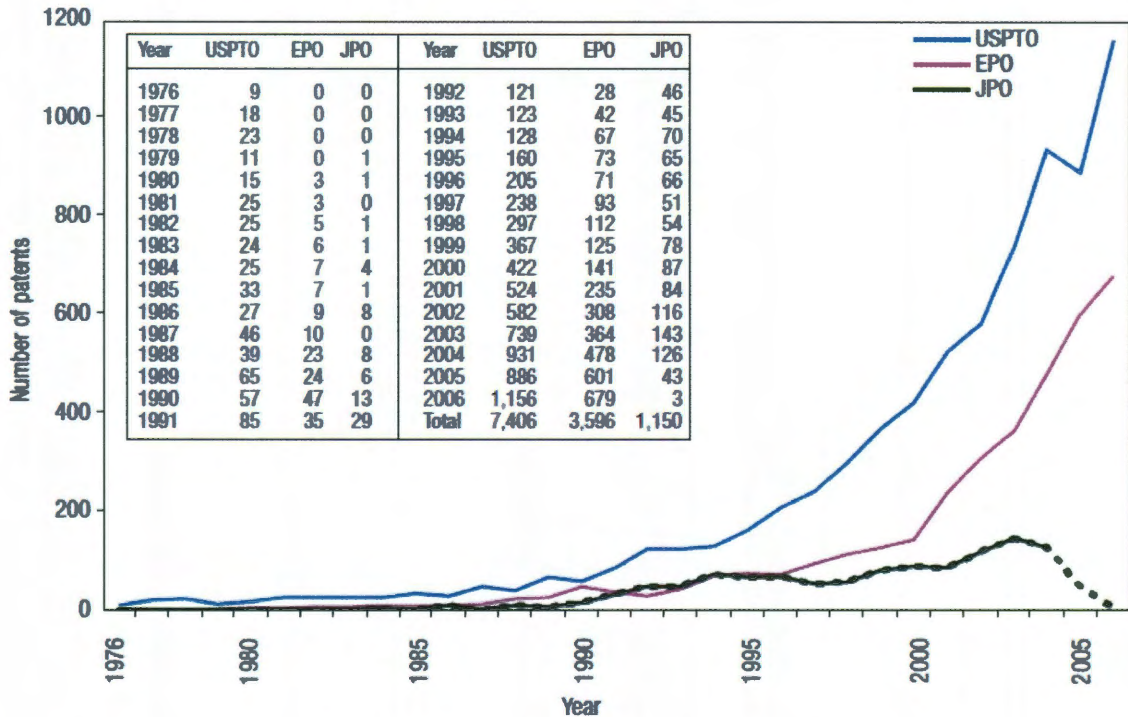


Figure 1.2: Number of nanotechnology patents published by the USPTO, EPO and JPO in the past 3 decades (Figure adapted from Chen *et al*).

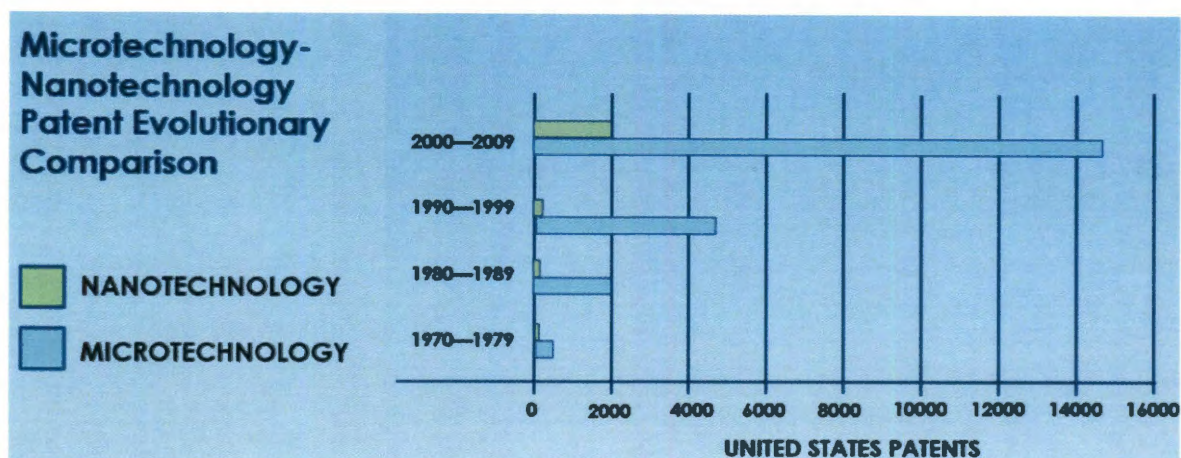


Figure 1.3: Number of patents issued for nanotechnology-based inventions vs. microtechnology-based inventions (Figure adapted from <http://smlperspectives.com>).

In terms of the impacts nanotechnology has made, its presence today is ubiquitous and has revolutionized practically all areas of research. Alongside Feynman's vision for miniaturization and molecular machines, nanotechnology holds the key to directly address at least four (energy, environment, terrorism/war and disease) of the ten world problems faced by humanity as identified by Rice chemist and Nobel-laureate Richard Smalley.²¹ Of these problems, the greatest problem that is currently facing humanity is the need for reliable, stable, and sustainable energy. In the following section, a brief overview is provided of recent impacts of nanotechnology in the area of energy.

1.2 Critical Impact Area of Nanotechnology: Energy

In the 2004 talk titled "Future Global Energy Prosperity: The Terawatt Challenge," Smalley called for the identification of reliable, stable, sustainable, and inexpensive sources of energy to solve the top problem that humanity is faced with.²¹ There are several ways that nanotechnology could be used to solve the energy problem; namely by producing, storing, and/or distributing energy. For instance, the use of new nanomaterials

such as carbon nanotube (CNT) wires was advocated to improve the efficiency of energy transmission.²¹⁻²³ Losses on account of resistive heating commonly associated with existing copper-based transmission cables could be overcome by this new technology, resulting in significant energy savings and lowering of production costs. These findings have made parallel impacts in the microelectronics industry where CNT-based interconnects are viewed as serious contenders to replace copper in order to sustain industry demands for higher device speed and greater miniaturization while also minimizing heat and sound production.^{23,24}

With respect to energy production and storage, nanomaterials such as photovoltaics¹⁵ could make solar cells a reality and address the renewable energy challenge. Furthermore, nanotechnology-based approaches such as pore-silicon technology¹⁹ and lithium-intercalation technology²⁵⁻²⁸ are high-potential candidates for the next generation of lithium-ion batteries^{19,23} and will significantly increase battery life and capacity.

Nanotechnology also has important parts to play in traditional areas of energy. The nanotechnology initiative of the Advanced Energy Consortium (AEC) champions the design of nanoreporters, nanomaterials with signaling, sensing, and detection capabilities for oil exploration and reservoir characterization. The grand objective here is to retrieve real-time and spatially-resolved physical (e.g., temperature, pressure, rock porosity, and permeability) and chemical (e.g., oil, water, gas and mineral type) information of an oil reservoir upon downhole injection of transportable nanoparticles (Fig. 1.4).²⁹⁻³³ The AEC further plans to use nanotechnology to develop the next-generation chemical and CO₂-foam based approaches for enhanced oil recovery (EOR).

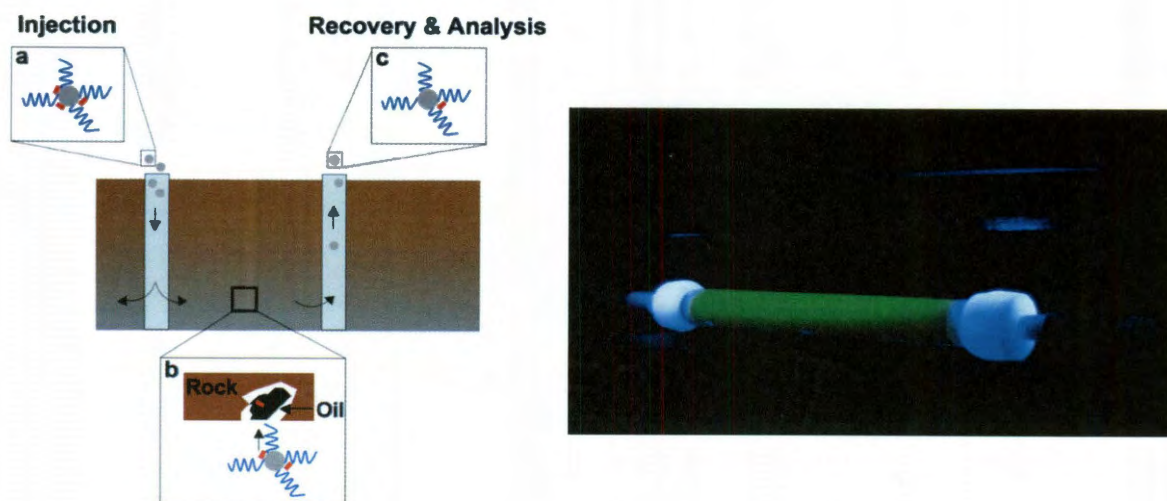


Figure 1.4: (Left) Schematic of flow of a nanoreporter with signaling molecules, through oil-saturated porous media. (Right) Flow of QDs as model nanoreporters through oil-free crushed calcite in a background of seawater. Excitation under a UV-Lamp shows illumination of the reservoir column from photoluminescence of QDs (Schematic at left is adapted from Berlin *et al*).

1.3 The Need for Stable Aqueous Nanoparticle Suspensions

In order to use NPs as nanoreporters they must be suspended in aqueous saline solutions (concentrations close to seawater) at high temperatures (~50-70 deg C) since these are common reservoir conditions. While NPs can be synthesized directly in aqueous media, limited control is obtainable in terms of size. Furthermore, a polydisperse NP population is often obtained from water-phase synthesis, leading to reduction in nanoscale properties. To overcome these limitations, NPs are thus typically synthesized in organic solvents, where a non-polar environment yields high degree of control in size and monodispersity.³⁸⁻⁴⁶ Once synthesized, it would be important to devise approaches to transfer NPs from oil phase to water.^{35, 36} In addition to oil-exploration and reservoir characterization, NPs in aqueous suspensions can be applied to numerous fields including medicine, catalysis, and environmental remediation. This leads me to describe the

motivation and layout of this thesis starting with an introduction of a new method of nanoparticle transfer which we devised. Such details and more are provided in the section below.

1.4 Research Motivation and Layout of the Thesis

The primary goal of this thesis was to formulate single-particle aqueous NP suspensions by developing a generic bilayer approach for NP phase-transfer using commercial surfactants.⁴⁷ In a previous transfer approach pioneered by Brinker and coworkers,⁴⁸ oil that contained NPs was dispersed in water to form oil-in-water emulsions upon which the emulsion was heated and oil was boiled off. In the process, surfactants formed bilayers with hydrophobic groups native to the NPs and rendered them water-dispersible.^{36, 49-52} This route was limited by low transfer efficiencies and transfer of NPs as aggregated clusters. The latter feature along with the laterally "loose" nature of the micelle were seen to adversely impact the optical properties of CdSe QDs, as evidenced by low photoluminescence (PL) and low values of quantum yield (QY). It has since remained a challenge to devise approaches that transfer NPs to water efficiently and effectively, without compromising their stability and properties.

We discovered a simple process modification in the addition of salt to water during the stage of emulsion formation by which phase-transfer of NPs could be strongly enhanced. NPs were found to transfer into salt-containing water as single NPs and within laterally compact micelles that better protected optical properties of QDs. The role of electrolyte in affecting NP phase-transfer is the subject of Chapter 2 of this thesis. With a model system constituting CdSe QDs as NPs, Aerosol-OT (AOT) as the surfactant and

NaCl as the salt, we found that over 90% QDs could be successfully transferred from hexane to salty-micelles of AOT, a number significantly higher than the 45-55% QDs that transferred to DI-water micelles of AOT. QDs in salty-micelles of AOT existed as single particles in contrast to clusters of 8-10 particles of QDs in DI micelles. The encapsulating salty-micelles rendered higher surfactant coverage and lateral compactness over the DI-micelle counterpart from "salting-out" of surfactants and screening of head-group repulsions by the salt ions (Fig. 1.5). Thus, optical properties of QDs such as PL and QY were better retained in salty-micelles.

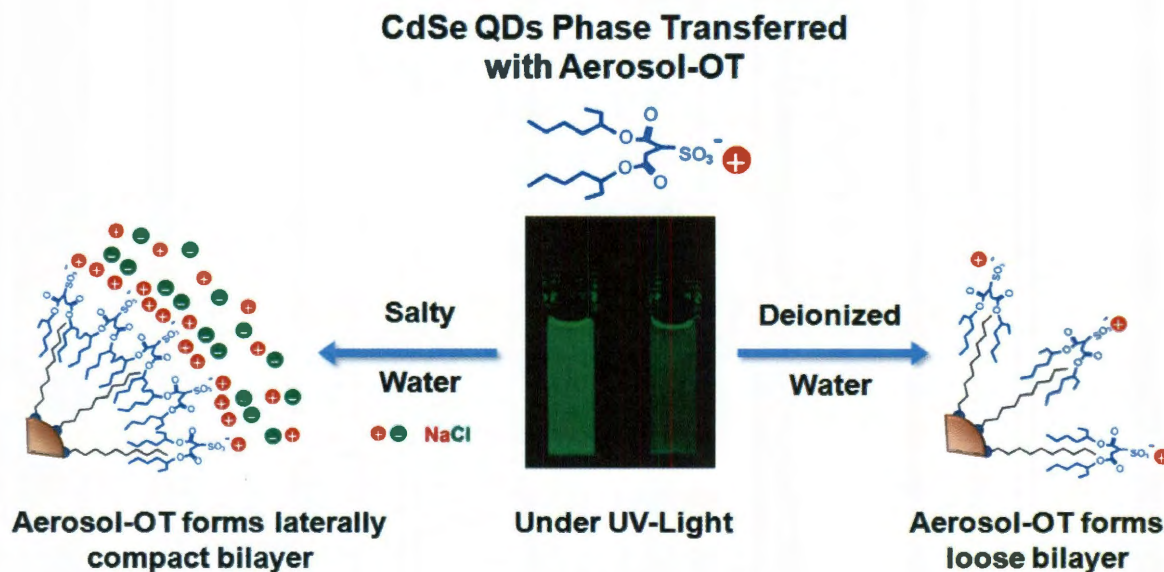


Figure 1.5: CdSe QDs transfer to salty-water within laterally compact bilayers of Aerosol-OT and to deionized water within loose bilayers of Aerosol-OT.

This work resulted in a publication in the *Journal of Physical Chemistry C*,⁵³ an assigned patent (WO/2010/019390),⁵⁴ and the best applied paper in Chemical Engineering (2010-2011) awarded by the American Institute of Chemical Engineers' - South Texas Society (AIChE-STC) regional chapter. The strength of this new approach lies in its simplicity and generic nature. The transfer scheme was found to be valid across different NP,

surfactant, and salt types. With the possible use of commercial grade surfactants, the process is now economically viable for many applications, including the design of nanoreporters and microfluidic formation of gels and nanoparticle assembled capsules which are the subjects of Chapters 4-6.

In Chapter 3, we studied a secondary function of NaCl-salt in emulsifying a hydrocarbon by the mechanism of spontaneous emulsification. This effect was seen to impact NP transfer yield, where smaller-sized hydrocarbon droplets that were stable to coalescence allowed for higher transfer efficiencies of QDs. Using AOT as the surfactant, emulsions of hexane-in-water and octane-in-water were found to phase-separate at shorter time scales when formed in DI water over salty-water (NaCl concentration = 3 g/L).

Nanoemulsions were seen to form spontaneously when Water-in-Oil (W/O) or Brine-in-Oil (B/O) microemulsions of a hydrocarbon (oil: octane), anionic surfactant (AOT) and water or NaCl-brine were diluted in varying levels of excess brine. The mechanism of emulsification was local supersaturation and nucleation of oil during the inversion process. For nanoemulsions formed in Winsor I, octane drops increased from initial levels of 150-250 nm to 500 nm - 1 μm over 24 hours. Growth followed an Ostwald ripening mechanism but reached the asymptotic stage described by the LSW theory only for dilution with salt-free water (Fig. 1.6). At the cross-over salinity (Winsor III), the nanoemulsions showed minimal growth with droplet size consistently remaining below 100 nm over 24 hours. Optical microscopy suggested that drops in both Winsor I and Winsor III regions were coated with a layer of the lamellar liquid crystal. The slower

growth at higher salinities was likely due to thicker layers for these conditions where surfactant films have low spontaneous curvature.

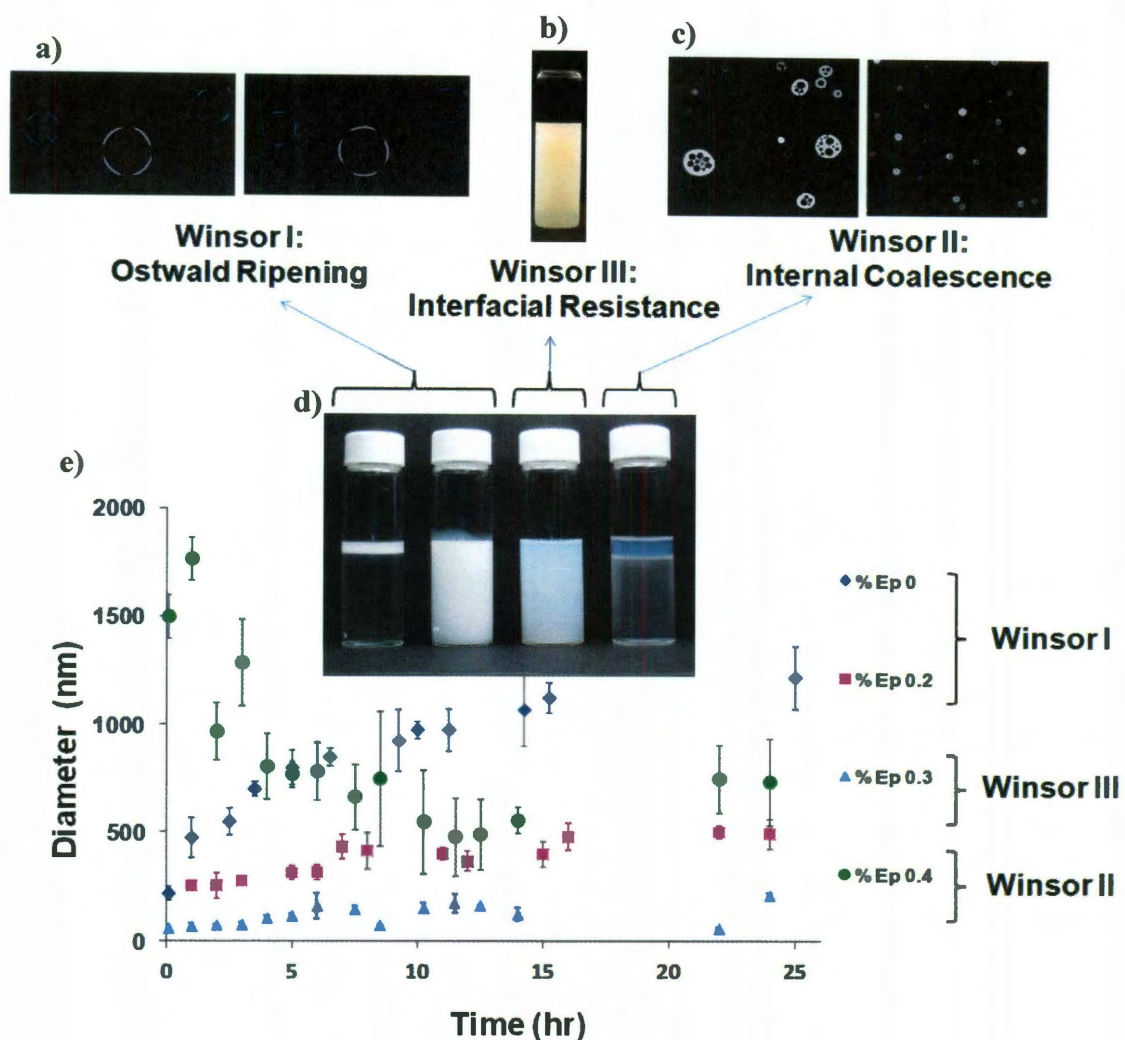


Figure 1.6: Upper inset shows a) birefringence from liquid crystal coating of AOT on octane droplets in Winsor I observed using cross-polarized microscopy, b) a visual image of octane in water nanoemulsions prepared at the cross-over salinity (Winsor III) under cross-polarizers, and c) multiple W/O/W emulsions observed using fluorescence microscopy. The middle inset (d) provides a visual comparison of the various octane/brine nanoemulsions formed in different Winsor domains after 28 days and the lower inset (e) shows the time-dependent droplet diameters of octane/brine nanoemulsions formed in different Winsor domains.

When nanoemulsions were prepared at salinity levels of the Winsor II domain, drops greater than 1 μm were consistently recorded for the first 5-7 hours after which size decreased to values below 1 μm that indicated droplet shrinkage. The large initial drops were from W/O/W multiple emulsions formed at a salinity that favored formation of W/O emulsions but with a large excess of water added during dilution. The number of internal water drops in multiple emulsions was found to decrease over time, but not their size, indicating coalescence of internal drops with the continuous water phase as one mechanism of drop shrinkage.

The influence of salinity in nucleating octane droplets and subsequent stabilization of octane by the lamellar phase of AOT were factors dominant in determining the initial droplet size of the nanoemulsion and droplet growth trends. The high charge on octane droplets helped assure stability to flocculation and coalescence, thereby allowing Ostwald ripening and mass transfer to control growth in the Winsor I and III regions, thus contributing to the stable nature of nanoemulsions. This work has been written as a manuscript and is due for submission in a topical journal of colloids.⁵⁵ This work was also presented in the oral sessions of Emulsions and Foams during the AIChE annual conferences at Philadelphia (2008) and Salt Lake City (2010).

In Chapter 4 of this thesis, we show how our method to phase-transfer NPs from oil to water can be used to design QD nanoreporters for downhole applications in oil exploration and recovery. While transport of colloidal NPs through porous media has been well-studied at ambient temperature and in low-to-zero salinity waters of aquatic systems, the possible downhole use of NPs has been severely challenged by the high salinity and temperature of petroleum reservoirs. We found that oleic acid-coated, 3-nm

CdSe quantum dots (QDs) with an outer coating of nonionic ethoxylated alcohol surfactant Neodol 91-7 demonstrated excellent colloidal stability in high-salt-content water (Fig. 1.7).

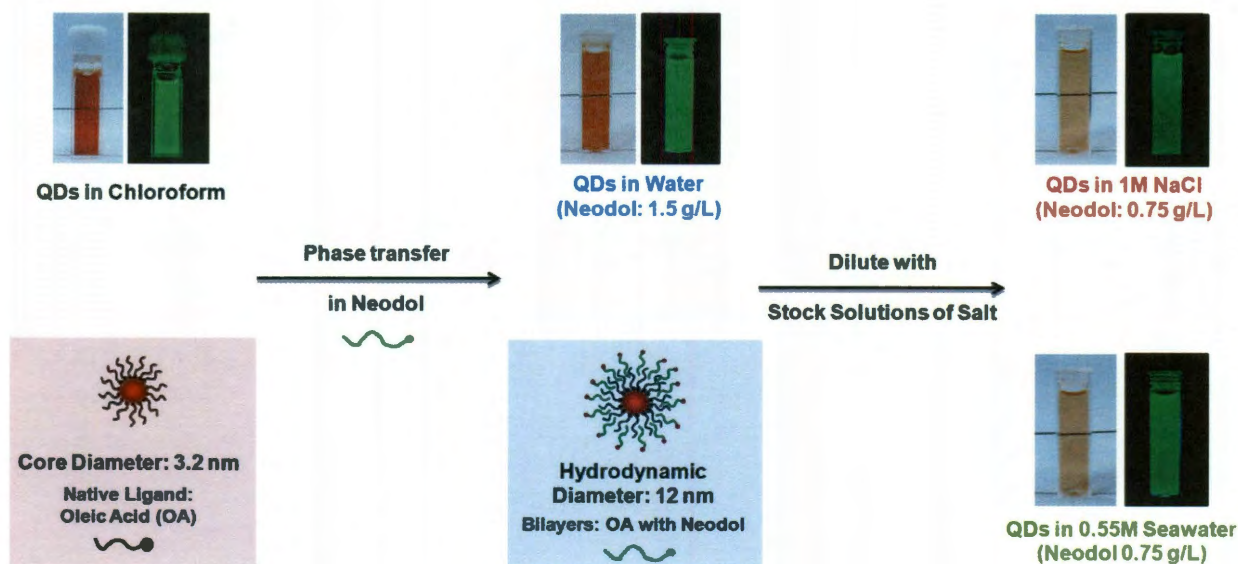


Figure 1.7: QD suspensions prepared in high salinity water (1M NaCl and 0.55M Seawater).

The QDs showed little aggregation in 1M NaCl and synthetic seawater (ionic strength 0.55M), according to dynamic light scattering analysis. They were also stable in the temperature range of 25-70°C, with the upper limit set by the cloud point temperature of the nonionic surfactant. As a model for non-aggregated salt-stable NPs, the QDs showed essentially unimpeded flow through packed columns of either crushed calcite or quartz sand, with >98% recovery under a wide range of salinities and temperatures. This work has been written as a manuscript to be submitted to a topical journal of nanotechnology. This work was also presented at the Advanced Energy Consortium's (AEC) bi-annual reviews in Austin (December 2010) and Boston (June 2011).⁵⁶

In Chapter 5, we describe approaches to extend colloidal stability of NPs to temperatures up to 100 °C under salinities of 1M NaCl, 1M KCl, 0.55M synthetic seawater and 1.77M ionic strength API brine (Fig. 1.8). These studies were conducted using carbon dots (C-Dot) since such NPs are more suitable for field studies than the QDs used for our earlier model nanoreporter studies.

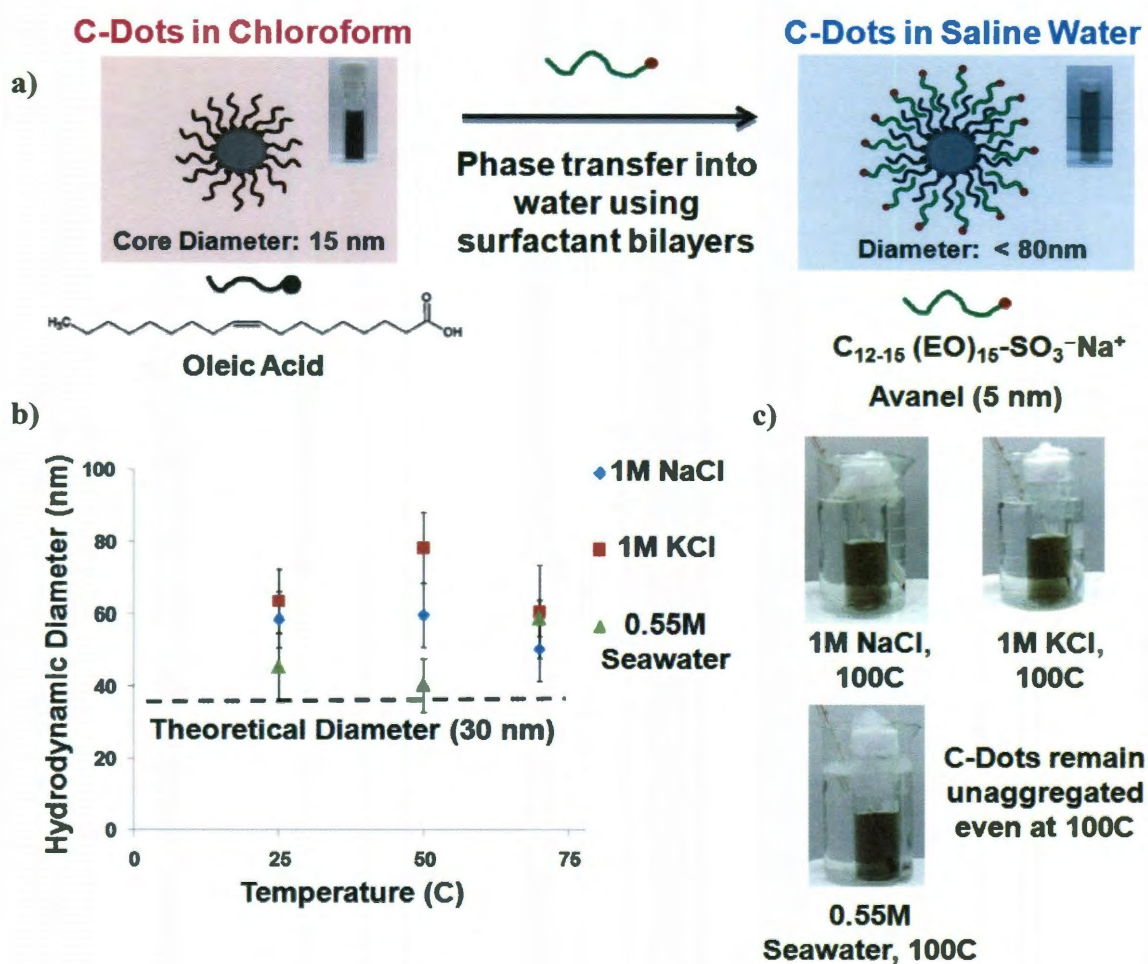


Figure 1.8: a) Schematic of process used to phase-transfer carbon dots from chloroform to saline water. b) Change in C-Dot diameters as a function of temperature in different salt solutions. c) Visual comparison of C-dot suspensions prepared in high salinity water (1M NaCl, 1M KCl and 0.55M Seawater) at 100 °C.

This was achieved through the selection of a hybrid surfactant with nonionic and anionic groups on the same molecule. The nonionic component of the surfactant rendered the molecule saline stable and the anionic component rendered it temperature stable. Having both groups on the same chain circumvented non-trivial challenges associated with formulating mixed micelles of nonionic and anionic surfactants. Furthermore, the prevalent use of hybrid surfactants in areas of EOR makes it easy to introduce nanoreporters as a component of the background fluid. Using Avanel S150 CGN as the surfactant, NPs such as QDs and C-Dots were made stable to aggregation. Avanel coated C-Dots showed unimpeded and tracer-like flow through calcite and quartz sand up to 70 °C.

In Chapter 6, an interesting spin-off application of the bilayer phase-transfer method was investigated in the study of tandem self-assembly of a cationic polymer, multivalent salt and NPs in laminar flow environments of a microchannel. In investigating tandem assembly, we found a unique and interesting behavior in that the polymer underwent ionic cross-linking by citrate ions to form viscoelastic gel phases. This trend differed from the formation of PAH-citrate aggregates under convection-dominant mixing in a beaker.⁵⁷ Given the compelling application of *in situ* gelation at a desired location in microchannels as possible flow regulatory devices,⁵⁸ we investigated the mechanism of gelation in the space of charge ratio of reactants, flow rates, and pH.⁵⁹ Gelation was found to occur in the polymer stream and not the citrate stream due to an appreciably higher diffusivity of citrate ions when compared to the gel and PAH, and due to laminar flow conditions in the microfluidic environment. Gel formation occurred when pH of the PAH stream was below the PAH pK_a value of 8.38 and when citrate was either

in disodium or trisodium forms. Gelation of PAH began with the formation of colloidal aggregates of PAH and citrate, which combined under shear flow to form non-continuous or continuous gels. Droplets of citrate formed within regions of continuous gels, as excess citrate anions diffused into the gel stream (Fig. 1.9).

NAC formation in microchannels was shown to be feasible, although under a narrow operating range of flow rate, charge ratio, and pH. These results were published in *Langmuir* and presented in the oral sessions of Microfluidics and Small Scale Flows, during the AIChE annual conferences in Salt Lake City (2007), Philadelphia (2008), and Nashville (2009).⁵⁹

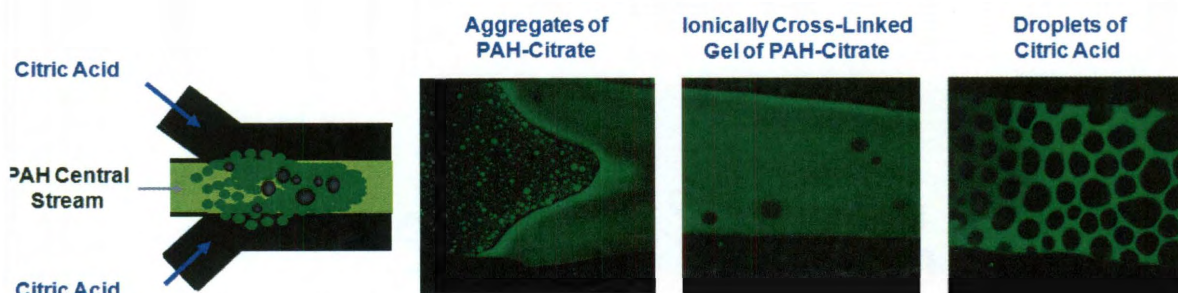


Figure 1.9: Ionic cross-linking of polyamine gels of PAH-citrate in a microfluidic channel.

A broader review article on the synthesis methods of nanoparticle assembled hollow constructs and their applications was published as a review article in *Advances in Polymer Science*.¹⁶ This thesis concludes in Chapter 7 with a summary of the results presented in Chapters 2-6 and recommendations for future work.

1.5 References

1. Drexler, K. E., *Nanosystems: Molecular Machinery, Manufacturing, and Computation*. Wiley: 1992.
2. <http://www.nano.gov/> National Nanotechnology Initiative.
3. Hodes, G., When small is different: Some recent advances in concepts and applications of nanoscale phenomena. *Advanced Materials* **2007**, 19, (5), 639-655.
4. Gullapalli, S.; Wong, M. S., Nanotechnology: A Guide to Nano-Objects. *Chemical Engineering Progress* **2011**, 107, (5), 28-32.
5. Smith, A. M.; Duan, H. W.; Mohs, A. M.; Nie, S. M., Bioconjugated quantum dots for in vivo molecular and cellular imaging. *Advanced Drug Delivery Reviews* **2008**, 60, (11), 1226-1240.
6. Biju, V.; Itoh, T.; Anas, A.; Sujith, A.; Ishikawa, M., Semiconductor quantum dots and metal nanoparticles: syntheses, optical properties, and biological applications. *Analytical and Bioanalytical Chemistry* **2008**, 391, (7), 2469-2495.
7. Murray, C. B.; Kagan, C. R.; Bawendi, M. G., Synthesis and characterization of monodisperse nanocrystals and close-packed nanocrystal assemblies. *Annual Review of Materials Science* **2000**, 30, 545-610.
8. Yu, W. W.; Peng, X. G., Formation of high-quality CdS and other II-VI semiconductor nanocrystals in noncoordinating solvents: Tunable reactivity of monomers. *Angewandte Chemie-International Edition* **2002**, 41, (13), 2368-2371.
9. Sun, C.; Lee, J. S. H.; Zhang, M. Q., Magnetic nanoparticles in MR imaging and drug delivery. *Advanced Drug Delivery Reviews* **2008**, 60, (11), 1252-1265.
10. Lin, J. J.; Chen, J. S.; Huang, S. J.; Ko, J. H.; Wang, Y. M.; Chen, T. L.; Wang, L. F., Folic acid-Pluronic F127 magnetic nanoparticle clusters for combined targeting, diagnosis, and therapy applications. *Biomaterials* **2009**, 30, (28), 5114-5124.
11. Nagesha, D. K.; Plouffe, B. D.; Phan, M.; Lewis, L. H.; Sridhar, S.; Murthy, S. K., Functionalization-induced improvement in magnetic properties of Fe₃O₄ nanoparticles for biomedical applications. *Journal of Applied Physics* **2009**, 105, (7).

12. Yavuz, C. T.; Mayo, J. T.; Yu, W. W.; Prakash, A.; Falkner, J. C.; Yean, S.; Cong, L. L.; Shipley, H. J.; Kan, A.; Tomson, M.; Natelson, D.; Colvin, V. L., Low-field magnetic separation of monodisperse Fe₃O₄ nanocrystals. *Science* **2006**, 314, (5801), 964-967.
13. Hildebrand, H.; Mackenzie, K.; Kopinke, F. D., Pd/Fe₃O₄ nano-catalysts for selective dehalogenation in wastewater treatment processes-Influence of water constituents. *Applied Catalysis B-Environmental* **2009**, 91, (1-2), 389-396.
14. Shipway, A. N.; Katz, E.; Willner, I., Nanoparticle arrays on surfaces for electronic, optical, and sensor applications. *Chemphyschem* **2000**, 1, (1), 18-52.
15. Asokan, S.; Krueger, K. M.; Colvin, V. L.; Wong, M. S., Shape-controlled synthesis of CdSe tetrapods using cationic surfactant ligands. *Small* **2007**, 3, (7), 1164-1169.
16. Kini, G. C.; Biswal, S. L.; Wong, M. S., Non-Layer-by-Layer Assembly and Encapsulation Uses of Nanoparticle-Shelled Hollow Spheres. In *Modern Techniques for Nano- and Microreactors/-Reactions*, Caruso, F., Ed. 2010; Vol. 229, pp 89-114.
17. Hildebrand, H.; Mackenzie, K.; Kopinke, F. D., Highly Active Pd-on-Magnetite Nanocatalysts for Aqueous Phase Hydrodechlorination Reactions. *Environmental Science & Technology* **2009**, 43, (9), 3254-3259.
18. Gopidas, K. R.; Whitesell, J. K.; Fox, M. A., Synthesis, characterization, and catalytic applications of a palladium-nanoparticle-cored dendrimer. *Nano Letters* **2003**, 3, (12), 1757-1760.
19. <http://cientifica.eu/blog/wp-content/uploads/downloads/2011/07/Global-Nanotechnology-Funding-Report-2011.pdf>
20. Chen, H. C.; Roco, M. C.; Li, X.; Lin, Y. L., Trends in nanotechnology patents. *Nature Nanotechnology* **2008**, 3, (3), 123-125.
21. Smalley, R. E., Future Global Energy *MRS Bulletin* **2005**, 30, 412-417.
22. Evans, J., Nanotechnology Carbon nanotube cables. *Chemistry & Industry* **2011**, (15), 6-6.

23. Ajayan, P. M.; Zhou, O. Z., Applications of carbon nanotubes. *Carbon Nanotubes* **2001**, 80, 391-425.
24. Kaushik, B. K.; Goel, S.; Rauthan, G., Future VLSI interconnects: optical fiber or carbon nanotube - a review. *Microelectronics International* **2007**, 24, (2), 53-63.
25. Gowda, S. R.; Reddy, A.; Zhan, X. B.; Ajayan, P. M., Building Energy Storage Device on a Single Nanowire. *Nano Letters* **2011**, 11, (8), 3329-3333.
26. Gowda, S. R.; Reddy, A. L. M.; Shaijumon, M. M.; Zhan, X. B.; Ci, L. J.; Ajayan, P. M., Conformal Coating of Thin Polymer Electrolyte Layer on Nanostructured Electrode Materials for Three-Dimensional Battery Applications. *Nano Letters* **2011**, 11, (1), 101-106.
27. Goyal, A.; Reddy, A. L. M.; Ajayan, P. M., Flexible Carbon Nanotube-Cu₂O Hybrid Electrodes for Li-Ion Batteries. *Small* **2011**, 7, (12), 1709-1713.
28. Kumar, A.; Reddy, A. L. M.; Mukherjee, A.; Dubey, M.; Zhan, X. B.; Singh, N.; Ci, L.; Billups, W. E.; Nagurny, J.; Mital, G.; Ajayan, P. M., Direct Synthesis of Lithium-Intercalated Graphene for Electrochemical Energy Storage Application. *ACS Nano* **2011**, 5, (6), 4345-4349.
29. Johnson, K., Nanoscale Technologies Leap Frog from Science Fiction into Real World Engineering. *The American Oil and Gas Reporter* 2010, pp 112-123.
30. Barron, A. R.; Tour, J. M.; Busnaina, A.; Jung, Y. J.; Somu, S.; Kanj, M. Y.; Potter, D.; Resasco, D. E.; J., U., Big things in small packages. *Oilfield Review* **2010**, 3, (22), 38-49.
31. Chapman, D.; Nelson-Thomas, C., Thing big, get small. *Exploration and Production Magazine* 2010, pp 50-53.
32. Berlin, J. M.; Yu, J.; Lu, W.; Walsh, E. E.; Zhang, L. L.; Zhang, P.; Chen, W.; Kan, A. T.; Wong, M. S.; Tomson, M. B.; Tour, J. M., Engineered nanoparticles for hydrocarbon detection in oil-field rocks. *Energy & Environmental Science* **2010**, 4, (2), 505-509.

33. Gilbert, R. B.; Lake, L. W.; Jablonowski, C. J.; Jennings, J. W.; Nunez, E. J., A Procedure for Assessing the Value of Oilfield Sensors. *SPE Reservoir Evaluation & Engineering* **2009**, 12, (4), 618-629.
34. Soultanidis, N.; Zhou, W.; Psarras, A. C.; Gonzalez, A. J.; Iliopoulou, E. F.; Kiely, C. J.; Wachs, I. E.; Wong, M. S., Relating n-Pentane Isomerization Activity to the Tungsten Surface Density of WO(x)/ZrO₂. *Journal of the American Chemical Society* **2010**, 132, (38), 13462-13471.
35. Yang, J.; Lee, J. Y.; Ying, J. Y., Phase transfer and its applications in nanotechnology. *Chemical Society Reviews* **2011**, 40, (3), 1672-1696.
36. Fan, H. Y., Nanocrystal-micelle: synthesis, self-assembly and application. *Chemical Communications* **2008**, (12), 1383-1394.
37. Yu, J.; Berlin, J. M.; Lu, W.; Zhang, L. L.; Kan, A. T.; Zhang, P.; Walsh, E. E.; Work, S. N.; Chen, W.; Tour, J. M.; Wong, M. S.; Tomson, M. B., Transport Study of Nanoparticles for Oilfield Application. In *SPE International Conference on Oilfield Scale*, Aberdeen, U.K., 2010.
38. Sun, S. H.; Zeng, H., Size-controlled synthesis of magnetite nanoparticles. *Journal of the American Chemical Society* **2002**, 124, (28), 8204-8205.
39. Yu, W. W.; Falkner, J. C.; Yavuz, C. T.; Colvin, V. L., Synthesis of monodisperse iron oxide nanocrystals by thermal decomposition of iron carboxylate salts. *Chemical Communications* **2004**, (20), 2306-2307.
40. Peng, Z. A.; Peng, X. G., Formation of high-quality CdTe, CdSe, and CdS nanocrystals using CdO as precursor. *Journal of the American Chemical Society* **2001**, 123, (1), 183-184.
41. Park, J.; An, K. J.; Hwang, Y. S.; Park, J. G.; Noh, H. J.; Kim, J. Y.; Park, J. H.; Hwang, N. M.; Hyeon, T., Ultra-large-scale syntheses of monodisperse nanocrystals. *Nature Materials* **2004**, 3, (12), 891-895.
42. Manna, L.; Milliron, D. J.; Meisel, A.; Scher, E. C.; Alivisatos, A. P., Controlled growth of tetrapod-branched inorganic nanocrystals. *Nature Materials* **2003**, 2, (6), 382-385.

43. Talapin, D. V.; Nelson, J. H.; Shevchenko, E. V.; Aloni, S.; Sadtler, B.; Alivisatos, A. P., Seeded growth of highly luminescent CdSe/CdS nanoheterostructures with rod and tetrapod morphologies. *Nano Letters* **2007**, 7, (10), 2951-2959.
44. Puentes, V. F.; Krishnan, K. M.; Alivisatos, A. P., Colloidal nanocrystal shape and size control: The case of cobalt. *Science* **2001**, 291, (5511), 2115-2117.
45. Jin, R. C.; Cao, Y. C.; Hao, E. C.; Metraux, G. S.; Schatz, G. C.; Mirkin, C. A., Controlling anisotropic nanoparticle growth through plasmon excitation. *Nature* **2003**, 425, (6957), 487-490.
46. Zhang, Z.; Wong, L. M.; Ong, H. G.; Wang, X. J.; Wang, J. L.; Wang, S. J.; Chen, H. Y.; Wu, T., Self-Assembled Shape- and Orientation-Controlled Synthesis of Nanoscale Cu₃Si Triangles, Squares, and Wires. *Nano Letters* **2008**, 8, (10), 3205-3210.
47. Kini, G. C. Bilayer Approaches for Nanoparticle Phase-Transfer. PhD Thesis, Rice University, Houston, 2011.
48. Fan, H. Y.; Yang, K.; Boye, D. M.; Sigmon, T.; Malloy, K. J.; Xu, H. F.; Lopez, G. P.; Brinker, C. J., Self-assembly of ordered, robust, three-dimensional gold nanocrystal/silica arrays. *Science* **2004**, 304, (5670), 567-571.
49. Fan, H. Y.; Chen, Z.; Brinker, C. J.; Clawson, J.; Alam, T., Synthesis of organo-silane functionalized nanocrystal micelles and their self-assembly. *Journal of the American Chemical Society* **2005**, 127, (40), 13746-13747.
50. Fan, H. Y.; Leve, E.; Gabaldon, J.; Wright, A.; Haddad, R. E.; Brinker, C. J., Ordered two- and three-dimensional arrays self-assembled from water-soluble nanocrystal-micelles. *Advanced Materials* **2005**, 17, (21), 2587.
51. Fan, H. Y.; Leve, E. W.; Scullin, C.; Gabaldon, J.; Tallant, D.; Bunge, S.; Boyle, T.; Wilson, M. C.; Brinker, C. J., Surfactant-assisted synthesis of water-soluble and biocompatible semiconductor quantum dot micelles. *Nano Letters* **2005**, 5, (4), 645-648.
52. Brinker, C. J.; Lu, Y. F.; Sellinger, A.; Fan, H. Y., Evaporation-induced self-assembly: Nanostructures made easy. *Advanced Materials* **1999**, 11, (7), 579.

53. Bagaria, H. G.; Kini, G. C.; Wong, M. S., Electrolyte Solutions Improve Nanoparticle Transfer from Oil to Water. *Journal of Physical Chemistry C* **2010**, 114, (47), 19901-19907.
54. Kini, G. C.; Bagaria, H. G.; Ko, W.-Y.; Wong, M. S. Converting Nanoparticles in Oil to Aqueous Suspensions. 2009.
55. Kini, G. C.; Biswal, S. L.; Wong, M. S.; Miller, C. A., Characteristics of Spontaneously Formed Nanoemulsions. *To be submitted* **2011**.
56. Kini, G. C.; Yu, J.; Wang, L.; Kan, A. T.; Tour, J. M.; Biswal, S. L.; Tomson, M. B.; Wong, M. S., Colloidal and Flow Behavior of Brine-Stable Quantum Dot Nanoparticles. *To be submitted* **2011**.
57. Murthy, V. S.; Rana, R. K.; Wong, M. S., Nanoparticle-assembled capsule synthesis: Formation of colloidal polyamine-salt intermediates. *Journal of Physical Chemistry B* **2006**, 110, (51), 25619-25627.
58. Calvert, P., Gel sensors and actuators. *MRS Bulletin* **2008**, 33, (3), 207-212.
59. Kini, G. C.; Lai, J.; Wong, M. S.; Biswal, S. L., Microfluidic Formation of Ionically Cross-Linked Polyamine Gels. *Langmuir* **2010**, 26, (9), 6650-6656.

Chapter 2

Electrolytes Improve Nanoparticle Transfer from Oil to Water

2.1 Nanoparticles Phase-Transfer Strategies

Nanoparticles (NPs) are often synthesized in organic solvents due to advantages of superior size control¹⁻⁵, size distribution control⁵⁻⁹, and shape control⁹⁻¹⁷ obtainable in a non-polar environment. Such fine control is achieved through the use of surface active (surfactant) agents or ligand molecules, which bind to the surface of NPs through polar head groups and render the NP solvent-dispersible by exposing their hydrophobic tails to the solvent (Fig. 2.1).

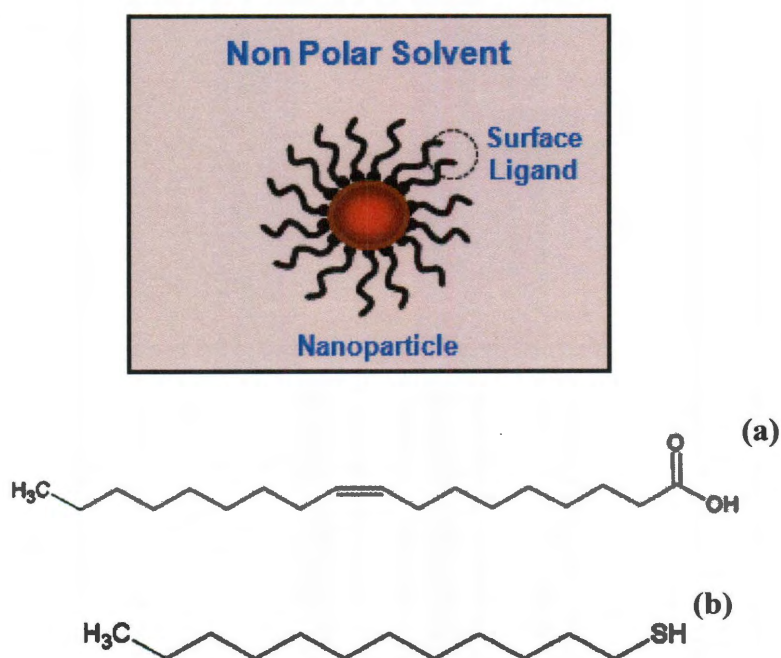


Figure 2.1: Nanoparticle (NP) dispersed in a non-polar solvent (oil) by surface ligand/surfactant molecules such as (a) oleic acid or (b) dodecanethiol. The hydrophilic (-COOH or -SH) groups of the ligands are chemically bound to the NP surface and the hydrophobic groups render oil-dispersibility to the NP.

(Note: In phase-transfer literature, water-dispersible NPs are often and interchangeably termed as water-soluble NPs.¹⁸ We will use the terminology of NPs being water-dispersible since NPs are never really solubilized from a molecular standpoint, and exist as discrete and distinct colloidal particles in organic and aqueous media).

Many significant applications featuring NPs require them to be in aqueous media as stable dispersions. These include but are not limited to fields of medicine¹⁸⁻³⁸, catalysis³⁹⁻⁴¹, and environmental sciences.³⁹⁻⁴⁴ To transfer NPs from oil to water, it is essential to modify the hydrophobic nature of the NP surface. To achieve this, several techniques have been developed that can be broadly categorized as ligand exchange methods and bilayer formation methods.⁴⁵

2.1.1 Ligand Exchange Methods

Ligand exchange is a process where native hydrophobic ligands on NPs are displaced by amphiphilic ligand molecules that have hydrophilic groups at both ends of their hydrocarbon chain. Upon exchange, the displacing ligand chemically binds to the NP surface with its hydrophilic end whilst the free hydrophilic end makes the NP water-dispersible. This process is also known as ‘ligand-exchange or place-exchange.’ Fig. 2.2 (a) depicts NP phase-transfer by the ligand/place-exchange process.^{30-34, 38, 46-75} A distinct benefit of this method is that by displacing native ligands small hydrodynamic diameters of NPs are maintained. For the case of QDs, smaller sizes are desired due to better colloidal stability, superior optical properties (quantum yield or QY) and photostability, and a higher probability for cell accessibility (endocytosis) in biological applications.^{30-32, 34, 51, 54, 67, 68, 74}

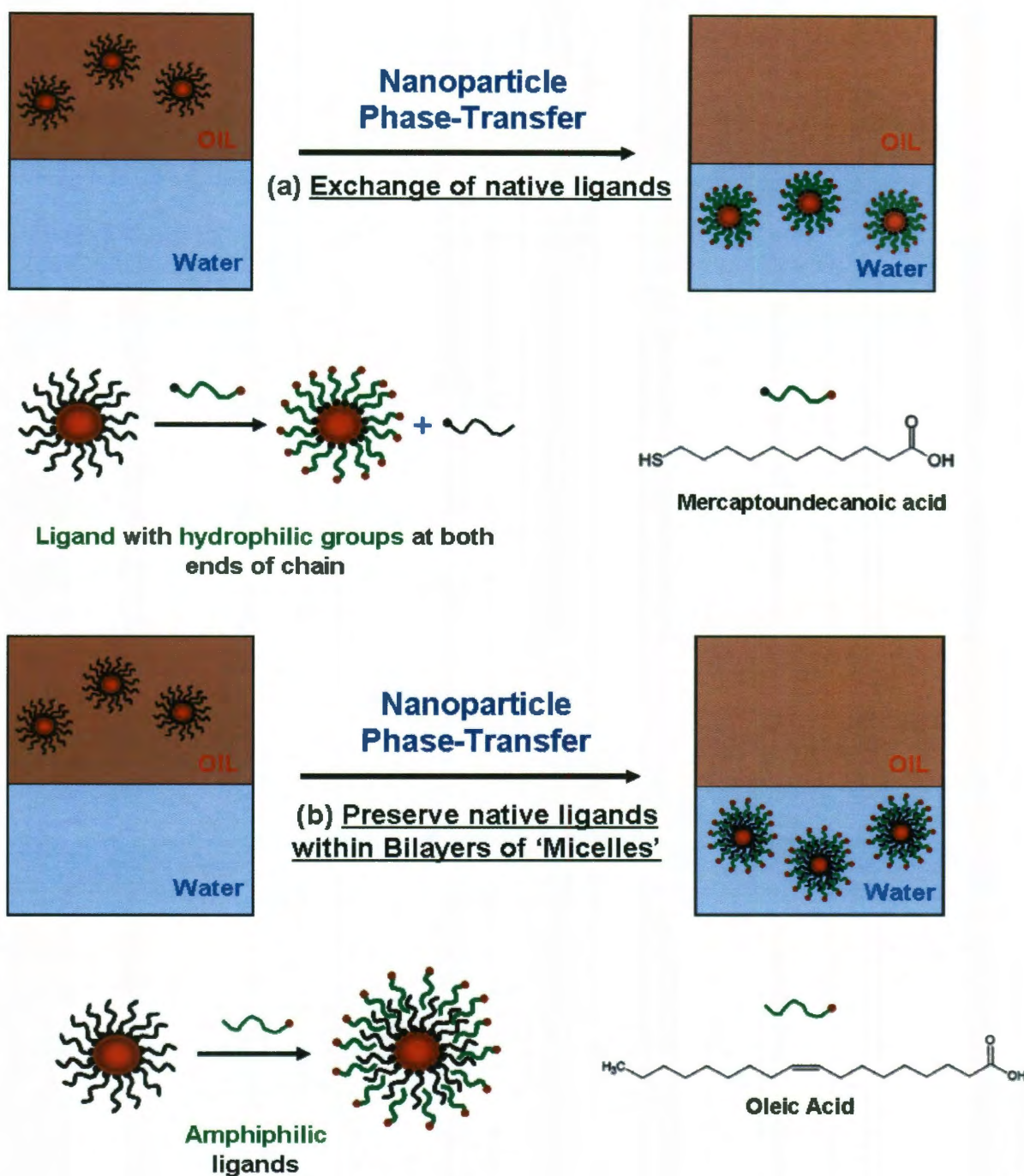


Figure 2.2: Schematic of two approaches to transfer nanoparticles (NPs) from oil to water by surface modification of NP surface. (a) Top Panel: NP phase-transfer through ligand or place exchange of native ligands on NP surface (in black) with ligands containing hydrophilic head groups (black and brown) at both ends of a hydrocarbon chain (in green), making NPs water-dispersible. An example of a commonly used ligand is 11-mercaptoundecanoic acid (MUA) with $-SH$ and $-OH$ hydrophilic head groups on either ends of an eleven carbon-chain hydrocarbon (b) Bottom Panel: NP phase-transfer

through formation of bilayers wherein, the native ligands on the NP surface are retained but phase-transfer is done using amphiphilic ligands, constituted of a hydrophobic tail group (in green) and hydrophilic head group (in brown). The hydrophobic group (in green) of the amphiphile associates with the hydrophobic end of the native ligand (in black) and the hydrophilic end (in brown) of the amphiphile makes the NP water-dispersible.

Likewise, magnetic iron-oxide NPs with small hydrodynamic diameters and high colloidal stability vastly improve magnetothermal therapy and magneto resonance imaging (MRI) for cancer cells on account of size-dependent thermal and contrast effects.^{22, 50, 55, 69, 70} In a few cases, careful selection of ligand molecules (such as those with silane or amino functionalities) have been used to stabilize NPs across a wide range of pH.^{38, 52} Another feature of the ligand-exchange route is that very high NP phase-transfer efficiency (nearing 100%) can be achieved (Fig. 2.3)

To engineer NPs with functional properties for applications in biosensing and diagnostics, exchanged ligands have been partially conjugated with protein/immuno/receptor or nucleotide molecules.^{30, 61} For the case of QDs, their unique optical and semiconducting properties have been synergistically combined to form biosensing, imaging, detection, and diagnostic assays.^{30-33, 38} Chan and Nie reported successful cell endocytosis and specific antibody/antigen recognition. CdSe QDs were conjugated with proteins and immunomolecules respectively.³⁰ Pathak *et al* synthesized QD probes by partially conjugating oligonucleotides onto ligand-exchanged dioxane moieties.⁶¹

Alongside the examples discussed above, Alivisatos and coworkers prepared semiconductor nanocrystals as fluorescent probes and demonstrated benefits of broad and continuous excitation spectra in mouse-fibroblasts labeling experiments over conventional fluorophores.³¹ In a similar manner, Chan and Nie reported formation of

water-dispersible QD solutions with superior luminescence and stability against photo bleaching over conventional organic dyes (Fig. 2.4).³⁰ In other variations, ligand exchange phase-transfer has been done using thermo responsive polymers^{47, 49} polymerization⁵², and ozonolysis reactions⁵⁷ of native ligands. Dithiocarbamate assembly that involves *in situ* ligand formation by mixing amines in carbon disulphide has proven effective to phase-transfer NPs.^{53, 71}

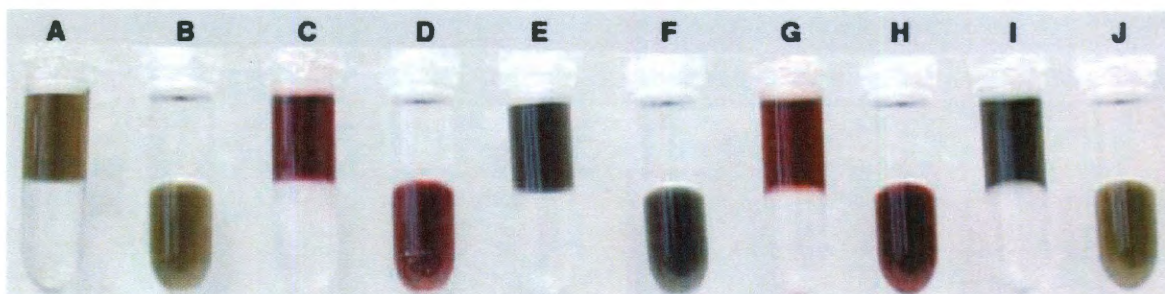


Figure 2.3: Phase-transfer of NPs from toluene to water by ligand-exchange with 11-mercaptoundecanoic acid (MUA). For each image pair, the left image corresponds to NPs in toluene before phase-transfer and the right image to NPs in water upon phase-transfer. (A, B: silver. C, D: gold. E, F: platinum. G, H: gold. I, J: palladium). For cases (A-H), phase-transfer efficiency was $\sim 100\%$, for case (I-J), phase-transfer efficiency was $> 90\%$. Note: Differences between gold NPs in pairs (C-D) and (G-H) are in the synthesis methods. (Figure adapted from Gittins and Caruso).

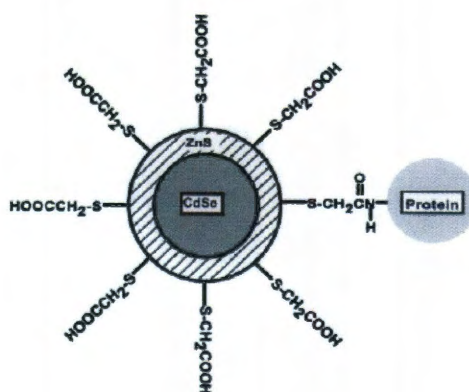


Figure 2.4: CdSe-ZnS core-shell QDs, transferred from chloroform to phosphate buffer saline (PBS) solution, upon ligand-exchange with mercaptoacetic acid. Conjugation of

the mercaptoacetic acid with protein (transferrin) translated to receptor-mediated endocytosis in cultured HeLa cells (Figure adapted from Chan and Nie).

Although ligand-exchange is an effective method for transferring NPs to aqueous phase and is invaluable in many applications, it has several limitations:

(i) NPs are susceptible to surface oxidation or corrosion due to insufficient protection of the NP surface during ligand-exchange.⁵⁴ NP phase-transfer by ligand-exchange sometimes requires multiple solvents or high temperatures (60 – 70 °C), making NPs prone to surface corrosion during the phase-transfer step itself. Although not reported explicitly, surface corrosion can be inferred by comparing the ultra-violet (UV) spectra of NPs, prior to and after ligand-exchange. A significant blue-shift in the position of the first exciton of CdSe QDs and Au NPs indicate a decrease in particle size thus suggesting surface corrosion.^{53, 67, 73} A recent report provides methods to overcome some of these drawbacks, particularly those of surface oxidation. However, it makes use of sophisticated custom-made polymeric molecules or ligands that are required to be designed for specific NP material types.^{62, 68}

(ii) Ligand exchange requires the design of different anchor groups for various NP materials to be phase-transferred. This limits each ligand exchange method to certain NPs and seriously constrains scale-up of the process from an economic standpoint. As an illustration, ligands with thiol groups are used to phase-transfer gold^{34, 56, 59, 73}, silver³⁴, platinum³⁴, iron-platinum⁶³, cobalt-platinum⁶⁵, and semiconductor NPs.^{30, 72} However, amido⁴⁷, dopamine^{46, 58, 69}, or silane³⁸ groups are required and used to phase-transfer iron-oxide NPs. The formulation of a generic route to ligand-exchange and phase transfer NPs

is a challenge yet to be realized that would constitute invaluable contribution to this field.⁶⁷

2.1.2 Bilayer Formation Methods

In contrast to the ligand exchange method, the general strategy of NP phase-transfer through bilayer formation involves preserving the hydrophobic surfactants (or ligands) native to the NP surface. Phase-transfer is affected using amphiphilic molecules such as surfactants^{35, 76-84}, polymers^{18, 36, 85-88}, glycol-or phospholipids⁸⁹⁻⁹², liposomes⁹³, and oligosaccharides such as cyclodextrin.⁹⁴ The hydrophobic parts of the amphiphiles form bilayers with the native surfactant/ligand via hydrocarbon-hydrocarbon interactions (also called hydrophobic interactions) and the hydrophilic parts of the amphiphiles render the NPs water-dispersible. Thus, the native ligand on the NP substrate is preserved. Fig. 2.2 (b) depicts NP phase-transfer through bilayer formation.

Unlike NPs phase-transferred by ligand-exchange, those phase-transferred in bilayers will have slightly higher hydrodynamic diameters due to retention of the native NP ligand. However, the high surface density coverage of bilayers imparts NPs with superior colloidal stability and protection against oxidation. Furthermore, unlike place-exchange where specificity of the displacing ligand's affinity to the NP surface is critical, bilayer formation with amphiphiles depends only on the native ligand on the NP and not on the NP. These minimize requirements to design and synthesize sophisticated and custom-made polymeric molecules often used in the ligand-exchange process. Hence, generic processes with the use of relatively simple and commercially available amphiphiles have been developed to facilitate phase-transfer of NPs, making this route

highly attractive for scale-up and commercialization.^{21, 54} Upon careful selection of amphiphilic molecules to form the bilayer, high NP phase-transfer yields and stable dispersibility across a wide range of temperatures, pH, and ionic strengths have been achieved.⁸⁰

There are however significant challenges relevant to NP phase-transfer with lipid bilayers which must be addressed. One particular problem with this method is that it is easy to form clusters of NPs within the encapsulating bilayer environment. In addition to lower colloidal stability, clusters of NPs such as those of the CdSe QD variant would result in self-quenching of photoluminescence (PL), thus lowering its optical properties. In this regard, Dubertret *et al* have successfully devised a simple method to transfer QDs from chloroform to water as single NPs through the use of phospholipids (Fig. 2.5), while Colvin and coworkers used oleic acid to obtain single NP dispersions of iron-oxide in water (Fig. 2.6). The latter group also showed the oleic acid approach to transfer iron-oxide as single NPs was an improvement over the clusters of two/three NPs previously obtained when IGEPAL[®] CO 630 (octylphenyl-polyethylene glycol) nonionic surfactant was used.⁸⁰

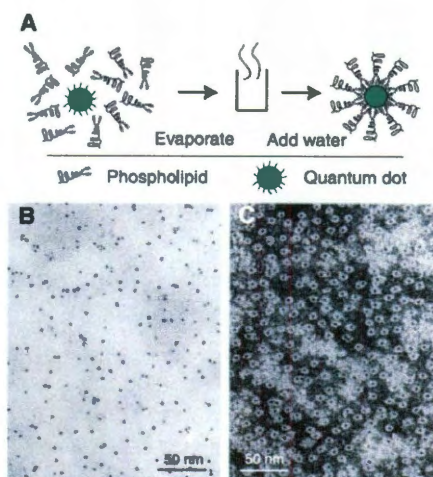


Figure 2.5: (A) Schematic representing phase-transfer of CdSe/ZnS QDs from chloroform to water using a mixture of phospholipids (n-poly (ethylene glycol) phosphatidylethanolamine (PEG-PE) and phosphatidylcholine (PC)). (B) TEM images of QDs without staining and (C) TEM Images of QDs with staining dye, reveal transfer as single QDs encapsulated in a phospholipid block-copolymer micelle (Figure adapted from Dubertret *et al*).

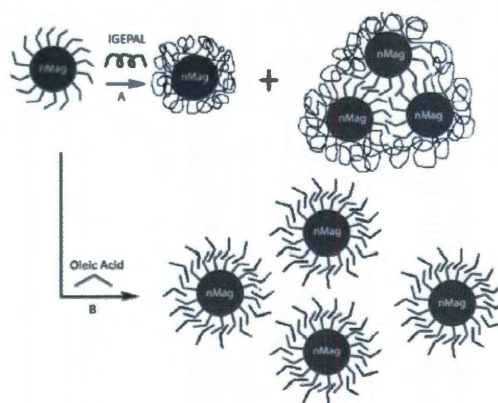


Figure 2.6: Transfer of oleic-acid stabilized iron-oxide NPs from hexane to water through bilayer formation with (A) IGEPAL®CO 630 (octylphenyl-polyethylene glycol: nonionic surfactant) and (B) oleic acid. Iron-oxide was phase-transferred as clusters of 2-3 NPs in IGEPAL®CO 630, as determined by dynamic light scattering (DLS) and as single NPs in oleic acid, as determined by DLS and small-angle X-Ray scattering (SAXS) (Figure adapted from Prakash *et al*).

Common strategies discussed in the literature that are used to affect bilayer formation include:

(i) Interfacial transfer of NPs from oil to water in a two phase system: In this process, NPs synthesized in oil are contacted with water containing amphiphilic molecules. Mixing is promoted through vigorous stirring or sonication, resulting in an increased contact area between amphiphilic molecules in water and oil droplets that contain NPs. Transfer is effected upon bilayer formation. This approach is particularly useful when NPs are prepared in solvents that have boiling points significantly higher than that of water, where conventional boiling off techniques becomes unfeasible. Limitations to this approach are that NPs are often transferred as clusters^{42, 54}, and complete NP phase-transfer is seldom feasible. Furthermore, upon phase-transfer, total separation of oil droplets from the aqueous phase is not possible, thus preventing use in food related applications and limiting its application to *in vitro* biological studies.^{35-37, 80, 81, 84-86, 88, 89, 94} Lees *et al* recently reported a novel and improved scheme involving sophisticated polymerization chemistry that yielded 100% phase-transfer efficiency of NPs along with colloidal stability across a pH range of 3-13. In their method, poly (styrene-co-maleic anhydride) or PSMA polymer was capped around QDs and polymerized to form a ring. An amine-terminated ligand was reacted with the PSMA-capped QDs that opened the maleic anhydride ring and incorporated the amine to impart water dispersibility to the QDs.³⁷ However, this method is yet to realize scale-up due to the highly specialized nature and high cost of the process.

(ii) Mixing NPs and the amphiphilic molecules in oil, boiling off the oil, and adding the aqueous medium^{18, 54, 78, 87, 91-93}: In this process, amphiphilic molecules are

initially dissolved in oil that contains NPs. The ternary system is then heated so as to boil-off oil prior to the addition of water to the binary residue of amphiphile and NPs. The presence of the amphiphile makes the NPs water-dispersible. The advantages are that NP phase-transfer can be affected from oils that have boiling points significantly higher than water. Further, the NP dispersions prepared through this route contain no trace of oil, making them suitable for biological and food related applications. The resulting dispersions can range from NPs existing as single to multiple nanocrystals clusters depending on the nature of amphiphile used. Anderson and Chan, Dubertret *et al* (Fig. 2.5), Pellegrino *et al* and Smith *et al* have reported formation of single NP dispersions when phospholipids or polymers were used as the amphiphile, based on a steric stabilization mechanism.^{18, 54, 87, 91} Transfer with polymers have additionally allowed for site conjugation with proteins and DNA or receptor molecules, thus making NPs functional for biological assays and diagnostics.^{18, 91} Furthermore, these amphiphiles have yielded NP-dispersions with high optical and colloidal stability that can be successfully formulated in high ionic-strength buffers.^{18, 54, 91}

When surfactants are used as amphiphiles, this route has shown mixed results and does not consistently preserve the initial NP size, colloidal stability, and optical properties and does not necessarily give high phase-transfer yields.^{54, 91} Thereby from the perspective of process economics, this method still requires high cost chemicals, restricting its applications to high-value biological areas.

(iii) Using amphiphilic molecules to form oil-in-water emulsions or microemulsions followed by boiling off the oil (*e.g.* chloroform, hexane)^{76, 77, 83} This extremely simple and elegant process was pioneered by Brinker and coworkers and has

paved the way to form stable dispersions of nanocrystals in water.⁷⁶ In this process, aqueous surfactant solutions are added to oil-containing NPs to form oil-in-water (O/W) microemulsions. The system is then heated to a temperature at which the oil boils off. As the oil evaporates, the surfactants form bilayers with the native ligand on the NP, thus dispersing them in water (Fig. 2.7). To utilize this route, it is necessary that the oil has a boiling point lower than that of water. Hence, the solvents from which NPs can be phase-transferred are few and limited (chloroform, hexane, and benzene). Brinker and coworkers transferred Au NPs to water by formulating chloroform/water microemulsions and boiling off the chloroform. Fan *et al* and Li *et al* used a similar approach to form biocompatible CdSe QDs in water with high optical stability. However, NPs were transferred as both single NPs as well as clusters of multiple NPs.^{76, 77, 83}

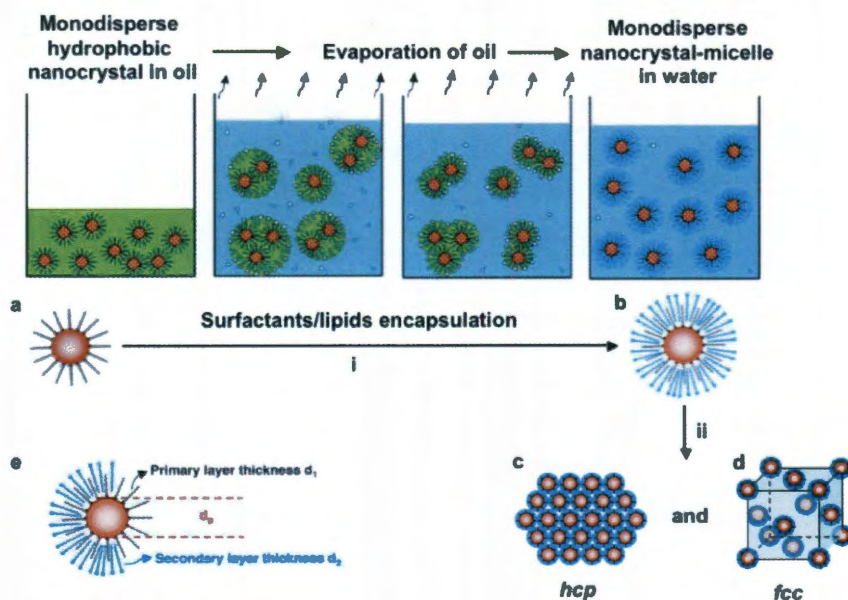


Figure 2.7: Transfer of Au NPs from chloroform to water by microemulsion formation. Aqueous surfactant solution of cetyltrimethylammonium bromide (CTAB) was added to the oil phase that contained nanoparticles (NPs), and stirred to form an oil/water microemulsion. The microemulsion was heated to a temperature above the boiling point of oil but below that of water to boil off oil, resulting in phase-transfer to water. NPs with

native ligands (a) transferred to water by encapsulation in bilayers of surfactant/phospholipids. (b) These NPs can self-assemble into ordered nanocrystal-micelle superlattices with (c) hexagonal close packed (hcp) or (d) face cubic closed (fcc) structures. (e) Thermodynamically defined interdigitated bilayers (Figure adapted from Fan *et al*).

The advantage of method (iii) over method (ii) is that, along with polymers, commercial surfactants and phospholipids can be used to disperse NPs in water. In addition to cost benefits, NPs encapsulated in bilayers of surfactants are very interesting colloidal systems that serve as starting materials to develop advanced ordered structures and devices from a bottom-up approach. As an example, Fan *et al* demonstrated versatile use of surfactant/phospholipid-encapsulated Au NPs for applications in biotagging and forming self-assembled nanocrystal-micelle superlattices. Upon reacting Au NPs encapsulated in surfactants and silicic acid, the material could be self-assembled or spin coated to form ordered Au/silica mesophases and were incorporated to form metal-insulator-metal (MIM) devices.^{76, 95, 96} More details regarding the processing of these colloidal materials will be presented in the following chapter.

The next section focuses on our unique contribution to this field through the development of a route we term, NP phase-transfer using “salty-water micelles.”⁹⁷ We have discovered that a small process modification in using salt-containing water to formulate oil/water nano or microemulsions dramatically improves NP phase-transfer yields and results in NP dispersions with higher colloidal stability than for the case where phase-transfer is carried out in plain-water / deionized (DI) / “no-salt” water micelles (method iii).

2.2 New Nanoparticle Phase-Transfer Concept: “Salty-Micelles”

2.2.1 Introduction

A popular approach to phase-transfer NPs through bilayer formation was pioneered by Brinker and coworkers, wherein microemulsions of oil containing NPs were formulated using surfactants and phase-transfer to water was carried out by heating the dispersion to temperatures above the boiling temperature of oil. Upon evaporation of oil, surfactants formed bilayers with native ligands on the NPs that rendered them water-dispersible.^{76, 77} However, NPs transferred by this route were not always in the form of single NPs, which was seen to occur only through the use of expensive phospholipids and in very select cases, through the use of commercial surfactants. For instance, Fan *et al* showed that CdSe QDs could be transferred as single nanocrystals with retention of optical properties when the amphiphile used was phospholipids.⁷⁷ Likewise, Brinker and coworkers had demonstrated successful transfer of Au NPs as single nanocrystals, using CTAB as the amphiphile.⁷⁶ Given the biological relevance of QDs and the low cost of surfactants such as CTAB, it was logical to attempt transfer of QDs to water using CTAB as the surfactant.

Upon investigating the transfer of QDs from chloroform to water using a microemulsion-based approach involving CTAB, we found high colloidal stability of QDs that transferred to water, but very poor optical stability in that PL was found to be completely quenched. Investigations with other surfactants such as sodium dodecyl benzene sulfonate (SDBS) and Aerosol-OT (AOT) also resulted in stable aqueous QD dispersions, but with poor PL. In a recent study, Li *et al* reported improvement in PL retention and quantum yield (QY) of CdSe/ZnS core-shell QDs, when transfer was

carried out in bilayers of Gemini surfactants. However, the uncommon and sophisticated nature of the surfactant (Gemini surfactants used in this study were commercially unavailable and synthesized by the authors) makes the economics of the process unfeasible. Furthermore, the authors' claim of optical benefits was not entirely convincing because the UV-vis spectra of the transferred QDs had a high background scatter (translating to high absorbance values) which could artificially increase their PL and QY values.⁸³ It thereby is an open challenge to devise approaches that transfer NPs to water efficiently and economically without compromising their stability and properties.

We have discovered that phase-transfer of NPs can be strongly enhanced and colloidal properties of resulting NP dispersions dramatically improved,⁹⁷ when a simple process modification is made to the process pioneered by Brinker and coworkers. The process modification involves adding salt to the water in which the emulsion/microemulsion is formulated. Upon boiling off the oil, NPs phase-transferred to salty-water micelles (or simply salty-micelles) resulting in NP dispersions different from those formed in DI-water/no-salt micelles. With a model system constituting CdSe QDs as NPs, AOT as the surfactant, and NaCl as the salt to be dissolved in water, we found that over 90% of CdSe QDs transferred from hexane to salty-micelles of AOT. This was statistically higher than the 45-55% QDs that transferred to DI-water micelles of AOT. Transmission electron microscopy (TEM), electron diffraction patterns, and UV-vis spectroscopy revealed that NPs phase-transferred in salty-micelles remain unchanged upon phase-transfer. Dynamic light scattering (DLS), analytical ultracentrifugation (AU), and small angle X-Ray scattering (SAXS) studies indicated that NPs transferred as individual and single particles. Electrophoretic mobility measurements and

thermogravimetric analysis (TGA) revealed a higher surface coverage of surfactant onto NPs when phase-transfer to water was carried out in the presence of salt. Spectroscopic studies with non-absorbing ZnO NPs and a UV-absorbing Nile Red dye revealed the bilayer region of the salty-micelle to be more hydrophobic than that of the DI-water micelle, indicating a higher lateral compactness. These translated to better retention in optical properties of QDs such as PL and QY when in salty-micelles. Finally, we established the generic nature of NP phase-transfer by this process through experiments with different NP compositions, shapes, sizes, surfactants, and salt types.

2.2.2 Materials and Methods

2.2.2.1 Synthesis of Nanoparticles

General Comment for all Nanoparticle Synthesis Routines

The following section describes procedures followed to synthesize NPs that are eventually used in phase-transfer studies or towards understanding the mechanism of phase transfer. All syntheses were carried out according to procedures in the literature. No further details are provided here unless pertaining to a process modification. Chemicals used along with supplier source, grade, and purity levels are provided. All chemicals were used as obtained, unless mentioned otherwise. Chemical grades and purity levels may be assumed to be of American Chemical Society (ACS) grade unless mentioned otherwise. Upon synthesis, all NPs were cleaned, separated and purified using solvents, as per procedures outlined in the literature. The following solvents were used, all of which were procured from Fischer Scientific: acetone, ethanol, methanol,

chloroform, toluene, and benzene. The readers are urged to follow necessary safety precautions associated with NP synthesis, as listed in the literature.

Buckminsterfullerene (Bucky balls/Carbon-60 or simply C₆₀) used in phase-transfer studies were kindly provided by Prof. M. B. Tomson (Department of Civil and Environmental Engineering, Rice University, chemical supplier: SCI, purity level – 99.99%) and Prof. P. M. Ajayan (Department of Mechanical Engineering and Materials Science, Rice University, Chemical supplier: BuckyUSA, purity level – 95%). Bucky balls (C₆₀) were dissolved in benzene at a concentration of 1.14 g/L for phase transfer.

Synthesis of CdSe Semiconductor Nanoparticles: Quantum Dots and Tetrapods

CdSe QDs were synthesized following the method of Yu and Peng⁵ and CdSe tetrapods were prepared as per the process described by Asokan *et al.*⁹⁸ Cadmium oxide (CdO, 99.99%), oleic acid (OA, technical grade – 90%), 1-octadecene (ODE, technical grade – 90%), and trioctylphosphine (TOP, 90%), and cetyltrimethylammonium bromide (CTAB) were all purchased from Aldrich. Selenium (Se - 99.99%) was obtained from Strem Chemicals.

Synthesis of Au (Metal) Nanoparticles

Synthesis of Au NPs was carried out following a procedure described by Prasad *et al* using dodecanthiol as the capping agent.⁹⁹ The chemicals used for Au NP synthesis and their suppliers are as follows: AuCl₃ (Alfa Aesar, 64.4% Au), didodecyldimethyl ammonium bromide (Aldrich, 98%), sodium borohydride (Acros, 98%), and dodecanethiol (Aldrich, 98%).

Synthesis of Iron-oxide Nanoparticles

Synthesis of iron-oxide NPs was carried out following a procedure described by Yu *et al.*³ Ferric oxy hydroxide (FeO(OH)), OA, and ODE used towards synthesis were procured from Aldrich.

Synthesis of Zinc-oxide Nanoparticles (for Solvatochromic Dye Experiments)

Zinc-oxide NPs were prepared with zinc acetate dihydrate (Aldrich, ACS reagent), OA, ethanol (200 proof), and tetramethylammonium hydroxide pentahydrate (Aldrich, >97%) as per the method of Moussodia *et al.*³²

2.2.2.2 Phase-Transfer of Nanoparticles

Synthesized and cleaned CdSe QDs (~3 nm in size, coated with oleate ligands) were suspended in hexane at a concentration of 235 $\mu\text{mol-QD/L}$ using extinction coefficient correlations reported by Peng and co-workers.⁴ The surfactant Aerosol-OT ("AOT" or sodium bis(2-ethylhexyl)sulfosuccinate from TCI America, 96% purity) was then dissolved in this suspension (30 mg-AOT/mL-hexane). In devising the procedure to phase-transfer QDs from oil to water, the final AOT (surfactant) concentration was fixed at 1.5 g/L to ensure that AOT was well above its critical micellar concentration (CMC) (The CMC of AOT at 25 °C is 0.155 g/L or 2.66 mM, as reported by Umlong and Ismail).¹⁰⁰

To standardize the concentration of QDs initially added to the water phase upon dilution (and before solvent evaporation), the following procedure was devised based on a non-invasive approach using UV-vis spectroscopy. The basic principle involves Beer

Lambert's law (Eq. 2.1) that relates absorbance (A) at the wavelength corresponding to the first exciton absorption peak of QDs, to its concentration (C) in solution:

$$A = \epsilon l C \quad (2.1)$$

Where: ϵ = Molar absorptivity ($L \text{ mol}^{-1} \text{ cm}^{-1}$), l = Path length of the quartz cuvette in which the sample is stored (1 cm) and C = Concentration of the compound in solution (mol L^{-1}).

To estimate NP concentration, the molar absorptivity is required. For this, published correlations by Yu *et al* were used that relate molar absorptivity (ϵ) to the diameter (D) of QDs by an empirical power law fit given by Eq. (2.2). The diameter of the QDs (D) is related to the wavelength (λ) corresponding to the first excitonic absorption peak as given by Eq. (2.3).⁴

$$\text{CdSe} : \epsilon = 5837(D)^{2.65} \quad (2.2)$$

$$\text{CdSe} : D = (1.6122 \times 10^{-9})\lambda^4 - (2.6575 \times 10^{-6})\lambda^3 + (1.6242 \times 10^{-3})\lambda^2 - (0.4277)\lambda + (41.57) \quad (2.3)$$

These correlations enable estimation of molar absorptivity solely by UV-vis spectroscopy, thus circumventing the estimation of QD diameter by elaborate electron microscope procedures or QD concentrations by methods such as Inductive Coupled Plasma Atomic Emission Spectroscopy (ICP-AES) that destroy the sample. It is important to note that Eqs. (2.2) and (2.3) are valid for QDs in the size range $0.9 \text{ nm} \leq D \leq 9 \text{ nm}$.⁴

From the above discussion, the absorbance value of the first excitonic absorption peak can be measured, and since l is known and ϵ can be estimated, the concentration of NPs in a solvent can be estimated using UV-vis spectroscopy. To standardize the concentration levels of QDs initially dosed to water, we adjusted the QD level in the AOT-hexane blend such that the effective AOT coverage on the surface of a single QD was equivalent to either one or ten monolayers of surfactants. The number of AOT molecules required to cover a QD surface depends on the size of the QD (obtainable from Eq. 2.3), the length of the stabilizing ligand used (oleic acid, 2 nm) and the head group area of AOT ($0.55 \text{ nm}^2/\text{molecule}$). As an illustration, for a green colored QD with the first excitonic absorption peak at 548 nm, the diameter of the bare dot from Eq. 2.3 is 3 nm and that with the oleic acid ligand is 7 nm. Thus, for an available surface area of QDs at 156 nm^2 , the number of AOT molecules required to form an equivalent monolayer is 285. In satisfying the constraint of an AOT concentration in water at 1.5 g/L, the estimated concentrations of QDs in water that corresponded to equivalent coverages of one and ten monolayers of AOT on QDs were $1.205 \text{ }\mu\text{M}$ and $12.05 \text{ }\mu\text{M}$, respectively. (Note: The concentration of NPs thus reported are the total number (moles) of QDs present (with ligands) per liter of solution). The equivalent values in absorbance units, obtained from Eqs. (2.1) and (2.2), for 3 nm QDs were 0.1279 and 1.279, respectively. Subsequently, 0.5 mL of this mixture was added to 10 mL of salt-containing water (3 g-NaCl/L, pH \sim 6) to form an oil-in-water (O/W) emulsion in which the total AOT concentration was \sim 1.5 g/L. This mixture was placed in a water bath at $85 \text{ }^\circ\text{C}$ for 30 min to boil off the hexane under magnetic stirring. A faintly turbid QD suspension was recovered after cooling to room temperature. This turbidity was removed via

centrifugation (8300 ×g for 1 hour), as confirmed by UV-vis spectroscopy, generating a "salty" QD suspension. The phase-transfer procedure was repeated using 10 mL of deionized (DI) water (resistivity of 18.2 MΩ·cm, pH ~ 6), generating a "no-salt" QD suspension.

Phase-transfer yield of CdSe QDs from hexane to salty and DI water was estimated from the following relation:

$$\% \text{ Phase Transfer Yield} = \frac{C_{QA}}{C_{QH}} = \frac{\text{Abs}(\lambda_{\text{FirstExciton}})_A}{\text{Abs}(\lambda_{\text{FirstExciton}})_H} \quad (2.4)$$

Where: C_{QA} = concentration of QDs in aqueous (DI or salty-water micelle) phase, $\text{Abs}(\lambda_{\text{FirstExciton}})_A$ = UV-vis absorbance value at first exciton wavelength of QDs in aqueous (DI or salty-water micelle) phase, C_{QH} = concentration of QDs in hexane (based on a 20-fold dilution of stock in hexane), $\text{Abs}(\lambda_{\text{FirstExciton}})_H$ = UV-vis absorbance value of first exciton of QDs in hexane (based on a 20-fold dilution of stock in hexane).

For experiments involving salts other than NaCl, phase transfer was conducted by simply replacing NaCl with the other salt (sodium sulfate, calcium chloride). All salts used for phase transfer were of ACS grade and were obtained from Fisher Scientific. Phase transfer of CdSe QDs with CTAB as the phase transfer agent was performed in the same manner as described above for AOT except for one difference - CTAB was dissolved directly in the salty (3 g-NaCl/L) and DI water at 1.5 g/L and not in the hexane suspension of QDs. This was done because, at the desired concentration, CTAB did not dissolve completely in hexane. Based on control experiments with AOT, we found that the outcome of our results did not change regardless of whether the surfactant was

dissolved in hexane or in the aqueous solution. Phase transfer of Au and ZnO NPs was conducted following the same procedure previously described above with AOT. C₆₀ was transferred using CTAB.

2.2.2.3 Nile Red Fluorescence Study

Nile Red (NR) studies to probe the polarity of the NP-AOT micelles were conducted using ZnO NPs. Phase transfer of ZnO NPs into "no-salt" water and salt-containing water (1, 3, and 5 g-NaCl/L) was performed with NR added to the ZnO+AOT in hexane stock such that the NR:AOT ratio was below 1:200. Upon phase transfer, the NR emission spectrum was collected using an excitation wavelength of 480 nm. Phase transfer was also performed without ZnO NPs to obtain emission spectra of NR-doped empty AOT micelles in DI water and salt-containing water (1, 3, and 5 g-NaCl/L). It is noteworthy that NR was found to be insoluble in DI and salty-water.

2.2.2.4 Colloidal Stability Study

The stability of AOT-encapsulated CdSe QDs in DI water and salty-water, spiked to varying levels of ionic strengths was studied as follows. QDs in salty-water were diluted with 3g-NaCl/L solution to bring the QD concentration to the same level as QDs in DI water. Subsequently, the QD dispersions were diluted five-fold in pre-made solutions of sodium chloride such that the final sodium chloride concentrations in the DI-water micelle and salty-water micelle solutions were 3, 7, 10, 12 and 15 g/L. The resulting solutions were centrifuged immediately at $8400 \times g$ for 1 hour and the supernatant was collected. The fraction of QDs remaining in the supernatant in DI (C_{DI}) and salty-

micelles (C_{SI}) was determined by comparing UV-vis spectra before and after centrifugation (Eqs. 2.5 and 2.6).

$$\text{Ionic Strength Stability (DI - Water Micelles)} = \frac{C_{DII}}{C_{DIR}} = \frac{\text{Abs}(\lambda_{\text{FirstExciton}})_{DII}}{\text{Abs}(\lambda_{\text{FirstExciton}})_{DIR}} \quad (2.5)$$

$$\text{Ionic Strength Stability (Salty - Water Micelles)} = \frac{C_{SI}}{C_{SR}} = \frac{\text{Abs}(\lambda_{\text{FirstExciton}})_{SI}}{\text{Abs}(\lambda_{\text{FirstExciton}})_{SR}} \quad (2.6)$$

Where: The reference concentration (R) of QDs in DI-water (C_{DIR}) and salty-water (C_{SR}) micelles were adjusted such that $C_{DIR} = C_{SR}$ prior to centrifugation.

2.2.2.5 Characterization

Dynamic Light Scattering (DLS):

The hydrodynamic diameter of NPs, stabilized in DI-water and salty-water micelles, were estimated using a Brookhaven ZetaPALS DLS instrument, with a BI-9000AT digital autocorrelater and a He-Ne Laser ($\lambda = 656 \text{ nm}$). All measurements were carried out at room temperature in standard 4 mL polystyrene cuvettes at a fixed scattering angle of 90° . For reliable statistics, cluster diameters were measured in triplicates, with each run over a time interval of 3 minutes. The diameters reported were number-intensity based, using appropriate CONTINS or NNLS fitting routines through the instrument software 9KDLSW. The autocorrelater estimates the effective diffusive coefficient (D) that is converted to the hydrodynamic diameter (a) using the Stokes-Einstein relationship (Eq. 2.7):

$$a = \frac{k_B T}{6\pi\eta D} \quad (2.7)$$

Where: k_B = Boltzmann's constant: $1.38 \times 10^{-23} \text{ JK}^{-1}$, T = temperature of the continuous phase (approximate solution temperature $\sim 298 \text{ K}$), and η = viscosity of the continuous phase ($1000 \text{ kg m}^{-1}\text{s}^{-1}$ for water). Note: Given that Stokes-Einstein's relationship is valid for a dilute colloidal system, the viscosity of the colloidal solution may be safely approximated to be equivalent to the viscosity of water.

Zeta Potential:

Zeta potential of NP dispersions was estimated from electrophoretic mobility measurements (μ_E) using the phase analysis light scattering (PALS) feature of the Brookhaven ZetaPALS instrument. Measurements were made at $25 \text{ }^\circ\text{C}$, using a dip-in (Uzgiris type) electrode for aqueous solutions in 4 mL polystyrene cuvettes. Based on the particle diameter (a) and salt concentration, either the Smoluchowski or Hückel approximation (Eq. 2.8) was used to determine the zeta potential (ζ).

$$\zeta = \frac{3\eta\mu_E}{2\epsilon_r\epsilon_0} f(\kappa a) \quad (2.8)$$

Where: κ = Debye parameter, η = viscosity of the continuous phase ($1000 \text{ kg m}^{-1}\text{s}^{-1}$ for water), μ_E = electrophoretic mobility of NPs, ϵ_0 = permittivity of free space ($8.854 \times 10^{-12} \text{ C}^2 \text{ N}^{-1} \text{ m}^{-2}$), ϵ_r = relative permittivity (78.5 for water) and $f(\kappa a)$ is the Henry's function that assumes a value of 1.5 for $\kappa a \gg 100$ (Smoluchowski approximation) and a value of 1 when $\kappa a < 1$ (Hückel approximation).

Analytical Ultracentrifuge:

Sedimentation coefficient of CdSe QDs in DI and salty micelles were measured on a Beckman Optima XL-A ultracentrifuge with the AnTi-60 rotor. The QDs in DI and salty water were spun at 20,000 rpm and 30,000 rpm, respectively. The data was analyzed using Ultrascan 7.1 to estimate the sedimentation coefficient as described in earlier reports.^{101, 102} Hydrodynamic diameters were calculated from the sedimentation coefficients by assuming a core-shell model, where CdSe with oleic acid (bound to CdSe surface) is modeled as the core and AOT forms the shell. The particle density was calculated based on the following relation (Eq. 2.9):^{101, 103}

$$\rho_{\text{particle}} = \rho_{\text{shell}} + \left(\frac{(R_H - t)^3}{R_H^3} \right) (\rho_{\text{core}} - \rho_{\text{shell}}) \quad (2.9)$$

For a 3 nm CdSe QD, the density of the core ρ_{core} was calculated to be 1.31 g/mL based on the bulk wurtzite CdSe density (5.8 g/mL), bulk liquid density of oleic acid (0.9 g/mL) and a 2 nm thick oleic acid layer on CdSe surface. For the salty water case, ρ_{particle} was estimated based on a thickness 't' of 1 nm for AOT and the bulk AOT density ($\rho_{\text{shell}} = 1$ g/mL) considering the compact nature of the AOT shell in salty water. The particle density for CdSe in DI water was calculated by factoring in the decreased charge density from zeta potential measurements ($\rho_{\text{shell}} = 0.23$ g/mL).

The hydrodynamic diameter was then obtained from the sedimentation coefficient by the following equation:

$$R_H = \sqrt{\frac{9\eta S_a}{2g(\rho_{\text{particle}} - \rho_{\text{solvent}})}} \quad (2.10)$$

Where, R_H is the hydrodynamic radius, η is the viscosity of the solvent, S_a is the sedimentation coefficient, g is the acceleration due to gravity, ρ_{solvent} is the density of the solvent, and ρ_{particle} is the calculated particle density.

UV-vis Spectroscopy:

As-synthesized and phase-transferred NPs were analyzed by UV-vis absorbance spectroscopy using a Shimadzu UV-vis (UV-24601 PC) spectrophotometer. Spectra were recorded in a scan range between 300 and 750 nm. NPs in organic phase were analyzed in quartz cuvettes and NPs in aqueous phase were analyzed using polystyrene cuvettes.

Photoluminescence (PL) Measurements:

PL of CdSe QDs and Nile Red-doped ZnO NPs were measured using a Jobin Yvon Fluoromax-3 fluorimeter. Both QDs and Nile Red samples were excited at a wavelength of 480 nm to collect their emission in the 500 to 800 nm range. PL intensity was determined by integrating the PL peak. Cuvettes used to obtain UV-vis spectra were also used for all PL measurements. PL stability of CdSe QDs in a DI and salty-water micelle environment was estimated as a function of time. Given that the initial concentration of QDs phase-transferred in DI-water micelles was always lower than those phase-transferred in salty-water micelles (see results and discussion), the QD levels were adjusted in salty-water micelles by diluting them with 3 g-NaCl/L solutions so as to match the concentration of QDs in DI-water micelles. Thereby, the basis to PL stability

comparison was at equal QD concentration levels in DI-water and salty-water micelles of AOT.

PL measurements were made at an excitation wavelength of 480 nm at various time intervals (over 3 months) and the respective integrated areas were recorded. PL stability was determined as the fraction of PL retained in DI/salty-micelles with respect to an equivalent concentration of QDs in hexane as the reference. PL measurements of QDs in hexane were made on days 1 and 70 and the average of PL values on these two days was used to compute PL retention. The relation employed is as follows (Eq. 2.11):

$$\% \text{ PL Retained} = \frac{\text{PL}_{A,t}}{\text{PL}_{H,t-\text{avg}}} \quad (2.11)$$

Where: $\text{PL}_{A,t}$ = Integrated PL area measured at an excitation wavelength of 480 nm for QDs in aqueous phase (A) (either DI or salty-water micelles of AOT), at a specific day (t), $\text{PL}_{H,t-\text{avg}}$ = Integrated PL area measured at an excitation wavelength of 480 nm for an equivalent concentration of QDs in hexane, as an average of day 1 and 70.

Quantum-Yield Measurements:

Quantum yield of CdSe QDs was measured in DI-water micelles of AOT, salty-micelles of AOT, and in hexane, following the procedure described in Jobin Yvon Horiba manual.¹⁰⁴ The standard (ST) used was Rhodamine 6G. In brief, prior to a measurement, the QDs dispersed in a specified environment (for example, salty-micelles of AOT prepared in 3 g-NaCl/L), were diluted in the corresponding solvent (salty water at 3g-NaCl/L). The UV-vis spectrum and absorbance value corresponding to the first exciton were recorded (The initial dilution was carried out to ensure the absorbance value

measured was below 0.1 units). At the concentrations where UV-vis measurements were made, the PL spectra of QDs were recorded and integrated PL areas evaluated. At least four sets of UV-vis absorbance values and corresponding integrated PL areas were measured at different levels of dilution. Plots of integrated PL area vs. UV-vis absorbance values at the first exciton were made. These plots were straight lines with gradient (Grad_x) and intercept = 0. The Quantum Yield (Φ_x) was measured using the following equation:

$$\Phi_x = \Phi_{\text{ST}} \left(\frac{\text{Grad}_x}{\text{Grad}_{\text{ST}}} \right) \left(\frac{\eta_x^2}{\eta_{\text{ST}}^2} \right) \quad (2.12)$$

Where: Φ_{ST} = Gradient of the standard (Rhodamine 6G in methanol), η_x = Refractive Index of the medium in which QY of QDs is to be estimated, η_{ST} = Refractive Index of medium in which the QY of the standard was estimated. In measuring QY, the slit-widths of the spectrophotometer were maintained at 2 cm.

Transmission Emission Microscopy (TEM):

As-synthesized and phase transferred NPs were imaged using a JEOL 2010 Transmission Electron Microscope, operated at 100 kV accelerating beam voltage. Samples were drop-cast on holey carbon TEM grids (Ted Pella Inc.) and dried overnight prior to imaging.

Thermogravimetric analysis (TGA):

CdSe QDs dispersed in hexane were prepared for TGA by drying under Argon. CdSe QDs phase transferred into no-salt and salty water were centrifuged on a Beckman Coulter Ultracentrifuge to separate the particles from the supernatant. The collected particles were dried under Argon. All samples were loaded in alumina pans and analyzed using a Q-600 Simultaneous TGA/DSC from TA Instruments operating with a temperature ramp rate of 5 °C/min under Argon.

2.2.3 New Phase-Transfer Scheme

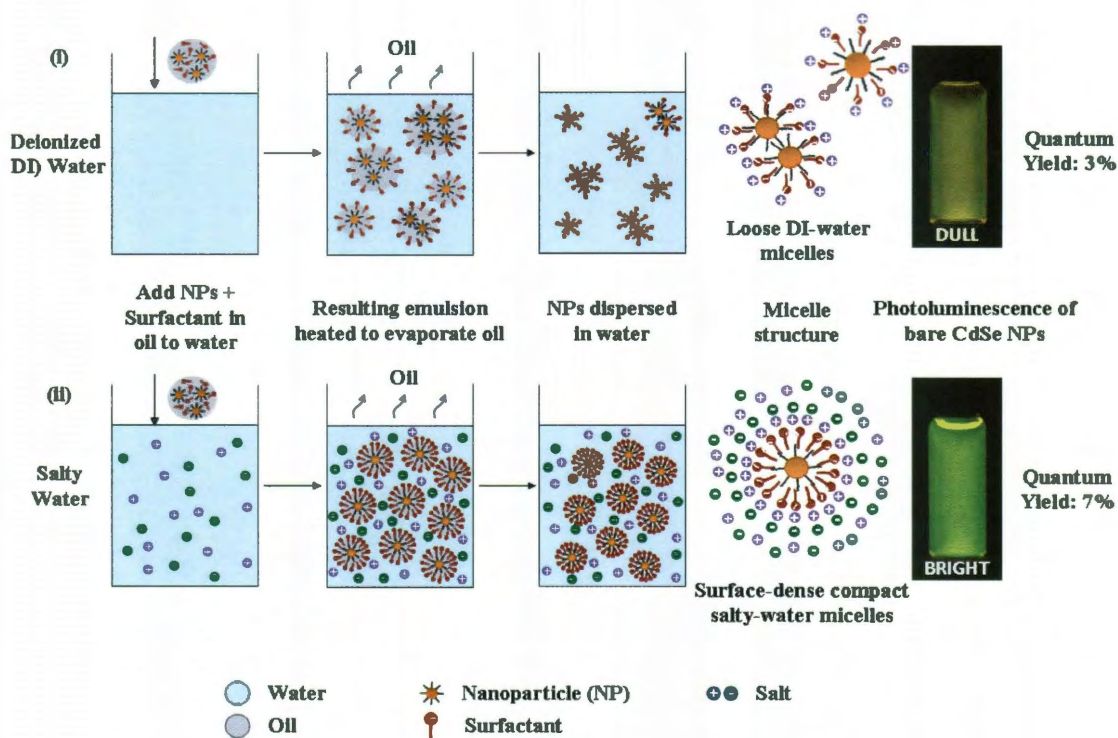
Phase-transfer of NPs using salty-micelles is depicted in the bottom panel of Fig. 2.8. As a starting reference point, the top panel of Fig. 2.8 (route (i)) is a representative schematic of the method pioneered by Brinker and coworkers⁷⁶, and is similar to the phase-transfer schematic described in Fig. 2.7. The differences are: (a) The surfactant used is AOT over CTAB. (It will be shown in a later section that CTAB could also successfully transfer QDs, however, the PL of QDs was better retained when transfer was carried out in micelles of AOT). (b) Brinker and coworkers formulated O/W microemulsions in transferring NPs to DI-water micelles, while our method employs O/W emulsions for NP phase transfer. In fact, we find from our independent investigations that there was little difference between the characteristics of NP-dispersions prepared in DI-water micelles, upon evaporating microemulsions vs. those obtained upon evaporating emulsions. As an example, we were able to transfer similar concentrations of CdSe QDs from hexane to water when AOT or CTAB concentrations used was 1.5 g-surfactant/L that corresponded to a (macro) emulsion domain. This was a significantly lower surfactant concentration

when compared with concentrations of AOT and CTAB at 28.6 g-surfactant/L (the latter used originally by Brinker and coworkers), where microemulsion domains exist. This finding allowed for a significant reduction in NP phase-transfer costs and thus, we performed all phase-transfer studies at a dosage of 1.5 g-surfactant/L.

The new method we have developed is depicted in the bottom panel of Fig 2.8 (Route (ii)). This method is similar to the Brinker's process (Route (i)) but with an important difference in that emulsion formulation is carried out in salt-containing water (or simply, salty-water). The starting rationale to carry out NP phase-transfer in salty-water is as follows: It is well known in surfactant literature that the solubility of ionic surfactants increases dramatically above a critical temperature known as the Krafft point or Krafft temperature (Fig. 2.9).^{105, 106} Above this temperature, the equilibrium structure of surfactants shift strongly from its "interfacially active" monomeric form to its micellar form which preferentially exists in the bulk.

The increase in aqueous-phase solubility of surfactants would also lower its ability to partition onto a hydrophobic substrate such as NPs. Thus, during the step of oil-evaporation (that is normally carried out well above the Krafft temperature: 60-85°C when the solvent is chloroform or hexane), encapsulation of NPs within surfactant micelles would be poor on account of higher surfactant solubility in water.^{76, 83, 95, 96, 107} Furthermore, repulsive electrostatic interactions between charged head groups of ionic surfactants would contribute to low surface density coverage of ionic surfactants on NP surfaces. These factors would result in low NP phase-transfer yields along with NPs transferring as clusters. An immediate implication of these effects is a loss in optical

properties of phase-transferred QDs. Photoluminescence of QDs in DI water, as observed under a UV-lamp showed QDs to appear as dull (QY = 3%).



(c)

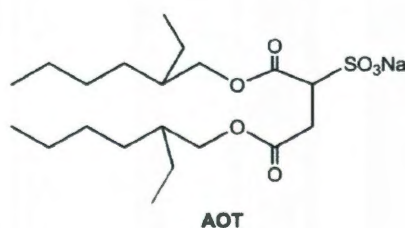


Figure 2.8: (a) Nanoparticle (NP) phase-transfer using plain/deionized (DI)-water micelles: Hexane containing CdSe QDs and Aerosol-OT (AOT) is added to DI water and mixed gently to form an emulsion. The concentration of AOT is 1.5 g/L. The emulsion is heated at 85 °C for 30 minutes to boil off the hexane, resulting in QDs encapsulated in DI water-micelles of AOT. DI-water micelles have a loosely packed structure, resulting in quenched photoluminescence (PL) in water and a quantum yield (QY) at 3%. (b) NP phase-transfer using salty-micelles: Hexane containing CdSe QDs and Aerosol-OT (AOT) is added to salt-containing water (NaCl at 3 g/L) and mixed gently to form an emulsion. The concentration of AOT is also maintained at 1.5 g/L. The emulsion is heated at 85 °C for 30 minutes to boil off the hexane, resulting in QDs encapsulated in

salty-micelles of AOT. Salty-micelles have laterally compact structure, resulting in strong retention of PL in water and a higher QY at 7%. (c) Structure of sodium bis(2-ethylhexyl)-sulfosuccinate (Aerosol-OT or AOT, figure reproduced from Nave *et al*)

To counter the surfactant solubility characteristics, we used the concept of the “salting-out” of surfactants by salts. The presence of salts is known to lower water-solubility of surfactants through a reorganization of the hydrogen-bond network with water.^{105, 106, 109} This effect termed “salting-out” would enhance surfactant partitioning onto the NP surface and possibly increase surfactant coverage. Furthermore, the presence of salt counter-ions, known to screen repulsive head-group interactions, could possibly compact the surfactant coverage. The PL of QDs in salty-water, as observed under the UV-lamp, was bright (QY = 7%).

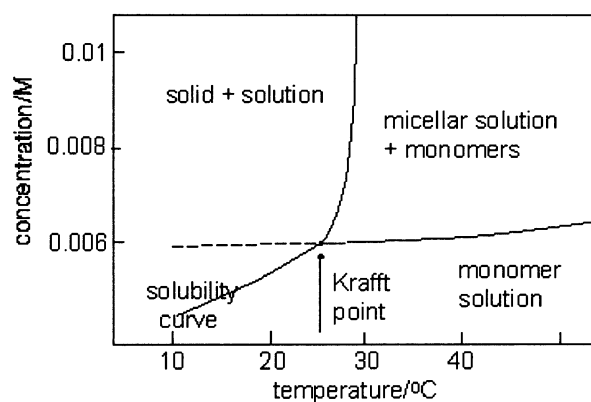


Figure 2.9: Solubility trends for ionic surfactants. The Krafft point or Krafft temperature is the point at which surfactant solubility equals the critical micelle concentration. Above this temperature, surfactants form a dispersed phase with a steep increase in solubility as micelles. Below the Krafft temperature, surfactants crystallize out of solution as hydrated crystals.

In the following sections, we describe the methods used to delineate the mechanism of NP phase-transfer in DI and salty-water micelles and to describe the nanostructure of resulting colloidal dispersions.

2.2.4 Results and Discussions

Diluted to the same concentrations, the respective salty and no-salt suspensions of CdSe QDs are shown in Fig. 2.10 (a). Their photoluminescence (PL) clearly differed from one another, illustrating the unexpected impact of high-salt-content water solutions (see also, Appendix A, Fig. A1). Measurements indicate PL intensity of QDs in salty water was more than twice that of QDs in DI water. The UV-vis absorbance spectra were similar to one another, with no apparent broadening or shifting of the absorbance features (Fig. 2.10 (b)). The PL spectra, too, were similar in shape and position. The QDs in salty water surprisingly retained PL better than QDs in no-salt water (Fig. 2.10 (c)). After 70 days, salty water QDs retained almost 60% of their initial PL intensity while QDs retained only ~10%. Similar long-term PL stability has only been reported for core-shell QDs (*e.g.*, CdSe/ZnS); for comparison, the shelf-life of commercially available ligand-exchanged core-shell QDs is 6 months¹¹⁰.

To assess the yield of phase-transfer of QDs from hexane to water, we quantified the QD concentrations through UV-vis spectroscopy. We found that $84\pm 8\%$ of the QDs was successfully transferred into salty water, but only $56\pm 2\%$ was transferred into DI water (Eq. 2.4). The balance of the QDs (as well as some AOT) was lost in the precipitate after centrifugation. The initial amounts of AOT and CdSe QDs corresponded roughly to a AOT-molecule: QD particle number ratio of 285:1, which was equivalent to a

theoretical monolayer coverage by AOT around the oleate-coated CdSe QDs, assuming a projected head group surface area of 0.55 nm^2 on 7.0 nm QDs (core diameter of 3.0 nm + twice the oleic acid length of 2 nm).¹¹¹

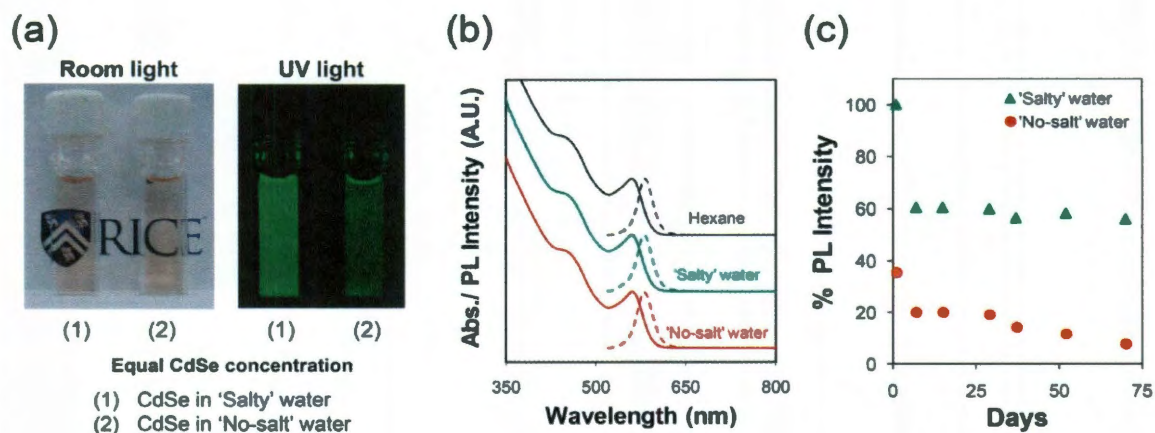


Figure 2.10: (a) Photographs of "salty" (3 g-NaCl/L = 51 mM; $0.6 \mu\text{mol-QD/L}$) and "no-salt" aqueous suspensions of 3.0-nm oleate-coated CdSe QDs ($0.6 \mu\text{mol-QD/L}$) under ambient and UV lighting (365 nm); phase-transfer agent = AOT. (b) UV-vis absorbance and photoluminescence (PL) spectra of oleate-coated CdSe QDs suspended in hexane, salty water, and no-salt water. (c) Percentage PL decrease of QD suspensions stored under ambient conditions as a function of time.

Increasing the AOT:CdSe ratio by 10 times by reducing the initial QD concentration (via decreasing CdSe concentration in hexane to $23.5 \mu\text{mol-QD/L}$ while keeping AOT at 1.5 g/L) improved the transfer yield into salty water to $100 \pm 3\%$, but reduced the yield into no-salt water to $48 \pm 1\%$ (Fig. 2.11). To understand the nature of the bilayer coating of the NPs in salty and DI water, we measured the zeta potential of CdSe QDs to be $-91 \pm 6 \text{ mV}$ and $-77 \pm 3 \text{ mV}$, respectively. A lower zeta potential of QDs in salty water was expected due to compression of the electric double layer. In our case, however, a higher zeta potential was observed, indicating a structural difference between the bilayer-coated QD structures in salty and no-salt environments.

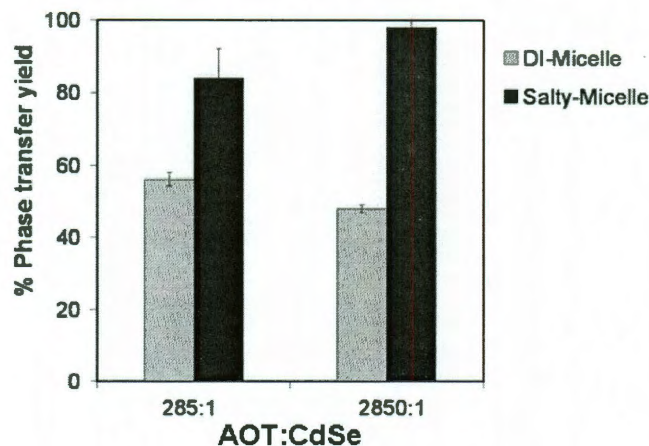


Figure 2.11: Phase-transfer yield of CdSe QDs transferred from hexane to salty-water and no-salt water with AOT at AOT: CdSe ratios of 285:1 (equivalent of 1 monolayer coverage of AOT on 3 nm CdSe QDs) and 2850:1 (equivalent of 10 monolayers coverage of AOT on 3 nm CdSe QDs).

We suggest that QDs have more AOT molecules packed within the outer leaflet of the bilayer when in the presence of an electrolyte, such that electrostatic repulsions between the negatively charged AOT head groups are screened more effectively (Fig. 2.12 (a)). This allows more AOT molecules to fit around the QD, leading to a higher surface charge density as reflected in the higher zeta potential. Similar effects of electrolytes have been reported for liposomes¹¹², micelles¹¹³, and air-water-supported surfactant monolayers.¹⁰⁰

The number of AOT molecules per QD in salty and no-salt water environments was calculated using the following empirical relationship developed by Loeb *et al* to solve the Poisson-Boltzmann equation for a highly charged sphere with zeta potential $\zeta < 150$ mV.¹¹⁵

$$\sigma = \frac{2\varepsilon\kappa k_B T}{\nu e_0} \left[\sinh\left(\frac{\nu e_0 \psi_0}{2k_B T}\right) + \frac{2 \tanh\left(\frac{\nu e_0 \psi_0}{4k_B T}\right)}{\kappa R_h} \right] \quad (2.13)$$

Where: σ is the surface charge density, ε is the dielectric constant, κ^{-1} is the Debye length (given by $\kappa^{-1} = \frac{0.304}{\sqrt{I}}$ in nanometers at 25 °C), I is ionic strength (mol/L), k_B is the Boltzmann constant, T is the temperature, ν is the counter ion valency, e_0 is the electron charge, ψ_0 is the surface potential, and R_h is the hydrodynamic radius of the QDs. Through DLS and analytical ultracentrifugation, the R_h of QDs suspended in salty water was determined to be ~4.5 nm, consistent with a particle core radius of 1.5 nm, oleate length of 2 nm, and AOT length of 1 nm. Interestingly, the R_h of QDs suspended in DI water was determined to be ~8.5 nm.

Assuming the surface potential was equal to the measured zeta potential and calculating the ionic strength from the concentrations of initial AOT (3.4 mmol/L) and NaCl, the surface charge density (σ) values in the salty ($I = 54.7$ mmol/L) and no-salt cases ($I = 3.4$ mmol/L) were found to be 0.072 and 0.020 C/m², respectively. These values corresponded to 69 and 15 AOT-molecules per QD particle; the presence of salt increased the AOT content by 4.6 times (see Appendix A, Fig. A2). The difference between these estimations from those made from Eq. 2.13 is likely due to the assumption that surface potential was not equal to the zeta potential.

The higher number of AOT molecules per QD in the salty case suggested that the AOT layer was more laterally dense than in the no-salt case, resulting in the AOT-oleate bilayer being more hydrophobic. To test this hypothesis, we studied the use of the

solvatochromic dye molecule Nile Red (NR), in which its fluorescence blue-shifts with decreasing polarity and increasing hydrophobicity.¹¹⁶ NR is soluble in hexane, fluorescing in the 500-700 nm range (Fig. 2.12 (b), trace 'i'). Virtually insoluble in water, NR was solubilized in water using AOT through the same phase transfer process, *i.e.*, a hexane/water/AOT/NR solution was prepared and heated for 30 min to evaporate away the hexane to form a micellar solution of NR. Tracking the NR fluorescence conveniently allowed us to conclude that 30 minutes was a sufficient length of heating time in the phase transfer process (see Appendix A, Fig. A3).

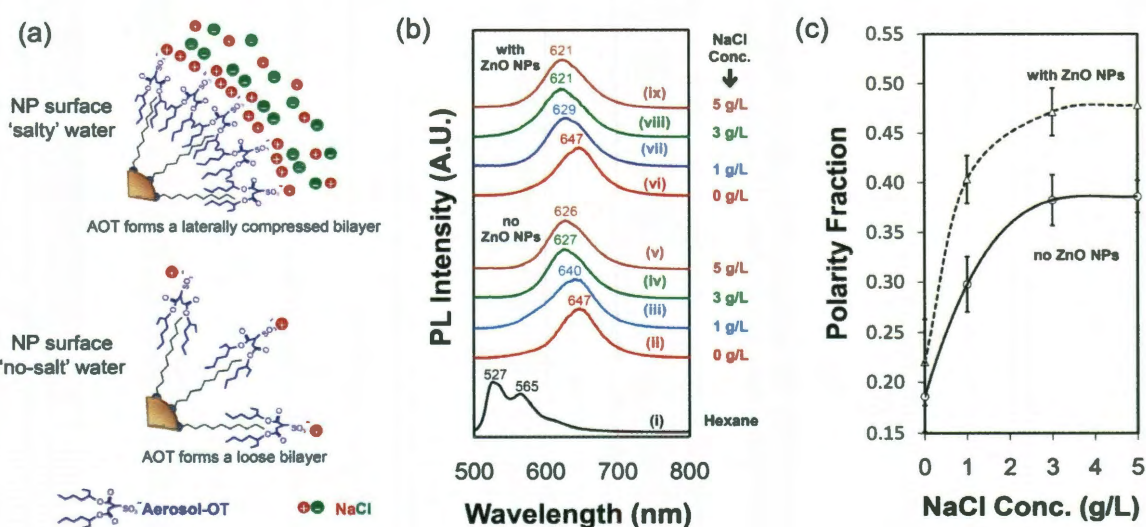


Figure 2.12: (a) Schematic showing AOT-oleate bilayer structure surrounding a NP under salty and no-salt conditions. (b) Emission spectra of Nile Red (i) in hexane; phase transferred with AOT into (ii) 0, (iii) 1, (iv) 3 and (v) 5 g-NaCl/L; and phase transferred with AOT and ZnO NPs into (vi) 0, (vii) 1, (viii) 3 and (ix) 5 g-NaCl/L. Excitation wavelength = 480 nm. (c) Plot of polarity fraction, $PF = I_{605} / (I_{605} + I_{650})$, as a function of NaCl concentration for samples phase transferred with and without ZnO NPs, where I_{605} and I_{650} are the average Nile Red PL intensities in the 10 nm band centered at 605 nm and 650 nm, respectively.

Fluorescence measurements of NR phase-transferred into water of varying salinity (0, 1, 3 and 5 g/L) showed a broad single peak that blue-shifted from 647 to 626 nm with

increasing salinity (Fig. 2.12 (b), traces 'ii' - 'v'). This subtly more hydrophobic nature of the AOT micelle interior came from the greater isolation of the water exterior due to the tighter packing of AOT molecules.

Because CdSe QDs and NR fluoresce in the same visible range, we chose to study ZnO NPs that did not interfere with NR fluorescence. We prepared ZnO particles (5-nm) solvothermally using oleic acid as the ligand¹¹⁷, and then phase-transferred them with NR into 0, 1, 3, and 5 g-NaCl/L solutions (Fig. 2.12 (b)). Without salt, a peak at 647 nm was observed (trace 'vi') similar to the case without the ZnO NPs (trace 'ii'). At the higher salinities, a blue solvatochromic shift up to 621 nm (traces 'vii' - 'ix') occurred, presumably indicative of an increasingly nonpolar environment of the AOT-oleate bilayer. Quantitative estimate of the change in polarity was obtained by calculating an empirically defined polarity fraction (PF)¹¹⁴, given by $PF = I_{605} / (I_{605} + I_{650})$, where I_{605} and I_{650} are the average NR fluorescence intensities in 10-nm range centered at 605 nm (non-polar environment) and 650 nm (polar environment), respectively. The PF of NR in the ZnO NP bilayers clearly increased with salinity, and the bilayers were slightly more hydrophobic than AOT micelles (Fig. 2.12 (c)). We thereby conclude that CdSe QDs in salty water had considerably greater long-term PL stability due to their bilayer being a better barrier against water penetration.

We quantified the size of CdSe QDs through several techniques. TEM analysis indicated an average diameter of 3.2 nm (relative standard deviation, RSD, of 16%), consistent with the first-exciton peak position of ~ 550 nm)⁴. No evidence of particle aggregation was seen in CdSe QDs phase transferred into no-salt or salt-containing water (Fig. 2.13 (a)). DLS measurements of the suspensions, however, indicated otherwise.

QDs in hexane and salty water were found to have D_h values of 6.9 ± 0.4 nm and 9 ± 2 nm, respectively, with the difference consistent with the presence of the AOT layer. QDs in DI water, on the other hand, had a D_h value of 17 ± 1 nm. While the transfer of QDs into salty water resulted in discrete and unaggregated particles, the transfer into DI water seemingly resulted in aggregates containing as many as 7 particles (*e.g.*, volume ratio = $(17\text{-nm})^3 / (9\text{-nm})^3 \sim 7$).

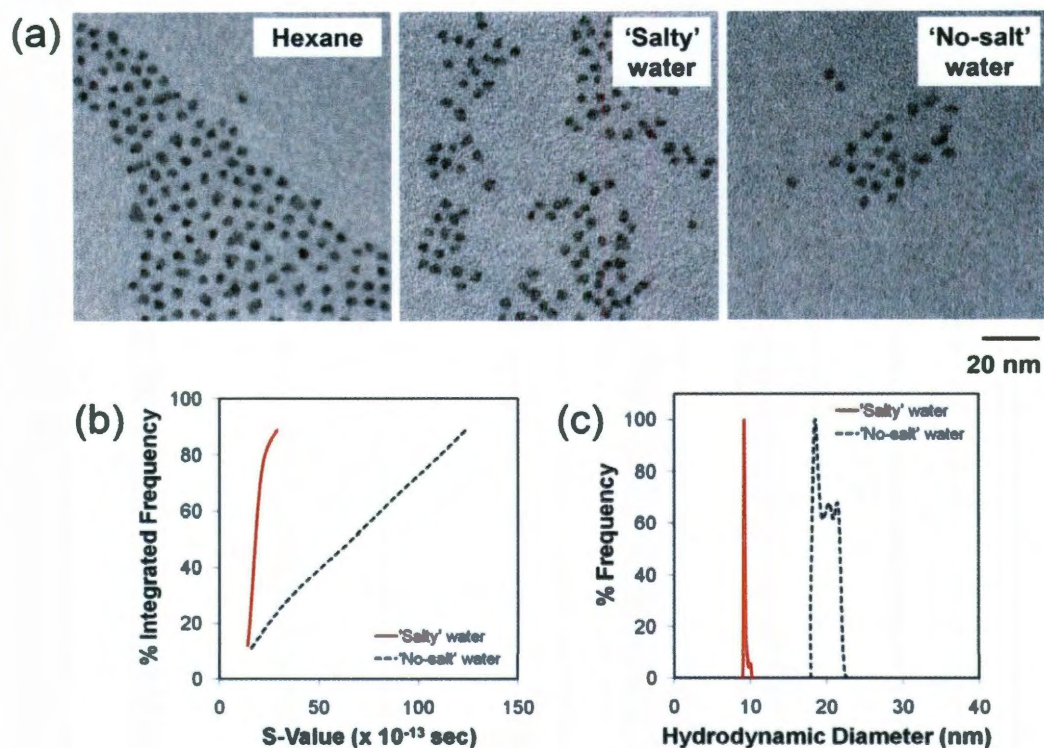


Figure 2.13: (a) TEM images of CdSe QDs drop-cast from hexane, salty, and no-salt suspensions. (b) Sedimentation coefficient distributions and (c) hydrodynamic diameter distributions of CdSe QDs in salty and no-salt water suspensions calculated from analytical ultracentrifugation measurements. 1 Svedberg = 10^{-13} sec.

The DLS results were confirmed through analytical ultracentrifugation experiments. The average sedimentation coefficients of CdSe QDs in salty and DI water were found to be

21 ± 0.5 S and 58 ± 5 S respectively (Fig. 2.13 (b)). For comparison, oleate-coated CdSe QDs (3-nm core diameter) dispersed in toluene were reported to have a sedimentation coefficient of 25 S,¹⁰² as estimated by from Eq. 2.10.

The QDs in salty and no-salt water had mean D_h values of 9.4 nm (1.1%) and 20 nm (4.5%), respectively (Fig. 2.13(c)). This aggregated state of QDs dispersed in DI water may be partially responsible for the observed lower QY through self-quenching (Fig. 2.10 (c)). It is not entirely clear why QDs are aggregated in the absence of salinity, but this could be related to observations that oil (hexane)-containing QDs and AOT, when mixed into a NaCl solution, formed stable nanometer-sized O/W emulsion droplets.

Unstable micron-sized emulsion droplets were formed when hexane-QD-AOT was added to DI water resulting in rapid coalescence and phase-separation of the oil phase (Fig. 2.14).^{118, 119} The role of salt in the emulsification of hydrocarbons and associated mechanisms of emulsion destabilization is the subject of Chapter 3 in this thesis.

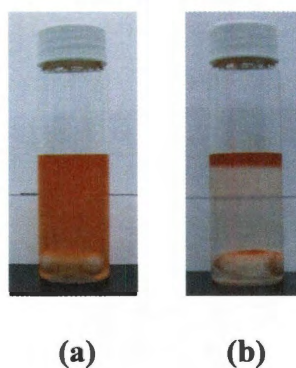


Figure 2.14: Emulsions of hexane in (a) salty-water (3 g-NaCl/L) and no-salt water 5 minutes upon formation. The hexane phase contains CdSe QDs with AOT as the emulsifier.

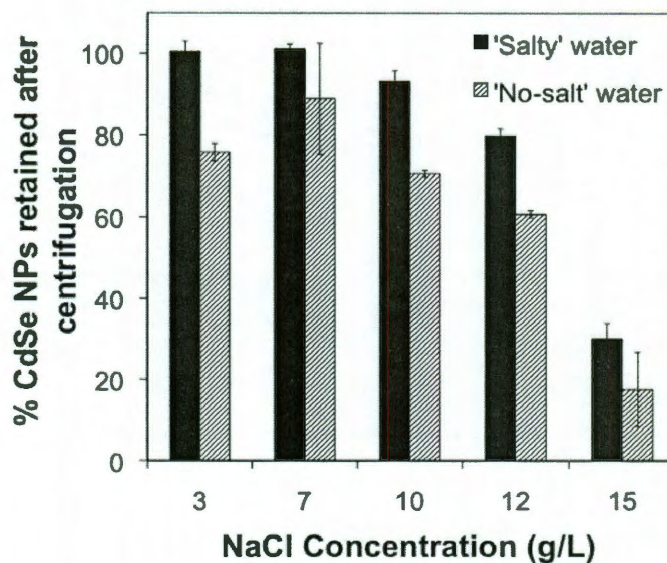


Figure 2.15: Colloidal stability of salty and no-salt suspensions of CdSe QDs at higher NaCl concentrations. pH = 6.

Lastly, to probe colloidal stability in greater detail, we first equalized QD concentrations in salty and no-salt water. Upon this, the salinity of both suspensions was systematically increased and after centrifugation, QDs that remained in suspension was measured using UV-vis. More than 20% of QDs were lost after salinity adjustment and centrifugation, indicating the no-salt suspension (in vial #2, Fig. 2.10 (a)) had lower colloidal stability than the salty suspension (in vial #1, Fig. 2.10 (b)). Increasing the salt content of both solutions further (up to 5 times), showed the salty suspension to be generally more stable than the no-salt suspension (Fig. 2.15). Salty suspensions of phase-transferred QDs would thus be suitably stable in human blood (equivalent salinity of ~ 9 g-NaCl/L), unlike DI water suspensions. It is conceivable that for phase-transferred QDs to be made colloiddally stable at higher salinities (for example, representative salinity values of sea water is 35 g-salts/L and that of downstream oil-containing reservoirs are 58.5 g-NaCl/L and 74.5 g-

KCl/L), appropriate selection of alternate surfactants becomes critical. These are the subjects of Chapters 3 and 4 in this thesis.

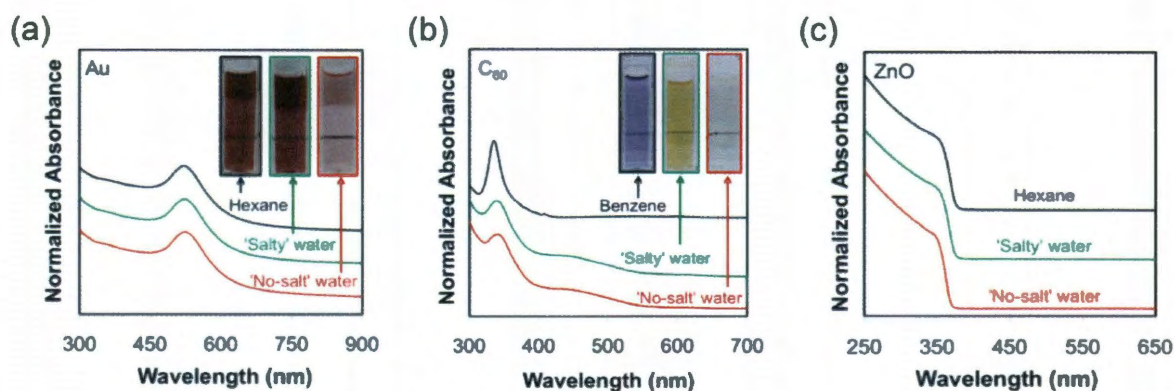


Figure 2.16: UV-vis absorbance spectra of (a) alkylthiol-coated Au NPs suspended in hexane, (b) C₆₀ suspended in benzene, and (c) oleate-coated ZnO NPs in hexane, and the corresponding salty (3 g/L NaCl) and no-salt water suspensions; phase-transfer agent = AOT (for Au and ZnO NPs) or CTAB (for C₆₀). Inset: photographs of NP suspensions.

Other NP compositions (*e.g.*, Au, C₆₀ and ZnO) and shapes (*e.g.*, tetrapods) have been successfully transferred with this technique. In all cases, (i) the amount of NPs transferred into salty water was always higher compared to DI water; (ii) the hydrodynamic diameter was smaller in the presence of salt; and (iii) charge density estimations (from zeta potential analysis) were always higher in the presence of salt (Table 2.1). Thiol-coated Au NPs with a diameter of 6.3-nm (RSD = 5.8%) were transferred into salty-water with high yield (87%), but the yield into DI water was considerably lower (17%) as shown by the much more dilute suspension (Fig. 2.16 (a)). The reason for higher transfer yield in salty-water is not fully understood although it appears that the decreased aqueous surfactant solubility in the presence of salt may be contributing to this effect. The decreased solubility would result in an increased

partitioning of surfactants to the emulsion interface, making more surfactant molecules available for NP stabilization after the oil phase is evaporated.

Table 2.1: Hydrodynamic diameter, zeta potential measurements and charge density estimations for different NPs phase transferred in no-salt and salt water (3 g-NaCl/L).

NP Type	Core Dia. (nm)	Ligand	Expec** 'D _h ' (nm)	Hydrodynamic Dia. 'D _h ' (nm)		Zeta Potential 'ζ' (mV)		Estimated Charge density 'σ' (C/m ²)	
				DI Water	3 g/L NaCl	DI Water	3 g/L NaCl	DI Water	3 g/L NaCl
CdSe QD	3	OA	9	17 ± 1	9 ± 2	-77 ± 3	-91 ± 6	-0.0203	-0.0724
Au	6.5	DDT	10.5	22.5 ± 2.5	9.3 ± 0.5	-64.6 ± 5.8	-88.1 ± 6.4	-0.015	-0.092
CdSe TP	20*	OA	20 #	31.9 ± 2.3	21.4 ± 1.7	-76.6 ± 3.4	-79 ± 5.9	-	-
C ₆₀ ^{&}	-	-	-	46.5 ± 4.4	21.4 ± 1.5	+71.3 ± 2.6	+68.9 ± 1.9	+0.016	+0.054
Fe ₂ O ₃	8	OA	14	29.8 ± 2.9	21.1 ± 1.6	-32.4 ± 4.0	-81.2 ± 2.4	-0.006	-0.07

** - expected hydrodynamic diameter for individually dispersed nanoparticle

* - the diameter of CdSe tetrapods was taken as twice the length of the arms (~10 nm)

- most of the AOT will form bilayers along the length of the TP arms. With the very small area of the arm tip, we can assume the hydrodynamic diameter to be the same as the core dia.

& - C₆₀ was transferred with cetyltrimethylammonium bromide (CTAB)

OA refers to oleic acid and DDT refers to dodecanthiol

It appears that C₆₀ buckyballs, which do not have an organic ligand coating, could also be phase-transferred into salty water in much the same manner (Fig. 2.16(b)). With the purplish color of the benzene suspension being a signature for unaggregated C₆₀¹²⁰, the yellowish color of the salty suspension indicated the presence of suspended but aggregated particles of C₆₀.¹²¹⁻¹²³ The no-salt suspension was not visibly yellow, as the transfer yield was quite low (~5%). Reports show that C₆₀ can be phase transferred directly without surfactant into water to produce "nC₆₀" aggregates by stirring C₆₀-containing tetrahydrofuran or toluene with water and removing the organic solvent.^{121, 123} In our processing, CTAB was needed for phase transfer to occur as control experiments

confirmed that C_{60} did not transfer into either salty or deionized water without CTAB. The benefits of using salt in the emulsion-based phase transfer of NPs appeared to be true not only for different NP types, but also for different surfactants (AOT and CTAB: See Appendix A, Fig. A4) and salts ($NaCl$, Na_2SO_4 and $CaCl_2$: See Appendix A, Figs. A5 and A6).

2.2.5 Conclusions

In conclusion, we have shown that a simple process modification of using salty-water instead of DI water in the emulsion-based method of transferring NPs from oil to water results in several benefits. Formation of compact surface-dense micelles in salty water better protects the surface of QDs and increases the transfer yield of NPs. The process results predominantly in individual NPs micelles with a narrow size distribution and high surface charge density due to better surfactant screening. These improvements increase the colloidal stability of the NPs making this process an elegant, economically promising, and effective method of transferring NPs from oil to water.

2.3 References

1. Sun, S. H.; Zeng, H., Size-controlled synthesis of magnetite nanoparticles. *Journal of the American Chemical Society* **2002**, 124, (28), 8204-8205.
2. Sun, S. H.; Murray, C. B.; Weller, D.; Folks, L.; Moser, A., Monodisperse FePt nanoparticles and ferromagnetic FePt nanocrystal superlattices. *Science* **2000**, 287, (5460), 1989-1992.
3. Yu, W. W.; Falkner, J. C.; Yavuz, C. T.; Colvin, V. L., Synthesis of monodisperse iron oxide nanocrystals by thermal decomposition of iron carboxylate salts. *Chemical Communications* **2004**, (20), 2306-2307.
4. Yu, W. W.; Qu, L. H.; Guo, W. Z.; Peng, X. G., Experimental determination of the extinction coefficient of CdTe, CdSe, and CdS nanocrystals. *Chemistry of Materials* **2003**, 15, (14), 2854-2860.
5. Yu, W. W.; Peng, X. G., Formation of high-quality CdS and other II-VI semiconductor nanocrystals in noncoordinating solvents: Tunable reactivity of monomers. *Angewandte Chemie-International Edition* **2002**, 41, (13), 2368-2371.
6. Peng, Z. A.; Peng, X. G., Formation of high-quality CdTe, CdSe, and CdS nanocrystals using CdO as precursor. *Journal of the American Chemical Society* **2001**, 123, (1), 183-184.
7. Park, J.; An, K. J.; Hwang, Y. S.; Park, J. G.; Noh, H. J.; Kim, J. Y.; Park, J. H.; Hwang, N. M.; Hyeon, T., Ultra-large-scale syntheses of monodisperse nanocrystals. *Nature Materials* **2004**, 3, (12), 891-895.
8. Manna, L.; Milliron, D. J.; Meisel, A.; Scher, E. C.; Alivisatos, A. P., Controlled growth of tetrapod-branched inorganic nanocrystals. *Nature Materials* **2003**, 2, (6), 382-385.
9. Talapin, D. V.; Nelson, J. H.; Shevchenko, E. V.; Aloni, S.; Sadtler, B.; Alivisatos, A. P., Seeded growth of highly luminescent CdSe/CdS nanoheterostructures with rod and tetrapod morphologies. *Nano Letters* **2007**, 7, (10), 2951-2959.
10. Peng, X. G.; Manna, L.; Yang, W. D.; Wickham, J.; Scher, E.; Kadavanich, A.; Alivisatos, A. P., Shape control of CdSe nanocrystals. *Nature* **2000**, 404, (6773), 59-61.

11. Puntès, V. F.; Krishnan, K. M.; Alivisatos, A. P., Colloidal nanocrystal shape and size control: The case of cobalt. *Science* **2001**, 291, (5511), 2115-2117.
12. Milliron, D. J.; Hughes, S. M.; Cui, Y.; Manna, L.; Li, J. B.; Wang, L. W.; Alivisatos, A. P., Colloidal nanocrystal heterostructures with linear and branched topology. *Nature* **2004**, 430, (6996), 190-195.
13. Yin, Y.; Alivisatos, A. P., Colloidal nanocrystal synthesis and the organic-inorganic interface. *Nature* **2005**, 437, (7059), 664-670.
14. Jin, R. C.; Cao, Y. C.; Hao, E. C.; Metraux, G. S.; Schatz, G. C.; Mirkin, C. A., Controlling anisotropic nanoparticle growth through plasmon excitation. *Nature* **2003**, 425, (6957), 487-490.
15. Zhang, Z.; Wong, L. M.; Ong, H. G.; Wang, X. J.; Wang, J. L.; Wang, S. J.; Chen, H. Y.; Wu, T., Self-Assembled Shape- and Orientation-Controlled Synthesis of Nanoscale Cu₃Si Triangles, Squares, and Wires. *Nano Letters* **2008**, 8, (10), 3205-3210.
16. Grzelczak, M.; Perez-Juste, J.; Mulvaney, P.; Liz-Marzan, L. M., Shape control in gold nanoparticle synthesis. *Chemical Society Reviews* **2008**, 37, (9), 1783-1791.
17. Tao, A. R.; Habas, S.; Yang, P. D., Shape control of colloidal metal nanocrystals. *Small* **2008**, 4, (3), 310-325.
18. Anderson, R. E.; Chan, W. C. W., Systematic investigation of preparing biocompatible, single, and small ZnS-capped CdSe quantum dots with amphiphilic polymers. *ACS Nano* **2008**, 2, (7), 1341-1352.
19. Levy, L.; Sahoo, Y.; Kim, K. S.; Bergey, E. J.; Prasad, P. N., Nanochemistry: Synthesis and characterization of multifunctional nanoclusters for biological applications. *Chemistry of Materials* **2002**, 14, (9), 3715-3721.
20. Roy, I.; Ohulchanskyy, T. Y.; Pudavar, H. E.; Bergey, E. J.; Oseroff, A. R.; Morgan, J.; Dougherty, T. J.; Prasad, P. N., Ceramic-based nanoparticles entrapping water-insoluble photosensitizing anticancer drugs: A novel drug-carrier system for photodynamic therapy. *Journal of the American Chemical Society* **2003**, 125, (26), 7860-7865.

21. Wu, X. Y.; Liu, H. J.; Liu, J. Q.; Haley, K. N.; Treadway, J. A.; Larson, J. P.; Ge, N. F.; Peale, F.; Bruchez, M. P., Immunofluorescent labeling of cancer marker Her2 and other cellular targets with semiconductor quantum dots. *Nature Biotechnology* **2003**, 21, (1), 41-46.
22. Lee, J. H.; Huh, Y. M.; Jun, Y.; Seo, J.; Jang, J.; Song, H. T.; Kim, S.; Cho, E. J.; Yoon, H. G.; Suh, J. S.; Cheon, J., Artificially engineered magnetic nanoparticles for ultra-sensitive molecular imaging. *Nature Medicine* **2007**, 13, (1), 95-99.
23. Mei, B. C.; Susumu, K.; Medintz, I. L.; Mattoussi, H., Polyethylene glycol-based bidentate ligands to enhance quantum dot and gold nanoparticle stability in biological media. *Nature Protocols* **2009**, 4, (3), 412-423.
24. Smith, A. M.; Duan, H. W.; Mohs, A. M.; Nie, S. M., Bioconjugated quantum dots for in vivo molecular and cellular imaging. *Advanced Drug Delivery Reviews* **2008**, 60, (11), 1226-1240.
25. Slowing, II; Vivero-Escoto, J. L.; Wu, C. W.; Lin, V. S. Y., Mesoporous silica nanoparticles as controlled release drug delivery and gene transfection carriers. *Advanced Drug Delivery Reviews* **2008**, 60, (11), 1278-1288.
26. Sun, C.; Lee, J. S. H.; Zhang, M. Q., Magnetic nanoparticles in MR imaging and drug delivery. *Advanced Drug Delivery Reviews* **2008**, 60, (11), 1252-1265.
27. Biju, V.; Itoh, T.; Anas, A.; Sujith, A.; Ishikawa, M., Semiconductor quantum dots and metal nanoparticles: syntheses, optical properties, and biological applications. *Analytical and Bioanalytical Chemistry* **2008**, 391, (7), 2469-2495.
28. Fang, C.; Zhang, M. Q., Multifunctional magnetic nanoparticles for medical imaging applications. *Journal of Materials Chemistry* **2009**, 19, (35), 6258-6266.
29. Duchesne, L.; Gentili, D.; Comes-Franchini, M.; Fernig, D. G., Robust Ligand Shells for Biological Applications of Gold Nanoparticles. *Langmuir* **2008**, 24, (23), 13572-13580.
30. Chan, W. C. W.; Nie, S. M., Quantum dot bioconjugates for ultrasensitive nonisotopic detection. *Science* **1998**, 281, (5385), 2016-2018.

31. Bruchez, M.; Moronne, M.; Gin, P.; Weiss, S.; Alivisatos, A. P., Semiconductor nanocrystals as fluorescent biological labels. *Science* **1998**, 281, (5385), 2013-2016.
32. Mattoussi, H.; Mauro, J. M.; Goldman, E. R.; Anderson, G. P.; Sundar, V. C.; Mikulec, F. V.; Bawendi, M. G., Self-assembly of CdSe-ZnS quantum dot bioconjugates using an engineered recombinant protein. *Journal of the American Chemical Society* **2000**, 122, (49), 12142-12150.
33. Medintz, I. L.; Uyeda, H. T.; Goldman, E. R.; Mattoussi, H., Quantum dot bioconjugates for imaging, labelling and sensing. *Nature Materials* **2005**, 4, (6), 435-446.
34. Gittins, D. I.; Caruso, F., Biological and physical applications of water-based metal nanoparticles synthesized in organic solution. *ChemPhysChem* **2002**, 3, (1), 110-113.
35. Gonzales, M.; Krishnan, K. M., Phase transfer of highly monodisperse iron oxide nanocrystals with Pluronic F127 for biomedical applications. *Journal of Magnetism and Magnetic Materials* **2007**, 311, (1), 59-62.
36. Yu, W. W.; Chang, E.; Falkner, J. C.; Zhang, J. Y.; Al-Somali, A. M.; Sayes, C. M.; Johns, J.; Drezek, R.; Colvin, V. L., Forming biocompatible and nonaggregated nanocrystals in water using amphiphilic polymers. *Journal of the American Chemical Society* **2007**, 129, (10), 2871-2879.
37. Lees, E. E.; Nguyen, T. L.; Clayton, A. H. A.; Mulvaney, P.; Muir, B. W., The Preparation of Colloidally Stable, Water-Soluble, Biocompatible, Semiconductor Nanocrystals With a Small Hydrodynamic Diameter. *ACS Nano* **2009**, 3, (5), 1121-1128.
38. De Palma, R.; Peeters, S.; Van Bael, M. J.; Van den Rul, H.; Bonroy, K.; Laureyn, W.; Mullens, J.; Borghs, G.; Maes, G., Silane ligand exchange to make hydrophobic superparamagnetic nanoparticles water-dispersible. *Chemistry of Materials* **2007**, 19, (7), 1821-1831.
39. Pradeep, T.; Anshup, Noble metal nanoparticles for water purification: A critical review. *Thin Solid Films* **2009**, 517, (24), 6441-6478.
40. Hildebrand, H.; Mackenzie, K.; Kopinke, F. D., Highly Active Pd-on-Magnetite Nanocatalysts for Aqueous Phase Hydrodechlorination Reactions. *Environmental Science & Technology* **2009**, 43, (9), 3254-3259.

41. Hildebrand, H.; Mackenzie, K.; Kopinke, F. D., Pd/Fe₃O₄ nano-catalysts for selective dehalogenation in wastewater treatment processes-Influence of water constituents. *Applied Catalysis B-Environmental* **2009**, 91, (1-2), 389-396.
42. Yavuz, C. T.; Mayo, J. T.; Yu, W. W.; Prakash, A.; Falkner, J. C.; Yean, S.; Cong, L. L.; Shipley, H. J.; Kan, A.; Tomson, M.; Natelson, D.; Colvin, V. L., Low-field magnetic separation of monodisperse Fe₃O₄ nanocrystals. *Science* **2006**, 314, (5801), 964-967.
43. Mayo, J. T.; Yavuz, C.; Yean, S.; Cong, L.; Shipley, H.; Yu, W.; Falkner, J.; Kan, A.; Tomson, M.; Colvin, V. L., The effect of nanocrystalline magnetite size on arsenic removal. *Science and Technology of Advanced Materials* **2007**, 8, (1-2), 71-75.
44. Li, Q. L.; Mahendra, S.; Lyon, D. Y.; Brunet, L.; Liga, M. V.; Li, D.; Alvarez, P. J. J., Antimicrobial nanomaterials for water disinfection and microbial control: Potential applications and implications. *Water Research* **2008**, 42, (18), 4591-4602.
45. Yang, J.; Lee, J. Y.; Ying, J. Y., Phase transfer and its applications in nanotechnology. *Chemical Society Reviews* 40, (3), 1672-1696.
46. Nagesha, D. K.; Plouffe, B. D.; Phan, M.; Lewis, L. H.; Sridhar, S.; Murthy, S. K., Functionalization-induced improvement in magnetic properties of Fe₃O₄ nanoparticles for biomedical applications. *Journal of Applied Physics* **2009**, 105, (7), 07B317.
47. Robinson, I.; Alexander, C.; Tung, L. D.; Fernig, D. G.; Thanh, N. T. K., Fabrication of water-soluble magnetic nanoparticles by ligand-exchange with thermo-responsive polymers. *Journal of Magnetism and Magnetic Materials* **2009**, 321, (10), 1421-1423.
48. Ji, M. L.; Yang, W. L.; Ren, Q. G.; Lu, D. R., Facile phase transfer of hydrophobic nanoparticles with poly(ethylene glycol) grafted hyperbranched poly(amido amine). *Nanotechnology* **2009**, 20, (7), 075101.
49. Shen, L.; Pich, A.; Fava, D.; Wang, M. F.; Kumar, S.; Wu, C.; Scholes, G. D.; Winnik, M. A., Loading quantum dots into thermo-responsive microgels by reversible transfer from organic solvents to water. *Journal of Materials Chemistry* **2008**, 18, (7), 763-770.

50. Tromsdorf, U. I.; Bigall, N. C.; Kaul, M. G.; Bruns, O. T.; Nikolic, M. S.; Mollwitz, B.; Sperling, R. A.; Reimer, R.; Hohenberg, H.; Parak, W. J.; Forster, S.; Beisiegel, U.; Adam, G.; Weller, H., Size and surface effects on the MRI relaxivity of manganese ferrite nanoparticle contrast agents. *Nano Letters* **2007**, *7*, (8), 2422-2427.
51. Duan, H. W.; Nie, S. M., Cell-penetrating quantum dots based on multivalent and endosome-disrupting surface coatings. *Journal of the American Chemical Society* **2007**, *129*, (11), 3333-3338.
52. Lattuada, M.; Hatton, T. A., Functionalization of monodisperse magnetic nanoparticles. *Langmuir* **2007**, *23*, (4), 2158-2168.
53. Dubois, F.; Mahler, B.; Dubertret, B.; Doris, E.; Mioskowski, C., A versatile strategy for quantum dot ligand exchange. *Journal of the American Chemical Society* **2007**, *129*, (3), 482-483.
54. Smith, A. M.; Duan, H. W.; Rhyner, M. N.; Ruan, G.; Nie, S. M., A systematic examination of surface coatings on the optical and chemical properties of semiconductor quantum dots. *Physical Chemistry Chemical Physics* **2006**, *8*, (33), 3895-3903.
55. Peng, S.; Wang, C.; Xie, J.; Sun, S. H., Synthesis and stabilization of monodisperse Fe nanoparticles. *Journal of the American Chemical Society* **2006**, *128*, (33), 10676-10677.
56. Latham, A. H.; Williams, M. E., Versatile routes toward functional, water-soluble nanoparticles via trifluoroethyl ester-PEG-thiol ligands. *Langmuir* **2006**, *22*, (9), 4319-4326.
57. Lee, S. Y.; Harris, M. T., Surface modification of magnetic nanoparticles capped by oleic acids: Characterization and colloidal stability in polar solvents. *Journal of Colloid and Interface Science* **2006**, *293*, (2), 401-408.
58. Hong, R.; Fischer, N. O.; Emrick, T.; Rotello, V. M., Surface PEGylation and ligand exchange chemistry of FePt nanoparticles for biological applications. *Chemistry of Materials* **2005**, *17*, (18), 4617-4621.
59. Woehrle, G. H.; Warner, M. G.; Hutchison, J. E., Ligand exchange reactions yield subnanometer, thiol-stabilized gold particles with defined optical transitions. *Journal of Physical Chemistry B* **2002**, *106*, (39), 9979-9981.

60. Murray, C. B.; Norris, D. J.; Bawendi, M. G., Synthesis and Characterization of Nearly Monodisperse CDE (E = S, SE, TE) Semiconductor Nanocrystallites. *Journal of the American Chemical Society* **1993**, 115, (19), 8706-8715.
61. Pathak, S.; Choi, S. K.; Arnheim, N.; Thompson, M. E., Hydroxylated quantum dots as luminescent probes for in situ hybridization. *Journal of the American Chemical Society* **2001**, 123, (17), 4103-4104.
62. Querner, C.; Reiss, P.; Bleuse, J.; Pron, A., Chelating Ligands for nanocrystals' surface functionalization. *Journal of the American Chemical Society* **2004**, 126, (37), 11574-11582.
63. Bagaria, H. G.; Ada, E. T.; Shamsuzzoha, M.; Nikles, D. E.; Johnson, D. T., Understanding mercapto ligand exchange on the surface of FePt nanoparticles. *Langmuir* **2006**, 22, (18), 7732-7737.
64. Jana, N. R.; Earhart, C.; Ying, J. Y., Synthesis of water-soluble and functionalized nanoparticles by silica coating. *Chemistry of Materials* **2007**, 19, (21), 5074-5082.
65. Gehl, B.; Aleksandrovic, V.; Erbacher, M.; Juergens, B.; Schurenberg, M.; Kornowski, A.; Weller, H.; Baumer, M., Ligand exchange with thiols: Effects on composition and morphology of colloidal CoPt nanoparticles. *ChemPhysChem* **2008**, 9, (6), 821-825.
66. Wang, J.; Xu, J.; Goodman, M. D.; Chen, Y.; Cai, M.; Shinar, J.; Lin, Z. Q., A simple biphasic route to water soluble dithiocarbamate functionalized quantum dots. *Journal of Materials Chemistry* **2008**, 18, (27), 3270-3274.
67. Smith, A. M.; Nie, S., Minimizing the hydrodynamic size of quantum dots with multifunctional multidentate polymer ligands. *Journal of the American Chemical Society* **2008**, 130, (34), 11278-11279.
68. Kairdolf, B. A.; Smith, A. M.; Nie, S., One-pot synthesis, encapsulation, and solubilization of size-tuned quantum dots with amphiphilic multidentate ligands. *Journal of the American Chemical Society* **2008**, 130, (39), 12866-12867.
69. Xu, C. J.; Xu, K. M.; Gu, H. W.; Zheng, R. K.; Liu, H.; Zhang, X. X.; Guo, Z. H.; Xu, B., Dopamine as a robust anchor to immobilize functional molecules on the iron oxide shell of magnetic nanoparticles. *Journal of the American Chemical Society* **2004**, 126, (32), 9938-9939.

70. Zhang, T. R.; Ge, J. P.; Hu, Y. P.; Yin, Y. D., A general approach for transferring hydrophobic nanocrystals into water. *Nano Letters* **2007**, 7, (10), 3203-3207.
71. Zhao, Y.; Perez-Segarra, W.; Shi, Q. C.; Wei, A., Dithiocarbamate assembly on gold. *Journal of the American Chemical Society* **2005**, 127, (20), 7328-7329.
72. Dorokhin, D.; Tomczak, N.; Han, M. Y.; Reinhoudt, D. N.; Velders, A. H.; Vancso, G. J., Reversible Phase Transfer of (CdSe/ZnS) Quantum Dots between Organic and Aqueous Solutions. *ACS Nano* **2009**, 3, (3), 661-667.
73. Gittins, D. I.; Caruso, F., Spontaneous phase transfer of nanoparticulate metals from organic to aqueous media. *Angewandte Chemie-International Edition* **2001**, 40, (16), 3001-3004.
74. Nann, T., Phase-transfer of CdSe@ZnS quantum dots using amphiphilic hyperbranched polyethylenimine. *Chemical Communications* **2005**, (13), 1735-1736.
75. Sastry, M., Phase transfer protocols in nanoparticle synthesis. *Current Science* **2003**, 85, (12), 1735-1745.
76. Fan, H. Y.; Yang, K.; Boye, D. M.; Sigmon, T.; Malloy, K. J.; Xu, H. F.; Lopez, G. P.; Brinker, C. J., Self-assembly of ordered, robust, three-dimensional gold nanocrystal/silica arrays. *Science* **2004**, 304, (5670), 567-571.
77. Fan, H. Y.; Leve, E. W.; Scullin, C.; Gabaldon, J.; Tallant, D.; Bunge, S.; Boyle, T.; Wilson, M. C.; Brinker, C. J., Surfactant-assisted synthesis of water-soluble and biocompatible semiconductor quantum dot micelles. *Nano Letters* **2005**, 5, (4), 645-648.
78. Goodman, C. A.; Frankamp, B. L.; Cooper, B. A.; Rotello, V. A., Surfactant layering on mixed monolayer-protected gold clusters. *Colloids and Surfaces B-Biointerfaces* **2004**, 39, (3), 119-123.
79. Meriguet, G.; Dubois, E.; Perzynski, R., Liquid-liquid phase-transfer of magnetic nanoparticles in organic solvents. *Journal of Colloid and Interface Science* **2003**, 267, (1), 78-85.
80. Prakash, A.; Zhu, H. G.; Jones, C. J.; Benoit, D. N.; Ellsworth, A. Z.; Bryant, E. L.; Colvin, V. L., Bilayers as Phase Transfer Agents for Nanocrystals Prepared in Nonpolar Solvents. *ACS Nano* **2009**, 3, (8), 2139-2146.

81. Swami, A.; Kumar, A.; Sastry, M., Formation of water-dispersible gold nanoparticles using a technique based on surface-bound interdigitated bilayers. *Langmuir* **2003**, 19, (4), 1168-1172.
82. Gorelikov, I.; Matsuura, N., Single-step coating of mesoporous silica on cetyltrimethyl ammonium bromide-capped nanoparticles. *Nano Letters* **2008**, 8, (1), 369-373.
83. Li, H. B.; Wang, X. Q.; Gao, Z. N.; He, Z. K., Gemini surfactant for fluorescent and stable quantum dots in aqueous solution. *Nanotechnology* **2007**, 18, (20), 205603.
84. Swami, A.; Jadhav, A.; Kumar, A.; Adyanthaya, S. D.; Sastry, M., Water-dispersible nanoparticles via interdigitation of sodium dodecylsulphate molecules in octadecylamine-capped gold nanoparticles at a liquid-liquid interface. *Proceedings of the Indian Academy of Sciences-Chemical Sciences* **2003**, 115, (5-6), 679-687.
85. Mohammadi, Z.; Cole, A.; Berkland, C. J., In Situ Synthesis of Iron Oxide within Polyvinylamine Nanoparticle Reactors. *Journal of Physical Chemistry C* **2009**, 113, (18), 7652-7658.
86. Muir, B. W.; Moffat, B. A.; Harbour, P.; Coia, G.; Zhen, G. L.; Waddington, L.; Scoble, J.; Krah, D.; Thang, S. H.; Chong, Y. K.; Mulvaney, P.; Hartley, P., Combinatorial Discovery of Novel Amphiphilic Polymers for the Phase Transfer of Magnetic Nanoparticles. *Journal of Physical Chemistry C* **2009**, 113, (38), 16615-16624.
87. Pellegrino, T.; Manna, L.; Kudera, S.; Liedl, T.; Koktysh, D.; Rogach, A. L.; Keller, S.; Radler, J.; Natile, G.; Parak, W. J., Hydrophobic nanocrystals coated with an amphiphilic polymer shell: A general route to water soluble nanocrystals. *Nano Letters* **2004**, 4, (4), 703-707.
88. Roth, P. J.; Kim, K. S.; Bae, S. H.; Sohn, B. H.; Theato, P.; Zentel, R., Hetero-Telechelic Dye-Labeled Polymer for Nanoparticle Decoration. *Macromolecular Rapid Communications* **2009**, 30, (14), 1274-1278.
89. Singh, S.; Patel, P.; Jaiswal, S.; Prabhune, A. A.; Ramana, C. V.; Prasad, B. L. V., A direct method for the preparation of glycolipid-metal nanoparticle conjugates: sophorolipids as reducing and capping agents for the synthesis of water re-dispersible silver nanoparticles and their antibacterial activity. *New Journal of Chemistry* **2009**, 33, (3), 646-652.

90. Kasture, M.; Singh, S.; Patel, P.; Joy, P. A.; Prabhune, A. A.; Ramana, C. V.; Prasad, B. L. V., Multiutility sophorolipids as nanoparticle capping agents: Synthesis of stable and water dispersible Co nanoparticles. *Langmuir* **2007**, *23*, (23), 11409-11412.
91. Dubertret, B.; Skourides, P.; Norris, D. J.; Noireaux, V.; Brivanlou, A. H.; Libchaber, A., In vivo imaging of quantum dots encapsulated in phospholipid micelles. *Science* **2002**, *298*, (5599), 1759-1762.
92. Nida, D. L.; Nitin, N.; Yu, W. W.; Colvin, V. L.; Richards-Kortum, R., Photostability of quantum dots with amphiphilic polymer-based passivation strategies. *Nanotechnology* **2008**, *19*, (3), 035701.
93. Feng, L. Y.; Kong, X. G.; Chao, K. F.; Sun, Y. J.; Zeng, Q. H.; Zhang, Y. L., Efficient phase transfer of hydrophobic CdSe quantum dots: From nonpolar organic solvent to biocompatible water buffer. *Materials Chemistry and Physics* **2005**, *93*, (2-3), 310-313.
94. Wang, Y.; Wong, J. F.; Teng, X. W.; Lin, X. Z.; Yang, H., "Pulling" nanoparticles into water: Phase transfer of oleic acid stabilized monodisperse nanoparticles into aqueous solutions of alpha-cyclodextrin. *Nano Letters* **2003**, *3*, (11), 1555-1559.
95. Fan, H. Y.; Leve, E.; Gabaldon, J.; Wright, A.; Haddad, R. E.; Brinker, C. J., Ordered two- and three-dimensional arrays self-assembled from water-soluble nanocrystal-micelles. *Advanced Materials* **2005**, *17*, (21), 2587.
96. Fan, H. Y., Nanocrystal-micelle: synthesis, self-assembly and application. *Chemical Communications* **2008**, (12), 1383-1394.
97. Bagaria, H. G.; Kini, G. C.; Wong, M. S., Electrolyte Solutions Improve Nanoparticle Transfer from Oil to Water. *Journal of Physical Chemistry C* **2010**, *114*, (47), 19901-19907.
98. Asokan, S.; Krueger, K. M.; Colvin, V. L.; Wong, M. S., Shape-controlled synthesis of CdSe tetrapods using cationic surfactant ligands. *Small* **2007**, *3*, (7), 1164-1169.
99. Prasad, B. L. V.; Stoeva, S. I.; Sorensen, C. M.; Klabunde, K. J., Digestive ripening of thiolated gold nanoparticles: The effect of alkyl chain length. *Langmuir* **2002**, *18*, (20), 7515-7520.

100. Umlong, I. M.; Ismail, K., Micellization of AOT in aqueous sodium chloride, sodium acetate, sodium propionate, and sodium butyrate media: A case of two different concentration regions of counterion binding. *Journal of Colloid and Interface Science* **2005**, 291, (2), 529-536.
101. Jamison, J. A.; Krueger, K. M.; Mayo, J. T.; Yavuz, C. T.; Redden, J. J.; Colvin, V. L., Applying analytical ultracentrifugation to nanocrystal suspensions. *Nanotechnology* **2009**, 20, (35), 10.
102. Jamison, J. A.; Krueger, K. M.; Yavuz, C. T.; Mayo, J. T.; LeCrone, D.; Redden, J. J.; Colvin, V. L., Size-dependent sedimentation properties of nanocrystals. *ACS Nano* **2008**, 2, (2), 311-319.
103. Hiemenz, P. C.; Rajagopalan, R., *Principles of Colloid and Surface Chemistry*. 3rd ed.; Marcel Dekker: New York, 1997.
104. Yvon, H. J. A Guide to Recording Fluorescence Quantum Yields. <http://www.horiba.com/fileadmin/uploads/Scientific/Documents/Fluorescence/quantumyieldstrad.pdf> (17th August 2009),
105. Israelachvili, J. N., *Intermolecular and Surface Forces*. Academic Press: New York, 1991.
106. Evans, D. F., Wennerström, H, *The Colloidal Domain: Where Physics, Chemistry, Biology and Technology Meet*. 2 ed.; Wiley-VCH: 1999.
107. Isojima, T.; Suh, S. K.; Sande, J. B. V.; Hatton, T. A., Controlled Assembly of Nanoparticle Structures: Spherical and Toroidal Superlattices and Nanoparticle-Coated Polymeric Beads. *Langmuir* **2009**, 25, (14), 8292-8298.
108. Nave, S.; Eastoe, J.; Penfold, J., What is so special about Aerosol-OT? 1. Aqueous systems. *Langmuir* **2000**, 16, (23), 8733-8740.
109. Rosen, M. J., *Surfactants and Interfacial Phenomena*. 2nd edition ed.; Wiley Interscience: New York, 1989.
110. Invitrogen™ Qdot® ITK™ Carboxyl Quantum Dots. <http://probes.invitrogen.com/media/pis/mp19020.pdf> (5/19/2010),

111. De, T. K.; Maitra, A., Solution Behavior of Aerosol-OT in Non Polar-Solvents. *Advances in Colloid and Interface Science* **1995**, 59, 95-193.
112. Carrion, F. J.; Delamaza, A.; Parra, J. L., The Influence of Ionic-Strength and Lipid Bilayer Charge on the Stability of Liposomes. *Journal of Colloid and Interface Science* **1994**, 164, (1), 78-87.
113. Adler, J. J.; Singh, P. K.; Patist, A.; Rabinovich, Y. I.; Shah, D. O.; Moudgil, B. M., Correlation of particulate dispersion stability with the strength of self-assembled surfactant films. *Langmuir* **2000**, 16, (18), 7255-7262.
114. Ye, F.; Cui, C.; Kirkeminde, A.; Dong, D.; Collinson, M. M.; Higgins, D. A., Fluorescence Spectroscopy Studies of Silica Film Polarity Gradients Prepared by Infusion-Withdrawal Dip-Coating. *Chemistry of Materials* **2010**, 22, (9), 2970-2977.
115. Hunter, R. J., *Zeta Potential in Colloid Science: Principles and Applications*. Academic Press: London, 1981.
116. Greenspan, P.; Fowler, S. D., Spectrofluorometric Studies of the Lipid Probe, Nile Red. *Journal of Lipid Research* **1985**, 26, (7), 781-789.
117. Moussodia, R. O.; Balan, L.; Merlin, C.; Mustin, C.; Schneider, R., Biocompatible and stable ZnO quantum dots generated by functionalization with siloxane-core PAMAM dendrons. *Journal of Materials Chemistry* **2010**, 20, (6), 1147-1155.
118. Nishimi, T.; Miller, C. A., Spontaneous emulsification of oil in aerosol-OT/water/hydrocarbon systems. *Langmuir* **2000**, 16, (24), 9233-9241.
119. Wang, L. J.; Mutch, K. J.; Eastoe, J.; Heenan, R. K.; Dong, J. F., Nanoemulsions prepared by a two-step low-energy process. *Langmuir* **2008**, 24, (12), 6092-6099.
120. Ajie, H.; Alvarez, M. M.; Anz, S. J.; Beck, R. D.; Diederich, F.; Fostiropoulos, K.; Huffman, D. R.; Kratschmer, W.; Rubin, Y.; Schriver, K. E.; Sensharma, D.; Whetten, R. L., Characterization of the Soluble All-Carbon Molecules C₆₀ and C₇₀. *Journal of Physical Chemistry* **1990**, 94, (24), 8630-8633.

121. Brant, J.; Lecoanet, H.; Hotze, M.; Wiesner, M., Comparison of electrokinetic properties of colloidal fullerenes (n-C-60) formed using two procedures. *Environmental Science & Technology* **2005**, 39, (17), 6343-6351.
122. Chen, K. L.; Elimelech, M., Aggregation and deposition kinetics of fullerene (C-60) nanoparticles. *Langmuir* **2006**, 22, (26), 10994-11001.
123. Lyon, D. Y.; Adams, L. K.; Falkner, J. C.; Alvarez, P. J. J., Antibacterial activity of fullerene water suspensions: Effects of preparation method and particle size. *Environmental Science & Technology* **2006**, 40, (14), 4360-4366.

Chapter 3

Spontaneous Emulsification of Hydrocarbon/Aerosol-OT/Brine Systems

3.1 Introduction

In Chapter 2, we described a new development in the method to phase-transfer NPs from oil to water.¹ We showed that the presence of electrolytes improved phase-transfer efficiency of NPs in bilayers of surfactants. Addition of electrolytes transferred NPs as single particles and with higher surfactant coverage on the NP surface over those in no-salt water. The lateral compactness of salty-micelles in the presence of electrolytes was higher than in DI-water micelles - a key factor in conserving optical properties of CdSe QDs.

It is not entirely clear why NPs transfer as aggregated clusters in the absence of salinity and as single particles when transferred with salt. This could be related to observations that oil (hexane)-containing QDs and AOT, when mixed into NaCl-brine, formed nanometer-sized O/W emulsion droplets that were stable to coalescence. On the other hand, unstable micron-sized emulsion droplets formed when the hexane-QD-AOT blend was added to DI water (Fig. 2.14). NaCl thus in addition to salting-out AOT to the QD surface as described in Chapter 2, also serves to emulsify hexane into tiny droplets and stabilize them against coalescence for several hours. A point noteworthy is that emulsification of hexane droplets, both in NaCl-brine and DI water, required minimal external energy or was restricted to gentle mixing. The role of NaCl in emulsifying a hydrocarbon by the mechanism of spontaneous emulsification is the subject of this chapter.

Spontaneous emulsification, i.e., emulsification which occurs without application of external work, is an intriguing phenomenon which has attracted considerable past

attention.²⁻⁶ It is useful in that for suitable conditions, emulsions having small droplets can be formed without application of high shear rates, which may be impractical in some situations or have adverse effects on materials being used.⁷⁻⁹ In recent years, formation and application of nanoemulsions, thermodynamically unstable emulsions having droplet sizes down to 100 nm and even smaller, have been investigated. While nanoemulsions can be prepared at high shear rates using suitable homogenizers,^{8,9} the discussion here is limited to nanoemulsions formed spontaneously for applications such as personal and household care products,^{5, 6, 10, 11} drug delivery,^{5-7, 11-21} particle synthesis,^{1, 5-7, 21-23}, detergency.^{5, 6, 24-26} and nanoparticle phase-transfer.¹ Reviews on nanoemulsions formed by both external mechanical means and spontaneous emulsification may be found elsewhere.^{3, 5, 6, 18, 22}

Although it has been proposed that spontaneous emulsification may be caused by mechanical mechanisms such as interfacial turbulence and interfacial expansion due to negative interfacial tension, the emphasis here is on spontaneous formation of emulsions resulting from local supersaturation.^{2, 3, 5, 6} Supersaturation can be produced by changes in composition^{3, 5-7, 18, 20-22, 26-37}, temperature^{5-7, 18, 36, 38-40} or pressure.¹⁸ Local composition can be varied by mixing and/or diffusion when liquids not in equilibrium are contacted, by chemical reaction, or by some combination of these effects.⁴¹ Understanding emulsification produced by local supersaturation requires, among other things, knowledge of equilibrium phase behavior for the system at conditions of interest.^{2-7, 18, 26-}

44

In this body of work, the primary interest is in processes involving spontaneous emulsification which can convert all of an initial oil-rich phase containing one or more

surfactants and a small amount of water or NaCl-brine to small droplets. Towards the above, external inputs of energy such as high-shear mixing is not required although in a select few cases, gentle mixing is used to hasten homogenization, a process known as self-emulsification. In the emulsification process, the initial composition is an oil-continuous solution or an oil-continuous microemulsion. Previous work had shown that emulsions consisting entirely of small droplets of oil -- in some cases nanoemulsions -- could be generated in many such systems by completely converting the initial phase to a phase that was supersaturated in oil, leading to nucleation of tiny oil droplets.^{3, 5, 6, 26-28, 33} The desired emulsions of micro- or nanodroplets could be obtained if aggregation, coalescence, and growth by Ostwald ripening were minimized.

If the spontaneous curvature of the surfactant films in the initial microemulsion favors water-in-oil (W/O) arrangement, supersaturation in oil can be achieved by a combination of reversing the sign of the spontaneous curvature to favor an-oil-in-water (O/W) arrangement and increasing the water-to-oil ratio in the system (Fig. 3.1). One method of reversing the spontaneous curvature is to change the surfactant composition of the films either by mass transfer of surfactants into or out of the films by diffusion^{3-6, 26-28, 33, 35} (Fig. 3.2) or by chemical reactions.⁴¹ For ionic surfactant systems, changes in ionic strength can cause spontaneous curvature to reverse, causing self-emulsification.²⁸ Another is to change the temperature near the film, which leads to what Shinoda has called Phase Inversion Temperature or PIT emulsification.^{7, 23, 38-40, 45-47} The temperature change must take the system across the PIT, where spontaneous curvature is zero. For ionic surfactant systems, changes in ionic strength can cause spontaneous curvature to reverse, causing self-emulsification.²⁸

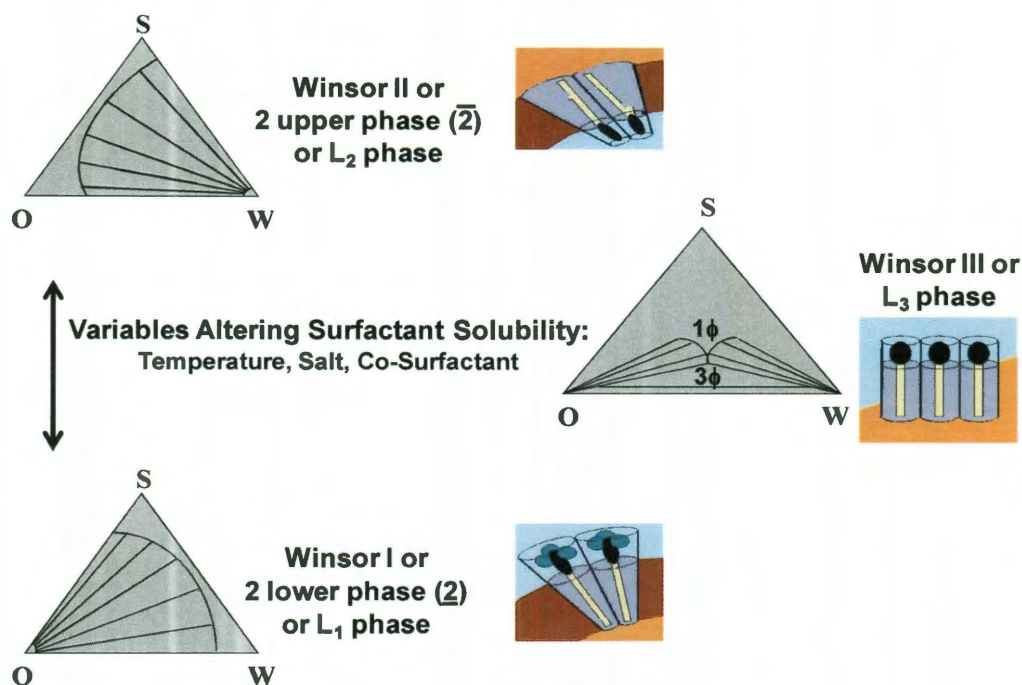


Figure 3.1: Transitions between Winsor I \leftrightarrow Winsor III \leftrightarrow Winsor II domains of ternary Oil/Surfactant/Water systems. Surfactant solubility altering variables such as temperature, salt, and co-surfactants change the spontaneous curvature of the surfactant from what favors an Oil-in-Water configuration (Winsor I) to a Water-in-Oil configuration (Winsor II).

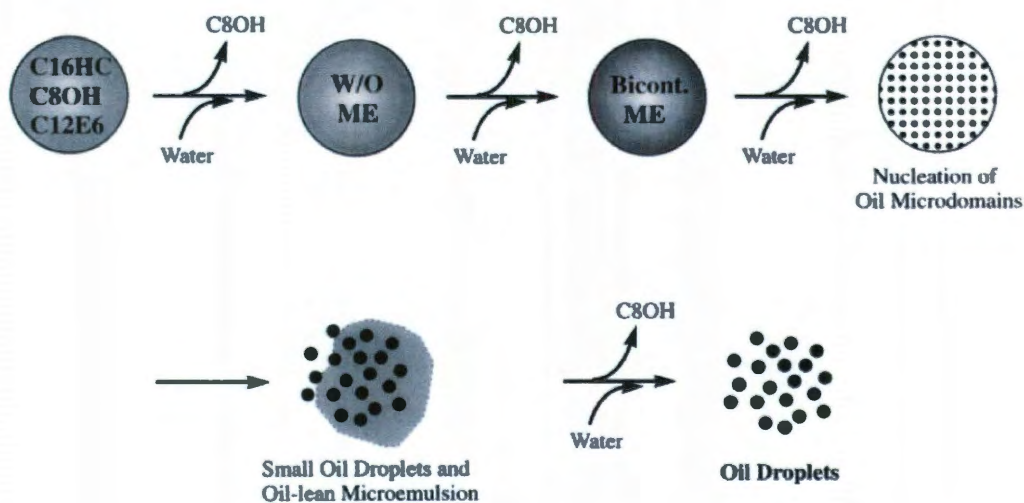


Figure 3.2: Spontaneous emulsification of hexadecane produced by a diffusion-based mechanism from mass transfer of octanol out of and mass transfer of water into an oil droplet comprising of hexadecane/ C_8OH / $C_{12}E_6$ droplet (adapted from Rang and Miller).

For suitable conditions dilution with water or brine yields O/W nanoemulsions whose droplets can remain small for considerable time if, when nucleated, they are coated with a thin layer of the lamellar phase, which hinders flocculation and coalescence and slows Ostwald ripening.^{3-7, 25-44} Most past work on spontaneous emulsification has focused on determining when it will occur in a system or class of systems, what mechanism(s) causes it, and, in some cases, the mean droplet size or size distribution at some chosen “end” of the process.^{3, 5, 6, 25, 33, 35} Less attention has been given to quantifying the initial mean size and size distribution, tracking droplet size changes with time, and elucidating mechanism(s) of droplet growth. This information is often relevant to the effective design of applications that are based on nanoemulsions.

The present work shows and discusses changes over time in mean droplet size for different compositions where spontaneous emulsification occurs upon dilution with water or NaCl brine of an oil-rich n-octane/anionic surfactant/water or NaCl brine mixture. Also discussed are the mechanisms of droplet growth or shrinkage operating in different Winsor regimes. The anionic surfactant used is sodium bis(2-ethylhexyl)sulfosuccinate, commonly known as Aerosol OT or AOT.

For this study, octane was selected as the hydrocarbon over hexane that was used for NP phase-transfer. This was due to the following reasons: (i) Extensive phase diagrams and the cross-over salinity for Octane/AOT/Water/NaCl-Brine system are readily available. (ii) Hexane (being volatile) does not easily allow for long term studies to monitor droplet size evolution, hence a higher molecular weight hydrocarbon in octane (with lower vapor pressure) and that belongs to the same homologous series was used. Further, through the use of available empirical correlations³⁸, the findings of

destabilization mechanisms for octane-based emulsions can be conveniently extrapolated to the Hexane/AOT/Water/NaCl-Brine system.

Kunieda and Shinoda reported that the conditions for obtaining balanced microemulsions solubilizing equal amounts of oil and NaCl brine were nearly the same with AOT for n-octane and i-octane.^{47, 48} At 25°C the required salinity is approximately 0.3% NaCl by weight. Both Kellay *et al* using n-octane and Maugey and Belloq using i-octane found similar values.^{44, 49} However, the former group reported that the phase in equilibrium with excess brine and oil was the lamellar liquid crystalline phase and not a microemulsion. A diagram presented by the latter group shows that the lamellar phase exists very close to the balanced condition at 0.3% NaCl but does not make clear whether a microemulsion is present. Perhaps the situation is similar to that reported by Hackett and Miller for other anionic surfactant systems where both phases can coexist with excess oil and brine for some conditions near the balanced state.⁵⁰

As shown below, the type of emulsion or nanoemulsion formed during self-emulsification in the Octane/AOT/(water or NaCl brine) system and the time-dependent behavior of droplet size depend mainly on the salinity of the brine used to dilute the initial oil-continuous microemulsion. When NaCl concentration is below 0.3 wt%, where spontaneous curvature favors an O/W arrangement (Winsor I region), an O/W nanoemulsion forms with initial droplet sizes of 150-250 nm that increase over time to 500 nm - 1 μm . When NaCl concentration is 0.3 wt% (Winsor III region), a nanoemulsion with drops of order 50-100nm, whose droplets grow little over time, is observed. At higher salinities, where spontaneous curvature favors a W/O arrangement (Winsor II region) but where water-to-oil ratio is high after dilution, W/O/W multiple

emulsions are formed with drop size decreasing with increasing time.⁶ It bears emphasis that in most of our experiments the final mean drop size was below 1 μm , which was achieved without external energy inputs.⁶

Electrophoresis studies showed nanoemulsions to have highly negative zeta potentials (-60 mV to -120 mV). The corresponding high negative charge on the octane droplets helped assure stability to flocculation and coalescence, thereby allowing mass transfer to control growth in the Winsor I and III regions and contributed to the stable nature of the nanoemulsions.

3.2 Materials and Methods

3.2.1 Preparation of Microemulsions

For microemulsions prepared with water, the compositions of investigated systems were (in weight ratios of Octane/AOT/Water), 60/30/10, 70/20/10, and 80/10/10. Reagent grade (99.9% pure) *n*-octane (or simply octane) was procured from Sigma Aldrich, USA. Aerosol-OT [AOT: sodium bis(2-ethylhexyl) sulfosuccinate] was obtained from TCI America. Sodium chloride (reagent grade) was obtained from Merck, USA. Ultra pure water with 18.2 M Ω -cm resistivity (Barnstead Nanopure Diamond System) was used in the preparation of all solutions and microemulsions. All chemicals were used as obtained and without any further purification. For microemulsions prepared with brine, the base composition of the system was 70/20/10 (in weight ratios of Octane/AOT/NaCl-Brine). The brine concentrations (expressed as % ϵ , where $\epsilon = \left(\frac{\text{salt}}{\text{salt} + \text{water}} \right)$) were 0.2, 0.3, and 0.4, all by weight. All microemulsions prepared were stored in stoppered containers to prevent changes in composition from evaporation.

3.2.2 Preparation of Nanoemulsions

For droplet growth and size studies, nanoemulsions were prepared by diluting microemulsions in excess brine at 25°C such that final AOT concentration was at 1.5 g/L (0.15 wt %). The typical batch size of nanoemulsions prepared was 30 mL. Emulsions mostly formed spontaneously; although, in a few situations, minimal agitation (restricted to gentle hand shaking or self-emulsification) was required. Brine concentrations were chosen such that nanoemulsions formed in various Winsor (I, III, and II) regions.⁴⁴ For phase-behavior studies, nanoemulsions were prepared at AOT concentrations of 1.5 and 15 g/L, stored in 30 mL stoppered vials, and visually inspected under plain and polarized light to determine phase domains and detect the possible presence of liquid crystalline phases of AOT.

3.2.3 Characterization of Emulsions

3.2.3.1 Phase Behavior Studies

For phase-behavior studies, nanoemulsions were prepared as per the method described above. Nanoemulsions at the higher AOT concentration were especially prepared to clearly delineate octane domains from brine by a higher octane volume fraction. Photographs were taken periodically under controlled illumination over a time duration spanning 4 weeks.

3.2.3.2 Polarized Light Screening System

Polarized light screening technique was used to capture macroscopic liquid crystalline domains of AOT in nanoemulsions prepared at different salinity levels.⁵¹ In this set up,

diffused light was transmitted through a polarizer set at 0°, with an analyzer set orthogonal to it. Nanoemulsion vials were placed in between the polarizer and analyzer and liquid crystalline phases were identified by bright birefringence patterns displayed with polarized light.

3.2.3.3 Interfacial-Tension Measurements

Interfacial tension (IFT) between octane and nanoemulsions prepared at various brine salinities were measured using a spinning-drop tensiometer (University of Texas Model 300). A drop of octane was injected into the capillary tube containing the emulsion. For gravitational effects to be negligible and certain approximations to be valid, the capillary was rotated at high angular velocities (ω) so that the ratio of the length of the cylindrical oil drop (L) to its diameter (d) exceeded four.⁵²

Octane-nanoemulsion IFT (γ) was calculated using the relation:

$$\gamma = \frac{\pi}{8} \left(\frac{d}{\eta} \right)^3 \frac{\Delta\rho}{\omega^2} \quad (3.1)$$

Where: d = diameter of the cylinder, η = refractive index of the continuous phase (measured using a Milton Roy Refractometer), $\Delta\rho$ is the density difference between the continuous and dispersed phases, and (ω) is the angular velocity. For a specific capillary rotation, droplet shape remained constant over several minutes, indicating negligible effects of dynamic tensions.

3.2.3.4 Dynamic Light Scattering

Droplet size of nanoemulsions was determined using ZetaPALS (Brookhaven Instruments Corporation) DLS instrument at 25 °C with a He-Ne laser ($\lambda = 656 \text{ nm}$), a detector set at 90°, and a BI-9000AT digital autocorrelater that records scattered light. The laser was stabilized for a recommended time of 15 minutes prior to making measurements and periodically tested against a company-supplied polystyrene standard (diameter: $92 \pm 3 \text{ nm}$) to ensure reliable functioning of the instrument. Nanoemulsions prepared were transferred to 4 mL stoppered-polystyrene cuvettes and analyzed in triplicates over intervals of 3 minutes to ensure reproducibility. Droplet diameter measurements were carried out as a function of time. Prior to each measurement, the sealed cuvettes were gently hand shaken to ensure homogenization. The diffusion coefficient of the dispersed phase (octane) was estimated using a built-in routine and the droplet diameter was calculated using the Stokes-Einstein relationship (Eq. 2.7). Volume and intensity-based nonlinear constrained least square (NNLS) and CONTIN fitting routines were used to size droplet diameters by the instrument software 9KDLSW.

3.2.3.5 Zeta Potential Measurements

Zeta potential of the nanoemulsions was estimated from electrophoretic mobility measurements using phase analysis light scattering (PALS) in the Brookhaven ZetaPALS setup. A dip-in (Uzgiris type) electrode with 4 mL polystyrene cuvettes was used and measurements were carried out at 25 °C. Henry's equation (Eq. 2.8), valid for the condition $0.01 \leq \kappa a \leq 100$, was used to calculate zeta potential (ζ), using either Smoluchowski's or Hückel's approximation.^{53, 54}

3.2.3.6 Optical Microscopy

Optical and fluorescence microscopy studies of nanoemulsions were carried out with an optical microscope (Olympus IX71), under an oil-immersion 100X objective lens (Numerical Aperture (NA) = 1.4). For microscopy studies, a 70/20/10 Octane/AOT/Water microemulsion was prepared where octane was doped with a hydrophobic, octane-soluble dye (Nile Red, Sigma Aldrich, $\lambda_{\text{Excitation}} = 450\text{-}500\text{ nm}$, $\lambda_{\text{Emission}} = 528\text{-}605\text{ nm}$).

Nanoemulsions were prepared at 1.5 g/L AOT and in different Winsor salinities. Small volumes (15 μL) of these nanoemulsions were transferred onto a microscope slide and sealed under a cover slip. These nanoemulsions were observed in bright field and fluorescence modes (Texas Red Filter) over several time durations across 24 hours. In addition, polarized light microscopy studies were performed with a Zeiss Axioplan 2 polarized light microscope using a 10X lens and a 63X oil-immersion lens with 1.4 NA. Images were taken under bright field and cross-polarizer modes. For the latter, the polarizer was set at 0° and -45° and the analyzer set orthogonal at 90° and $+45^\circ$ respectively. Studies were carried out over 4 weeks, with fresh microscope slides prepared from the same stock of nanoemulsions, till the lamellar coating of AOT at the octane/water grew thick enough to show birefringence.

3.3 Results and Discussions

3.3.1 Phase Behavior and Interfacial Tensions of Octane-AOT-Brine Systems

In the present study, spontaneous emulsification was generated by dilution with water or NaCl-brine of oil-continuous microemulsions having Octane/AOT/Water compositions

with ratios of 60/30/10, 70/20/10, and 80/10/10 by weight (Fig. 3.3). These ratios were chosen because they were used previously in video microscopy experiments for the same system.²⁸ AOT concentration after dilution was set at 1.5 g/L, where all of the oil was emulsified. However, identification of phases present was facilitated by using higher oil and surfactant concentrations.

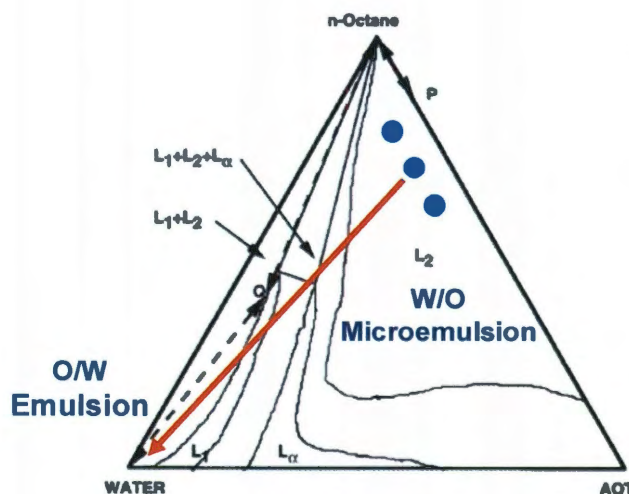


Figure 3.3: Phase diagram of n-Octane/AOT/Water ternary system. The three blue dots represent (from bottom to top) 60/30/10, 70/20/10, and 80/10/10 weight ratios of Octane/AOT/Water corresponding to an L_2 phase or W/O microemulsion phase. The red arrow corresponds to the dilution levels (but not dilution path) from the L_2 domains to O/W emulsion domains where AOT concentration levels are 1.5 g/L (adapted from Nishimi and Miller).

Figs. 3.4 and 3.5 shows phase behavior for dilution at four salinities of 70/20/10 salt-free microemulsions to final AOT concentrations of 1.5 g/L and 15 g/L, respectively, resulting in water-continuous nanoemulsions. Images taken across several time points showed creaming/separation of an oil-rich phase when dilutions were made with NaCl solutions having $\% \epsilon = 0, 0.2, \text{ and } 0.4$. Based on information from the literature of this system, (phase behavior studies by Maugey and Bellocq - (Fig. 3.6)⁴⁴, Kunieda and

Shinoda^{47, 48}, Kellay *et al* ⁴⁹) and on the sharp minimum in IFT at $\% \epsilon = 0.3$ (to be discussed in Fig. 3.8), it is concluded that phase behavior is in the Winsor I region for $\% \epsilon = 0$ and 0.2 and in the Winsor II region for $\% \epsilon = 0.4$. Indeed for $\% \epsilon = 0.4$ separation of an oil-continuous microemulsion can be seen after 28 days in Fig. 3.4 and after 4, 14, and 28 days in Fig. 3.5.

For dilution with $\% \epsilon = 0.3$, bulk phase separation did not occur even after 4 weeks and a uniform blue nanoemulsion was seen for AOT at 1.5 g/L. It is not considered to be an equilibrium single-phase microemulsion because oil and brine solubilization would be nearly equal at this salinity, in contrast to the actual composition where there is far more brine than oil. For AOT at 15 g/L the cloudiness for $\% \epsilon = 0.3$ indicates the presence of an emulsion or dispersion but with drops or particles small enough that no substantial creaming occurs. In addition Fig. 3.7 shows some static birefringence. Probably both oil drops and the lamellar liquid crystalline phase are dispersed in the aqueous phase although whether present as separate entities or as small oil drops coated by the lamellar phase is not clear. In the latter case the lower density of octane and the higher density of AOT compared to water could result in an overall drop density near that of the continuous phase and little creaming as observed. When phase behavior studies were carried out with 70/20/10 Octane/AOT/Brine microemulsions made with internal brine salinities at $\% \epsilon = 0.2, 0.3, \text{ or } 0.4$, behavior similar to that of Figs. 3.4, 3.5 and 3.7 was seen.

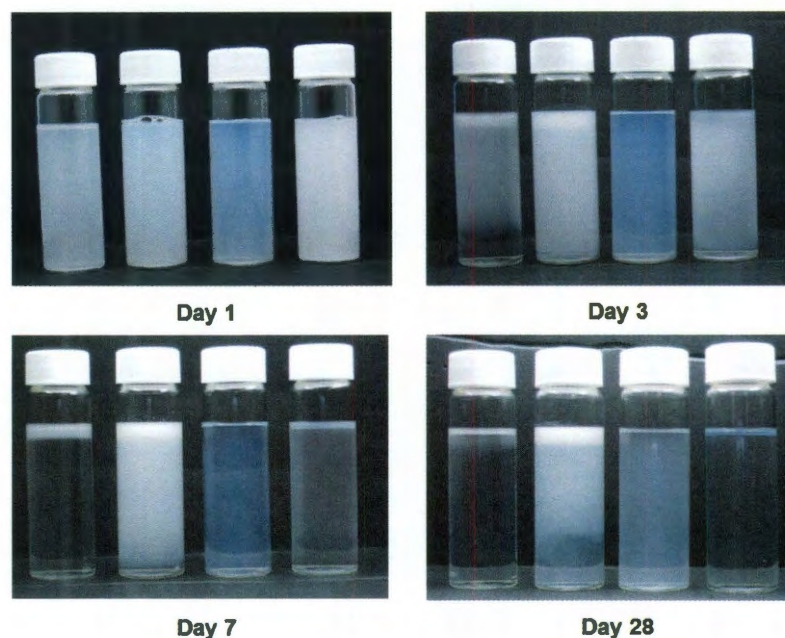


Figure 3.4: Time-based phase-behavior of nanoemulsions prepared by diluting W/O microemulsions of Octane/AOT/Water (70/20/10) in different levels of excess brine. In each panel, bulk NaCl-brine salinities correspond to $\% \epsilon = 0, 0.2, 0.3,$ and 0.4 . Final AOT concentration in all solutions was 1.5 g/L .

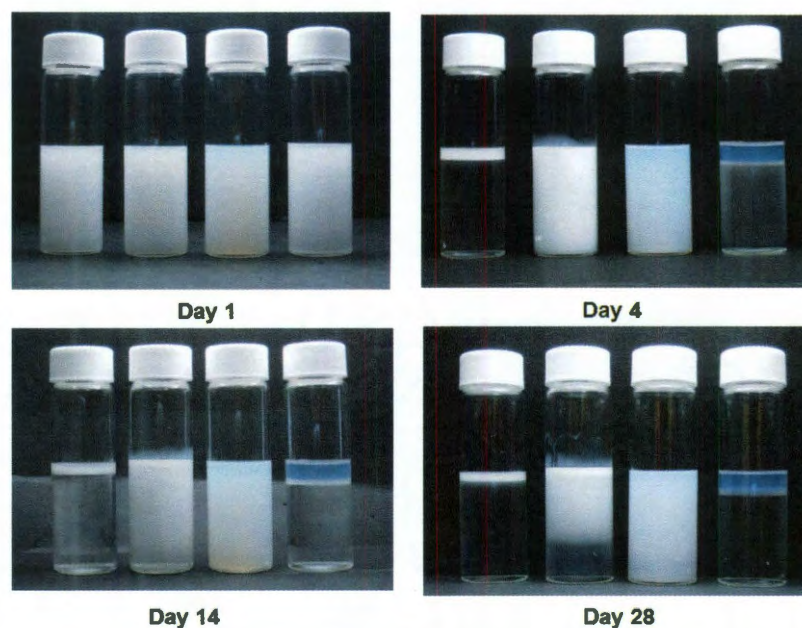


Figure 3.5: Time-based phase-behavior of nanoemulsions prepared by diluting W/O microemulsions of Octane/AOT/Water (70/20/10) in different levels of excess brine. In each panel, bulk NaCl-brine salinities correspond to $\% \epsilon = 0, 0.2, 0.3,$ and 0.4 . Final AOT concentration in all solutions was 15 g/L .

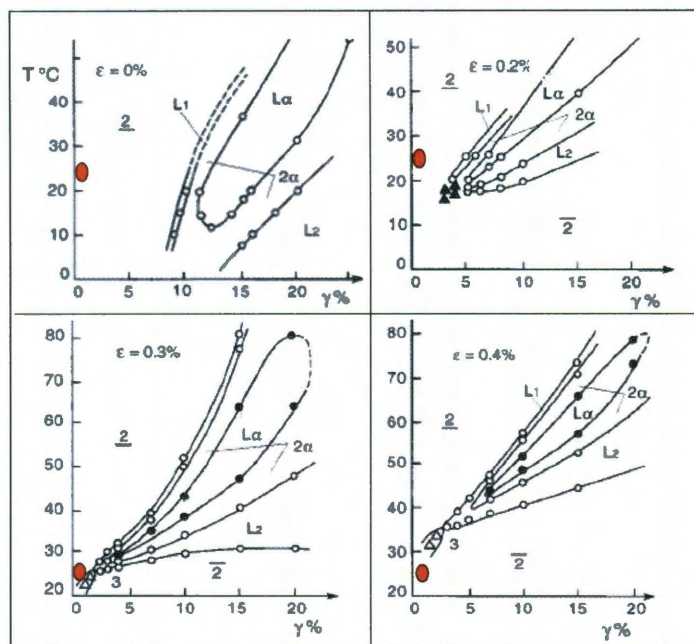


Figure 3.6: Temperature vs. surfactant concentration ($\gamma\%$) phase behavior plots for different NaCl concentrations ($\epsilon\%$) of iso-Octane/AOT/Brine systems. The red dots correspond to room temperature ($25\text{ }^{\circ}\text{C}$) and AOT concentration of 1.5 g/L at which Octane/Brine emulsions for this study were formulated. Cross over salinity is seen to be at $\epsilon = 0.3$ (adapted from Maugé and Bellocq).

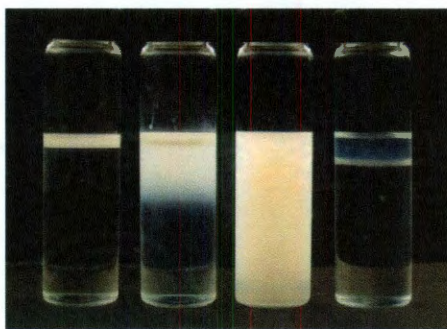


Figure 3.7: Nanoemulsions formed by W/O microemulsions of Octane/AOT/Water (70/20/10) in different levels of excess brine, as seen through cross-polarizers on day 4 with a polarized light screening system. In the image, bulk NaCl-brine salinities correspond to $\epsilon = 0, 0.2, 0.3,$ and 0.4 . Final AOT concentration in all solutions was at 15 g/L . Birefringence is observed in nanoemulsion formed at $\epsilon = 0.3$, indicating the lamellar liquid crystalline phase of AOT.

Interfacial tensions (IFTs) were measured between drops of n-octane and nanoemulsions made by diluting microemulsions having all three initial Octane/AOT/Water ratios indicated above with water and NaCl brine. From Fig. 3.8, it can be seen that IFT was lowest (0.07 mN m^{-1}) by 1-2 orders of magnitude when the brine concentration ($\% \epsilon$) was 0.3 and instead of 0, 0.2, and 0.4.

This result further confirmed that cross-over salinity for the system, where spontaneous curvature is near zero, occurs near $\% \epsilon = 0.3$, a result consistent with our phase behavior results and previously reported studies.^{44, 47, 49, 55} IFT measurements were made within 1 hour after forming the nanoemulsions. Typically several measurements at different speeds of rotation were made within a 2-hour period. During this time, variation of steady state IFT was found to be negligible.

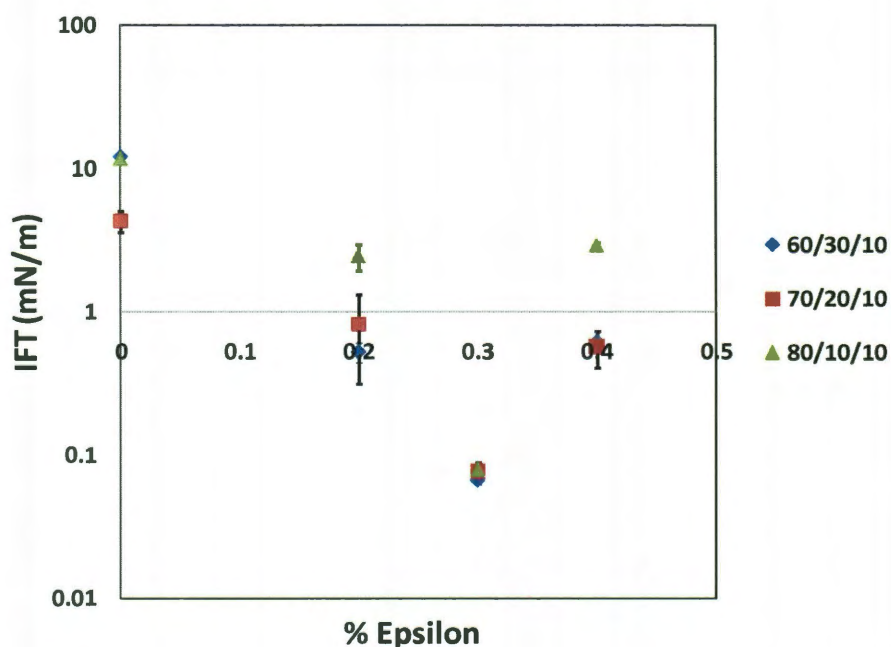


Figure 3.8: Interfacial tensions of octane with nanoemulsions prepared by diluting various W/O microemulsions of Octane: AOT: Water (60/30/10, 70/20/10, and 80/10/10) in different levels of excess brine (AOT = 1.5 g/L).

It is noteworthy that the absolute value of the lowest IFT measured was 1-2 orders higher in magnitude than previous measurements reported by Aveyard *et al* for the same surfactant with n-heptane at low surfactant concentrations.⁵⁵ However, the salinity range of the lowest tensions is very narrow⁵⁷, so that IFT in our system could well have been lower by an order of magnitude for $\% \epsilon$ only slightly different from 0.3.

3.3.2 Droplet Size Evolution Upon Diluting W/O Microemulsions and B/O Microemulsions in Different Winsor Salinities

When W/O microemulsions of Octane/AOT/Water were diluted in excess water or brine, O/W nanoemulsions formed. As indicated previously, the final surfactant concentration was fixed at 1.5 g-AOT/L. Three regimes of time-variant octane droplet size and growth rates were found that corresponded to the three Winsor domains of phase behavior discussed above. In this section, these trends are discussed for nanoemulsions formed from initial microemulsions having a 70/20/10 ratio of Octane/AOT/Water (Fig. 3.9). Similar trends in droplet size were observed for nanoemulsions derived from 60/30/10 and 80/10/10 ratios (see Appendix B: Fig. B1). Section 3.4 gives further information on drop size distribution for the nanoemulsions and discussion of growth mechanisms responsible for the different variations of drop size with time across different Winsor regions.

Fig. 3.9 shows plots of mean drop size as a function of time when the initial 70/20/10 microemulsions contained no salt. When dilution was with water, mean drop diameter was about 200 nm when the first measurement was made some two minutes after initial contact. Diameter increased with time, reaching about 1.2 μm after 24 hours.

Initial drop size was about the same, but small decreases in growth rate and drop diameter after 24 hours were seen at very low salinity ($\% \epsilon = 0.02$). When salinity was raised to $\% \epsilon = 0.2$, initial drop size was again about the same but growth rates and drop size after 24 hours were significantly smaller, the latter being approximately 500-600 nm. Thus, qualitative behavior was similar for all three experiments where final phase behavior was of the Winsor I type. At the cross-over salinity ($\% \epsilon = 0.3$, Winsor III region), a bluish nanoemulsion formed with an initial droplet mean diameter of 50-60 nm. Growth rate was low, with the mean diameter remaining under 150 nm after 24 hours. When the microemulsion was diluted into the Winsor II regime with brine having $\% \epsilon = 0.4$ and 1.0, droplet diameters measured 1-3 μm for the first three hours. Subsequently diameters decreased to between 500-700 nm after 24 hours.

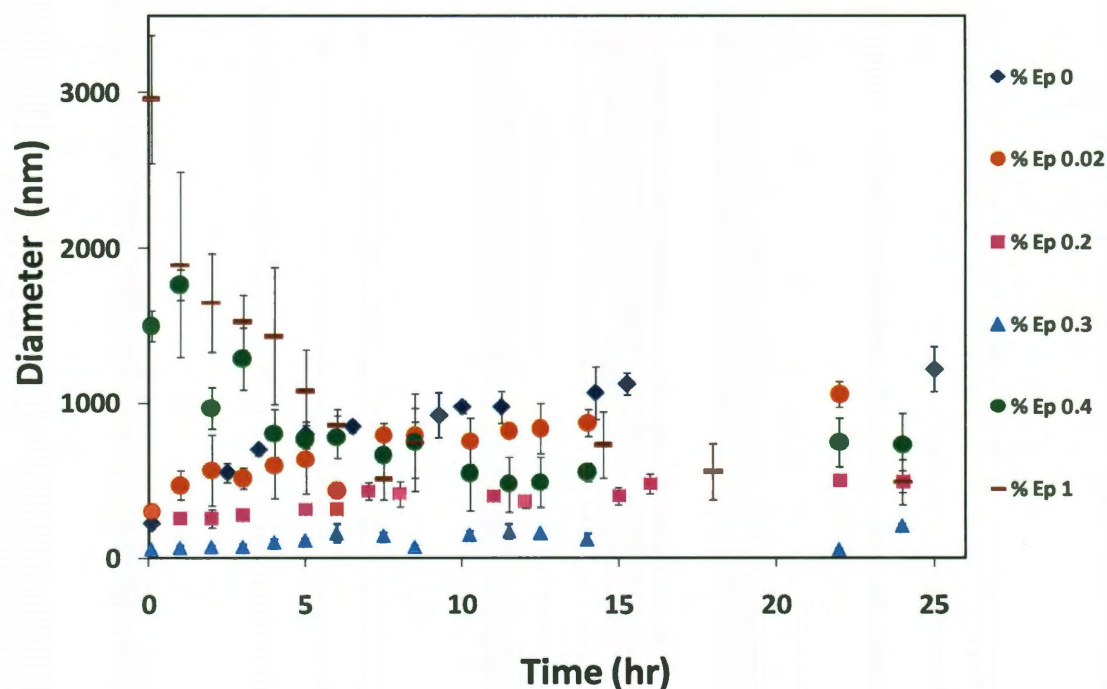


Figure 3.9: Octane drop size study with respect to time in Octane/Brine nanoemulsions obtained by diluting 70/20/10 Octane/AOT/Water microemulsions in different levels of excess brine (AOT = 1.5 g/L).

Similar trends in the three Winsor regions were observed for nanoemulsions derived from Octane/AOT/Brine microemulsions (B/O microemulsions). Behavior is shown in Fig. 3.10 for nanoemulsions derived from B/O microemulsions with a 70/20/10 composition ratio and a salinity of the brine phase ($\% \epsilon$) of 0.3 (Also see Appendix B, Fig. B2). A noteworthy difference was that nanoemulsions prepared at specific brine salinity by diluting B/O microemulsions had droplet sizes lower than corresponding nanoemulsions prepared by diluting W/O microemulsions.⁵⁶ The most apparent difference for instance were emulsions prepared by inverting the 70/20/10 W/O microemulsion in excess brine ($\% \epsilon = 0.2$), that yielded octane drops that increased in diameter from 200 nm to 850 nm over 24 hours (Fig. 3.9). In comparison, a 70/20/10 B/O microemulsion with internal salinity at $\% \epsilon = 0.3$ gave octane drops that marginally increased from 200 nm to ~ 250 nm (Fig. 3.10).

It is noteworthy that the selected AOT concentration of 1.5 g/L at which nanoemulsions were prepared and studied was sufficient to ensure that the entire oil-water interface was stabilized by AOT. From droplet size diameters measured by DLS, the interfacial areas of octane at specific time points were estimated. Thus, using an AOT head group area of 0.69 nm^2 , the required number of AOT monomers to stabilize the octane/water interface was estimated.⁵⁷⁻⁵⁹ It was found that the available AOT monomers were at least twice (except when initial droplet diameter was 40 nm) the number that would theoretically be required to stabilize octane droplets. Furthermore, the number of AOT molecules that were not engaged at the octane/water or octane/brine interface was in sufficient excess so as to stack up as lamellar liquid crystals.

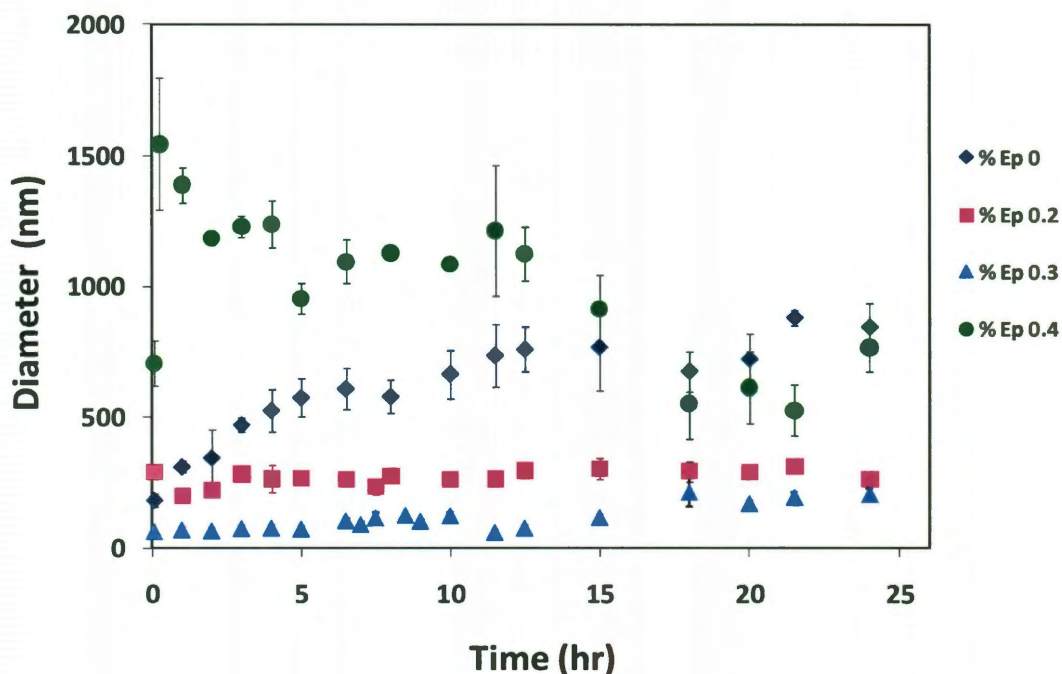


Figure 3.10: Octane drop size study with respect to time in octane/brine nanoemulsions obtained by diluting 70/20/10 Octane/AOT/Brine ($\% \varepsilon = 0.3$) microemulsions in different levels of excess brine (AOT = 1.5 g/L).

3.3.3 Zeta Potential of Octane Droplets in Different Winsor Regimes

To obtain insights into changes in octane droplet growth and size, zeta potential measurements were made. As depicted in Fig. 3.11, zeta potential of the octane droplets was greater (more negative) than -60 mV and independent of time over 24 hours for nanoemulsions derived from 70/20/10 Octane/AOT/Water microemulsions. The high negative values suggest strong electrostatic repulsion acting to stabilize the nanoemulsions. The magnitude of zeta potential decreased significantly with increase in salinity levels, which could be attributed to electrostatic charge screening of sulfonate groups on AOT by Na^+ counter-ions. Similar trends in zeta potentials were observed for nanoemulsions prepared from 60/30/10 and 80/10/10 W/O microemulsions (See

Appendix B, Fig. B3).⁵⁶ Zeta potentials measurements were used to estimate the area/molecule of AOT at the Octane-Water (or Brine) interface.

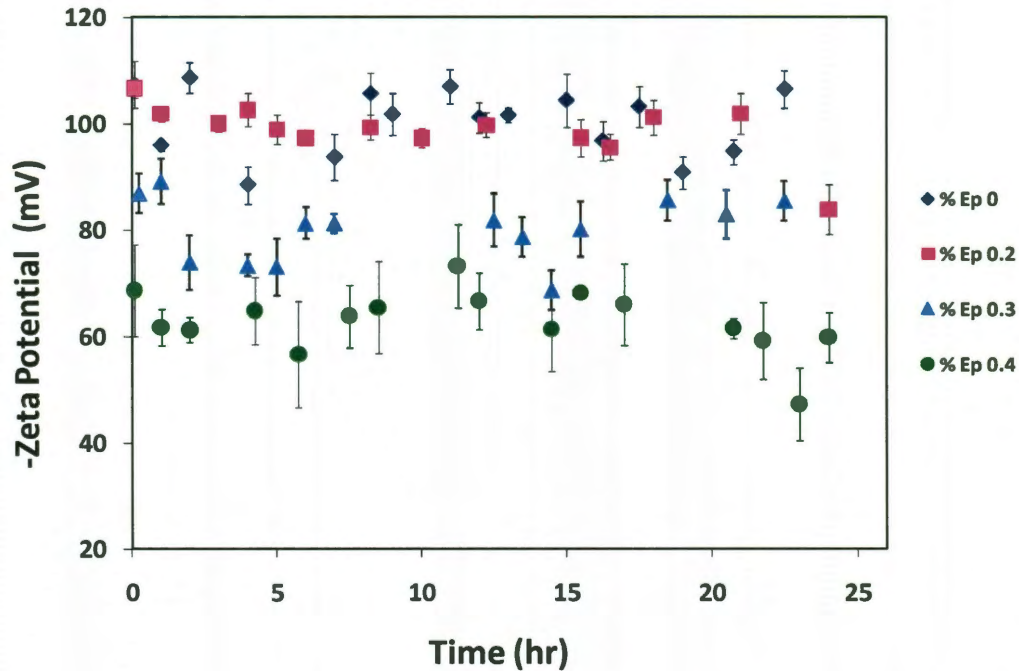


Figure 3.11: Zeta potential of Octane/Brine nanoemulsions obtained by diluting 70/20/10 Octane/AOT/Water microemulsions in different concentrations of excess brine (AOT = 1.5 g/L).

Loeb *et al* derived the following equation for the relationship between surface charge and surface potential in a diffuse electrical double layer for a slightly curved spherical surface

($\kappa R \gg 1$).^{53, 54}

$$\sigma = \frac{2\epsilon\kappa T}{ve_0} \left[\sinh\left(\frac{ve_0\Psi_0}{2k_B T}\right) + \frac{2\eta}{\kappa R} \right] \quad (3.2)$$

Where: σ = surface charge density in Cm^{-2} , ϵ = total permittivity, where $\epsilon = \epsilon_0\epsilon_r$, ϵ_0 = permittivity of free space ($8.854 \times 10^{-12} \text{ C}^2\text{J}^{-1}\text{m}^{-1}$) and ϵ_r = relative permittivity of

water (80.1), κ = Debye parameter (inverse of the Debye screening length κ^{-1} , calculated for a 1:1 electrolyte in nm as $\kappa^{-1} = \frac{0.304}{\sqrt{[C]}}$, where C = concentration of electrolyte in molar units⁶⁰), k_B = Boltzmann's constant (1.381×10^{-23} JK⁻¹), T = temperature (298 K), ν = valency of counter-ion ($\text{Na}^+ = +1$), e_0 = charge on electron (-1.6×10^{-19} C), ψ_0 = surface potential (JC⁻¹, surface potential is approximately equal to be the zeta potential for indifferent ions^{54, 60}), $\eta = \tanh\left(\frac{\nu e_0 \psi_0}{4k_B T}\right)$, and R = radius of droplet. From the surface charge density calculated for several corresponding experimental points in Figs. 3.9 and 3.11, the area per molecule of AOT at the Octane-Water (Brine) interface was estimated to range between (0.45 - 4) nm²/molecule.

This range agrees in order of magnitude with AOT head-group areas reported in literature (0.58-0.70) nm²/molecule.^{57-59, 61} There are likely cases where head-group areas were over-estimated by this procedure. For one, counter-ion binding was neglected with the result that the number of AOT molecules at the interface may be greater than that corresponding to the surface charge. This is on account of the approximation we made of using zeta potential to be equivalent to surface potential in Eq. 3-2. While the approximation holds good for higher ionic strengths ($\% \epsilon = 0.2-0.4$) where electrical double layers are compressed from the counter-ions of salt and the potential drop between the surface and diffuse plane is not significantly large, the approximation begins to break down at $\% \epsilon = 0$, where the source of ionic strength is solely from free AOT molecules. Another factor that possibly causes overestimation of head group area is that if AOT is present in the liquid crystal phase, the assumption of the monolayer is no

longer valid since all AOT molecules will not be present at the interface of octane droplets.

3.4 Mechanism of Octane Droplet Growth in Nanoemulsions

Three distinct trends of nanoemulsion droplet growth were seen corresponding to the Winsor regimes into which W/O microemulsions were diluted. In the sections below, we discuss the trends observed and rationalize possible mechanisms that govern droplet growth.

3.4.1 Nanoemulsion Droplet Growth in Water ($\% \epsilon = 0$)

Fig. 3.12 shows the growth trends of octane droplets when nanoemulsions were prepared in water. Starting from an initial droplet diameter of 200-300 nm, octane droplets grew to around 1 micron in 24 hours. No significant differences in droplet size were found in the first 6-7 hours for the three initial compositions shown. Qualitatively however, the 60/30/10 derived nanoemulsion showed the fastest growth rate of the three nanoemulsions beyond 7 hours, and its droplet diameters became statistically greater than those of the 80/10/10 derived nanoemulsion during this time period.

Nishimi and Miller had previously found that microemulsion compositions with at least 25 wt% of AOT and 10 wt% of water underwent vigorous emulsification upon contact with excess water.²⁸ At lower AOT concentrations, convection driven by Marangoni flow set in near the injected droplets and was accompanied by little emulsification. Their observations were made from experiments performed in a small rectangular capillary cell and over relatively short time scales (typically between 30

seconds to 3 minutes). In the present study emulsification studies were carried out over longer time durations, extending to several tens of hours. Vigorous emulsification of octane was observed in all cases, albeit sometimes only after several minutes. For instance while an AOT-rich 60/30/10 microemulsion underwent instantaneous and rapid emulsification, formulations such as the 80/10/10 compositions with lower AOT and higher octane content showed considerable delays in emulsification.

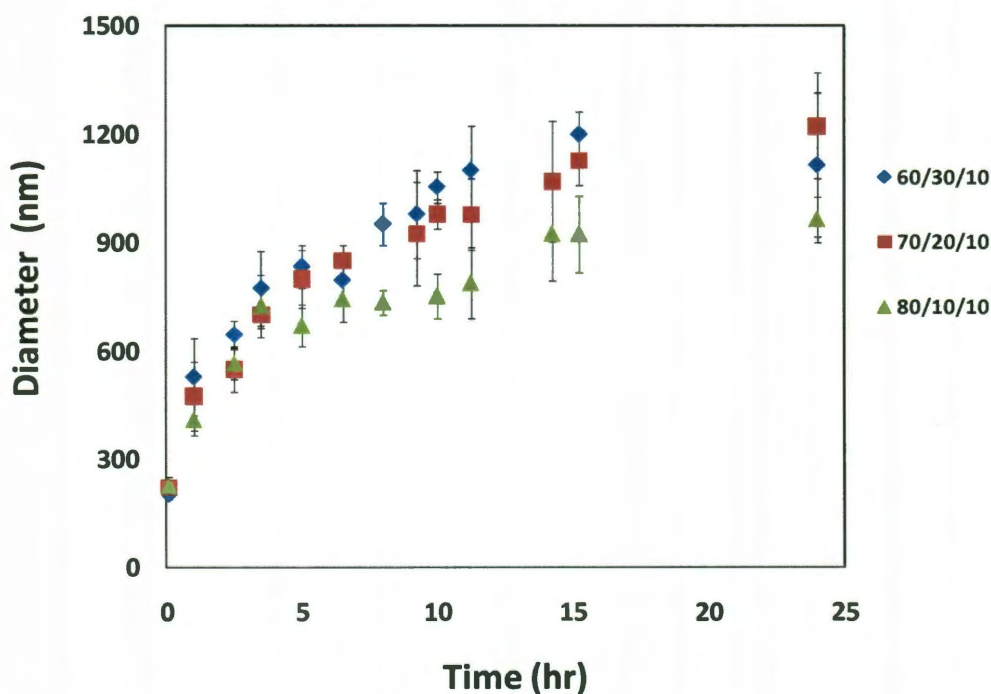


Figure 3.12: Octane droplet size evolution of nanoemulsions formed by diluting W/O microemulsion compositions (Octane-AOT-Water: 60/30/10, 70/20/10, 80/10/10) in excess water (Winsor I) (AOT = 1.5 g/L).

Destabilization of oil/water emulsions can be attributed to flocculation, coalescence, or Ostwald ripening. The first two mechanisms seem unlikely in view of the high zeta potentials shown in Fig. 3.11, which indicate substantial electrostatic repulsion among drops. Additional arguments against these mechanisms are given in Section 3.4.2 below.

The size distribution of the drops formed when dilution was with salt-free water ($\% \varepsilon = 0$) was unimodal, particularly for time periods of 1-15 hours (Table 3.1).

Table 3.1: Population distribution of octane nanoemulsions at select time points showing unimodal distribution when 70/20/10 Octane/AOT/Water microemulsions were diluted in excess water ($\% \varepsilon = 0$, AOT = 1.5 g/L)

Time (hr)	Droplet Population			Droplet Size	
	Diameter (d) (nm)	G(d)*	C(d)**	Mean Diameter ¹ (nm)	% Deviation ¹
1	193	20	27	234	18.1
	231	100	88		
	278	20	100		
5	727	26	21	803	7.68
	800	100	85		
	850	50	100		
10	815	25	6	946	9.67
	844	95	29		
	900	100	53		
	950	95	75		
	1010	100	97		
	1047	80	100		

* G(d) = Weighting function generated by autocorrelator

** C(d) = Cumulative distribution function generated by autocorrelator

¹For a droplet population, the autocorrelator determines the mean diameter using the formulae listed below.

$$\text{Mean diameter} = \left(\frac{\sum_i d_i^3 G(d_i)}{\sum_i G(d_i)} \right)^{\frac{1}{3}}, \quad \% \text{ Deviation} = \frac{\text{Standard Deviation}}{\text{Mean Diameter}} \times 100$$

This behavior is characteristic of the asymptotic stage of Ostwald ripening where larger droplets grow at the expense of smaller droplets. The driving force is increased solubility

of dispersed octane droplets in the continuous phase as droplet curvature increases. Consequently, there is a higher concentration of solubilized dispersed phase molecules around smaller droplets than larger droplets that gives rise to a concentration gradient and results in transport of molecules from smaller to larger droplets.⁶²⁻⁶⁶

The asymptotic growth of oil droplets by Ostwald ripening can be described by the Lifshitz-Slyozov-Wagner (LSW)^{67, 68} theory, which predicts a variation of mean droplet radius (r_N^3) with elapsed time (t) when droplets grow through molecular diffusion. The growth/ripening rate (ω_3) is given by Eq. 3.3:

$$\omega_3 = \frac{dr_N^3}{dt} = \frac{8}{9} \left[\frac{DC_\infty \gamma V_m^2}{RT} \right] \quad (3.3)$$

Where: ω_3 = growth/ripening rate with a subscript of 3 indicating a cubic variation of droplet radius (r_N) with time, C_∞ = equilibrium solubility of octane in water ($6.83 \times 10^{-3} \text{ mol m}^{-3}$)⁶⁹, γ = interfacial tension between octane and nanoemulsion (measured between 0.4-1.2 mN m⁻¹, (Fig. 3.8), V_m = molar volume of octane ($0.000164 \text{ m}^3 \text{ mol}^{-1}$)⁶⁹, R = gas constant ($8.314 \text{ J mol}^{-1} \text{ K}^{-1}$), and T = temperature (298 K). D = molecular diffusivity of octane ($\text{m}^2 \text{ s}^{-1}$, estimated to be $\sim 7.56 \times 10^{-6} \text{ cm}^2 \text{ s}^{-1}$ at 298K and consistent with the literature⁷⁰ as calculated from the Wilke-Chang equation⁷¹,

$$D = 7.4 \times 10^{-8} \frac{\sqrt{\psi_B M_B T}}{\mu V_A^{0.6}} \quad \text{where, } \psi_B = \text{association parameter (2.6 for water), } M_B =$$

molecular weight of octane (114 gmol^{-1}), T = temperature (298 K), μ = viscosity of octane (~ 0.514 centipoise at 298 K), and V_A = molar volume of water ($18 \text{ cm}^3/\text{mol}$)).

Using the above parameters, the theoretically estimated growth rate ($\omega_{3,theo}$) was found to range between $(2.18 - 6.07) \times 10^{-25} \text{ m}^3 \text{ s}^{-1}$ (Table 3.2), which is consistent with calculated growth rates reported in the literature for comparable hydrocarbons (octane-decane).^{64, 66, 72-75} We found that, based on the data of Fig. 3.12, the cube of the mean radius showed a reasonably linear dependence on time, as shown in Fig. 3.13, but that the slope ($\omega_{3,expt}$) was greater than the predicted ($\omega_{3,theo}$) by a factor of 3-14. In the literature, experimentally determined growth rates of hydrocarbon/water emulsions have been reported to exceed calculated growth rates by a factor of 1-3 orders of magnitude.^{64, 66, 70, 73-76} Thus, growth by diffusion-controlled Ostwald ripening seems a reasonable explanation for our results in salt-free systems.

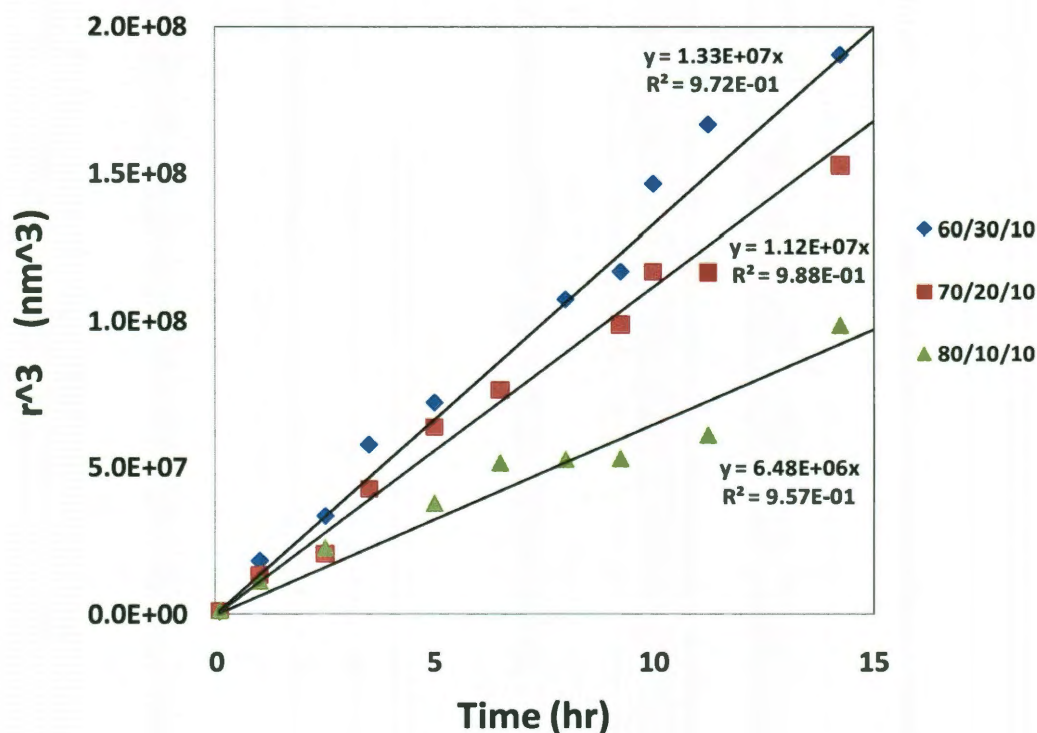


Figure 3.13: Plot of R^3 vs. t for nanoemulsions prepared by diluting 60/30/10, 70/20/10, and 80/10/10 Octane/AOT/Water microemulsions in excess water (Winsor I domain, AOT = 1.5 g/L).

Linear time variation of R^3 was also observed when nanoemulsions were formed by diluting 70/20/10 (Octane/AOT/Brine) B/O microemulsions in excess water, i.e., initial microemulsions with water replaced by NaCl solutions having $\% \epsilon$ of 0.2, 0.3 and 0.4. As in the salt-free case, droplet size distributions were found to be unimodal.⁵⁶ Furthermore, experimentally determined ripening rates ω_3 were slightly lower for nanoemulsions derived from initial B/O microemulsions than from initial microemulsions containing water (See Appendix B4 Fig. B4) but still greater by factors of between 3-5, than the theoretical values of ω_3 shown in Table 3.2. Because mixing during nanoemulsion formation is incomplete, salinity may be nonzero near the growing drops, which would reduce both IFT and octane solubility and hence growth rate, according to Eq. 3.3.

Table 3.2: Comparison of experimentally measured and theoretically calculated Ostwald Ripening Rates of octane/water nanoemulsions when excess brine is zero ($\% \epsilon = 0$, AOT = 1.5 g/L).

Starting microemulsion to prepare nanoemulsion	$\omega_{3,\text{expt}}$ (experimentally measured) ($\text{m}^3 \text{s}^{-1}$)	γ (octane-nanoemulsion IFT) (mN m^{-1})	$\omega_{3,\text{theo}}$ (theoretically estimated) ($\text{m}^3 \text{s}^{-1}$)	Factor ($\omega_{3,\text{expt}}/\omega_{3,\text{theo}}$)
60/30/10	3.69×10^{-24}	12.03	6.07×10^{-25}	6
70/20/10	3.11×10^{-24}	4.32	2.18×10^{-25}	14
80/10/10	1.80×10^{-24}	11.9	6.01×10^{-25}	3

When viewed under the optical microscope in fluorescence mode, droplets with mean diameters of the order of 1 μm were observed 24 hours after forming the nanoemulsions in $\% \epsilon = 0$ (Fig. 3.14, top panel). The population appeared to be unimodal, which is consistent with the DLS results. When observed under the microscope through cross-

polarizers, birefringence was not initially observed. However, after about 4 weeks and after a few octane droplets had grown to reach larger dimensions (diameters of 10 - 50 μm), birefringence was clearly observed at the octane/water interface (Fig. 3.14, bottom panel), demonstrating the presence of a layer of the lamellar liquid crystalline phase.

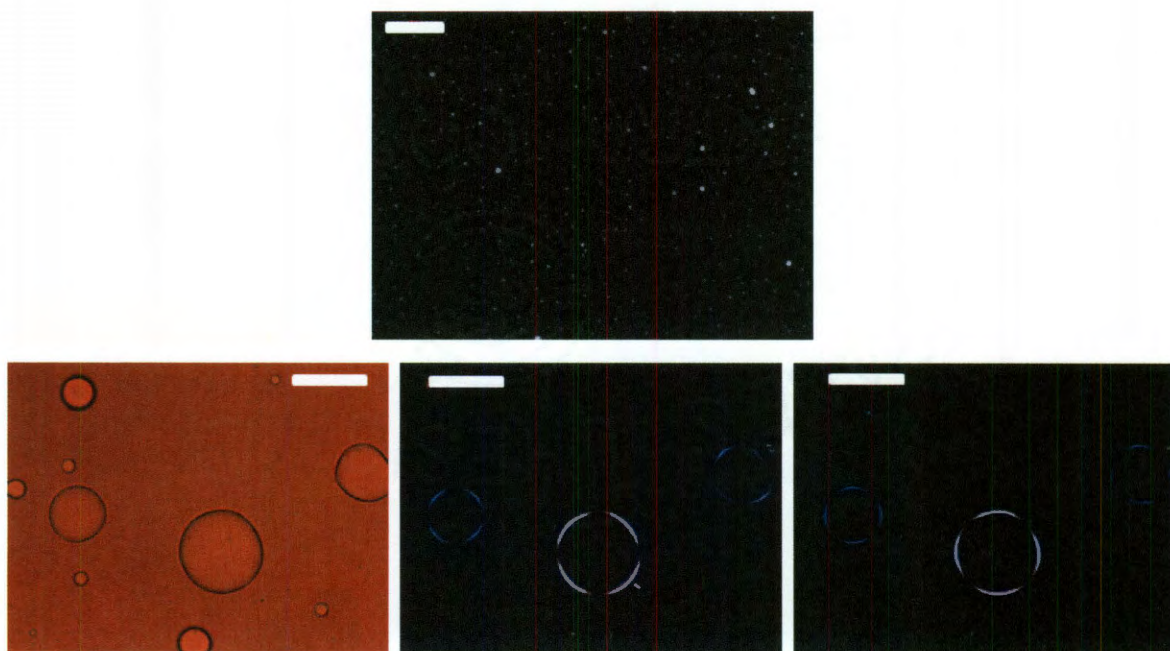


Figure 3.14: Optical micrographs of nanoemulsions (upon diluting 70/20/10 Octane/AOT/Water microemulsion) in excess water, $\% \varepsilon = 0$, AOT = 1.5 g/L. (a) Top panel, image under fluorescence mode, 24 hour upon forming nanoemulsions (Scale bar: 10 μm). (b) Bottom panel. Images taken in bright field and under cross-polarizers after 4 weeks (all scale bars: 50 μm). Prominent birefringence patterns observed around large octane droplets (25-50 μm) and at the octane/water interface for (i) Central image: polarizer set at 0° and analyzer set orthogonal at 90° . (ii) Right corner image: polarizer set at -45° and analyzer set orthogonal at $+45^\circ$.

Upon rotating the polarizer/analyzer arrangement from a $0^\circ/90^\circ$ configuration to a $-45^\circ/+45^\circ$ configuration, a corresponding shift in the regions of dark bands to that of the shift in polarizer/analyzer configuration occurred. Weak birefringence could be seen through the microscope eyepiece for drops with diameters below about 10 μm , but was

not captured by the photographs. The absence of visible birefringence during the first 24 hours of growth is consistent with the conclusion above that growth during this period is due to diffusion-controlled Ostwald ripening.

Probably the lamellar phase coating is nonexistent or very thin initially but thickens over time and could eventually provide an interfacial resistance to mass transfer of octane between the drops and aqueous solution. This is consistent with the fact that a thicker lamellar phase coating with increasing salinity provides greater interfacial resistance to mass transfer of octane. This is also consistent with the observed slower growth rates when dilution of a W/O microemulsion is made in NaCl solutions, for instance with $\% \epsilon = 0,2$ and $0,3$, than with water (Fig. 3.9). This is also consistent with the fact that nanoemulsions formed upon diluting B/O microemulsions show slower growth rates in $\% \epsilon = 0$ when compared with a nanoemulsion formed with a W/O microemulsion (Fig. 3.15).

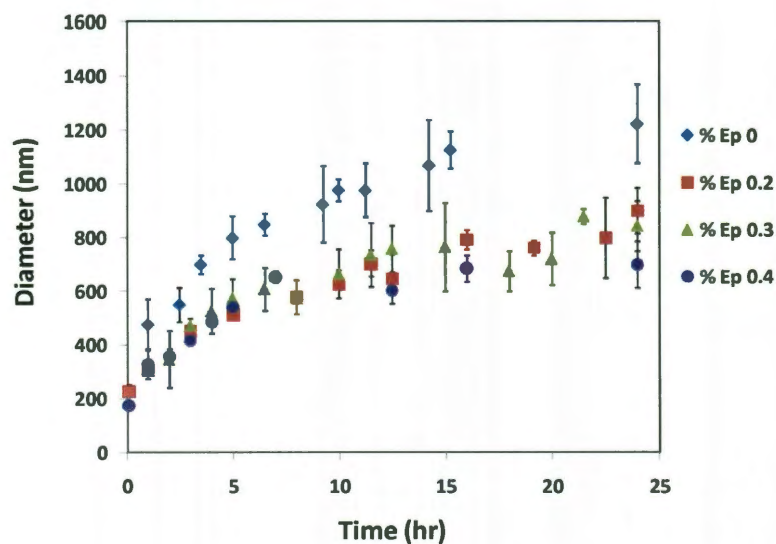


Figure 3.15: Octane droplet size study with respect to time in Octane/Brine nanoemulsions obtained by diluting 70/20/10 Octane/AOT/Brine microemulsions with different levels of internal salinity ($\% \epsilon = 0, 0.2, 0.3, \text{ and } 0.4$) in excess water ($\% \epsilon = 0$,

Winsor I) (AOT = 1.5 g/L). The presence of internal salinity slows down droplet growth rate.

3.4.2 Droplet Growth in Brine ($\% \epsilon = 0.2$ and 0.3)

Fig. 3.5 shows that oil drops in emulsions produced when a 70/20/10 Octane/AOT/Water microemulsion is diluted in brine with NaCl content of 0.2% ($\% \epsilon = 0.2$) have average initial diameters of some 200-300 nm, the same as for dilution with water ($\% \epsilon = 0$). However, the rate of increase in diameter with time was much less for $\% \epsilon = 0.2$. Because the zeta potential is high in both cases (approximately -100 mV, according to Fig. 3.11), it seems unlikely, as indicated previously, that changes in electrostatic repulsion among drops was responsible for the observed difference in growth rates. Similar differences between growth rates at $\% \epsilon = 0$ and 0.2 were seen when initial microemulsion compositions were W/O microemulsions of Octane/AOT/Water at 60/30/10 and 80/10/10 (see Appendix B, Fig. B1) and B/O microemulsions with 70/20/10 composition contained NaCl-brine instead of DI water (Figs. 3.6 and 3.15 and 3.16). That the growth rate is not controlled by electrostatics was further supported by the even slower, indeed minimal, growth rate shown in Fig. 3.9 for $\% \epsilon = 0.3$ although zeta potential had decreased to about -80 mV (Fig. 3.11), a change which would be expected to increase flocculation and/or coalescence and hence increase growth rate if electrostatic effects were controlling droplet growth.⁵⁶

Light scattering measurements showed that the drop size distribution was bimodal for the 70/20/10 Octane/AOT/Water microemulsion diluted in brine with $\% \epsilon = 0.2$ and 0.3 for most of the 24-hour period after emulsion formation (Table 3.3 and Table 3.4). Thus, Ostwald ripening for these experiments is not in the asymptotic growth stage where

drop size distribution is unimodal and Eq. 3.3 does not apply. Nevertheless, mass transfer of octane from small to large drops via the bulk aqueous phase can still occur. The higher salinity and hence lower spontaneous curvature should facilitate development of a lamellar phase coating of the octane drops. However, it is not possible to tell from the information available whether the decrease in growth rate stems mainly from an interfacial resistance produced by the coating or from the decrease in IFT and solubility of octane in brine at the higher salinity, both of which would act to decrease growth rate in the diffusion-controlled case.

The most striking difference between drop size data for dilution of 70/20/10 microemulsions with brines having $\% \epsilon = 0.2$ and 0.3 is that the initial mean drop size was considerably smaller for $\% \epsilon = 0.3$, being as low as 40 nm (Figs. 3.9, 3.10, 3.16 and 3.17). The initial size difference was small for 60/30/10 and 80/10/10 initial microemulsion compositions (see Appendix B, Fig. B1), diameters being approximately 180 nm.⁵⁶ Growth rates are generally low and comparable for the two salinities for a given initial microemulsion composition though lower for $\% \epsilon = 0.3$ where noticeable differences exist. For nanoemulsions formed at this salinity by diluting 70/20/10 B/O microemulsions, growth rates were marginally lower than that formed by diluting the 70/20/10 W/O microemulsion. At this salinity, emergence of the lamellar phase takes place upon phase-inversion, even in the absence of internal salinity in the starting microemulsion.⁴⁴ This is supported by static and streaming birefringence demonstrated by all nanoemulsions prepared at $\% \epsilon = 0.3$, as observed with the polarized light screening method and reported in the section above.

Table 3.3: Population distribution of octane nanoemulsions at select time points showing bimodal distribution when 70/20/10 Octane/AOT/Water microemulsions were diluted in excess brine ($\% \epsilon = 0.2$, AOT = 1.5 g/L).

Time (hr)	Droplet Population				Mean ¹ (nm)	% Deviation ¹
	Population	Diameter (d) (nm)	G(d)*	C(d)**		
1	1a	81	8	1	95.1	10.34
		86	45	8		
		91	84	21		
		96	97	36		
		102	59	45		
	1b	271	16	50	347.2	13.73
		287	59	59		
		322	100	75		
		341	96	90		
		361	54	98		
		380	14	100		
5	5a	105	13	3	141.5	20.89
		118	48	11		
		131	82	24		
		147	84	39		
		164	45	46		
		184	8	47		
	5b	323	47	55	433.9	16.69
		361	58	70		
		404	85	85		
		452	100	96		
		506	95	100		
10	10a	97	15	5	123.1	19.5
		113	15	9		
		132	28	18		
		153	6	20		
	10b	242	29	30	350.8	22.81
		282	36	42		
		328	100	73		
		382	43	87		
		445	41	100		

* G(d) = Weighting function generated by autocorrelator

** C(d) = Cumulative distribution function generated by autocorrelator

¹For a droplet population, the autocorrelator determines the mean diameter using the formulae listed below.

$$\text{Mean diameter} = \left(\frac{\sum_i d_i^3 G(d_i)}{\sum_i G(d_i)} \right)^{\frac{1}{3}} \quad \% \text{ Deviation} = \frac{\text{Standard Deviation}}{\text{Mean Diameter}} \times 100$$

For a bimodal population, we estimate the mean and standard deviations of the two populations separately using the above formulae. The mean (and standard deviation) of the overall populations for time periods 1, 5 and 10 hours were 237 (± 31), 304 (± 30) and 395 (± 27) nm respectively, averaged over 3 DLS runs.

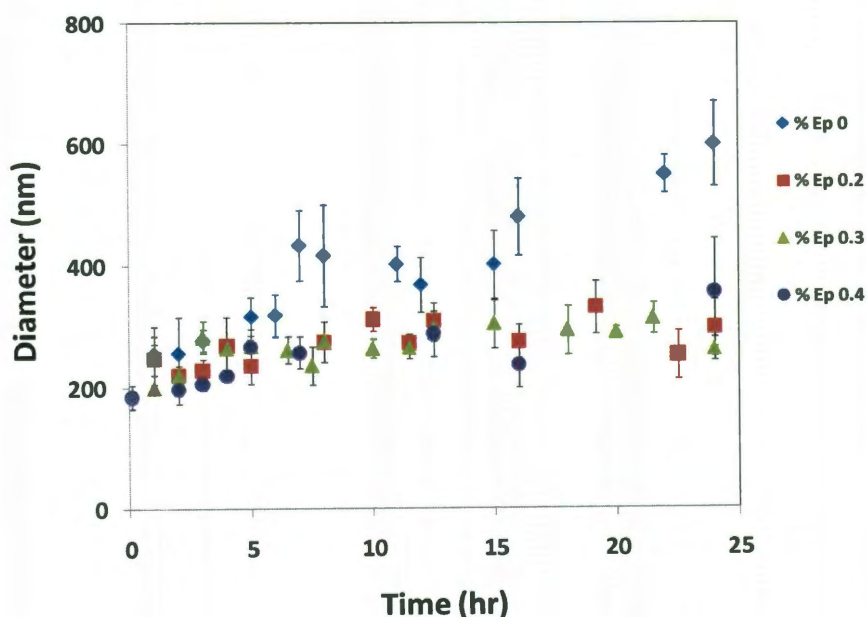


Figure 3.16: Octane droplet size study with respect to time in Octane/Brine nanoemulsions obtained by diluting 70/20/10 Octane/AOT/Brine microemulsions with different levels of internal salinity ($\% \epsilon = 0, 0.2, 0.3,$ and 0.4) in excess brine ($\% \epsilon = 0.2,$ Winsor I) (AOT = 1.5 g/L). The presence of internal salinity slows down droplet growth rate due to emergence of the lamellar phase of AOT. Overall growth rates in brine ($\% \epsilon = 0.2$) are slower when compared to emulsions formed in excess water ($\% \epsilon = 0$).

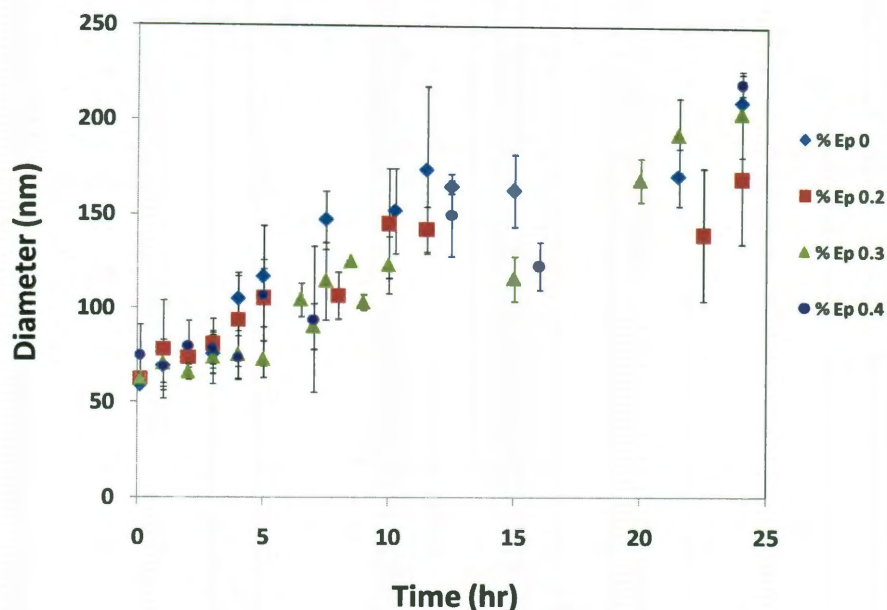


Figure 3.17: Octane droplet size study with respect to time in Octane/Brine nanoemulsions obtained by diluting 70/20/10 Octane/AOT/Brine microemulsions having different levels of internal salinity ($\% \epsilon = 0, 0.2, 0.3,$ and 0.4) in excess brine ($\% \epsilon = 0.3$, Winsor III), (AOT = 1.5 g/L). At the cross-over, the presence of internal salinity slowed down droplet growth rate due to emergence of the lamellar phase of AOT such that perceptible difference was seen in growth rates of nanoemulsions derived from microemulsion compositions with internal brine vs. that with internal water. Overall growth rates in brine ($\% \epsilon = 0.3$) are slower when compared to emulsions formed in excess water ($\% \epsilon = 0$) and lower brine salinity ($\% \epsilon = 0.2$).

For nanoemulsions prepared at $\% \epsilon = 0.3$, optical studies in fluorescence could not give conclusive information on droplet size and size distribution on account of the tiny size of the droplets, which had diameters < 250 nm, below the limit of optical resolution. Further, the presence of liquid crystalline phase of AOT could not be observed under cross-polarizers, even 4 weeks after nanoemulsion preparation. This again is plausibly on account of the small size of oil droplets. In view of the birefringence in the phase behavior experiments at $\% \epsilon = 0.3$ and the liquid crystal coating of the drops at the lower salinities where spontaneous curvature is greater and hence less favorable for formation of the lamellar phase, it seems plausible that a thin layer of liquid crystal also coats the

drops at $\% \epsilon = 0.3$. Nanoemulsions formed in brine salinity of 0.2 ($\% \epsilon = 0.2$), were viewed under fluorescence and cross-polarizers. Twenty four hours upon formation, images in fluorescence mode revealed a bimodal distribution wherein one population had a size that ranged between 1.5-3 μm and the other population was $< 0.8 \mu\text{m}$ (Fig. 3.18, top panel). Since the fluorescence signal from the larger droplets is stronger than those emitted by smaller droplets, the camera is expected to preferentially capture signal from the larger population.

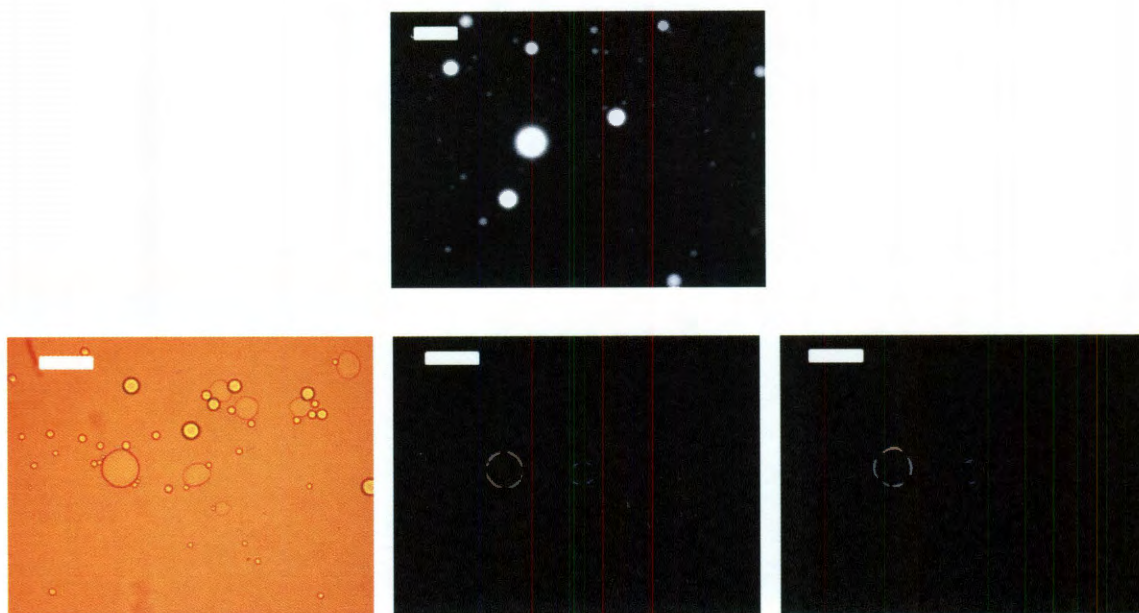


Figure 3.18: Optical micrographs of nanoemulsions (upon diluting 70/20/10 Octane/AOT/Water microemulsion) in brine with salinity, $\% \epsilon = 0.2$ (AOT = 1.5 g/L). (a) Top panel: Image under fluorescence mode 24 hour upon forming nanoemulsions (Scale bar: 10 μm) (b) Bottom panel. Images taken in bright field and under cross-polarizers after 4 weeks. Prominent birefringence patterns observed for around large octane droplets (30-50 μm) and at the octane/water interface for (i) Central image: polarizer set at 0° and analyzer set orthogonal at 90° . (ii) Right corner image: polarizer set at -45° and analyzer set orthogonal at $+45^\circ$ (all scale bars: 100 μm).

This and the fact that the smaller droplet population (as sized by DLS) is near the theoretical limit of optical resolution (500 - 600 nm) allows for the inference that fluorescence studies reveals only the bimodal nature of the population and size range, but not precisely the size. The larger population as seen by fluorescence can possibly explain the observations of creaming in $\phi = 0.2$, as seen in Figs. 3.4, 3.5 and 3.7. Here, the larger droplets can cream and rise as a separate layer in the oil domain. Also, the upper limit of reliable size measurement by DLS is $\sim 3 \mu\text{m}$. Hence, while a larger population exists, the population sized by the laser was the smaller fraction that remained emulsified and in the path of the laser.

Under crossed polarizers, birefringence was not observed for $\phi = 0.2$ until droplet size increased and the liquid crystal coating became sufficiently thick. Birefringence around the drops appeared 4 weeks upon preparation, and was clearly perceivable only for the larger droplet population, similar to the case where $\phi = 0$.⁵⁶ As in the previous case, the smaller droplet population showed weak birefringence and was visible through the microscope eye piece but not to the camera, suggesting a thin liquid crystal coating. Nonetheless, the presence of the liquid crystal coating was confirmed by rotating the incident angles of the orthogonal polarizer/analyzer arrangement and observing the corresponding shift in dark bands.

Table 3.4: Population distribution of octane droplets at select time points showing unimodal and bimodal distributions when 70/20/10 Octane/AOT/Water microemulsions were diluted in excess brine (%ε = 0.3, AOT = 1.5 g/L).

Time (hr)	Droplet Population				Mean ¹ (nm)	% Deviation ¹
	Population	Diameter (d) (nm)	G(d)*	C(d)**		
1	1	28.7	11	2	40.2	24.9
		31.1	86	16		
		33.7	90	30		
		36.5	95	46		
		39.5	100	45		
		42.3	95	48		
		46.3	90	50		
		50.2	26	59		
		54.3	24	75		
		58.5	3	100		
5	5a	37.5	98	28	50.5	11.7
		47.8	100	57		
		60.9	98	86		
	5b	262	25	93	302.2	16.8
		334	25	100		
	10	10a	33	10	4	42.2
41			39	22		
50			13	27		
10b		167	20	36	218.8	28
		204	100	80		
		250	40	98		
		306	6	100		

* G(d) = Weighting function generated by autocorrelator

** C(d) = Cumulative distribution function generated by autocorrelator

¹For a droplet population, the autocorrelator determines the mean diameter using the formulae listed below.

$$\text{Mean diameter} = \left(\frac{\sum_i d_i^3 G(d_i)}{\sum_i G(d_i)} \right)^{\frac{1}{3}}, \quad \% \text{ Deviation} = \frac{\text{Standard Deviation}}{\text{Mean Diameter}} \times 100$$

For a bimodal population, we estimate the mean and standard deviations of the two populations separately using the above formulae. The mean (and standard deviation) of the overall populations for time periods 1, 5 and 10 hours were 41 (± 5), 140 (± 30) and 173 (± 22) nm respectively, averaged over 3 DLS runs.

3.4.3 Nanoemulsions Formed in Brine ($\% \epsilon = 0.4$)

When dilution occurs with brine having a salinity higher than the crossover concentration of $\% \epsilon = 0.3$, initial drop diameters are $1 \mu\text{m}$ or larger – much larger than those seen initially at lower salinities. Moreover, the basic trend shown for $\% \epsilon = 0.4$, according to Figs. 3.9 and 3.10 is a decrease in diameter during approximately the first ten hours, the opposite trend to that described above for lower salinities. Because the initial microemulsion is oil continuous and because spontaneous curvature of the surfactant films after dilution with brine having $\% \epsilon = 0.4$ favors oil-continuous microemulsions, no inversion process yielding small droplets occurs as observed at lower salinities. Instead convection accompanying the dilution process breaks the initial W/O microemulsion into drops. This mechanism is consistent with a larger mean drop size in the first few hours for the experiment with $\% \epsilon = 1.0$ than with $\% \epsilon = 0.4$ (Fig. 3.9) because interfacial tension between microemulsion and brine increases as salinity increases beyond the crossover salinity of $\% \epsilon = 0.3$. Moreover, bulk water drops are incorporated into the microemulsion, forming a W/O/W multiple emulsion, as observed by Nishimi and Miller with optical microscopy for similar conditions in this system, because the higher salinity promotes stability of W/O emulsions.²⁸

Fluorescence microscopy of emulsions formed at $\% \varepsilon = 0.4$ confirmed the existence of multiple emulsions (Fig. 3.19, left image). Further, drop sizes for $t < 4$ hours largely agreed with those measured by DLS. However, a few larger drops (diameters $> 3 \mu\text{m}$) were observed, which were not captured by DLS, being outside its range of measurement. The decrease in drop size with time shown in Figs. 3.9 and 10 could be caused by some combination of further breakup due to convection and to coalescence of the internal water droplets of the multiple emulsions with the external water phase. Mass transfer of water between internal and external water phases may also occur, the direction of transfer being to the phase having lower ionic strength.

Fig. 3.19 (right image) corroborates that coalescence of internal water drops with the external aqueous phase is one mechanism for the observed decrease in drop size. Several hours after dilution of the original W/O microemulsion with brine, multiple emulsions initially having octane drops with many internal water droplets changed to multiple emulsions with smaller octane drops and with a single internal water droplet. It is noteworthy that no birefringence was observed under crossed polarizers 4 weeks after preparation. This observation is consistent with the literature wherein octane/AOT/brine systems move away from the lamellar liquid crystalline phase of AOT into domains of Winsor II having nonzero values of spontaneous curvature.

One additional possibility for the observed decrease in drop size with time is that the larger drops present during the first few hours for dilution with $\% \varepsilon = 0.4$ than with lower salinities increases the likelihood that the largest drops may cream to the air-water interface. In addition, the likelihood of coalescence there to form a thin oil layer is also higher because the zeta potential is lower and because O/W emulsions are generally less

stable in the Winsor II region than at lower salinities. If such an oil layer does form, its oil would likely not be dispersed to drops small enough to be included in subsequent measurements of size distribution, which would shift the mean drop size to lower values than in the absence of creaming/coalescence.

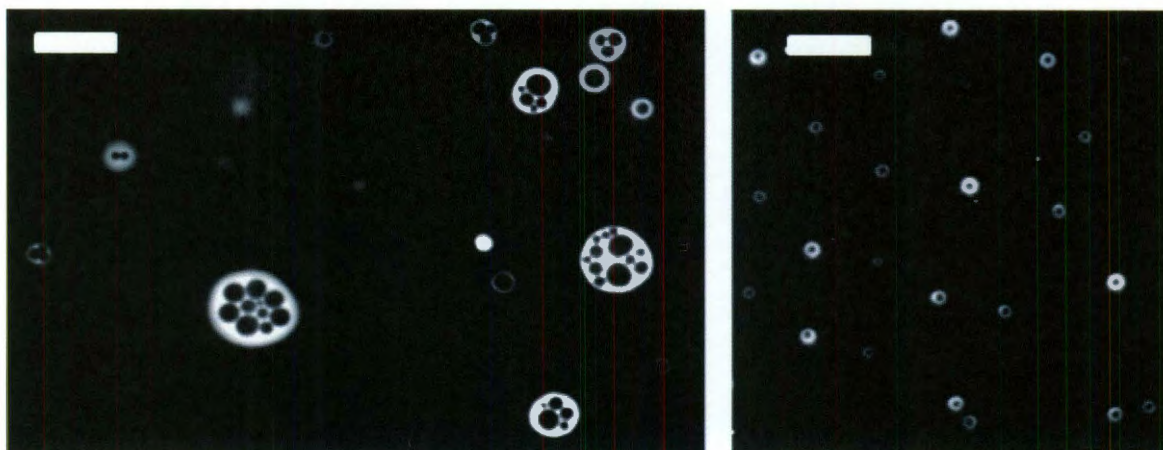


Figure 3.19: (Left) Multiple emulsions of water/octane/water, observed under fluorescence mode (Texas Red Filter, Nile-Red dye), 4 hours upon diluting 70/20/10 Octane/AOT/Water microemulsions in brine at $\% \epsilon = 0.4$ (AOT = 1.5 g/L). (Right) Multiple emulsions with internally coalesced droplets observed at 12 hours. White color corresponds to octane domains; black color corresponds to water/brine domains. All scale bars = 10 μm .

3.5 Conclusions

Droplet size evolution of nanoemulsions formed by diluting W/O and B/O microemulsions of octane/AOT/(water or NaCl brine) in excess water or NaCl brine was investigated by interfacial tension, dynamic light scattering (DLS), electrophoresis, optical microscopy and phase-behavior studies. In DLS studies covering the first 24 hours after nanoemulsion formation, three distinct trends of size evolution were observed that correlated with different Winsor regimes. O/W nanoemulsions formed spontaneously by diluting W/O or B/O microemulsions with water or low-salinity brine in the Winsor I

regime had low initial mean droplet diameters of 150-250 nm owing to local supersaturation and renucleation of the oil phase during the inversion process. The data suggest that the observed growth of these droplets over time was caused by mass transfer. However, the well known asymptotic region of Ostwald ripening described by LSW theory was found only when the initial microemulsions were diluted with salt-free water. At the higher cross-over salinity (Winsor III), O/W nanoemulsions formed spontaneously by a similar mechanism showed minimal growth with diameters consistently remaining below 100 nm for at least one day. Because birefringence was observed for these conditions with crossed sheets of polarizing material it may be that an interfacial resistance causing the low mass transfer and growth rates was present as a result of a lamellar-phase coating of the tiny octane drops, Formation of the lamellar phase is favored for these conditions where spontaneous curvature is near zero.

At the even higher salinity levels in the Winsor II domain, drop diameters greater than 1 μm were consistently recorded for the first 5-7 hours, but they later decreased to values below 1 μm . The high salinity favored W/O emulsions but the large water excess dictated that water is the continuous phase. As a result, W/O/W multiple emulsions were formed initially. Drop size decreased over time, an important mechanism being coalescence of internal water droplets with the bulk aqueous phase.

Electrophoresis showed the nanoemulsions to be highly negatively charged (zeta potentials of -60 mV to -120 mV). The magnitude of zeta potential decreased with increasing salinity. The high charge helped assure stability of the nanoemulsions to flocculation and coalescence, thereby allowing mass transfer to control growth rate in the Winsor I and III regions.

3.6 References

1. Bagaria, H. G.; Kini, G. C.; Wong, M. S., Electrolyte Solutions Improve Nanoparticle Transfer from Oil to Water. *Journal of Physical Chemistry C* **2010**, 114, (47), 19901-19907.
2. Davies, J. T.; Rideal, E. K., Interfacial phenomena. In *Interfacial phenomena*, 1963; p.
3. Miller, C. A., Spontaneous Emulsification Produced by Diffusion - A Review. *Colloids and Surfaces* **1988**, 29, (1), 89-102.
4. Pena, A. A.; Miller, C. A., Solubilization rates of oils in surfactant solutions and their relationship to mass transport in emulsions. *Advances in Colloid and Interface Science* **2006**, 123, 241-257.
5. Lopez-Montilla, J. C.; Herrera-Morales, P. E.; Pandey, S.; Shah, D. O., Spontaneous emulsification: Mechanisms, physicochemical aspects, modeling, and applications. *Journal of Dispersion Science and Technology* **2002**, 23, (1-3), 219-268.
6. Miller, C. A., Behavior of Emulsions and Microemulsions: Implications for Nanosystems. In *Nanoscience: Colloidal and Interfacial Aspects*, Starov, V. M., Ed. CRC Press: Boca Raton, 2010; Vol. 147.
7. Anton, N.; Vandamme, T. F., The universality of low-energy nano-emulsification. *International Journal of Pharmaceutics* **2009**, 377, (1-2), 142-147.
8. Wilking, J. N.; Mason, T. G., Irreversible shear-induced vitrification of droplets into elastic nanoemulsions by extreme rupturing. *Physical Review E* **2007**, 75, (4), 041407.
9. Mason, T. G.; Wilking, J. N.; Meleson, K.; Chang, C. B.; Graves, S. M., Nanoemulsions: formation, structure, and physical properties. *Journal of Physics-Condensed Matter* **2006**, 18, (41), R635-R666.
10. Wang, L. J.; Li, X. F.; Zhang, G. Y.; Dong, J. F.; Eastoe, J., Oil-in-water nanoemulsions for pesticide formulations. *Journal of Colloid and Interface Science* **2007**, 314, (1), 230-235.

11. Guglielmini, G., Nanostructured novel carrier for topical application. *Clinics in Dermatology* **2008**, 26, (4), 341-346.
12. Kim, B. S.; Yang, M. W.; Lee, K. M.; Kim, C. S., In vitro permeation studies of nanoemulsions containing ketoprofen as a model drug. *Drug Delivery* **2008**, 15, (7), 465-469.
13. Nielsen, F. S.; Petersen, K. B.; Mullertz, A., Bioavailability of probucol from lipid and surfactant based formulations in minipigs: Influence of droplet size and dietary state. *European Journal of Pharmaceutics and Biopharmaceutics* **2008**, 69, (2), 553-562.
14. Rao, S.; Shao, J., Self-nanoemulsifying drug delivery systems (SNEDDS) for oral delivery of protein drugs I. Formulation development. *International Journal of Pharmaceutics* **2008**, 362, (1-2), 2-9.
15. Rao, S. V. R.; Yajurvedi, K.; Shao, J., Self-nanoemulsifying drug delivery system (SNEDDS) for oral delivery of protein drugs III. In vivo oral absorption study. *International Journal of Pharmaceutics* **2008**, 362, (1-2), 16-19.
16. Shakeel, F.; Baboota, S.; Ahuja, A.; Ali, J.; Shafiq, S., Skin permeation mechanism and bioavailability enhancement of celecoxib from transdermally applied nanoemulsion. *Journal of Nanobiotechnology* **2008**, 6, Article No.: 8.
17. Shakeel, F.; Baboota, S.; Ahuja, A.; Ali, J.; Shafiq, S., Celecoxib Nanoemulsion for Transdermal Drug Delivery: Characterization and In Vitro Evaluation. *Journal of Dispersion Science and Technology* **2009**, 30, (6), 834-842.
18. Pouton, C. W., Formulation of self-emulsifying drug delivery systems. *Advanced Drug Delivery Reviews* **1997**, 25, (1), 47-58.
19. Kumar, M.; Pathak, K.; Misra, A., Formulation and Characterization of Nanoemulsion-Based Drug Delivery System of Risperidone. *Drug Development and Industrial Pharmacy* **2009**, 35, (4), 387-395.
20. Ling, I. M.; Li, W. H.; Wang, L. H., In Vitro Skin Permeation Efficiency Study on Natural Flavornoid Extracts Incorporated into Nano-Emulsions. *Asian Journal of Chemistry* **2009**, 21, (8), 6237-6246.

21. Bouchemal, K.; Briancon, S.; Perrier, E.; Fessi, H., Nano-emulsion formulation using spontaneous emulsification: solvent, oil and surfactant optimisation. *International Journal of Pharmaceutics* **2004**, 280, (1-2), 241-251.
22. Anton, N.; Benoit, J. P.; Saulnier, P., Design and production of nanoparticles formulated from nano-emulsion templates - A review. *Journal of Controlled Release* **2008**, 128, (3), 185-199.
23. Anton, N.; Gayet, P.; Benoit, J. P.; Saulnier, P. In *Nano-emulsions and nanocapsules by the PIT method: An investigation on the role of the temperature cycling on the emulsion phase inversion*, 2007; pp 44-52.
24. Srivastava, V. K.; Kini, G.; Rout, D., Detergency in spontaneously formed emulsions. *Journal of Colloid and Interface Science* **2006**, 304, (1), 214-221.
25. Lopez-Montilla, J. C.; James, M. A.; Crisalle, O. D.; Shah, D. O., Surfactants and protocols to induce spontaneous emulsification and enhance detergency. *Journal of Surfactants and Detergents* **2005**, 8, (1), 45-53.
26. Miller, C. A.; Raney, K. H., Solubilization Emulsification Mechanisms of Detergency. *Colloids and Surfaces A-Physicochemical and Engineering Aspects* **1993**, 74, (2-3), 169-215.
27. Miller, C. A.; Neogi, P., *Interfacial Phenomena*. 2nd ed.; CRC Press: Boca Raton, 2008; Vol. 139, p 501.
28. Nishimi, T.; Miller, C. A., Spontaneous emulsification of oil in aerosol-OT/water/hydrocarbon systems. *Langmuir* **2000**, 16, (24), 9233-9241.
29. Maestro, A.; Sole, I.; Gonzalez, C.; Solans, C.; Gutierrez, J. M., Influence of the phase behavior on the properties of ionic nanoemulsions prepared by the phase inversion composition method. *Journal of Colloid and Interface Science* **2008**, 327, (2), 433-439.
30. Wang, L. J.; Mutch, K. J.; Eastoe, J.; Heenan, R. K.; Dong, J. F., Nanoemulsions prepared by a two-step low-energy process. *Langmuir* **2008**, 24, (12), 6092-6099.
31. Lamaallam, S.; Bataller, H.; Dicharry, C.; Lachaise, J., Formation and stability of miniemulsions produced by dispersion of water/oil/surfactants concentrates in a large

amount of water. *Colloids and Surfaces A-Physicochemical and Engineering Aspects* **2005**, 270, 44-51.

32. Shahidzadeh, N.; Bonn, D.; Aguerre-Chariol, O.; Meunier, J., Spontaneous emulsification: relation to microemulsion phase behaviour. *Colloids and Surfaces A-Physicochemical and Engineering Aspects* **1999**, 147, (3), 375-380.

33. Rang, M. J.; Miller, C. A., Spontaneous emulsification of oils containing hydrocarbon, nonionic surfactant, and oleyl alcohol. *Journal of Colloid and Interface Science* **1999**, 209, (1), 179-192.

34. Shahidzadeh, N.; Bonn, D.; Meunier, J., A new mechanism of spontaneous emulsification: Relation to surfactant properties. *Europhysics Letters* **1997**, 40, (4), 459-464.

35. Rang, M. J.; Miller, C. A.; Hoffmann, H. H.; Thunig, C., Behavior of hydrocarbon/alcohol drops injected into dilute solutions of an amine oxide surfactant. *Industrial & Engineering Chemistry Research* **1996**, 35, (9), 3233-3240.

36. Porras, M.; Solans, C.; Gonzalez, C.; Martinez, A.; Guinart, A.; Gutierrez, J. M. In *Studies of formation of W/O nano-emulsions*, 2004; 2004; pp 115-118.

37. Wang, L.; Tabor, R.; Eastoe, J.; Li, X.; Heenan, R. K.; Dong, J., Formation and stability of nanoemulsions with mixed ionic-nonionic surfactants. *Phys Chem Chem Phys* **2009**, 11, (42), 9772-8.

38. Salager, J. L.; Forgiarini, A.; Marquez, L.; Pena, A.; Pizzino, A.; Rodriguez, M. P.; Rondo- Gonzalez, M. In *Using Emulsion Inversion in Industrial Processes*, 2004; pp 259-272.

39. Tadros, T.; Izquierdo, R.; Esquena, J.; Solans, C. In *Formation and Stability of Nano-emulsions*, 2004; pp 303-318.

40. Izquierdo, P.; Feng, J.; Esquena, J.; Tadros, T. F.; Dederen, J. C.; Garcia, M. J.; Azemar, N.; Solans, C., The influence of surfactant mixing ratio on nano-emulsion formation by the PIT method. *Journal of Colloid and Interface Science* **2005**, 285, (1), 388-394.

41. Nishimi, T.; Miller, C. A., Spontaneous emulsification produced by chemical reactions. *Journal of Colloid and Interface Science* **2001**, 237, (2), 259-266.
42. Shahidzadeh, N.; Bonn, D.; Meunier, J.; Nabavi, M.; Airiau, M.; Morvan, M., Dynamics of spontaneous emulsification for fabrication of oil in water emulsions. *Langmuir* **2000**, 16, (25), 9703-9708.
43. Miller, C. A., Dissolution Rates of Surfactants. In *Interfacial Processes and Molecular Aggregation of Surfactants*, 2008; Vol. 218, pp 3-24.
44. Maugey, M.; Bellocq, A. M., Effect of added salt and poly(ethylene glycol) on the phase behavior of a balanced AOT-water-oil system. *Langmuir* **1999**, 15, (25), 8602-8608.
45. Shinoda, K.; Arai, H., Correlation between Phase Inversion Temperature in Emulsion + Cloud Point in Solution of Nonionic Emulsifier *Journal of Physical Chemistry* **1964**, 68, (12), 3485.
46. Shinoda, K.; Arai, H., Effect of Phase Volume on Phase Inversion Temperature of Emulsions Stabilized with Nonionic Surfactants *Journal of Colloid and Interface Science* **1967**, 25, (3), 429.
47. Kunieda, H.; Shinoda, K., Solution Behavior and Hydrophile-Lipophile Balance Temperature in the Aerosol OT-Isooctane-Brine System - Correlation between Micro-Emulsions and Ultralow Interfacial-Tensions. *Journal of Colloid and Interface Science* **1980**, 75, (2), 601-606.
48. Kunieda, H.; Shinoda, K., Solution Behavior of Aerosol-OT-Water-Oil System. *Journal of Colloid and Interface Science* **1979**, 70, (3), 577-583.
49. Kellay, H.; Binks, B. P.; Hendrikx, Y.; Lee, L. T.; Meunier, J., Properties of Surfactant Monolayers in Relation to Microemulsion Phase-Behavior *Advances in Colloid and Interface Science* **1994**, 49, 85-112.
50. Hackett, J. L.; Miller, C. A., *SPE Res. Eng.* **1988**, 3, 791.
51. Ghosh, O.; Miller, C. A., Liquid-Crystalline and Microemulsion Phase-Behavior in Alcohol-Free Aerosol-OT/Oil/Brine Systems. *Journal of Physical Chemistry* **1987**, 91, (17), 4528-4535.

52. Seifert, A. M.; Wendorff, J. H., Spinning Drop Experiments on Interfacial Phenomena - Theoretical Background and Experimental-Evidence. *Colloid and Polymer Science* **1992**, 270, (10), 962-971.
53. Hunter, R. J., *Zeta Potential in Colloid Science: Principles and Applications*. Academic Press: New York, 1981.
54. Evans, D. F.; Wennerstrom, H., *The Colloidal Domain: Where Physics, Chemistry Biology and Technology Meet*. 2nd ed.; Wiley-VCH: New York, 1999.
55. Aveyard, R.; Binks, B. P.; Clark, S.; Mead, J., Interfacial-Tension Minima in Oil-Water Surfactant Systems - Behavior of Alkane Aqueous NaCl Systems containing Aerosol-OT. *Journal of the Chemical Society-Faraday Transactions I* **1986**, 82, 125-142.
56. Kini, G. C. Bilayer Approaches for Nanoparticle Phase-Transfer. PhD Thesis, Rice University, Houston, 2011.
57. Kotlarchyk, M.; Chen, S. H.; Huang, J. S., Temperature-Dependence of Size and Polydispersity in a 3-Component Micro-Emulsion by Small-Angle Neutron-Scattering *Journal of Physical Chemistry* **1982**, 86, (17), 3273-3276.
58. Meier, W., Poly(oxyethylene) adsorption in water oil microemulsions: A conductivity study. *Langmuir* **1996**, 12, (5), 1188-1192.
59. Li, Z. X.; Lu, J. R.; Fragneto, G.; Thomas, R. K.; Binks, B. P.; Fletcher, P. D. I.; Penfold, J., Neutron reflectivity studies of Aerosol-OT monolayers adsorbed at the oil/water, air/water and hydrophobic solid/water interfaces. *Colloids and Surfaces A-Physicochemical and Engineering Aspects* **1998**, 135, (1-3), 277-281.
60. Israelachvili, J., *Intermolecular and Surface Forces*. 2nd ed.; Academic Press: London, 1991; p 450.
61. Aveyard, R.; Binks, B. P.; Mead, J., Interfacial-Tension Minima in Oil-Water Surfactant Systems - Effects of Alkane Chain-Length and Presence of Normal-Alkanols in Systems containing Aerosol OT. *Journal of the Chemical Society-Faraday Transactions I* **1986**, 82, 1755-1770.
62. Taylor, P., Ostwald Ripening in Emulsions. *Colloids and Surfaces A-Physicochemical and Engineering Aspects* **1995**, 99, (2-3), 175-185.

63. Taylor, P., Ostwald ripening in emulsions. *Advances in Colloid and Interface Science* **1998**, 75, (2), 107-163.
64. Taylor, P., Ostwald ripening in emulsions: estimation of solution thermodynamics of the disperse phase. *Advances in Colloid and Interface Science* **2003**, 106, 261-285.
65. Kabalnov, A. S.; Makarov, K. N., Ostwald Ripening in Hydrocarbon Emulsions - Experimental Test of Equation for Absolute Rates. *Colloid Journal of the USSR* **1990**, 52, (4), 589-595.
66. Kabalnov, A. S.; Makarov, K. N.; Pertzov, A. V.; Shchukin, E. D., Ostwald Ripening in Emulsions 2. Ostwald Ripening in Hydrocarbon Emulsions - Experimental-Verification of Equation for Absolute Rates. *Journal of Colloid and Interface Science* **1990**, 138, (1), 98-104.
67. Lifshitz, I. M.; Slyozov, V. V., The Kinetics of Precipitation from Supersaturated Solid Solutions. *Journal of Physics and Chemistry of Solids* **1961**, 19, (1-2), 35-50.
68. Wagner, C., Theorie Der Alterung Von Niederschlagen Durch Umlosen (Ostwald-Reifung). *Zeitschrift Fur Elektrochemie* **1961**, 65, (7-8), 581-591.
69. Lide, D. R., *CRC Handbook of Chemistry and Physics*. 79 ed.; CRC Press: Boca Raton, 1998.
70. Sakai, T.; Kamogawa, K.; Nishiyama, K.; Sakai, H.; Abe, M., Molecular diffusion of oil/water emulsions in surfactant-free conditions. *Langmuir* **2002**, 18, (6), 1985-1990.
71. Bird, R. B.; Stewart, W. E.; Lightfoot, E. N., *Transport Phenomena*. 2nd ed.; John Wiley and Sons: 2006.
72. Djerdjev, A. M.; Beattie, J. K., Enhancement of Ostwald ripening by depletion flocculation. *Langmuir* **2008**, 24, (15), 7711-7717.
73. Weiss, J.; Herrmann, N.; McClements, D. J., Ostwald ripening of hydrocarbon emulsion droplets in surfactant solutions. *Langmuir* **1999**, 15, (20), 6652-6657.

74. Ariyaprakai, S.; Dungan, S. R., Influence of surfactant structure on the contribution of micelles to Ostwald ripening in oil-in-water emulsions. *Journal of Colloid and Interface Science* **2010**, 343, (1), 102-108.
75. Soma, J.; Papadopoulos, K. D., Ostwald ripening in sodium dodecyl sulfate-stabilized decane-in-water emulsions. *Journal of Colloid and Interface Science* **1996**, 181, (1), 225-231.
76. Mun, S. H.; McClements, D. J., Influence of interfacial characteristics on Ostwald ripening in hydrocarbon oil-in-water emulsions. *Langmuir* **2006**, 22, (4), 1551-1554.

Chapter 4

Colloidal and Flow Behavior of Brine-Stable Quantum Dot Nanoparticles

4.1 Introduction

The continuing increase in energy demand worldwide has motivated recent efforts to design nanomaterials with signaling, sensing, and detection capabilities for oil exploration.¹⁻⁶ The general objective is to retrieve real-time, spatially-resolved physical (e.g., temperature⁷⁻¹³, pressure¹⁰, rock porosity, and permeability¹⁴) and chemical (e.g., oil^{5, 6, 15, 16}, water^{7, 17, 18}, gas^{19, 20}, and mineral type²¹) information of an oil reservoir after downhole injection of transportable particles.

Contrast-enhancing agents help detect specific targets at threshold levels and through nanoscale properties, enhance response and resolution of existing x-ray, electromagnetic, and seismic-based detection methods.^{1-4, 22-28} Sensing agents are based on the concept of information gathering via changes in their physical or chemical state during subsurface transport and their subsequent retrieval and analysis.^{1-5, 7, 8, 12-20, 28-33} There have been recent efforts to fabricate miniaturized electronic devices as sensing agents that measure, store, and communicate reservoir properties.^{1-4, 9-11, 16, 34-45}

Tour and coworkers recently synthesized carbon-based submicron particles with hydrocarbon sensing capability, in which a hydrophobic compound is released when transporting through oil-containing rock.^{5, 6} These "nanoreporters," ~140-nm polyvinyl alcohol-coated carbon particles, flowed rapidly through oil- and non-oil-containing sandpack columns in deionized water at room temperature, and with little deposition. Some aggregation was observed in salt-containing water after several days, which resulted in partial particle entrapment during flow experiments.

Conditions in a reservoir are usually very harsh, with water salinities approaching those of seawater and higher and with temperatures ranging between 70-150 °C.¹⁻³ A challenging aspect in the design of contrast-enhancing or sensing agents is the need for high colloidal stability under reservoir-relevant conditions. Additionally, if such agents are supported on particles, these agents should be unaggregated and non-interacting with the reservoir minerals during their transport. Whereas much is known about colloidal stability in low-to-no salt-containing aquatic systems⁴⁶, there are very few studies in which nanoparticles have been specifically designed to be stable in high-salt-containing water.^{22, 47}

Here we report a robust method in preparing salt-stable nanoparticle (NP) suspensions and for assessing their transport behavior using packed columns. Using oleic acid-coated CdSe quantum dots (QDs) as a model NP because of their small size (<10 nm) and size-dependent optical properties, we identified a commercially available nonionic surfactant (Neodol 91-7, referred hereafter as Neodol) as a suitable outer NP coating that provided water dispersibility. The QD/Neodol combination showed remarkable stability to aggregation at high salinities (1M NaCl and 0.55M synthetic seawater) and temperatures up to 70 °C. These NPs exhibited nearly unimpeded flow through crushed-calcite columns at these reservoir-relevant salt conditions and temperatures.

4.2 Colloidal Stability of Nanoparticles: The Role of Intermolecular Forces

For successful transport and breakthrough of NPs through reservoirs, NP dispersions need to be stable under reservoir conditions of high salinities and temperatures. Within

the scope of this work, salinities at 1M NaCl and 0.55M synthetic seawater (containing among others, Ca^{2+} and Mg^{2+} ions) and an upper temperature limit of 70°C are considered representative of a reservoir. To stabilize nanoparticles under such conditions, it is important to understand the role of intermolecular forces, which becomes the basis to judiciously select a stabilizing surface-active (surfactant) agent.

4.2.1 Nanoparticles Stabilized by Electrostatics

The net energy of interaction ($V_{\text{NET DLVO}}$) between two charged colloidal particles is well described by the Derjaguin-Landau-Verwey-Overbeek (DLVO) theory to be the sum of the attractive van der Waals (V_{VDW}) energy and repulsive electrical energy (V_{EDL}).⁴⁸

$$V_{\text{NET DLVO}} = V_{\text{VDW}} + V_{\text{EDL}} \quad (4.1)$$

For spherical nanoparticles⁴⁶:

$$V_{\text{VDW}} = -\frac{A_{121}a_1a_2}{6h(a_1 + a_2)\left(1 + \frac{14h}{\lambda}\right)} \quad (4.2)$$

Where: A_{121} is the Hamaker interaction parameter between two like particles interacting across a medium, given by $A_{121} = \left(\sqrt{A_{22}} - \sqrt{A_{11}}\right)^2$, with A_{11} = Hamaker constant for particle (1) and A_{22} = Hamaker constant of medium 2, h = distance of separation between two nanoparticle,^{46, 48} and " λ " is the characteristic wavelength associated with interactions between NPs. Gregory showed these effects to be of electromagnetic origin, prevalent at dimensions of ~ 100 nm and lower.^{46, 49} It is noteworthy that at λ values over

100 nm, $\frac{h}{\lambda}$ approaches zero and the expression in Eq. 4.2 reduces to the familiar form for van der Waals interactions between two spherical colloidal particles^{46, 48}:

$$V_{\text{VDW}} = -\frac{A_{121}a_1a_2}{6h(a_1 + a_2)}. \text{ For the scenario where NPs are QDs interacting in aqueous}$$

media, $A_{11} \sim 0.72 \times 10^{-20}\text{J}$ and $A_{22} \sim 4 \times 10^{-20}\text{J}$. Hence, $A_{121} = 1.32 \times 10^{-20}\text{J}$.^{46 48} Further, a_1 and a_2 are hydrodynamic radii of particles (here $a_1 = a_2 = 9.5\text{ nm}$ for CdSe QDs stabilized by AOT when in water and is 4.5 nm for CdSe QDs stabilized by QDs in salty water).⁴⁷ Note: The negative sign in Eq. 4.2 denotes van der Waals to be an attractive force.

The repulsive electrical energy is given by:

$$V_{\text{EDL}} = 64\pi\epsilon_0\epsilon_r \frac{a_1a_2}{(a_1 + a_2)} \left(\frac{k_b T}{ze}\right)^2 \Gamma_1\Gamma_2 \exp(-\kappa h) \quad (4.3)$$

Where: ϵ_0 = permittivity of free space, ($8.856 \times 10^{-12}\text{ C}^2\text{J}^{-1}\text{m}^{-1}$), ϵ_r = relative permittivity (80 for water), k_b = Boltzmann's constant ($1.38 \times 10^{-23}\text{ JK}^{-1}$), T = temperature (298 K), z = valency of ion (+1 for Na^+ , K^+ and +2 for Ca^{2+} , Mg^{2+}), e = charge on electron

($-1.6 \times 10^{-19}\text{ C}$), $\Gamma_1 = \tanh\left(\frac{ze\psi_1}{4k_b T}\right)$, where ψ_1 = surface potential of particle 1,

$\Gamma_2 = \tanh\left(\frac{ze\psi_2}{4k_b T}\right)$, where ψ_2 = surface potential of particle 2. For the scenario where

QDs are stabilized in bilayers of the anionic surfactant AOT, $\Gamma_1 = \Gamma_2$. Furthermore,

κ = Debye parameter, which is the inverse Debye screening length (κ^{-1}), defined as:

$$\kappa^{-1} = \left(\frac{\epsilon_0 \epsilon_r k_b T}{e^2 \sum_i c_i z_i^2} \right)^{\frac{1}{2}} \quad (4.4)$$

Where c_i refers to the concentration in molar units and z_i refers to the valency of a particular species i . All other terms that appear in the parenthesis have been defined before in the context of Eq. 4.3. For a 1:1 electrolyte such as NaCl and KCl, Eq. 4.4 becomes:

$$\kappa^{-1} = \frac{0.304}{\sqrt{C}} \text{ nm} \quad (4.5)$$

Where C = concentration of electrolyte in molar units.⁴⁸ In a similar manner, for cases of 1:2 and 2:1 electrolytes such as CaCl_2 , MgCl_2 and Na_2SO_4 ,

$$\kappa^{-1} = \frac{0.176}{\sqrt{C}} \text{ nm} \quad (4.6)$$

Where C = concentration of electrolyte in molar units.⁴⁸ Figs. 4.1 and 4.2 depict the net energy of interaction between two QDs stabilized by AOT, in different concentrations of NaCl and CaCl_2 . In generating the energy-distance curves, the surface potential ψ was approximated to be equivalent to the zeta potential, ζ . For QDs stabilized by AOT, this value was measured to be -77 mV in DI water.⁴⁷ From Fig. 4.1, it can be seen that in the absence of salinity, the interaction energy is of a repulsive nature and its magnitude exceeds $k_B T$ energy units by a factor of 10 and to distances of separation well beyond 10

μm . As salt is introduced into the system, two effects are noticeable - (i) The order of the long range repulsion begins to reduce substantially, i.e, the first cross-over from the repulsion to attraction interaction energy domains occur at $5.5 \mu\text{m}$ for 0.001M salinity ($\kappa^{-1} = 9.61 \text{ nm}$), at $1.65 \mu\text{m}$ for 0.01M salinity ($\kappa^{-1} = 3.04 \text{ nm}$), at $0.4 \mu\text{m}$ for 0.1M salinity ($\kappa^{-1} = 0.961 \text{ nm}$), and $0.08 \mu\text{m}$ for 1M salinity ($\kappa^{-1} = 0.304 \text{ nm}$).

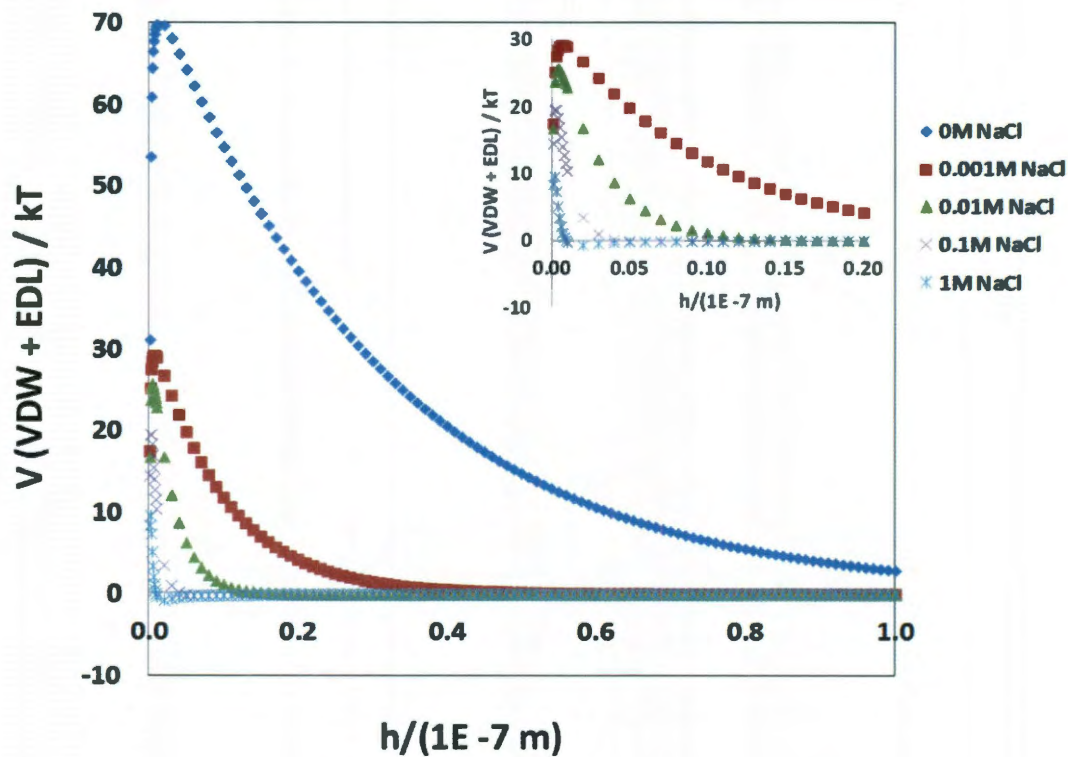


Figure 4.1: Net DLVO Interaction Energy for QDs stabilized by AOT at varying levels of NaCl concentrations (Inset figure - Magnified regions of energy-distance profile for QDs stabilized by AOT in different concentrations of NaCl).

This cross-over at long-range corresponds to the well-known secondary minimum or flocculation region of the DLVO theory. (ii) The magnitude of the repulsive energy barrier progressively reduces from $70 k_B T$ units in 0M NaCl salinity to under $20 k_B T$ units in 1M NaCl salinity. Upon overcoming this barrier, particles enter into a primary

energy regime where irreversible coagulation occurs. The above two effects of salts have been attributed to charge screening from salt counter-ions that result in electrical double layer compression. This promotes flocculation/coagulation of colloidal/nanoparticle dispersions and eventually results in their destabilization.⁴⁸

The effect of valency on colloidal/nanoparticle stability also follows from the DLVO theory, wherein the critical coagulation concentration (CCC) depends on the valency (z) of salt ions and scales as $CCC \sim \frac{1}{z^6}$ (Schulz-Hardy Rule) for large zeta potentials (when $\frac{ze\psi}{4k_bT} \gg 1$) and scales as $CCC \sim \frac{1}{z^2}$ for low zeta potential (when $\frac{ze\psi}{4k_bT} \ll 1$). Hence, in the scenarios of divalent or multivalent ions (such as Ca^{2+} and Mg^{2+} in synthetic seawater), onset of flocculation/coagulation should occur at much lower concentrations than for monovalent ions (such as Na^+ and K^+ ions). Fig. 4.2 depicts the interaction energy between QDs stabilized by AOT in the presence of divalent Ca^{2+} . A significant effect emerges in altering interaction energies by divalent ions, when compared to equal concentrations of monovalent Na^+ ions.

Firstly, the screening lengths at corresponding salinities reduce in that $\kappa^{-1} = 5.56$ nm while at 0.001M $CaCl_2$ salinity, which further decreases to 1.76 nm, 0.556 nm, and 0.176 nm when salinities are increased to 0.01M, 0.1M and 1M $CaCl_2$ respectively. This lowers the distance at the long range order where cross-over occurs from the repulsive to the attractive interaction regime. Second, the magnitude of the primary repulsive barrier in the $CaCl_2$ environment decreases more significantly when compared to $NaCl$ and results in earlier onset of NP coagulation.

When ionic surfactants are used to bring about electrostatic stabilization, other non-DLVO effects can come into play which will have destabilizing effects on the colloidal particle. Ionic surfactants are particularly sensitive to salt-induced precipitation. This is especially seen in the environment of divalent ions such as Ca^{2+} and Mg^{2+} since the solubility product of the divalent salt of the ionic surfactant is lower than of its monovalent ion counterpart. These have resulted in NP and colloidal aggregation at salinities lower than what the DLVO theory predicts.

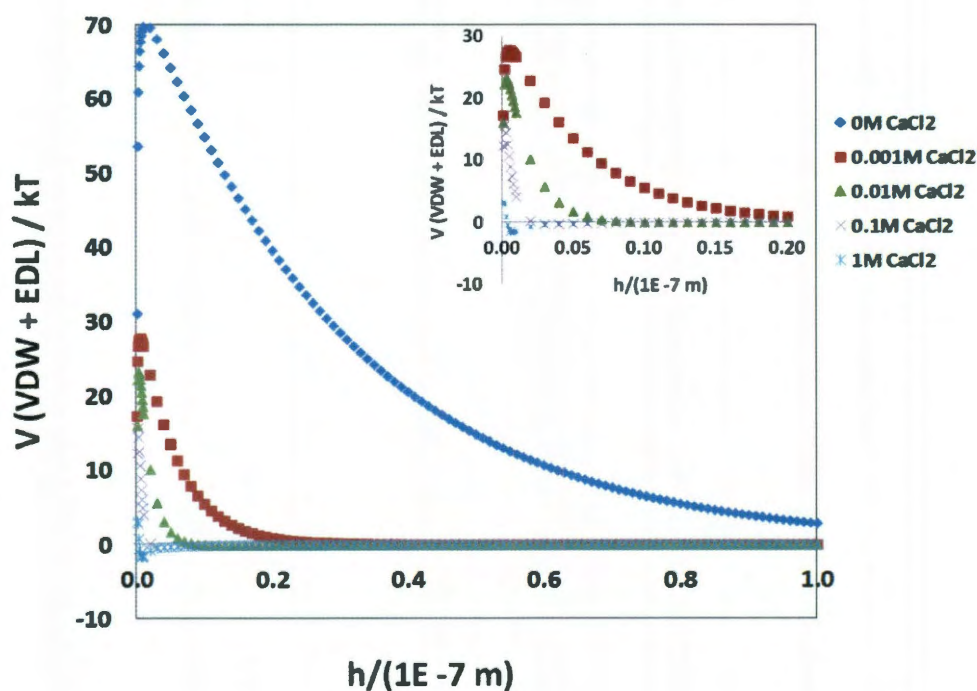


Figure 4.2: Net DLVO Interaction Energy for QDs stabilized by AOT at varying levels of CaCl_2 concentrations (Inset figure - Magnified regions of energy-distance profile for QDs stabilized by AOT in different concentrations of CaCl_2).

Steric hindrance can be devised as a strategy to counter some of the salt-induced destabilizing effects as seen above. Nonionic surfactants such as alkyl alcohol ethoxylates have high salt-tolerance and are more suited in formulating salt-tolerant QD dispersions.

However, nonionic surfactants are temperature-sensitive and above a critical temperature termed as the cloud point, they phase-separate from water by a dehydration mechanism to form a micellar-rich secondary phase.⁵⁰⁻⁵² It follows that in applications featuring nonionic surfactants, one must operate below its cloud point⁵³ or conversely, nonionic surfactants must be selected with cloud points above the temperature of applications.⁵³⁻⁵⁵ In the following section, we discuss the energy-distance curve of steric-stabilized NPs.

4.2.2 Nanoparticles Stabilized by Steric Hindrance

Analogous to the net interaction expression described by the DLVO theory, the net energy of interaction between two colloidal particles that are steric-stabilized is the sum of attractive van der Waals (V_{VDW}) and repulsive steric hindrance (V_{ST}).

$$V_{Net} = V_{VDW} + V_{ST} \quad (4.7)$$

For spherical nanoparticles, V_{ST} is described by:

$$V_{ST} = 2\pi \frac{a_1 a_2}{(a_1 + a_2)} \left(\frac{k_b T}{s^3} \right) \int_L^h \left\{ \frac{8L}{5} \left[\left(\frac{2L}{h} \right)^{\frac{5}{4}} - 1 \right] + \frac{8L}{7} \left[\left(\frac{h}{2L} \right)^{\frac{7}{4}} - 1 \right] \right\} dh \quad (4.8)$$

Note: Eq. 4.8 is a modification of the Alexander-DeGennes equation for polymeric brushes grafted to a surface. For the case of low molecular weight polymers and polymeric nonionic surfactants, the equation is valid until $h < 2L$. The distance of separation s , between two nonionic surfactants on a surface is related to its surface excess Γ_A by the relationship.⁵⁶

$$s = \left(\frac{1}{\Gamma_A N_A} \right)^{0.5} \quad (4.9)$$

Where N_A is the Avogadro's number. Typical Γ_A values for nonionic surfactants are 10^{-6} mol/m², giving representative s values at ~ 13 nm. From Fig. 4.3, it can be seen that with an increase in surface coverage of nonionics on NPs, the magnitude of steric repulsion increases. When surfactant coverage is sparse, the net interaction energy takes the attractive form at short distances of separation. When a sufficiently dense coverage is obtained such that the distance of separation between two surfactant molecules is under 15 nm, the repulsive steric term dominates even at short separation distances.

Thus it follows that steric stabilization using nonionic surfactants can emerge as an alternate approach to stabilize NPs under high conditions of high salinity. For successful transport and breakthrough of NPs through reservoirs, NP dispersions need to be stable under reservoir conditions of high salinities and temperatures. Within the scope of this work, salinities at 1M NaCl, and 0.55M synthetic seawater (containing among others, Ca²⁺ and Mg²⁺ ions) and an upper temperature limit of 70 °C are considered representative of a reservoir. Aggregation of NP dispersions occurs above 100 mM ionic strength, well below these salinities.⁴⁶ To stabilize NPs for the conditions of a reservoir, appropriate processing routes and judicious selection of surfactants are required.^{22, 47}

Our previous experience of formulating QD dispersions by an emulsion-based transfer approach with ionic surfactants (Aerosol-OT) yielded stable unaggregated and single QDs coated by surfactant bilayers. However, the ionic nature of Aerosol-OT caused precipitation to occur beyond 0.25M NaCl,⁴⁷ and was thus inappropriate for this application.

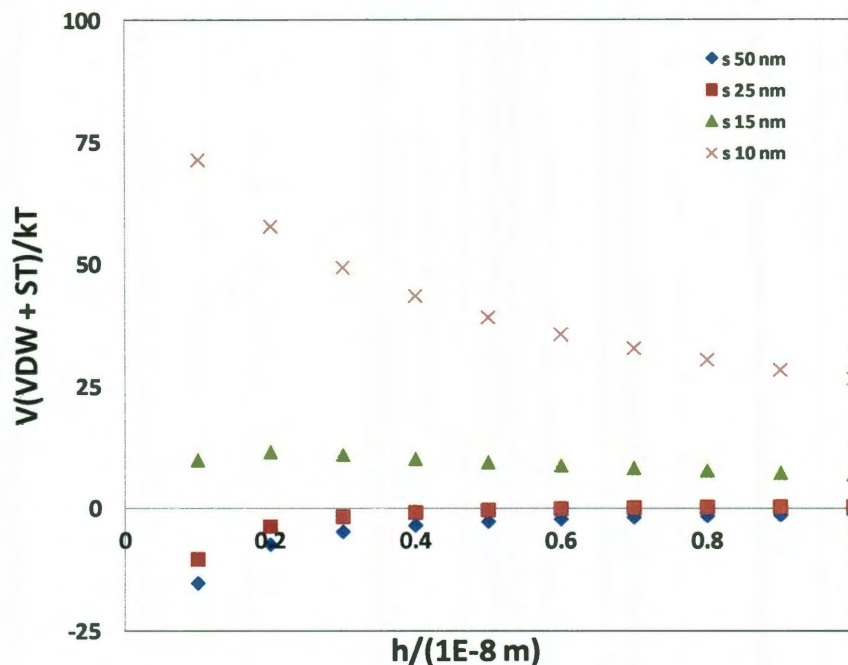


Figure 4.3: Net Interaction Energy for NPs stabilized by a nonionic surfactant as a function of surface coverage.

As an alternative, nonionic surfactants such as alkyl alcohol ethoxylates have high salt-tolerance and are more suited in formulating stable QD dispersions at higher ionic strengths.⁵¹ We therefore selected Neodol 91-7 (nonionic surfactant with a distribution of C₉-C₁₁ linear alkyl groups and 7 ethylene oxide groups, referred hereafter as Neodol), which had a measured cloud point of 74 °C.⁵⁷

4.3 Materials and Methods

4.3.1 Synthesis and Phase Transfer of Quantum Dots

Oleic acid-coated CdSe QDs were synthesized by the hot injection method following previously published procedures.^{58, 59} Cadmium oxide (CdO, 99.99%), oleic acid (OA, technical grade – 90%), 1-octadecene (ODE, technical grade – 90%), and trioctylphosphine (TOP, 90%) were all purchased from Aldrich. Selenium (Se - 99.99%)

was obtained from Strem Chemicals. All chemicals used in this study were used as supplied and without further purification. [Caution: Hot injection routes to synthesize QDs involve steps that may lead to hazardous explosive conditions] After purification, CdSe QDs were suspended in chloroform (Fischer, ACS grade), to which Neodol 91-7 (Shell Chemicals) was added (referred hereafter as Neodol). The final concentrations were 221 $\mu\text{mol-QD/L-chloroform}$ and 30 $\text{mg-Neodol/mL-chloroform}$. QD transfer from chloroform to water was carried out following a recently published protocol.⁴⁷ 1 mL of the QD/Neodol/chloroform solution blend was added to 20 mL of ultrapure water (18.2 $\text{M}\Omega\text{-cm}$ resistivity, $\text{pH} \sim 6.8$, Barnstead Nanopure Diamond System) to form an emulsion in which QDs solubilized in chloroform, constituted the dispersed phase and water formed the continuous phase. The emulsion was subsequently heated for 30 minutes at 90 °C so as to boil-off the chloroform (Fig. 4.4).

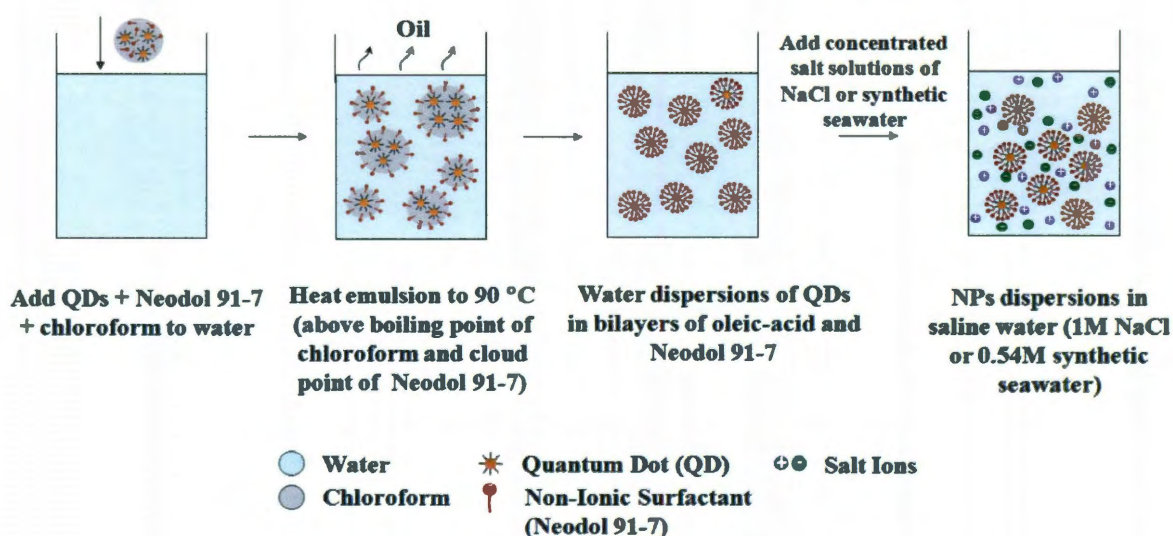


Figure 4.4: Schematic to formulate nanoparticle dispersions of QDs/Neodol 91-7 in saline water.

As the chloroform evaporated, the hydrophobic carbon chains (tail groups) of Neodol formed bilayers with oleic acid native to the QDs and the hydrophilic ethoxylated head groups project outwards towards water (denoted as QD/Neodol), rendering the QDs water-dispersible. QD/Neodol dispersions (pH 6.6) were diluted in pre-formulated stock solutions of salt so as to form dispersions of QD/Neodol in 1M NaCl and 0.55M synthetic seawater. Synthetic seawater is a solution of 3.5 mM CaCl₂, 5.5 mM MgCl₂, 19.8 mM KCl, 0.5M NaCl, 0.5 mM Na₂SO₄, and 2 mM NaHCO₃.^{5, 6} The pH value of the final QD/Neodol suspensions in 1M NaCl and synthetic seawater were 7.8, and 8.5, respectively. All chemicals for preparing stock solutions were procured from Merck. In all dispersions, the concentration of QDs was 4.5 μM and that of Neodol was 0.75g/L. It is to be noted that the phase-transfer of QDs, as reported in our earlier work, could be carried out directly in salt-containing water.⁴⁷ However, we found that the benefits of transfer in salt-containing water (higher phase-transfer yield, transfer of QDs as single-particles) as realized previously with a charged ionic surfactant (Aerosol-OT), diminished when carried out with a nonionic surfactant. Further, losses of salt due to crystallization at high phase-transfer temperature (90 °C) reduced the accuracy of final salt concentrations in the QD dispersions.

4.3.2 Characterization

4.3.2.1 Dynamic Light Scattering

The hydrodynamic diameter of QD/Neodol in different salt solutions was estimated across temperatures ranging from 6-70 °C by DLS. A Brookhaven ZetaPALS DLS instrument, with a BI-9000AT digital autocorrelator, a He-Ne Laser ($\lambda = 656$ nm) and a

temperature-stabilized sample holder was used for light scattering measurements. Samples were loaded in a stoppered quartz cuvette and pre-equilibrated at a specific temperature for at least 15 minutes. Sample measurements were made at a fixed scattering angle of 90°, over time intervals of 3 minutes and repeated at least 5 times for reliable statistics. Hydrodynamic diameters measured were number and volume-averaged and scattering data were fitted using CONTINS or NNLS fitting routines through the instrument software 9KDLSW. Number-based diameter (D_N) scales linearly with

diameter ($D_N = \frac{\sum D_i n_i}{\sum n_i}$) whereas volume-based diameter (D_V) scales as the cube of the

diameter ($D_V = \left(\frac{\sum D_i^3 n_i}{\sum n_i} \right)^{\frac{1}{3}}$), where n_i is the weighted mean of a sample population with

diameter D_i .⁶⁰ At temperatures below the cloud points of Neodol in respective DI and salt water environments, the number and volume-averaged diameters were in near agreement with each other. This indicated an absence of large aggregates in solution, when below the cloud point of Neodol.

It is also noteworthy that across all measurements below the cloud point of Neodol and in respective DI and salt water environments, bimodal populations were recorded. One of the populations that emerged consistently ranged between 5-9 nm. This population was lower than the theoretically estimated hydrodynamic diameter of QD/Neodol of ~ 12 nm (radius = core radius of QD = 1.6 nm, + linear length of oleic acid = 2.1 nm, + linear length of Neodol = 3.2 nm, – penetration depth of hydrophobic tail of Neodol ~ 1 nm) and was assigned to the population constituting empty micelles of Neodol. These were ascertained independently by making light scattering measurements

of control samples for plain Neodol (*i.e.*, Neodol without QDs), also prepared at 0.75 g/L and under respective conditions of salinities (DI water, 1M NaCl and 0.55M synthetic seawater). Thus, when below the cloud point, specific contributions from empty micelle populations were deducted so as to prevent underestimation of hydrodynamic diameter of QD/Neodol population. This bimodal nature of sample population ceased to exist at temperatures near the cloud points of Neodol in DI water (70 °C) and different salt environments (60°C for Neodol in 1M NaCl; 70 °C for Neodol in 0.55M synthetic seawater). Further, an increase in scattering counts from the laser and deviations between estimated number and volume-averaged hydrodynamic diameters indicated the onset of QD aggregation. It is noteworthy that although for the aforementioned cases where number and volume-averaged diameters differed, the order of magnitude sizes were similar and remained below 100 nm. That the phenomenon was found to be reversible (*i.e.*, upon cooling the solution, previously measured (and lower) hydrodynamic diameters of QD/Neodol were retained) confirmed QD aggregation at higher temperatures to correspond with micellar aggregation near the cloud point.

4.3.2.2 Zeta Potential

Zeta potential of QD/Neodol in DI water was estimated from electrophoretic mobility measurements using the phase analysis light scattering (PALS) feature of the Brookhaven ZetaPALS instrument. Measurements were made at 25 °C, using a dip-in electrode for aqueous solutions in 4 mL polystyrene cuvettes. Based on the particle size (12 nm) and salt concentration, the Smoluchowski approximations was used to determine zeta potential at $\sim -18 \pm 2$ mV. For QDs in high salinity solutions (1M NaCl and 0.55M synthetic seawater), measurements of zeta potentials were inconclusive on account of

poor reproducibility, and thus are not reported. This is also in line with assumptions behind theories for electrophoretic mobility that assume salts to be at low concentrations.

4.3.2.3 UV-vis Spectroscopy

Concentration of QDs was analyzed by UV-vis absorbance spectroscopy using a Shimadzu UV-vis (UV-24601 PC) spectrophotometer. 3-mL stoppered quartz cuvettes were used for QDs in chloroform; 1-mL quartz cuvettes or 4-mL polystyrene cuvettes were used for QDs in aqueous phase.

4.3.2.4 Transmission Emission Microscopy (TEM)

As-synthesized and phase transferred QDs were imaged using a JEOL 2010 transmission electron microscope, operating at a 100 kV accelerating beam voltage. Samples were drop-cast on holey carbon TEM grids (Ted Pella Inc) and dried overnight prior to imaging.

4.3.3 Breakthrough Studies

For breakthrough studies, packed columns of crushed calcite (Ward, Iceland spar 99.99% CaCO_3 106-250 μm) was set-up. The material was packed into glass columns (Omnifit borosilicate column, length (L) = 11 cm, inner diameter (d) = 1 cm) and connected to a syringe infusion pump (Harvard Apparatus Inc., Holliston MA) at the inlet. At the outlet, pre-weighed sample collection vials were placed to store solutions that underwent column breakthrough solutions (set-up shown in Fig. 4.5). The set-up was checked for leaks by flowing ultrapure water through the column at 8 mL/hr for 4 hours.

The pore volume (PV) of crushed calcite in the column was experimentally determined to be ~3.3 mL, employing a previously published tracer-based method using radioactive tritiated water ($^3\text{H}_2\text{O}$).⁶¹⁻⁶⁴ The water-filled porosity (ε) of the column material was estimated by the relation:

$$\varepsilon = \frac{\text{PV}}{\text{Column Volume}} \quad (4.10)$$

The porosity of calcite was estimated at 0.38. Further, the bulk density of calcite was estimated using the relation⁶²:

$$\varepsilon = 1 - \frac{\rho_b}{\rho_p} \quad (4.11)$$

Where ρ_p is the particle density of the column material (an intrinsic property). Using a particle density of calcite of 2.71 g/cc, the corresponding bulk density value was estimated at 1.67g/cc. Prior to each breakthrough run, the columns were flushed with a non-QD-containing salt solution for at least 4 hr so as to ensure equilibration with the column material before QD/Neodol in corresponding salt solutions were introduced. All volumetric flow rates (Q) used in this study were 8 mL/hr (corresponding to a Darcy velocity (v_d) of 2.44 m/d. The average linear pore velocity (v) was estimated from the relation:

$$v = \frac{v_d}{\varepsilon} = \frac{4Q}{\pi d^2 \varepsilon} \quad (4.12)$$

Where d is the inner diameter of the column (11 cm). The linear pore velocity of QD/Neodol in calcite was estimated at 6.4 m/d. It is noteworthy that Tomson and coworkers⁶⁵ and Weisner and coworkers⁶⁶⁻⁶⁸ among others⁶⁹⁻⁷² have reported velocity dependency of NP breakthrough and retention in columns. For most NPs, with the exception of fullerenes and their derivatives, NP retention by column material was found to increase as flow rates were lowered indicating that a higher residence time of NPs around the column material increased the probability of attachment. In our experiments, the operating velocity was selected to be the same or at least one order of magnitude lower than those previously used where NP attachment was observed. Hence we can consider our studies to be in a regime where velocity-induced effects for NP attachment are negligible in comparison to temperature-induced attachment effects.

Concentration of QDs in the column effluent (C_{exit}) was determined as a function of PV using UV-vis spectroscopy and the Beer-Lambert law with published size-dependent molar extinction coefficients of CdSe QDs.^{47, 73} Unless mentioned otherwise, the QD/Neodol dispersion was pumped through the column for 3.5 PV's before being replaced by the background salt solution. Flow of the salt solution was continued until no more QDs could be detected at the outlet (*i.e.*, $C_{\text{exit}} \sim 0$). Breakthrough curves, represented as plots of C_{exit}/C_0 (where C_0 representing the starting inlet concentration = 0.5 absorbance units) versus PV were subsequently created. For studies at higher temperatures, columns were immersed and equilibrated for 4 hours in a jacketed vessel, with temperature controlled by a Neslab RTE-111 waterbath. Transport coefficients (specifically retardation factor R , and dispersion coefficient D) were estimated by a 1D advection-convection model using the CXTFIT program (see Appendix C, Section C2).

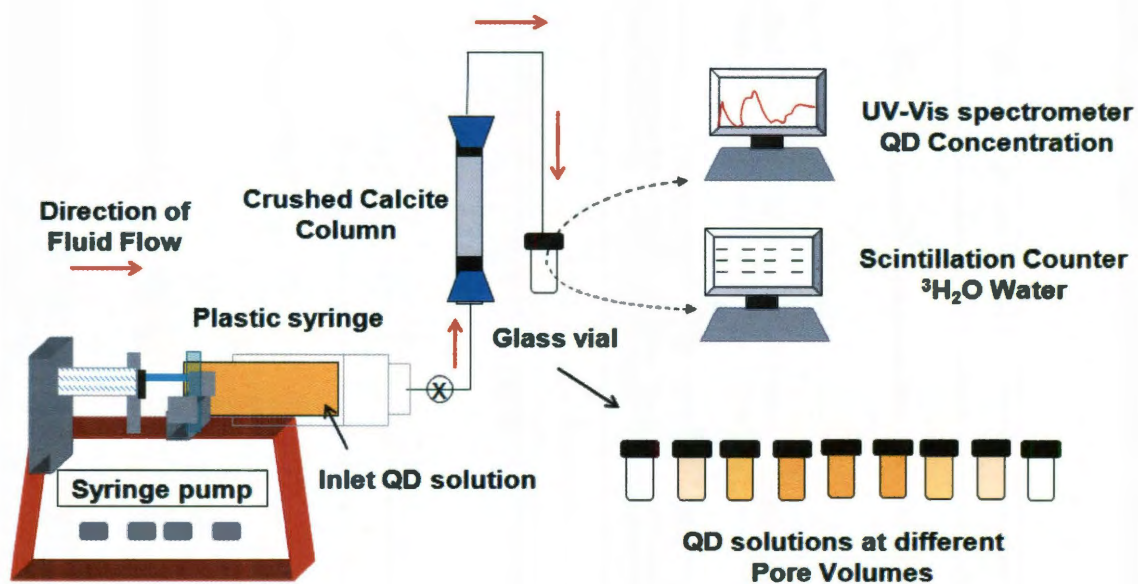


Figure 4.5: Experimental set-up of QD breakthrough studies through crushed calcite column.

4.3.3.1 Scintillation Counter

In tracer-breakthrough studies, the concentration of tritiated water ($^3\text{H}_2\text{O}$) was measured using a liquid scintillation counter (Beckman Instruments Inc., Fullerton CA). Tritiated water (Amersham Co.) diluted to an inlet concentration of $0.025 \mu\text{Ci/mL}$ ($1\mu\text{Ci} = 2.2 \times 10^6$ disintegrations per minute (DPM)) was flowed through a packed column at 8 mL/hr . Samples from the effluent stream were collected periodically in pre-weighed glass scintillation vials to which phenylxylylmethane-based liquid scintillation cocktails (Ready Safe, Beckman Coulter) were added at sample/cocktail ratios (v/v) of 0.1. The ratio of $^3\text{H}_2\text{O}$ concentration in the effluent (C) and $^3\text{H}_2\text{O}$ concentration before entering the packed column (C_0) was plotted against volume to obtain a tracer breakthrough curve (See Appendix C, Fig. C1).

4.4 Results and Discussions

4.4.1 Colloidal Properties of QDs/Neodol

Fig. 4.6 depicts the general preparation steps of aqueous dispersions of QDs (referred hereafter as "QD/Neodol") with three different salinities. The QDs were encapsulated by a bilayer of oleic acid and Neodol as per the procedure described in Fig. 4.4. For colloidal stability and breakthrough studies, aqueous QD/Neodol dispersions (~25 mL) were diluted in pre-formulated stock solutions (~ 25 mL) of salt so as to form dispersions of QD/Neodol in 1M NaCl and 0.55M synthetic seawater.^{5, 6} The final QD concentration in all solutions was 4.5 $\mu\text{mol-QD/L}$. The final Neodol concentration of 0.75 g/L was well above the critical micelle concentration of ~0.085 g/L in water^{51, 57}, such that Neodol micelles and Neodol-coated QDs co-existed in suspension (as detected via DLS). UV-vis spectroscopy and transmission electron microscopy (TEM) indicated the CdSe QDs were intact and undamaged after their transfer from chloroform to water and subsequent dilution in the various salt solutions (Fig. 4.7). The QD/Neodol dispersions at the various salinities were stable for several months (>3 months), with no visible signs of QD precipitation.

The stability of QDs in different salt environments and temperatures was studied by monitoring their hydrodynamic diameter (D_h) using dynamic light scattering (DLS) (Fig. 4.8). Both number and volume averaged hydrodynamic diameters were recorded. At room temperature and in DI water, QDs had a D_h of 11 ± 0.5 nm matching closely with the theoretically estimated D_h of QD/Neodol: $2 \times [1.6 \text{ nm (core radius of QD)} + 2.1 \text{ nm (linear length of oleic acid)} + 3.3 \text{ nm (linear length of Neodol),} - 1 \text{ nm (penetration depth of hydrophobic tail of Neodol)}] = 12 \text{ nm}$. This increased to 17 ± 1.2 nm at 70 °C. During

this clouding process with increasing temperature, the larger D_h values resulted from Neodol-coated QDs aggregating with other QDs and other Neodol micelles.

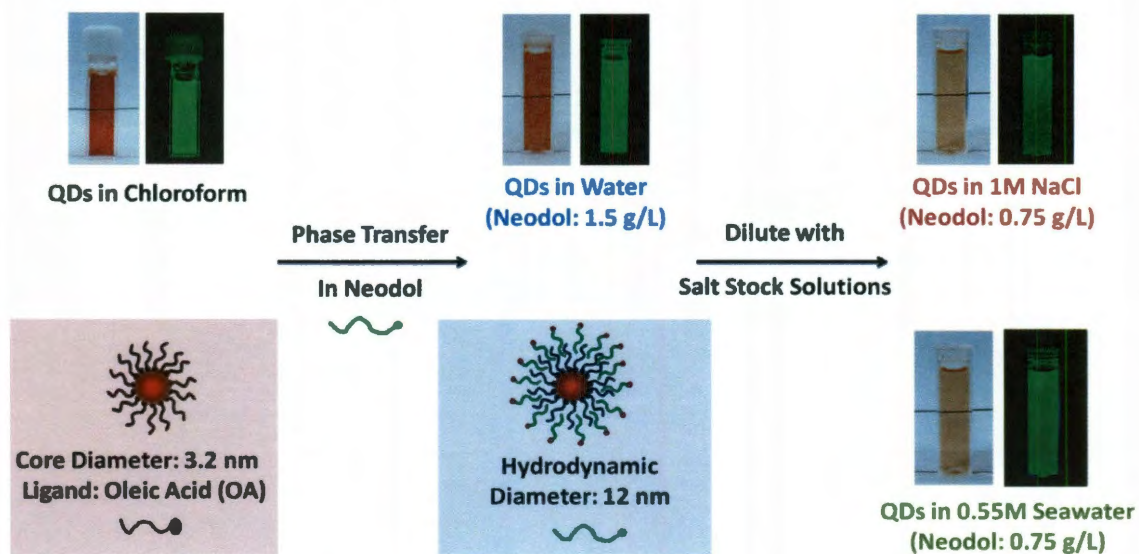


Figure 4.6: Phase-transfer of QDs from chloroform to water and different salt environments using bilayers of oleic acid and Neodol.

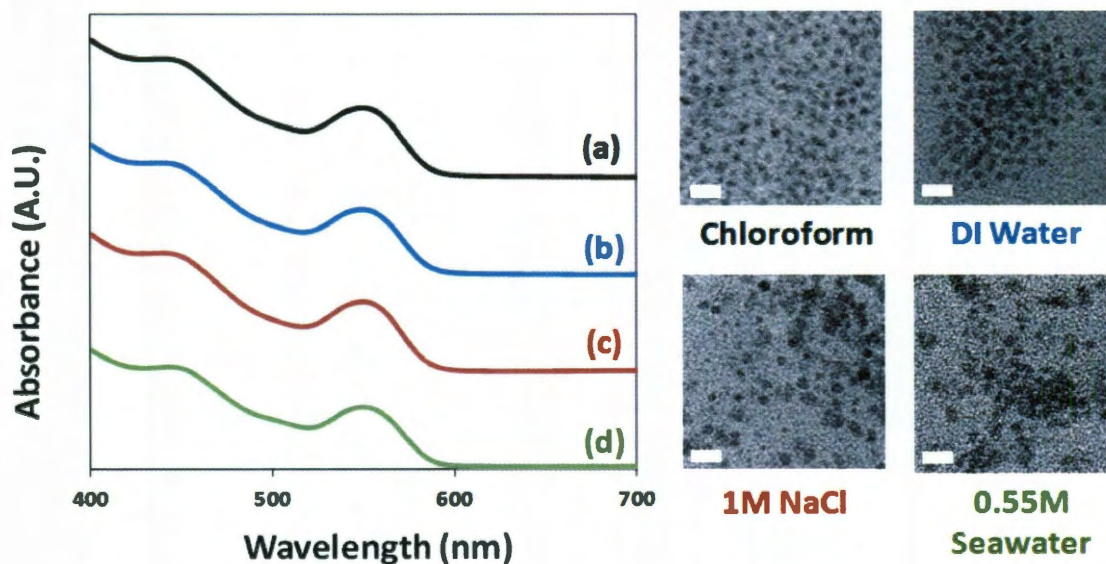


Figure 4.7: UV-vis spectra and TEM micrographs of QDs in chloroform and following phase-transfer to DI water and in various salt solutions. (All scale bars in TEM micrographs = 20 nm).

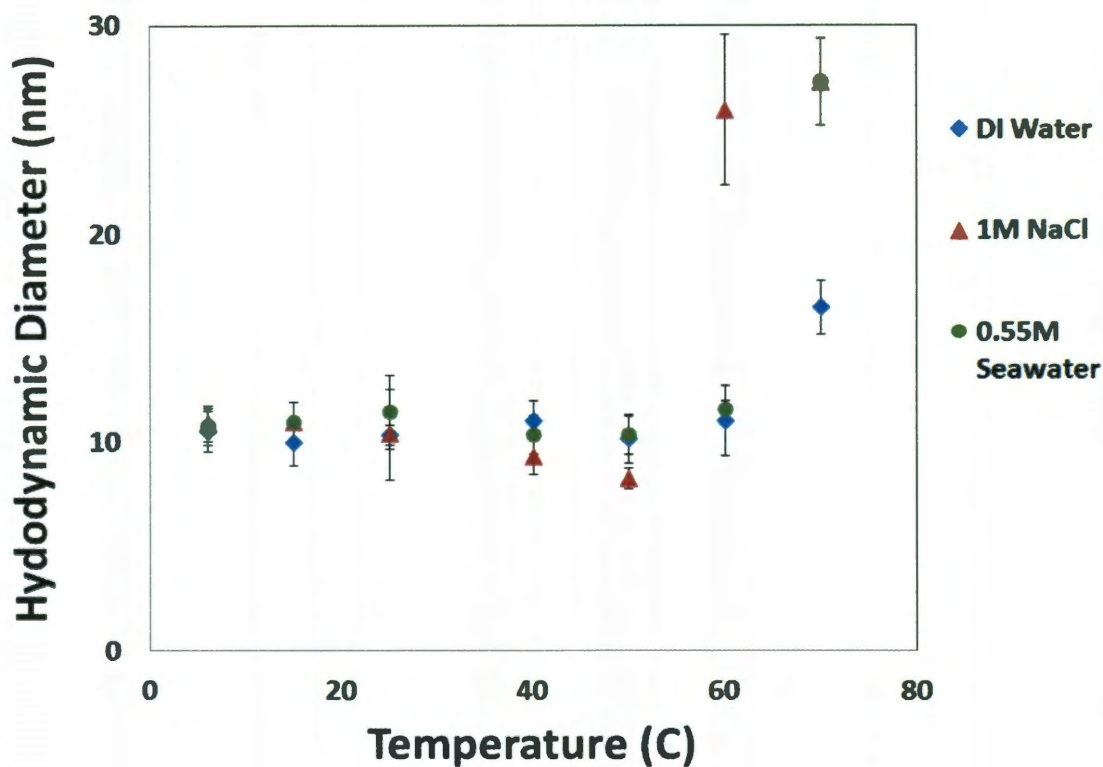


Figure 4.8: Hydrodynamic diameter of QD/Neodol as a function of temperature in water and in different salt environments. QD concentration in all DLS measurements was 4.5 μM and the Neodol concentration was 0.75 g/L.

When in synthetic seawater and 1M NaCl environments, the QDs had D_h values (~ 11 nm) similar to those in DI water, up to 60 $^{\circ}\text{C}$ and 50 $^{\circ}\text{C}$, respectively. Above these temperatures, aggregation of QDs occurred, leading to sizes of 27-29 nm. The QD suspensions in 1M NaCl, and synthetic seawater were similar (pH = 7.8 and 8.5, respectively), and so pH was likely not a factor in colloidal stability. Above their cloud points, the QD/Neodol dispersions were cloudy and opaque, and no settling was observed. Reducing the temperature below their cloud points caused the dispersions to revert to their clear and transparent forms, for which the original D_h values were

recovered. The aggregation of QD/Neodol was reversible, consistent with a different NP-nonionic surfactant system (silica NPs and Triton X-100).⁵²

The temperatures around which reversible aggregation occurred were coincident with the cloud point temperatures of the Neodol-only solutions in DI water, synthetic seawater, 1M NaCl, (determined to be ~70, ~70, and ~58 °C, respectively, via DLS and visual observation). The cloud points were depressed in the presence of 1M NaCl due to "salting-out" effects that make poly(ethylene oxide)-based nonionic surfactants easier to dehydrate.^{50, 51, 74, 75} Interestingly, the cloud point of Neodol in synthetic seawater did not differ from that of Neodol in DI water, in spite of the large quantity of salt (0.55M ionic strength). This non-effect may be due to the presence of "salting-in" electrolytes (MgCl₂, CaCl₂) that elevate the cloud point temperature and counteract the effect of "salting-out" electrolytes (NaCl, KCl, Na₂SO₄).⁵⁰ The measured cloud point of Neodol in DI water was lower than the reported value of 74 °C, perhaps due to the presence of Neodol surfactant of other chain lengths.⁵⁷

It is noteworthy that across all measurements below the cloud point of Neodol and in respective DI and saline environments, bimodal populations were recorded. One of the populations that emerged consistently ranged between 5-9 nm. This population was lower than the theoretically estimated hydrodynamic diameter of QD/Neodol of ~ 12 nm and was assigned to the population constituting empty micelles of Neodol. These were ascertained independently by making light scattering measurements of control samples for plain Neodol (*i.e.*, Neodol without QDs), also prepared at 0.75 g/L and under respective conditions of salinities (DI water, 1M NaCl and 0.55M synthetic seawater). Thus, when below the cloud point, specific contributions from empty micelle populations

were deducted so as to prevent underestimation of hydrodynamic diameter of QD/Neodol population. Furthermore, number and volume averaged hydrodynamic diameters were similar, indicating an absence of large aggregates.

This bimodal nature of sample population ceased to exist at temperatures at and above the cloud points of Neodol in DI water (70 °C) and different salt environments (58°C for Neodol in 1M NaCl, 70 °C for Neodol in 0.55M synthetic seawater). At such temperatures, scattering counts of the laser increased significantly and deviations between number and volume-averaged hydrodynamic diameters emerged, indicating onset of QD aggregation. Although number and volume-averaged diameters differed at the aforementioned temperatures, the order of magnitude of the diameters was similar and remained well below 100 nm.

4.4.2 Transport and Breakthrough of QD/Neodol through Packed Calcite Column

Calcite and dolomite are calcium carbonate minerals that account for over 60% of world reservoir formations, storing over 60% of proven oil reserves and 40% of proven natural gas reserves.⁵⁷ Silica-rich sandstone formations constitute the other significant reservoir variant. The natural affinity of alkyl ethoxylates to adsorb strongly to sandstone, particularly nearing their cloud points, is well known in surfactant literature.⁷⁶ The use of ethoxylated nonionics in sandstone reservoirs is thereby not practiced in areas of enhanced oil recovery⁷⁷ (see Appendix C, Section C3) transport and breakthrough of QD/Neodol through quartz sand).

Column studies of QD/Neodol in 0.55M synthetic seawater and 1M NaCl were carried out at temperatures of 25 °C, 50 °C, and 70 °C (Table 4.1). These conditions are

much harsher than those commonly used in packed column studies involving NP transport, *i.e.*, at low salinities (~ 100 mM or lower NaCl) and at room temperature.^{46, 61, 66-68, 72, 78-81} A synthetic seawater suspension of QD/Neodol was passed through the calcite packed column at different temperatures (Fig. 4.9a). At room temperature, the QDs achieved breakthrough at 1 pore volume (PV), defined at which the measured outlet QD concentration reaches 50% of the inlet concentration (*i.e.*, $C_{\text{exit}}/C_0 = 50\%$). This breakthrough behavior was similar to that of tritiated water flowing with 0.55M synthetic seawater through the calcite at room temperature (see Appendix C, Fig. C1). Tritiated water is considered an ideal tracer compound that does not interact with the carrier fluid or with the column material.⁶¹⁻⁶⁴ C_{exit}/C_0 of QD/Neodol reached $\sim 100\%$ at 1.5 PV's, indicative of complete breakthrough, and remained there until the QD/Neodol suspension flow was replaced by synthetic seawater. This switch was made at 3.5 PV's, unless mentioned otherwise. After C_{exit}/C_0 reached $\sim 0\%$, UV-vis analysis of the collected QD suspension indicated most of the particles ($\sim 96\%$) passed through the column with minor loss (Table 4.2). This loss of Neodol-coated QDs is due to a small fraction of QD/Neodol that show irreversible adsorption affinity onto calcite surfaces through hydrogen-bond interactions.⁸²

At the higher temperatures of 50 and 70 °C, the QDs achieved breakthrough between 1.1-1.3 PV's, and reached $\sim 100\%$ at 1.5-1.6 PV's. Most of the QDs ($>93\%$) also passed through the column without significant loss to the calcite column, indicating minor interaction with the column material at the higher temperatures (Table 4.2). When a 1M NaCl suspension of QD/Neodol was studied in the same manner at different temperatures (Fig. 4.9b), QD breakthrough of 50% occurred at nearly similar PVs (~ 1.1)

for all temperatures. While in the room temperature run, total C_{exit}/C_0 breakthrough of 100% occurred at ~ 1.25 PV's and remained steady until the inlet stream was replaced with NaCl at 3.3 PV. Roughly 91% of QDs were recovered, indicating that a larger fraction of QDs was retained compared to the synthetic seawater case.

Table 4.1: Parameters used for QD/Neodol breakthrough experiments.

Parameter	Value	Remarks
Column Length (L)	11 cm	--
Column Inner Diameter (d)	1 cm	--
Pore Volume (PV)	3.3 mL	PV estimated from tritiated water breakthrough experiments ⁶¹⁻⁶⁴
Porosity (ϵ)	0.38	Eq. 4.10
Soil particle radius (a_c)	106-250 μm	--
Particle density (ρ_p)	2.71 g/cc	--
Bulk density (ρ_b)	1.39 g/cc	Eq. 4.11
Volumetric flow rate (Q)	8 mL/hr	
Darcy velocity (v_d)	2.44 m/d	Eq. 4.12
Linear pore velocity	6.4 m/d	Eq. 4.12
Background salinity	1M NaCl and 0.55M synthetic seawater	
Temperature	25, 50 and 70 °C	--

Unusually, C_{exit}/C_0 reached maximum values of 125% and 138% at 50 °C and 70 °C, respectively, before falling to ~100-105%. QD recovery was 91-93% at all temperatures tested, indicating the loss of QDs were comparable (Table 4.2). The recovery was slightly lower when compared to corresponding cases where seawater is the background solution. That the suspension became more concentrated at higher temperatures in 1M NaCl background is suggestive that the kinetics of QD adsorption and desorption became more rapid at the higher temperatures, such that QDs accumulated within the first PV before releasing into the carrier fluid. Perhaps the QDs in the synthetic seawater case did not exhibit this behavior because Neodol had a lower solubility in 1M NaCl than in synthetic seawater, as evidenced by its cloud point being lower in 1M NaCl than in synthetic seawater.

Table 4.2: Percent recovery of QDs from calcite packed columns at different temperatures.

Carrier Fluid	25 °C	50 °C	70 °C
0.55M synthetic seawater	96	94	97
1M NaCl	91	93	92

The larger but similar D_h values of QDs in 1M NaCl and in synthetic seawater at 70 °C suggested that the >100% values of C_{exit}/C_0 were on account of the predominant effect brought about from the salting-out action by Na^+ ions. Alongside depressing the cloud point of Neodol, the salting-out effect would enhance adsorption of Neodol onto the

surface of calcite that would result in QDs encapsulated in bilayers of Neodol to deposit onto the calcite surface. That the nature of Neodol adsorption is partial and reversible is evident from subsequent QD release, as empty micelles of Neodol exchange with QD/Neodol previously associated with calcite. The more gradual nature of release at the 70 °C run compared to the 50 °C case is consistent with the proposed mechanism, since adsorption at and beyond the cloud point gets stronger as more number of ethoxylated groups on Neodol, that previously hydrogen-bonded with water, is now available for binding onto calcite.

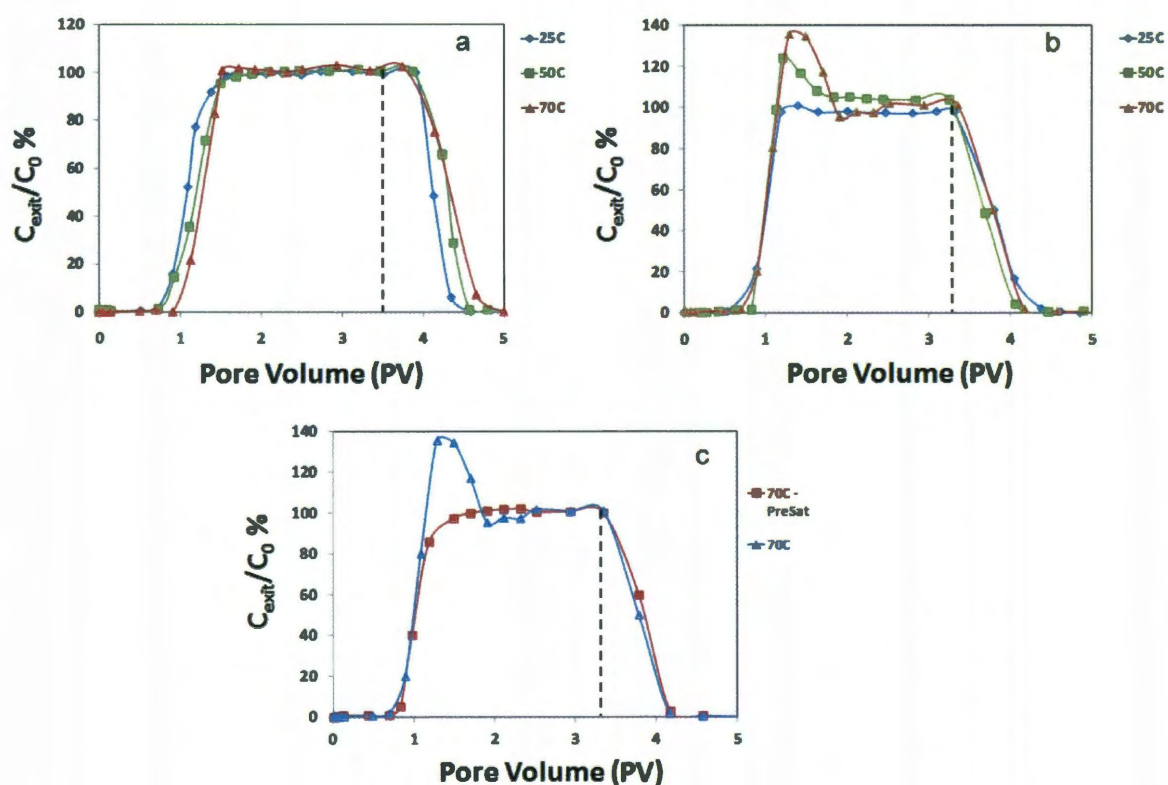


Figure 4.9: Breakthrough profiles of QD/Neodol in (a) 0.55M synthetic seawater and (b) 1M NaCl. A salt solution, passing through the column, is switched to the QD/Neodol suspension in the same salt solution at PV = 0. At PV ~ 3.0-3.5 (marked by a dashed vertical line), the QD/Neodol suspension is replaced by the same salt solution. (c) Breakthrough profiles of QD/Neodol at 70 °C in 1M NaCl background solution after

calcite is pre-saturated by solutions of 1M NaCl and 0.75 g/L Neodol/1M NaCl. The error bars on C_{exit}/C_0 were $\pm 2\%$.

To ascertain that the overshoot of C_{exit}/C_0 at higher temperatures was due to an adsorption based mechanism, a separate experiment was carried out where the calcite column was flushed with 1M NaCl solution containing Neodol at 0.75 g/L at 70 °C (instead of a plain 1M NaCl solution at the same temperature) prior to switching to a QD/Neodol suspension flow at $PV = 0$. The resulting breakthrough curve showed that C_{exit}/C_0 did not exceed 100%, and the QD recovery was $\sim 95\%$ (Fig. 4.9c). Similar behavior and QD recovery values were observed at 25 and 50 °C and indicated significant reduction in partial retention of QDs within calcite, when surface adsorption sites were pre-saturated with Neodol.

4.4.3 Modeling Transport and Breakthrough of QD/Neodol through Packed Calcite Column

Transport and breakthrough of QD/Neodol through packed porous columns can be described by the 1-D advection-dispersion equation⁶²:

$$R \frac{\partial C}{\partial t} = D \frac{\partial^2 C}{\partial x^2} - v \frac{\partial C}{\partial x} - \gamma C \quad (4.13)$$

Where: C represents concentration of NPs, t and x are the NP travel time and distance and v represents the linear flow velocity (also called the average pore-water velocity).

The term R, known as the retardation factor, is defined as:

$$R = 1 + \frac{\rho_b k_d}{\varepsilon} \quad (4.14)$$

Where ρ_b = soil bulk density, k_d = is an empirical distribution coefficient, alternately termed the partition coefficient and ε = porosity of column material. The distribution coefficient k_d emerges from the assumption of a linear adsorption relationship between the change in the amount of NP adsorbed (dq) on the porous media per unit mass of solid weight with respect to change in concentration (dC) of NP that flows. Hence, for a linear relationship of the form $q = k_d C$, the distribution coefficient in Eq. 4.14 is represented as

$k_d = \frac{dq}{dC}$. The retardation factor physically represents the interaction of transporting NP

with column material. From Eq. 4.14, R assumes a value of unity when k_d tends to zero, thereby representing no adsorption or non-interaction of NPs with the column material.

The other terms in Eq. 4.13, namely D and γ represent the dispersion coefficient and first-order removal rate constant respectively. The C_{exit}/C_0 for all studies attained values of unity and higher suggesting that γ is negligible ($\gamma \sim 0$). The CXTFIT routine was used to fit experimental breakthrough profiles (without the washout portion), by minimizing sums of least squares between experimental data and theoretical values of the analytical solution of Eq. 4.13, using R and D as fitting parameters (see Appendix C, Section C1 for details of curve fitting procedure).⁸³

When in synthetic seawater background, the progressive delay in breakthrough with temperature was captured by an increase in R (1.072 to 1.238) and a corresponding increase of the distribution coefficient k_d of QD/Neodol (0.0197 to 0.0437 ml/g) onto calcite (Table 4.3 and Fig. 4.10). These indicate temperature-dependent increase in

interactions and adsorption of QD/Neodol with calcite. The dispersion values increased from 0.028 to 0.08 cm² min⁻¹, but did not increase significantly between 50 and 70 °C where size increased from 12 nm to ~ 25 nm, suggesting dispersion to be temperature but not size dependent. Such dependency has been observed for tritiated water and other tracers.⁶²⁻⁶⁴ The R and k_d values are low relative to those reported in literature: these along with high total breakthrough (C_{exit}/C₀) of 100% and overall QD recovery of >95% show the efficacy of the Neodol coating in successful QD transport through porous media.

In 1M NaCl background and at room temperature, R and D coefficients of QD/Neodol (Fig. 4.10c, R = 1.001, D = 0.069 cm² min⁻¹) were similar to that of an ideal tracer such as tritiated water (Appendix C, Fig. C1, R = 1, D = 0.012 cm² min⁻¹). At higher temperatures, C_{exit}/C₀ was well over 100%, pointing to partial adsorption and release of QDs. Determining transport coefficients for these cases is beyond the scope of the CXTFIT routine. That the adsorption could be reduced by pre-saturating the calcite with Neodol was demonstrated at 70 °C by pre-flowing Neodol in 1M NaCl. Previously seen >100% C_{exit}/C₀ was seen to reduce to near 100% (Fig. 4.11) and transport coefficients evaluated showed increase in R and D (R = 1.11, D = 0.06 cm² min⁻¹) pointing to temperature induced adsorption and dispersion effects as previously seen in seawater.

It is interesting to note that although the D_h and cloud points of QD/Neodol in 1M NaCl were more responsive to temperature than in seawater, it did not translate to higher R values than those observed in seawater. These points to greater interparticle interactions between QD/Neodol in 1M NaCl than in seawater. This suggests that

QD/Neodol adsorption onto calcite in 1M NaCl background is not restricted to a monolayer. Interparticle attraction can lead to QD/Neodol stacking onto calcite leading to a buildup of NPs followed by exchange with empty micelles that gives the high values of overshoot. By saturating adsorption sites with Neodol, QD/Neodol attachment onto calcite initially as a monolayer and subsequently as multiple layers is circumvented.

Table 4.3: Transport coefficients of QD/Neodol flow through calcite packed columns.

Carrier Fluid (Flow Material)	Temperature	R	D (cm² min⁻¹)	k_d (mL g⁻¹)
0.55M Synthetic Seawater (Tritiated Water)	25 °C	1.0001	0.012	0
	70 °C	1.0003	0.020	0
0.55M Synthetic Seawater (QD/Neodol)	25 °C	1.072	0.069	0.0197
	50 °C	1.16	0.078	0.0437
	70 °C	1.238	0.082	0.0651
1M NaCl (QD/Neodol)	25 °C	1.001	0.039	0.003
	70 °C	1.118	0.06	0.0323

* Transport coefficients estimated for QD breakthrough when calcite was pre-saturated at 70 °C with 1M NaCl and 0.75 g/L Neodol.

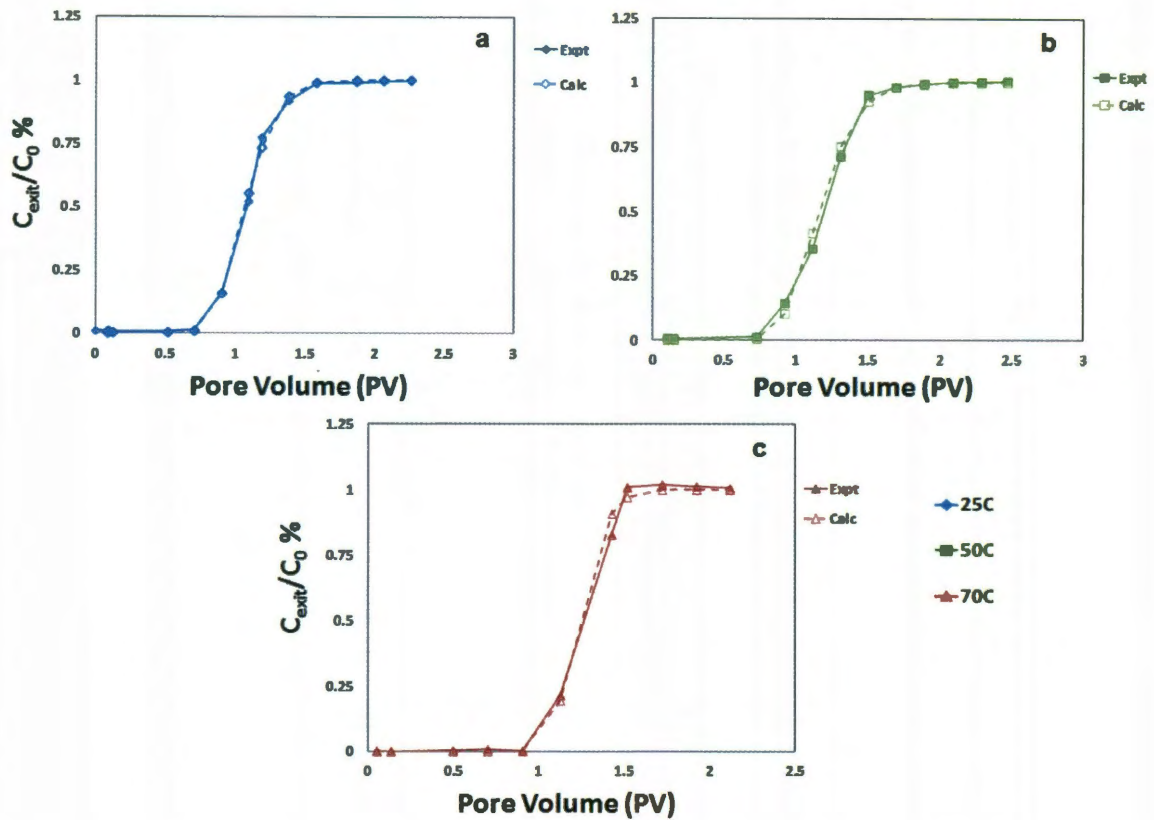


Figure 4.10: Experimental and fitted results for transport of QD/Neodol through crushed calcite in synthetic seawater background at (a) 25 °C (b) 50 °C (c) 70 °C.

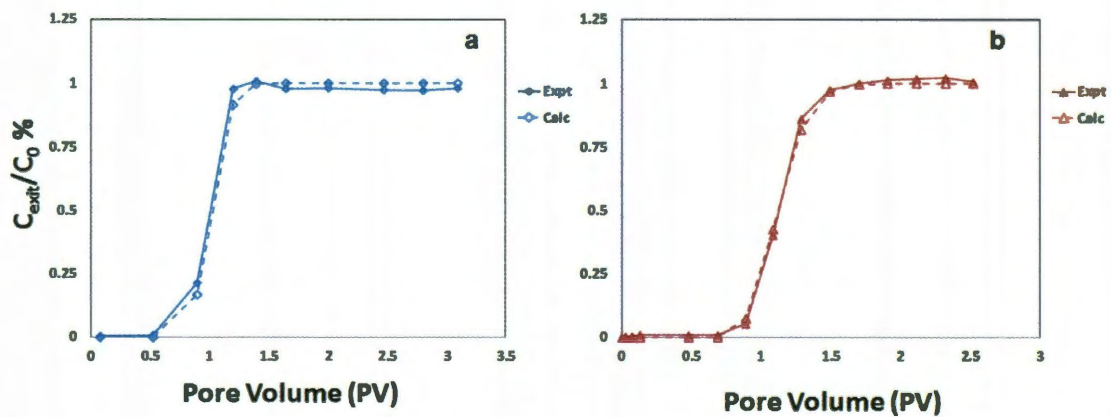


Figure 4.11: Experimental and fitted results for transport of QD/Neodol through crushed calcite in: (a) 1M NaCl background at 25 °C (b) 1M NaCl background at 70 °C upon pre-saturation with Neodol.

4.5 Conclusions

We showed that by coating NPs with Neodol nonionic surfactant, high stability to QD aggregation and successful transport through crushed calcite (100% breakthrough, > 95% QD recovery) could be obtained at salinity and temperature conditions, representative of a reservoir. To achieve this, the cloud point of the selected Neodol (74 °C) was above the temperature of application (70 °C). The type of background salinity was seen to affect the cloud point of Neodol - In seawater, the competing effects of salting-out and salting-in types of ions ensured high temperature stability of QDs, resulting in low adsorption onto calcite and high QD recovery (> 95%). In a 1M NaCl background, the salting-out action by Na⁺ ions was seen to lower the cloud point of Neodol, inducing strong partial adsorption of QD/Neodol onto calcite and interparticle attraction, thus resulting in an overshoot type release with relatively lower QD recovery (92%) at 70 °C. Observed overshoot was eliminated and higher (>95%) QD recovery was realized upon pre-saturating surface adsorption sites on calcite with a background solution of Neodol/1M NaCl.

4.6 References

1. Johnson, K., Nanoscale Technologies Leap Frog from Science Fiction into Real World Engineering. *The American Oil and Gas Reporter* 2010, pp 112-123.
2. Chapman, D.; Nelson-Thomas, C., Thing big, get small. *Exploration and Production Magazine* 2010, pp 50-53.
3. Barron, A. R.; Tour, J. M.; Busnaina, A.; Jung, Y. J.; Somu, S.; Kanj, M. Y.; Potter, D.; Resasco, D. E.; J., U., Big things in small packages. *Oilfield Review* **2010**, 3, (22), 38-49.
4. Gilbert, R. B.; Lake, L. W.; Jablonowski, C. J.; Jennings, J. W.; Nunez, E. J., A Procedure for Assessing the Value of Oilfield Sensors. *SPE Reservoir Evaluation & Engineering* **2009**, 12, (4), 618-629.
5. Berlin, J. M.; Yu, J.; Lu, W.; Walsh, E. E.; Zhang, L. L.; Zhang, P.; Chen, W.; Kan, A. T.; Wong, M. S.; Tomson, M. B.; Tour, J. M., Engineered nanoparticles for hydrocarbon detection in oil-field rocks. *Energy & Environmental Science* **2010**, 4, (2), 505-509.
6. Yu, J.; Berlin, J. M.; Lu, W.; Zhang, L. L.; Kan, A. T.; Zhang, P.; Walsh, E. E.; Work, S. N.; Chen, W.; Tour, J. M.; Wong, M. S.; Tomson, M. B., Transport Study of Nanoparticles for Oilfield Application. In *SPE International Conference on Oilfield Scale*, Aberdeen, U.K., 2010.
7. Stuart, M. A. C.; Huck, W. T. S.; Genzer, J.; Muller, M.; Ober, C.; Stamm, M.; Sukhorukov, G. B.; Szleifer, I.; Tsukruk, V. V.; Urban, M.; Winnik, F.; Zauscher, S.; Luzinov, I.; Minko, S., Emerging applications of stimuli-responsive polymer materials. *Nature Materials* **2010**, 9, (2), 101-113.
8. Saunders, A. E.; Koo, B.; Wang, X. Y.; Shih, C. K.; Korgel, B. A., Structural characterization and temperature-dependent photoluminescence of linear CdTe/CdSe/CdTe heterostructure nanorods. *ChemPhysChem* **2008**, 9, (8), 1158-1163.
9. Selvarasah, S.; Busnaina, A.; Dokmeci, M. R., Design, Fabrication, and Characterization of Three-Dimensional Single-Walled Carbon Nanotube Assembly and Applications As Thermal Sensors. *IEEE Transactions on Nanotechnology* **2010**, 10, (1), 13-20.

10. Wright, S. A.; Gianchandani, Y. B., Discharge-Based Pressure Sensors for High-Temperature Applications Using Three-Dimensional and Planar Microstructures. *Journal of Microelectromechanical Systems* **2009**, *18*, (3), 736-743.
11. Korgel, B. A., Semiconductor Nanowires: A Chemical Engineering Perspective. *AIChE Journal* **2009**, *55*, (4), 842-848.
12. Dirmyer, M. R.; Martin, J.; Nolas, G. S.; Sen, A.; Badding, J. V., Thermal and Electrical Conductivity of Size-Tuned Bismuth Telluride Nanoparticles. *Small* **2009**, *5*, (8), 933-937.
13. Seiffert, S.; Thiele, J.; Abate, A. R.; Weitz, D. A., Smart Microgel Capsules from Macromolecular Precursors. *Journal of the American Chemical Society* **2010**, *132*, (18), 6606-6609.
14. Javadpour, F.; Fisher, D., Nanotechnology-based micromodels and new image analysis to study transport in porous media. *Journal of Canadian Petroleum Technology* **2008**, *47*, (2), 30-37.
15. Li, J. X.; Yang, L. X.; Luo, S. L.; Chen, B. B.; Li, J.; Lin, H. L.; Cai, Q. Y.; Yao, S. Z., Polycyclic Aromatic Hydrocarbon Detection by Electrochemiluminescence Generating Ag/TiO₂ Nanotubes. *Analytical Chemistry* **2010**, *82*, (17), 7357-7361.
16. Cooper, J. S.; Raguse, B.; Chow, E.; Hubble, L.; Muller, K. H.; Wieczorek, L., Gold Nanoparticle Chemiresistor Sensor Array that Differentiates between Hydrocarbon Fuels Dissolved in Artificial Seawater. *Analytical Chemistry* **2010**, *82*, (9), 3788-3795.
17. Ibele, M.; Mallouk, T. E.; Sen, A., Schooling Behavior of Light-Powered Autonomous Micromotors in Water. *Angewandte Chemie-International Edition* **2009**, *48*, (18), 3308-3312.
18. Sen, A.; Ibele, M.; Hong, Y.; Velegol, D., Chemo and phototactic nano/microbots. *Faraday Discussions* **2009**, *143*, 15-27.
19. Chen, S. S.; Moore, A. L.; Cai, W. W.; Suk, J. W.; An, J. H.; Mishra, C.; Amos, C.; Magnuson, C. W.; Kang, J. Y.; Shi, L.; Ruoff, R. S., Raman Measurements of Thermal Transport in Suspended Monolayer Graphene of Variable Sizes in Vacuum and Gaseous Environments. *ACS Nano* **2011**, *5*, (1), 321-328.

20. Lai, X. Y.; Li, J.; Korgel, B. A.; Dong, Z. H.; Li, Z. M.; Su, F. B.; Du, J. A.; Wang, D., General Synthesis and Gas-Sensing Properties of Multiple-Shell Metal Oxide Hollow Microspheres. *Angewandte Chemie-International Edition* **2011**, 50, (12), 2738-2741.

21. Alonso, U.; Missana, T.; Patelli, A.; Ceccato, D.; Albarran, N.; Garcia-Gutierrez, M.; Lopez-Torrubia, T.; Rigato, V., Quantification of Au nanoparticles retention on a heterogeneous rock surface. *Colloids and Surfaces A-Physicochemical and Engineering Aspects* **2009**, 347, (1-3), 230-238.

22. Kotsmar, C.; Yoon, K. Y.; Yu, H. Y.; Ryoo, S. Y.; Barth, J.; Shao, S.; Prodanovic, M.; Milner, T. E.; Bryant, S. L.; Huh, C.; Johnston, K. P., Stable Citrate-Coated Iron Oxide Superparamagnetic Nanoclusters at High Salinity. *Industrial & Engineering Chemistry Research* **2010**, 49, (24), 12435-12443.

23. Ingram, D. R.; Kotsmar, C.; Yoon, K. Y.; Shao, S.; Huh, C.; Bryant, S. L.; Milner, T. E.; Johnston, K. P., Superparamagnetic nanoclusters coated with oleic acid bilayers for stabilization of emulsions of water and oil at low concentration. *Journal of Colloid and Interface Science* **2010**, 351, (1), 225-232.

24. Heitsch, A. T.; Smith, D. K.; Patel, R. N.; Ress, D.; Korgel, B. A., Multifunctional particles: Magnetic nanocrystals and gold nanorods coated with fluorescent dye-doped silica shells. *Journal of Solid State Chemistry* **2008**, 181, (7), 1590-1599.

25. Mehrmohammadi, M.; Yoon, K. Y.; Qu, M.; Johnston, K. P.; Emelianov, S. Y., Enhanced pulsed magneto-motive ultrasound imaging using superparamagnetic nanoclusters. *Nanotechnology* **2011**, 22, (4), 8.

26. Qian, M. C.; Reber, A. C.; Ugrinov, A.; Chaki, N. K.; Mandal, S.; Saavedra, H. M.; Khanna, S. N.; Sen, A.; Weiss, P. S., Cluster-Assembled Materials: Toward Nanomaterials with Precise Control over Properties. *ACS Nano* **2010**, 4, (1), 235-240.

27. Matson, M. L.; Wilson, L. J., Nanotechnology and MRI contrast enhancement. *Future Medicinal Chemistry* **2010**, 2, (3), 491-502.

28. Chaturvedi, N.; Hong, Y. Y.; Sen, A.; Velegol, D., Magnetic Enhancement of Phototaxing Catalytic Motors. *Langmuir* **2010**, 26, (9), 6308-6313.

29. Hong, Y. Y.; Diaz, M.; Cordova-Figueroa, U. M.; Sen, A., Light-Driven Titanium-Dioxide-Based Reversible Microfireworks and Micromotor/Micropump Systems. *Advanced Functional Materials* **2010**, 20, (10), 1568-1576.
30. Schrick, B.; Hydutsky, B. W.; Blough, J. L.; Mallouk, T. E., Delivery vehicles for zerovalent metal nanoparticles in soil and groundwater. *Chemistry of Materials* **2004**, 16, (11), 2187-2193.
31. Sundararajan, S.; Lammert, P. E.; Zudans, A. W.; Crespi, V. H.; Sen, A., Catalytic motors for transport of colloidal cargo. *Nano Letters* **2008**, 8, (5), 1271-1276.
32. Sundararajan, S.; Sengupta, S.; Ibele, M. E.; Sen, A., Drop-Off of Colloidal Cargo Transported by Catalytic Pt-Au Nanomotors via Photochemical Stimuli. *Small* **2010**, 6, (14), 1479-1482.
33. Ibele, M. E.; Lammert, P. E.; Crespi, V. H.; Sen, A., Emergent, Collective Oscillations of Self-Mobile Particles and Patterned Surfaces under Redox Conditions. *ACS Nano* **2010**, 4, (8), 4845-4851.
34. Adams, M. L.; Loncar, M.; Scherer, A.; Qiu, Y. M., Microfluidic integration of porous photonic crystal nanolasers for chemical sensing. *IEEE Journal on Selected Areas in Communications* **2005**, 23, (7), 1348-1354.
35. Park, S.; An, J.; Suk, J. W.; Ruoff, R. S., Graphene-Based Actuators. *Small* **2010**, 6, (2), 210-212.
36. Aguilar, C. A.; Haight, R.; Mavrokefalos, A.; Korgel, B. A.; Chen, S. C., Probing Electronic Properties of Molecular Engineered Zinc Oxide Nanowires with Photoelectron Spectroscopy. *ACS Nano* **2009**, 3, (10), 3057-3062.
37. Babinec, T. M.; Hausmann, B. J. M.; Khan, M.; Zhang, Y. A.; Maze, J. R.; Hemmer, P. R.; Loncar, M., A diamond nanowire single-photon source. *Nature Nanotechnology* **2010**, 5, (3), 195-199.
38. Gianchandani, Y. B.; Wright, S. A.; Eun, C. K.; Wilson, C. G.; Mitra, B., Exploring microdischarges for portable sensing applications. *Analytical and Bioanalytical Chemistry* **2009**, 395, (3), 559-575.

39. Greswell, R. B.; Rahman, S. H.; Cuthbert, M. O.; Tellam, J. H., An inexpensive flow-through laser nephelometer for the detection of natural colloids and manufactured nanoparticles. *Journal of Hydrology* **2010**, 388, (1-2), 112-120.
40. Jung, Y. J.; Kar, S.; Talapatra, S.; Soldano, C.; Viswanathan, G.; Li, X. S.; Yao, Z. L.; Ou, F. S.; Avadhanula, A.; Vajtai, R.; Curran, S.; Nalamasu, O.; Ajayan, P. M., Aligned carbon nanotube-polymer hybrid architectures for diverse flexible electronic applications. *Nano Letters* **2006**, 6, (3), 413-418.
41. Lavigne, J. J.; Savoy, S.; Clevenger, M. B.; Ritchie, J. E.; McDoniel, B.; Yoo, S. J.; Anslyn, E. V.; McDevitt, J. T.; Shear, J. B.; Neikirk, D., Solution-based analysis of multiple analytes by a sensor array: Toward the development of an "electronic tongue". *Journal of the American Chemical Society* **1998**, 120, (25), 6429-6430.
42. Sohn, Y. S.; Goodey, A.; Anslyn, E. V.; McDevitt, J. T.; Shear, J. B.; Neikirk, D. P., A microbead array chemical sensor using capillary-based sample introduction: toward the development of an "electronic tongue". *Biosensors & Bioelectronics* **2005**, 21, (2), 303-312.
43. Seo, K.; Wober, M.; Steinvurzel, P.; Schonbrun, E.; Dan, Y. P.; Ellenbogen, T.; Crozier, K. B., Multicolored Vertical Silicon Nanowires. *Nano Letters* **2011**, 11, (4), 1851-1856.
44. Yilmaz, C.; Kim, T. H.; Somu, S.; Busnaina, A. A., Large-Scale Nanorods Nanomanufacturing by Electric-Field-Directed Assembly for Nanoscale Device Applications. *IEEE Transactions on Nanotechnology* **2010**, 9, (5), 653-658.
45. Duque, J. G.; Pasquali, M.; Schmidt, H. K., Antenna Chemistry with Metallic Single-Walled Carbon Nanotubes. *Journal of the American Chemical Society* **2008**, 130, (46), 15340-15347.
46. Petosa, A. R.; Jaisi, D. P.; Quevedo, I. R.; Elimelech, M.; Tufenkji, N., Aggregation and Deposition of Engineered Nanomaterials in Aquatic Environments: Role of Physicochemical Interactions. *Environmental Science & Technology* **2010**, 44, (17), 6532-6549.
47. Bagaria, H. G.; Kini, G. C.; Wong, M. S., Electrolyte Solutions Improve Nanoparticle Transfer from Oil to Water. *Journal of Physical Chemistry C* **2010**, 114, (47), 19901-19907.

48. Israelachvili, J., *Intermolecular and Surface Forces*. 2nd ed.; Academic Press: London, 1991; p 450.
49. Gregory, J., Approximate Expressions for Retarded van der Waals Interaction. *Journal of Colloid and Interface Science* **1981**, 83, (1), 138-145.
50. Morini, M. A.; Messina, P. V.; Schulz, P. C., The interaction of electrolytes with non-ionic surfactant micelles. *Colloid and Polymer Science* **2005**, 283, (11), 1206-1218.
51. Rosen, M. J., *Surfactants and Interfacial Phenomena*. 3rd ed.; Wiley-Interscience: New York, 2004.
52. Mustafina, A. R.; Elistratova, J. G.; Bochkova, O. D.; Burilov, V. A.; Fedorenko, S. V.; Konovalov, A. I.; Soloveva, S. Y., Temperature induced phase separation of luminescent silica nanoparticles in Triton X-100 solutions. *Journal of Colloid and Interface Science* **2011**, 354, (2), 644-649.
53. Hinze, W. L.; Pramauro, E., A Critical-Review of Surfactant-Mediated Phase Separations (Cloud-Point Extractions) - Theory and Applications. *Critical Reviews in Analytical Chemistry* **1993**, 24, (2), 133-177.
54. Alam, M. S.; Kumar, S.; Naqvi, A. Z.; Kabir ud, D., Study of the cloud point of an amphiphilic antidepressant drug: Influence of surfactants, polymers, and non-electrolytes. *Colloids and Surfaces A-Physicochemical and Engineering Aspects* **2006**, 287, (1-3), 197-202.
55. Alam, M. S.; Naqvi, A. Z.; Kabir ud, D., Influence of additives on the clouding phenomenon of chlorpromazine hydrochloride solutions. *Colloids and Surfaces B-Biointerfaces* **2008**, 63, (1), 122-128.
56. Giribabu, K.; Ghosh, P., Adsorption of nonionic surfactants at fluid-fluid interfaces: Importance in the coalescence of bubbles and drops. *Chemical Engineering Science* **2007**, 62, (11), 3057-3067.
57. http://www.slb.com/services/industry_challenges/carbonates.aspx
58. Asokan, S.; Krueger, K. M.; Alkhaldeh, A.; Carreon, A. R.; Mu, Z. Z.; Colvin, V. L.; Mantzaris, N. V.; Wong, M. S., The use of heat transfer fluids in the synthesis of

high-quality CdSe quantum dots, core/shell quantum dots, and quantum rods. *Nanotechnology* **2005**, 16, (10), 2000-2011.

59. Asokan, S.; Krueger, K. M.; Colvin, V. L.; Wong, M. S., Shape-controlled synthesis of CdSe tetrapods using cationic surfactant ligands. *Small* **2007**, 3, (7), 1164-1169.

60. Hiemenz, P. L.; Rajagopalan, R., *Principles of Colloid and Surface Chemistry*. 3rd ed.; CRC Press: Boca Raton, 1997; p 672.

61. Cheng, X. K.; Kan, A. T.; Tomson, M. B., Study of C-60 transport in porous media and the effect of sorbed C-60 on naphthalene transport. *Journal of Materials Research* **2005**, 20, (12), 3244-3254.

62. Bear, J., *Hydraulics of Groundwater*. McGraw Hills: New York, 1979.

63. Kirkham, D.; Powers, W. L., *Advanced Soil Physics*. John Wiley & Sons Inc: New York, 1972.

64. Kirkham, M. B., *Principles of Soil and Plant Water Relations*. Elsevier Academic Press: San Diego, 2005.

65. Zhang, P.; Fan, C. F.; Lu, H. P.; Kan, A. T.; Tomson, M. B., Synthesis of Crystalline-Phase Silica-Based Calcium Phosphonate Nanomaterials and Their Transport in Carbonate and Sandstone Porous Media. *Industrial & Engineering Chemistry Research* **2011**, 50, (4), 1819-1830.

66. Lecoanet, H. F.; Bottero, J. Y.; Wiesner, M. R., Laboratory assessment of the mobility of nanomaterials in porous media. *Environmental Science & Technology* **2004**, 38, (19), 5164-5169.

67. Lecoanet, H. F.; Wiesner, M. R., Velocity effects on fullerene and oxide nanoparticle deposition in porous media. *Environmental Science & Technology* **2004**, 38, (16), 4377-4382.

68. Espinasse, B.; Hotze, E. M.; Wiesner, M. R., Transport and retention of colloidal aggregates of C-60 in porous media: Effects of organic macromolecules, ionic composition, and preparation method. *Environmental Science & Technology* **2007**, 41, (21), 7396-7402.

69. Choy, C. C.; Wazne, M.; Meng, X. G., Application of an empirical transport model to simulate retention of nanocrystalline titanium dioxide in sand columns. *Chemosphere* **2008**, 71, (9), 1794-1801.
70. Li, Y. S.; Wang, Y. G.; Pennell, K. D.; Abriola, L. M., Investigation of the transport and deposition of fullerene (C60) nanoparticles in quartz sands under varying flow conditions. *Environmental Science & Technology* **2008**, 42, (19), 7174-7180.
71. Raychoudhury, T.; Naja, G.; Ghoshal, S., Assessment of transport of two polyelectrolyte-stabilized zero-valent iron nanoparticles in porous media. *Journal of Contaminant Hydrology* **2010**, 118, (3-4), 143-151.
72. Ben-Moshe, T.; Dror, I.; Berkowitz, B., Transport of metal oxide nanoparticles in saturated porous media. *Chemosphere* **2010**, 81, (3), 387-393.
73. Yu, W. W.; Qu, L. H.; Guo, W. Z.; Peng, X. G., Experimental determination of the extinction coefficient of CdTe, CdSe, and CdS nanocrystals. *Chemistry of Materials* **2003**, 15, (14), 2854-2860.
74. Hey, M. J.; Jackson, D. P.; Yan, H., The salting-out effect and phase separation in aqueous solutions of electrolytes and poly(ethylene glycol). *Polymer* **2005**, 46, (8), 2567-2572.
75. Kenkare, P. U.; Hall, C. K.; Kilpatrick, P. K., The effects of salts on the lower consolute boundary of a nonionic micellar solution. *Journal of Colloid and Interface Science* **1996**, 184, (2), 456-468.
76. Curbelo, F. D. S.; Santanna, V. C.; Neto, E. L. B.; Dutra, T. V.; Dantas, T. N. C.; Neto, A. A. D.; Garnica, A. I. C., Adsorption of nonionic surfactants in sandstones. *Colloids and Surfaces A-Physicochemical and Engineering Aspects* **2007**, 293, (1-3), 1-4.
77. Curbelo, F. D. S.; Barros, E. L.; Dutra, T. V.; Dantas, T. N. C.; Garnica, A. I. C., Oil recovery by ionic and nonionic surfactants and adsorption in sandstones. *Afinidad* **2006**, 63, (524), 291-295.
78. He, F.; Zhang, M.; Qian, T. W.; Zhao, D. Y., Transport of carboxymethyl cellulose stabilized iron nanoparticles in porous media: Column experiments and modeling. *Journal of Colloid and Interface Science* **2009**, 334, (1), 96-102.

79. Phenrat, T.; Kim, H. J.; Fagerlund, F.; Illangasekare, T.; Lowry, G. V., Empirical correlations to estimate agglomerate size and deposition during injection of a polyelectrolyte-modified Fe-0 nanoparticle at high particle concentration in saturated sand. *Journal of Contaminant Hydrology* **2010**, 118, (3-4), 152-164.
80. Phenrat, T.; Saleh, N.; Sirk, K.; Kim, H. J.; Tilton, R. D.; Lowry, G. V., Stabilization of aqueous nanoscale zerovalent iron dispersions by anionic polyelectrolytes: adsorbed anionic polyelectrolyte layer properties and their effect on aggregation and sedimentation. *Journal of Nanoparticle Research* **2008**, 10, (5), 795-814.
81. Solovitch, N.; Labille, J.; Rose, J.; Chaurand, P.; Borschneck, D.; Wiesner, M. R.; Bottero, J. Y., Concurrent Aggregation and Deposition of TiO₂ Nanoparticles in a Sandy Porous Media. *Environmental Science & Technology* **2010**, 44, (13), 4897-4902.
82. Gupta, R.; Mohanty, K. K., Temperature Effects on Surfactant-Aided Imbibition Into Fractured Carbonates. *SPE Journal* **2010**, 15, (3), 587-597.
83. Parker, J. C.; van Genuchten, M. T., *Determining Transport Parameters from Laboratory and Field Tracer Experiments*. Virginia Agricultural Experiment Station: Blacksburg, 1984.

Chapter 5

Colloidal and Flow Behavior of Brine and Temperature-Stable C-Dot Nanoreporters

5.1 Introduction

In the previous chapter, we described a facile approach to formulate brine suspensions of QDs with stability in 1M NaCl and 0.55M seawater brine.¹ The process involved transfer of QDs into bilayers of a nonionic surfactant Neodol 91-7 (referred to as Neodol). The nonionic type of surfactant was selected due to its tolerance to high ionic strengths, where ionic surfactants are typically known to precipitate.²⁻⁴ Furthermore, the selection criterion of the nonionic surfactant was such that its cloud point (for Neodol 91-7, cloud point = 74 °C) was above the temperature of application (70 °C). It emerged from the study that QDs transferred as single particle suspensions and were stable to aggregation at temperatures below and upto the cloud point of Neodol. Aggregation was found to be reversible, i.e, the NP suspension appeared cloudy above the cloud point but changed to a clear suspension when temperature was lowered to below the cloud point where QDs were found to re-attain their single particle sizes. Aggregation of QDs at elevated temperatures was thus attributed to a phenomenon governed by micellar aggregation.⁵

The salt-type comprising the background salinity was an important factor that affected QD aggregation. Salting-out action of NaCl lowered cloud point of Neodol to 58 °C, causing QD aggregation to commence at 60 °C (Fig. 4.8).^{2, 6-8} This was found to impede transport of QDs through calcite in a NaCl background, particularly at elevated temperatures (Fig. 4.9 (b)) on account of partial adsorption of Neodol onto calcite sites. The above and the limited use of ethoxylated nonionics in sandstone reservoirs⁹ were factors that could severely limit the use of Neodol-coated nanoreporters for real-time downhole applications.¹

In this chapter, the focus is on two aspects of a new nanoreporter design. The first is the selection of an alternate coating as a replacement for Neodol with a view to extend tolerance to aggregation to 100 °C in various saline backgrounds. Furthermore and in light of toxicity and cost-related issues of CdSe QDs,^{10, 11} a different core material that is non-toxic and inexpensive in oleic-acid functionalized carbon-black (C-Dot) was selected.¹²

In selecting a surfactant with extended stability to temperatures beyond 70 °C, a nonionic surfactant with a higher degree of ethoxylation could have been used. For a constant C-chain length, a higher degree of ethoxylation is known to increase cloud point,² however, applications in quartz-sand reservoirs would yet remain an issue. We thereby decided to move towards a hybrid surfactant-type such as Avanel S150 CGN, with a molecular structure of $C_{12-15}EO_{15}SO_3^-Na^+$. This surfactant has nonionic (EO) and anionic (SO_3^-) groups on the same molecule. Such hybrid surfactants were recently synthesized by oil and chemical companies such as Shell and BASF for chemical enhanced oil recovery (chemical EOR) applications in reservoirs where ionic strengths (1-3 M NaCl or KCl) and temperatures (upto 120 °C) are extreme.¹³ Having the nonionic and anionic groups on the same molecule also helps bypass the often effective but non-trivial approach to develop EOR strategies using mixed-surfactant micelles of nonionic and anionic surfactants.^{2, 14}

In the next section, we describe the procedure to synthesize C-Dots and their phase-transfer in saline backgrounds of Avanel. We also discuss preliminary breakthrough results of C-Dot/Avanel with calcite and quartz sand as column material.

5.2 Materials and Methods

5.2.1 Synthesis and Phase-Transfer of C-Dots in Bilayers of Avanel

Oleic acid-coated carbon-black (called C-Dots) were synthesized as per the procedure devised by Han *et al.*¹⁵ For synthesis, carbon black (diameter mean: 15 nm) was procured from Cabot Corp., dichloromethane (CH₂Cl₂), potassium permanganate (KMnO₄), hydrochloric acid (HCl, 36.5 wt%), n-hexane (95%), acetone, oleic acid (OA, technical grade – 90%) and acetic acid were purchased from Fischer Scientific and tetrabutyl ammonium bromide (TBABr 99%) was purchased from Acros Organics. For phase-transfer, the hybrid non-ionic anionic surfactant Avanel S150 CGN (called Avanel from here on) was procured from BASF. All chemicals were used as received and without any further purification.

Towards synthesis, 1g carbon black and 300 mL CH₂Cl₂ were added into a 500 mL three-necked round bottom flask (RBF) (Fig. 5.1). The mixture was sonicated for 30 minutes to result in a fine dispersion. In a separate beaker, 3g TBABr (dissolved in 30 mL deionized water), 0.75g KMnO₄ (dissolved in 20 mL deionized water) and 30 mL acetic acid were mixed and added to the dispersion in the RBF. The resulting mixture was stirred vigorously at 25 °C for 24 hours using a magnetic stirrer set-up. Upon this, the mixture was washed with 0.1M HCl solution, precipitated with acetone and centrifuged at 3500 rpm for 1 hour. The supernatant was discarded and the residue was retained, to which the steps of washing with acetone, sonication and centrifugation were repeated thrice. The resulting product was hydroxylated carbon black that was left overnight for drying.

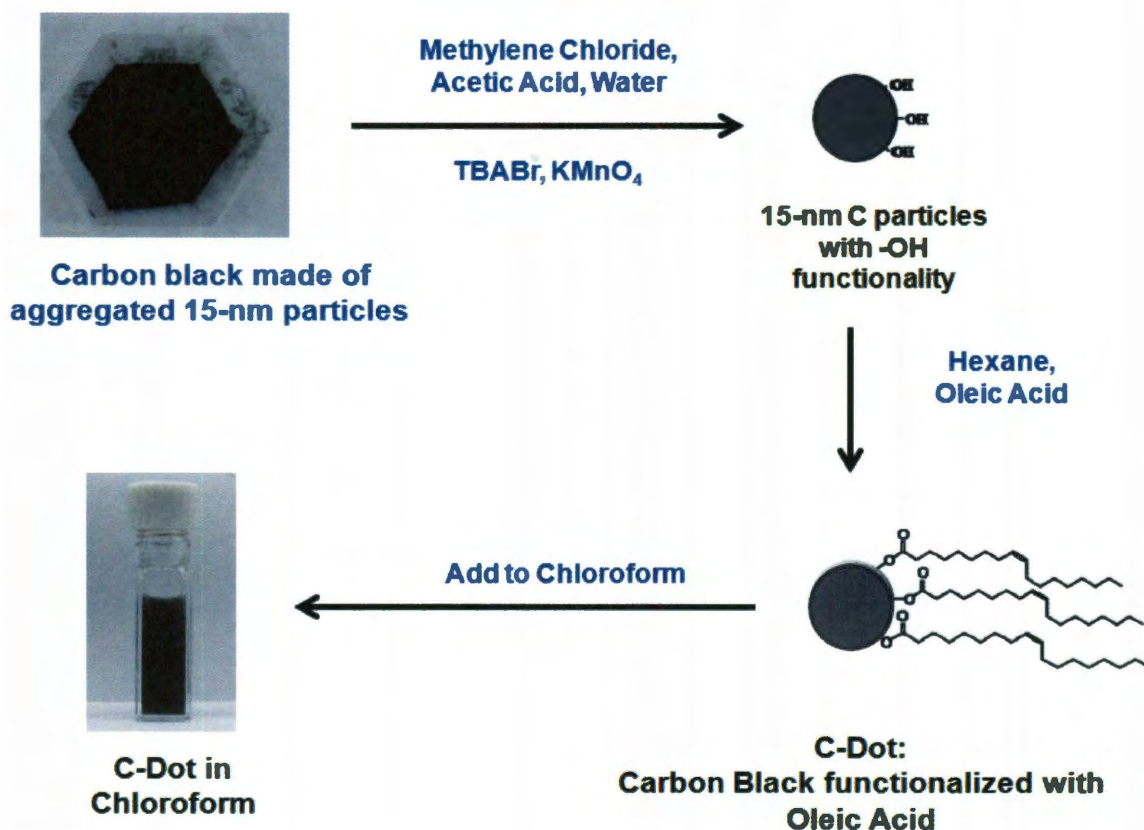


Figure 5.1: Synthesis procedure of C-Dots from hydroxylation of carbon black and functionalization with oleic acid.

For functionalization with oleic acid, 0.1g of the hydroxylated carbon black was dispersed in 100 mL of n-hexane in a 250 mL RBF. To this dispersion, 1g oleic acid was added and the mixture was stirred vigorously under magnetic stirring for 4 hours and at 60 °C under reflux. The resulting product was carbon black with oleic acid functionality (called carbon-dots or C-dots) which was precipitated from hexane using acetone and cleared off excess unreacted oleic acid by sonication and centrifugation. The C-dots obtained were dried overnight and suspended in chloroform to form a concentrated stock solution at 400 ppm, estimated by UV-vis spectroscopy and previously published calibration curves.^{12, 16}

For phase-transfer, solutions of Avanel at 0.75 g/L were prepared in saline water compositions of 1M NaCl, 1M KCl, and 0.55M synthetic seawater. Another saline water composition (API brine, 8 wt.% CaCl₂ and 2 wt.% NaCl, 1.77M ionic strength) with higher concentration of divalent ions was introduced as per recommendations by the Advanced Energy Consortium (AEC) so as to simulate conditions in reservoirs with high divalent ion concentration. 4 mL of C-dots in chloroform was added to these solutions and heated at 90 °C for 30 minutes as per the procedure described in Section 2.2.3. It is to be noted that unlike phase-transfer in Neodol, the presence of salt was important to result in high transfer yields due to the ionic component of Avanel. Fig. 5.2 depicts the schematic of C-dots transfer to 1M NaCl, 1M KCl and 0.55M seawater solutions and Fig. 5.3 depicts the schematic of C-dots upon transfer to 1.77M API brine.

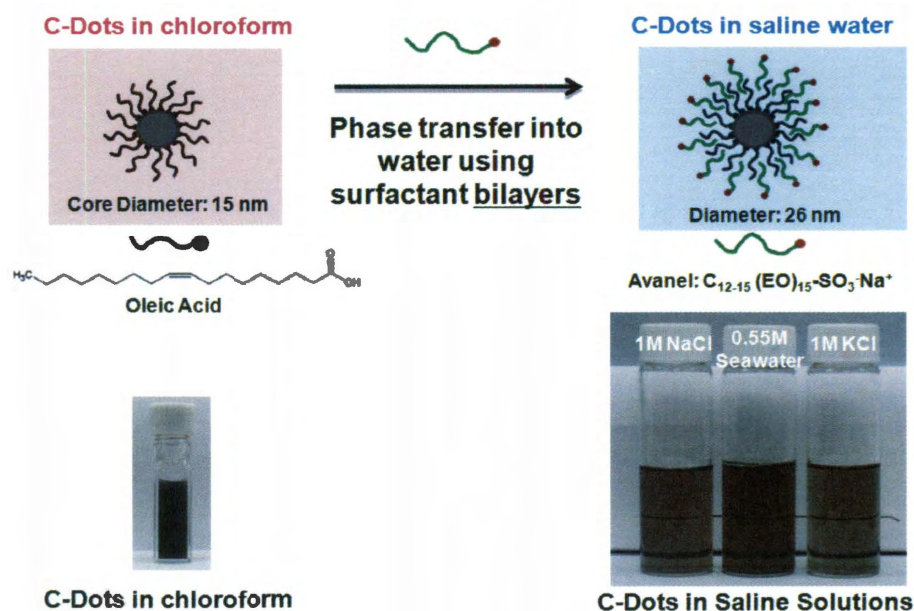


Figure 5.2: Transfer of C-Dots into bilayers of Avanel in various saline environments. The concentration of C-Dots in 1M NaCl and 1M KCl is 15 ppm and in 0.55M seawater is 80 ppm.

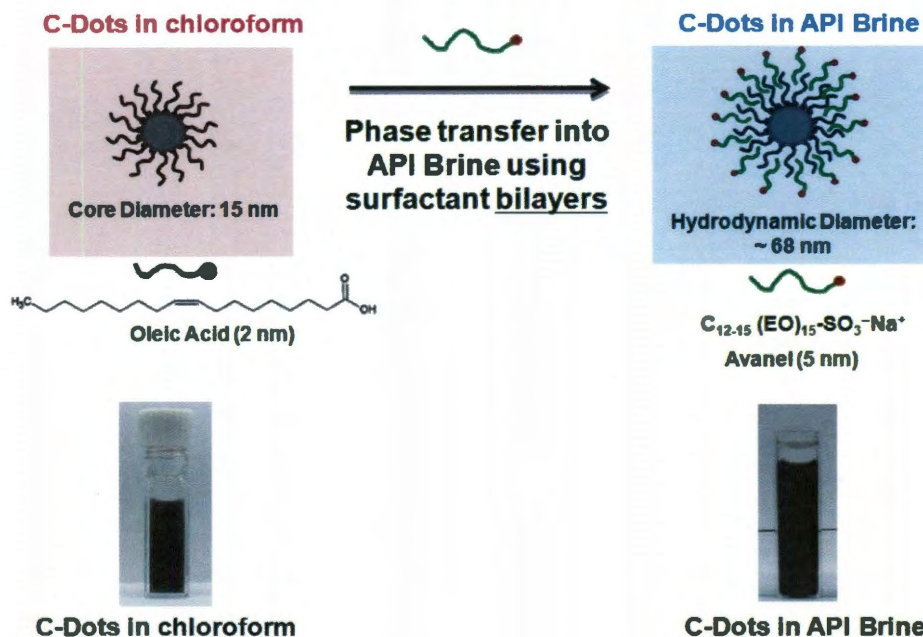


Figure 5.3: Transfer of C-Dots into bilayers of Avanel in API brine. Concentration of C-Dots in API brine is 100 ppm.

5.2.2 Characterization

5.2.2.1 Dynamic Light Scattering

The hydrodynamic diameter of C-Dot/Avanel in different salt solutions was estimated across temperatures ranging from 6-70 °C by DLS, as per the method described in section 4.3.2.1. Hydrodynamic diameters measured were number and volume-averaged and scattering data were fitted using CONTINS or NNLS fitting routines through the instrument software 9KDLSW. Number-based diameter (D_N) scales linearly with

diameter ($D_N = \frac{\sum D_i n_i}{\sum n_i}$) whereas volume-based diameter (D_V) scales as the cube of the

diameter ($D_V = \left(\frac{\sum D_i^3 n_i}{\sum n_i} \right)^{\frac{1}{3}}$), where n_i is the weighted mean of a sample population with diameter D_i .¹⁷

5.2.2.2 Zeta Potential

Zeta potential of C-Dot/Avanel in DI water was estimated from electrophoretic mobility measurements as per the method described in section 4.3.2.2. The zeta potential in DI water was -35 ± 4 mV. For C-Dots in high salinity solutions, measurements of zeta potentials were inconclusive on account of poor reproducibility, and are thus not reported. This is consistent with previous studies reported in section 4.3.2.2 and is also in accordance with assumptions behind theories for electrophoretic mobility that require salts to be at low concentrations.^{18, 19}

5.2.2.3 UV-vis Spectroscopy

Concentration of QDs was analyzed by UV-vis absorbance spectroscopy using a Shimadzu UV-vis (UV-24601 PC) spectrophotometer. Details of the procedure are described in Section 4.3.2.3. Concentrations were estimated using previously developed calibration curves.^{12, 16}

5.2.3 Breakthrough Studies

Preliminary breakthrough studies of C-Dot/Avanel were carried out in packed columns of crushed calcite and quartz sand in API brine background as per the procedure described in section 4.3.3. Prior to breakthrough runs in crushed-calcite, the column was flushed

with a background solution comprising of 0.75 g/L Avanel in 1.77M API brine (termed as Avanel/API brine). It is important to mention that the equilibration step with Avanel/API brine was carried out to prevent a permanent attachment of negatively charged C-Dot/Avanel onto positively charged calcite. This was observed in our initial set of experiments where equilibration was carried out with API brine background and breakthrough of C-Dot/Avanel was poor. For flow through quartz-sand, equilibration was done with 1.77M API brine upon which C-Dot/Avanel in API brine was flowed. On account of the negative charge of quartz-sand, equilibration with Avanel/API brine was not required. All volumetric flow rates (Q) used in this study was 8 mL/hr (corresponding to a Darcy velocity (v_d) of 2.44 m/d).

Concentration of C-Dots in the column effluent (C_{exit}) was determined as a function of PV using UV-vis spectroscopy and Beer-Lambert's law using previously published calibration curves.^{12, 16} Unless mentioned otherwise, the C-Dot/Avanel dispersion was pumped through the column for 3.5 PV's before being replaced by the background salt solution. Flow of the salt solution was continued until no more C-Dots could be detected at the outlet (*i.e.*, $C_{\text{exit}} \sim 0$). Breakthrough curves, represented as plots of C_{exit}/C_0 (where C_0 representing the starting inlet concentration = 0.5 absorbance units) versus PV were subsequently created. For studies at higher temperatures, columns were immersed and equilibrated for 4 hours in a jacketed vessel, with temperature controlled by a Neslab RTE-111 waterbath.

5.3 Results and Discussions

5.3.1 Colloidal Properties of C-Dots/Avanel

Fig. 5.1 shows variations in hydrodynamic diameters of C-Dots/Avanel in different saline backgrounds of 1M NaCl, 1M KCl and 0.55M seawater and as a function of temperature.

Fig. 5.2 shows variations in hydrodynamic diameters of C-Dots/Avanel in 1.77M API brine. The hydrodynamic diameters remained under 100 nm and did not vary significantly across the temperature range studied. It is to be noted that C-Dots in Avanel were not single particles and existed as clusters, different from the hydrodynamic diameters calculated by theory. This was possibly on account of an initial size distribution in the starting carbon black population.¹²

Beyond 70 °C which is the limit of the existing heating set up of the DLS machine, stability to aggregation was tested by equilibrating the samples in a paraffin oil bath set at 100 °C, over a period of 12 hours. The solutions were seen to remain clear and with no visible signs of settling, suggesting that the C-Dots were stable to aggregation even at elevated temperatures.

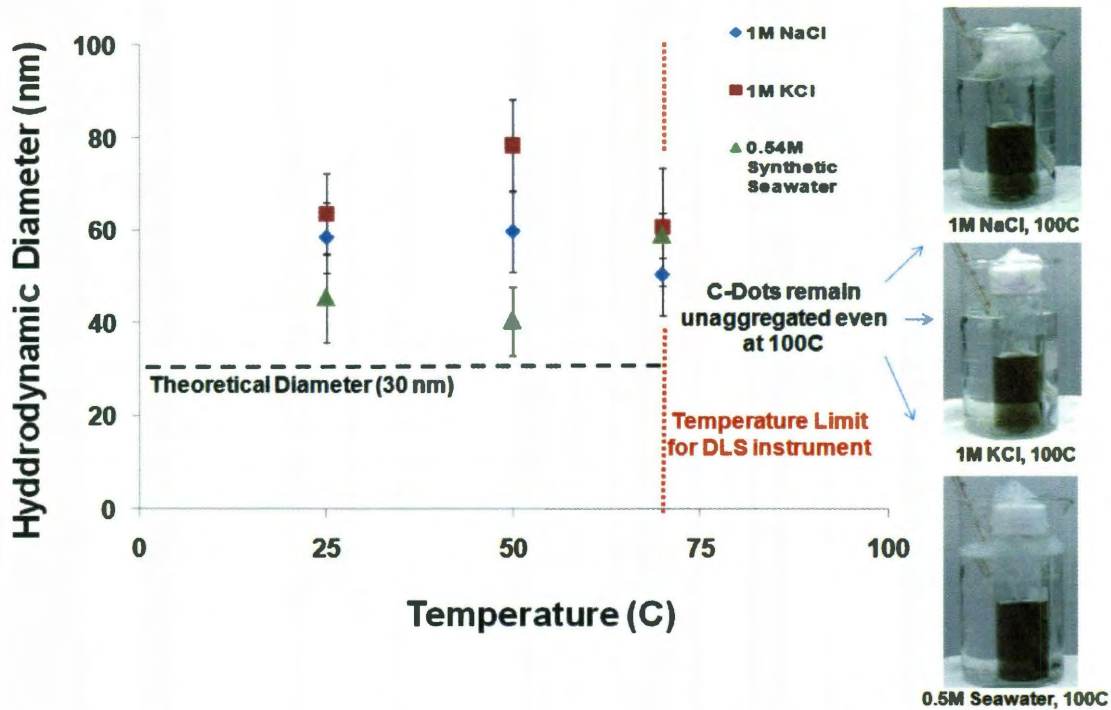


Figure 5.4: Hydrodynamic diameters of C-Dot/Avanel as a function of temperature in saline backgrounds of 1M NaCl, 1M KCl and 0.55M seawater.

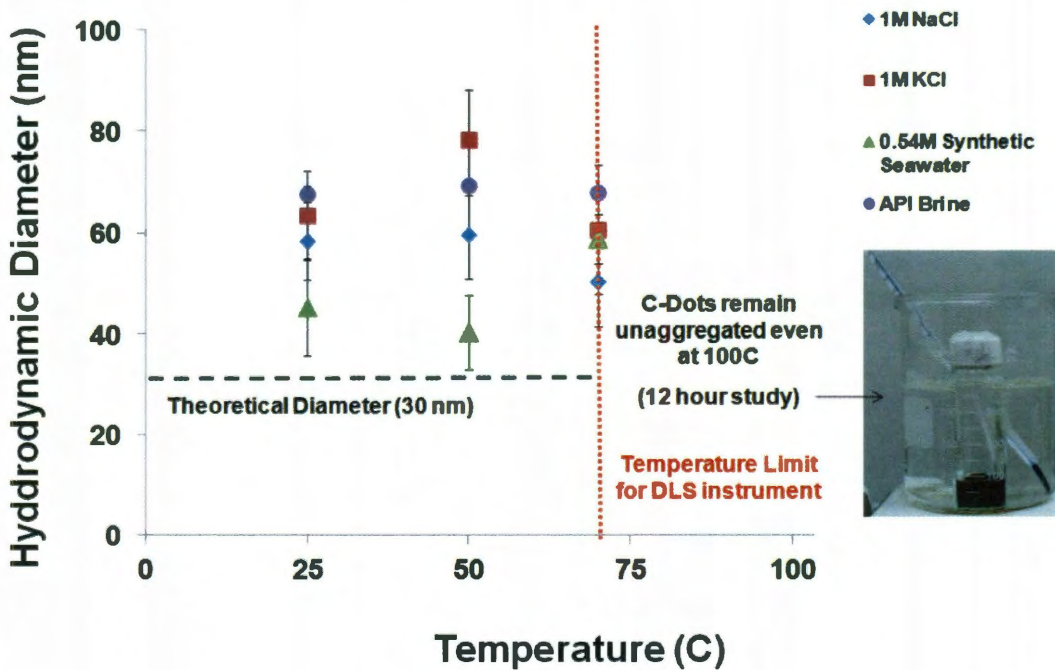


Figure 5.5: Hydrodynamic diameters of C-Dot/Avanel as a function of temperature in 1.77M API Brine.

5.3.2 Transport and Breakthrough of C-Dot/Avanel through Crushed-Calcite and Quartz Sand Columns

Transport and breakthrough profiles of C-Dot/Avanel through crushed-calcite and quartz sand columns are depicted in Figs. 5.6 and 5.7 respectively. The background salinity was 1.77M API brine. For transport study through calcite, C-Dot recovery was <10% when pre-equilibration prior to C-Dot/Avanel flow was made with API brine. Recovery dramatically improved to >95% when pre-equilibration was carried out with Avanel/API brine. Recovery improved to >95% when pre-equilibration was carried out with Avanel/API brine. Pre-equilibration with Avanel ensured positively charged adsorption sites on calcite were saturated and allowed for unimpeded transport of C-Dot/Avanel.

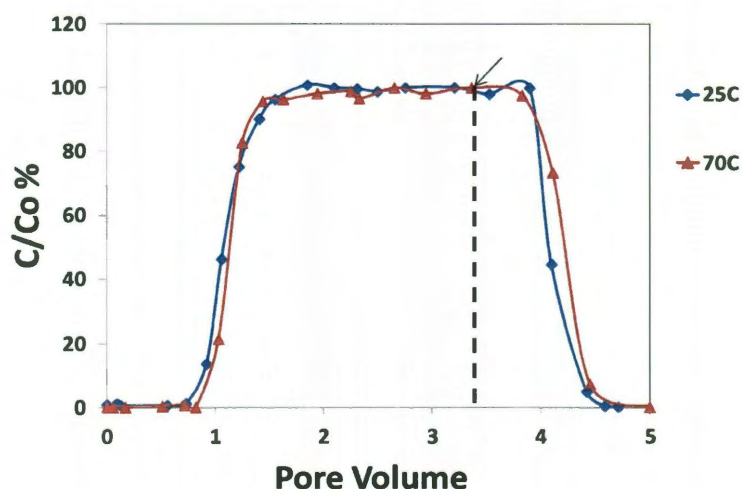


Figure 5.6: Breakthrough profiles of C-Dot/Avanel in 1.77M API brine background through crushed-calcite columns at 25 °C and 70 °C. The calcite-columns were pre-saturated with 0.75 g/L Avanel/1.77M API brine before C-Dot/Avanel in 1.77M API brine was introduced into the column. At 3.5 PV's as indicated by the dashed black line, the C-Dot solution was replaced by 0.75 g/L Avanel/1.77M API brine.

Alongside a high recovery, tracer-like behavior of C-Dots was observed, where 50% breakthrough was found to occur between 1-1.2 PV's, at temperatures up to 70 °C. Given that API Brine composition is 8 wt% NaCl (that corresponds to ~ 1.36M NaCl) and for

1M NaCl background, overshoot was observed with QD/Neodol at higher temperatures, the hybrid Avel surfactant proves effective in facilitating NP transport at higher temperatures.

Fig. 5.7 shows flow of C-Dot/Avel in 1.77M API brine through quartz-sand. The recovery of C-Dots post flow and breakthrough was high (> 90%) and the negative charge of quartz-sand did not require a pre-equilibration step with Avel/API brine. Breakthrough of C-Dot continued to be delayed (1.2-1.6 PV's) relative to transport profiles observed for calcite. However, previously observed high overshoot as seen in QD/Neodol did not occur, indicating lower adsorption affinity for Avel onto quartz.

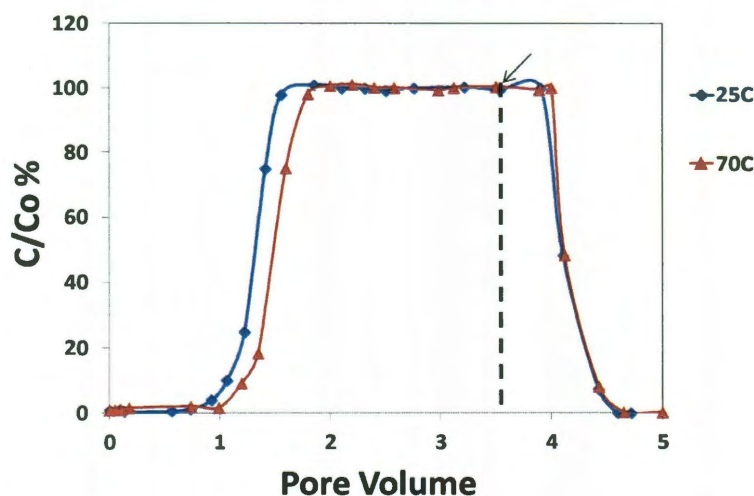


Figure 5.7: Breakthrough profiles of C-Dot/Avel in 1.77M API brine background through quartz sand columns at 25 °C and 70 °C. The quartz-sand column was pre-saturated with 1.77M API brine before C-Dot/Avel in 1.77M API brine was introduced into the column. At 3.6 PV's as indicated by the dashed black line, the C-Dot solution was replaced by 1.77M API brine.

5.4 Conclusions

Non-toxic and inexpensive C-Dot/Avel reporters were formulated by oleic-acid functionalization of hydroxylated carbon-black and subsequent transfer to bilayers of

Avanel. The resulting nanoreporters demonstrated high stability in salt backgrounds of 1M NaCl, 1M KCl, 0.55M seawater and 1.77M API brine and up to temperatures of 100 °C. Flow and transport studies in API brine background through crushed-calcite and quartz-sand showed largely unimpeded flow with high recovery. Flow through calcite required a pre-equilibration step with Avanel/API brine to saturate positively charged adsorption sites. Flow through quartz-sand did not require the pre-equilibration with Avanel. While C-Dot retardation through quartz-sand was higher than calcite, delay was lower and without overshoot when compared to nanoreporters formulated with Neodol. The Avanel coating thus provides a way to nanoreporter design with high colloidal stability and tracer-like breakthrough characteristics.

5.5 References

1. Kini, G. C.; Yu, J.; Wang, L.; Tour, J. M.; Kan, A. T.; Biswal, S. L.; Tomson, M. B.; Wong, M. S., Colloidal and Convective Transport Behavior of Saline-stable Quantum Dot Nanoparticles. *To be submitted* **2011**.
2. Rosen, M. J., *Surfactants and Interfacial Phenomena*. 3rd ed.; Wiley-Interscience: New York, 2004.
3. Bagaria, H. G.; Kini, G. C.; Wong, M. S., Electrolyte Solutions Improve Nanoparticle Transfer from Oil to Water. *Journal of Physical Chemistry C* **2010**, *114*, (47), 19901-19907.
4. Petosa, A. R.; Jaisi, D. P.; Quevedo, I. R.; Elimelech, M.; Tufenkji, N., Aggregation and Deposition of Engineered Nanomaterials in Aquatic Environments: Role of Physicochemical Interactions. *Environmental Science & Technology* **2010**, *44*, (17), 6532-6549.
5. Mustafina, A. R.; Elistratova, J. G.; Bochkova, O. D.; Burilov, V. A.; Fedorenko, S. V.; Konovalov, A. I.; Soloveva, S. Y., Temperature induced phase separation of luminescent silica nanoparticles in Triton X-100 solutions. *Journal of Colloid and Interface Science* **2011**, *354*, (2), 644-649.
6. Hey, M. J.; Jackson, D. P.; Yan, H., The salting-out effect and phase separation in aqueous solutions of electrolytes and poly(ethylene glycol). *Polymer* **2005**, *46*, (8), 2567-2572.
7. Kenkare, P. U.; Hall, C. K.; Kilpatrick, P. K., The effects of salts on the lower consolute boundary of a nonionic micellar solution. *Journal of Colloid and Interface Science* **1996**, *184*, (2), 456-468.
8. Morini, M. A.; Messina, P. V.; Schulz, P. C., The interaction of electrolytes with non-ionic surfactant micelles. *Colloid and Polymer Science* **2005**, *283*, (11), 1206-1218.
9. Curbelo, F. D. S.; Barros, E. L.; Dutra, T. V.; Dantas, T. N. C.; Garnica, A. I. C., Oil recovery by ionic and nonionic surfactants and adsorption in sandstones. *Afinidad* **2006**, *63*, (524), 291-295.
10. Werlin, R.; Priester, J. H.; Mielke, R. E.; Kramer, S.; Jackson, S.; Stoimenov, P. K.; Stucky, G. D.; Cherr, G. N.; Orias, E.; Holden, P. A., Biomagnification of cadmium

selenide quantum dots in a simple experimental microbial food chain. *Nature Nanotechnology* **2011**, 6, (1), 65-71.

11. Derfus, A. M.; Chan, W. C. W.; Bhatia, S. N., Probing the cytotoxicity of semiconductor quantum dots. *Nano Letters* **2004**, 4, (1), 11-18.
12. Berlin, J. M.; Yu, J.; Lu, W.; Walsh, E. E.; Zhang, L. L.; Zhang, P.; Chen, W.; Kan, A. T.; Wong, M. S.; Tomson, M. B.; Tour, J. M., Engineered nanoparticles for hydrocarbon detection in oil-field rocks. *Energy & Environmental Science* **2010**, 4, (2), 505-509.
13. Puerto, M.; Hirasaki, G. J.; Miller, C. A.; Barnes, J. R., Surfactant Systems for EOR in High-Temperature, High-Salinity Environments. In *SPE Improved Oil Recovery Symposium* Tulsa, 2010.
14. Ogino, K.; Abe, M., *Mixed Surfactant Systems*. 2nd ed. ed.; CRC Press: New York, 1992; p 472.
15. Han, H.; Lee, J.; Park, D. W.; Shim, S. E., Surface Modification of Carbon Black by Oleic Acid for Miniemulsion Polymerization of Styrene. *Macromolecular Research* **2010**, 18, (5), 435-441.
16. Yu, J.; Berlin, J. M.; Lu, W.; Zhang, L. L.; Kan, A. T.; Zhang, P.; Walsh, E. E.; Work, S. N.; Chen, W.; Tour, J. M.; Wong, M. S.; Tomson, M. B., Transport Study of Nanoparticles for Oilfield Application. In *SPE International Conference on Oilfield Scale*, Aberdeen, U.K., 2010.
17. Hiemenz, P. L.; Rajagopalan, R., *Principles of Colloid and Surface Chemistry*. 3rd ed.; CRC Press: Boca Raton, 1997; p 672.
18. Evans, D. F., Wennerström, H., *The Colloidal Domain: Where Physics, Chemistry, Biology and Technology Meet*. 2 ed.; Wiley-VCH: 1999.
19. Hunter, R. J., *Zeta Potential in Colloid Science: Principles and Applications*. Academic Press: London, 1981.

Chapter 6

Microfluidic Formation of Ionically Crosslinked Polyamine Gels

6.1 Introduction

In Chapter 2, we had described a new phase-transfer strategy to create stable colloidal dispersions of single NPs encapsulated in salty-micelles of surfactants. Subsequently in Chapters 4 and 5, we demonstrated approaches to formulate NPs that were stable to aggregation under conditions of high ionic strengths and temperatures. We also investigated their flow and transport through crushed calcite and sand-pack columns, material that simulate a reservoir.

In this chapter, we shift our focus to a microfluidic environment where controlled flow and diffusion-limited conditions of mixing prevail. A research area in our group deals with the tandem assembly of NPs on a polymer-salt aggregate template to result in nanoparticle assembled capsules (NACs), where NPs constitute the shell wall.¹⁻⁶ Thus far, NAC synthesis has been carried out in a batch mode, with limited control possible on the spatial deposition of NPs. Further, only a limited variety of water-dispersible NPs can be used to form NACs. We decided to expand the scope of NAC synthesis on a continuous mode basis in microfluidics, using a wider variety of water-dispersible NPs, now obtainable through salty-micelle encapsulation. Further, the laminar flow environments can be used to form new variant of NACs with spatial control over NP deposition.

In attempting tandem assembly in microchannels, we found a unique and unexpected behavior in that polymer-salt aggregates which serve as templates to assemble NPs as NACs, fused to form viscoelastic gels under shear from reactant flow rates. These gels form *in situ* and at room temperature, exhibit shear-thickening behavior as the polymer is cross-linked to form viscoelastic gel phases, and remain stable and

intact even upon cessation of flow. Upon reviewing literature of gel formation in microfluidics, we realized the significance of these findings in the possibility of using *in situ* formed gels as flow regulators in microchannels. Current methods to regulate flow in microchannels involving gels require elaborate micromachining and lithographic methods. Thereby, in this chapter, we describe our investigations on the mechanism of forming ionically crosslinked polyamine gels in microfluidic channels. We begin this chapter by providing a brief introduction to the field of microfluidics.

6.1.1 Microfluidics and its Unique Environment

Prof. G.M. Whitesides, one of the pioneers in developing the field of microfluidics,⁷ defines microfluidics as “the science and technology of systems that manipulate small (pico to atto liters) amounts of fluids, using channels with dimensions of tens to hundreds of micrometers.” The development of this fascinating field came about from attempts to miniaturize the field of analysis. The following were the drivers to miniaturization:

(i) The use of very small quantities of samples and reagents, thus minimizing consumption and cost (particularly important in high value industries such as pharmaceuticals).

(ii) The ability to carry out rapid separations and detections, while achieving high resolution and sensitivity.

(iii) Requirements of small footprints and portable nature of the device.

Fig. 6.1 (i) depicts one of the most basic microfluidic devices, comprising of three inlet channels that merge to form the main channel. The first generation microfluidic channels were made of silicon, glass and hard polymers, but ever since the advent of the “wonder

polymeric material” - polydimethylsiloxane or PDMS and advances in the field of microelectronics, the miniaturization of channels have undergone a sea of change, resulting in devices that serve as “Labs on a Chip” (Fig. 6.1 (ii)), and now even “Factories on a Chip.”⁷ Squires and Quake, in their comprehensive review on fluid physics at the nanoliter scale, discuss the analogy between miniaturization in microfluidics and microelectronics.⁸

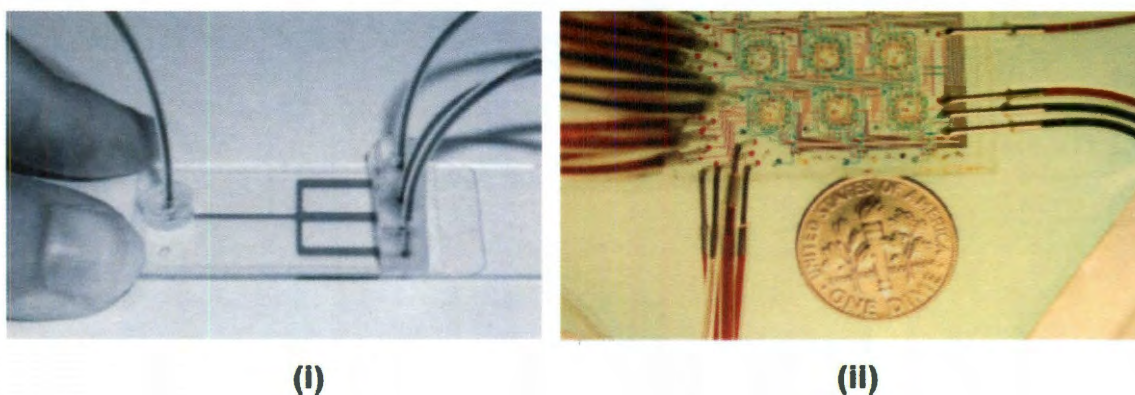


Figure 6.1: (i) A simple microchannel comprising three inlet channels merging to form a main central channel. (ii) A highly miniaturized “Lab on a Chip” type of microfluidic device – Microfluidic Chemostat. This device is used to study growth of microbial populations. The human finger and the United States dime coin gives a sense of scale and the dramatic extent of miniaturization going from (i) to (ii). (Fig. 6.1 (i), adapted from Beebe *et al.* Fig. 6.1 (ii), adapted from Whitesides G.M. (2006)).

As a consequence, microfluidics has now grown into a wide research theme that has impacted and contributed to the development of several disciplines in a way that it is bound to change the world and in the way that we live. In fact, the July 2006 edition of the prestigious scientific journal *Nature*, exclusively covered “Lab on a Chip” as its core theme. This issue featured perspectives from leaders on various disciplines of microfluidics, namely miniaturized chemical analysis, optofluidics, single molecule

probing, control and detection of chemical reactions, biology and global health, thus announcing the coming of age of microfluidics as a field.^{7, 9-14}

So what is so special about the microfluidic environment that has triggered off so many developments? The obvious characteristic is its small size, whose compelling advantages have already been discussed. The non obvious is the flow characteristics of fluids in microchannels, namely that of laminar flow.

Fig. 6.2 illustrates the laminar flow profiles observed in microfluidic channels. The consequence of laminar flow is that mixing between fluid layers starts at the interface upon which, it becomes diffusion limited (poor mixing). These can be further understood in terms of two important dimensionless numbers that are critical in describing the essential microfluidic environment – the Reynolds and Péclet Numbers.

6.1.2 Reynolds Number

In Whitesides' definition of microfluidics, a key specification was the dimensions of the channel, namely tens to hundreds of microns. At these scales, mass transport in fluids is dominated by viscous dissipation and inertial effects are generally negligible. The ratio of inertial and viscous effects is captured by the Reynolds number (N_{Re}) which is defined below as:

$$N_{Re} = \frac{d\rho v}{\mu} = \frac{\rho v^2}{\frac{\mu v}{d}} = \frac{\text{Inertial Forces}}{\text{Viscous Forces}} \quad (6-1)$$

Where: d = diameter of the pipe, v = velocity of the fluid, ρ = density of the fluid, and μ = viscosity of the fluid.

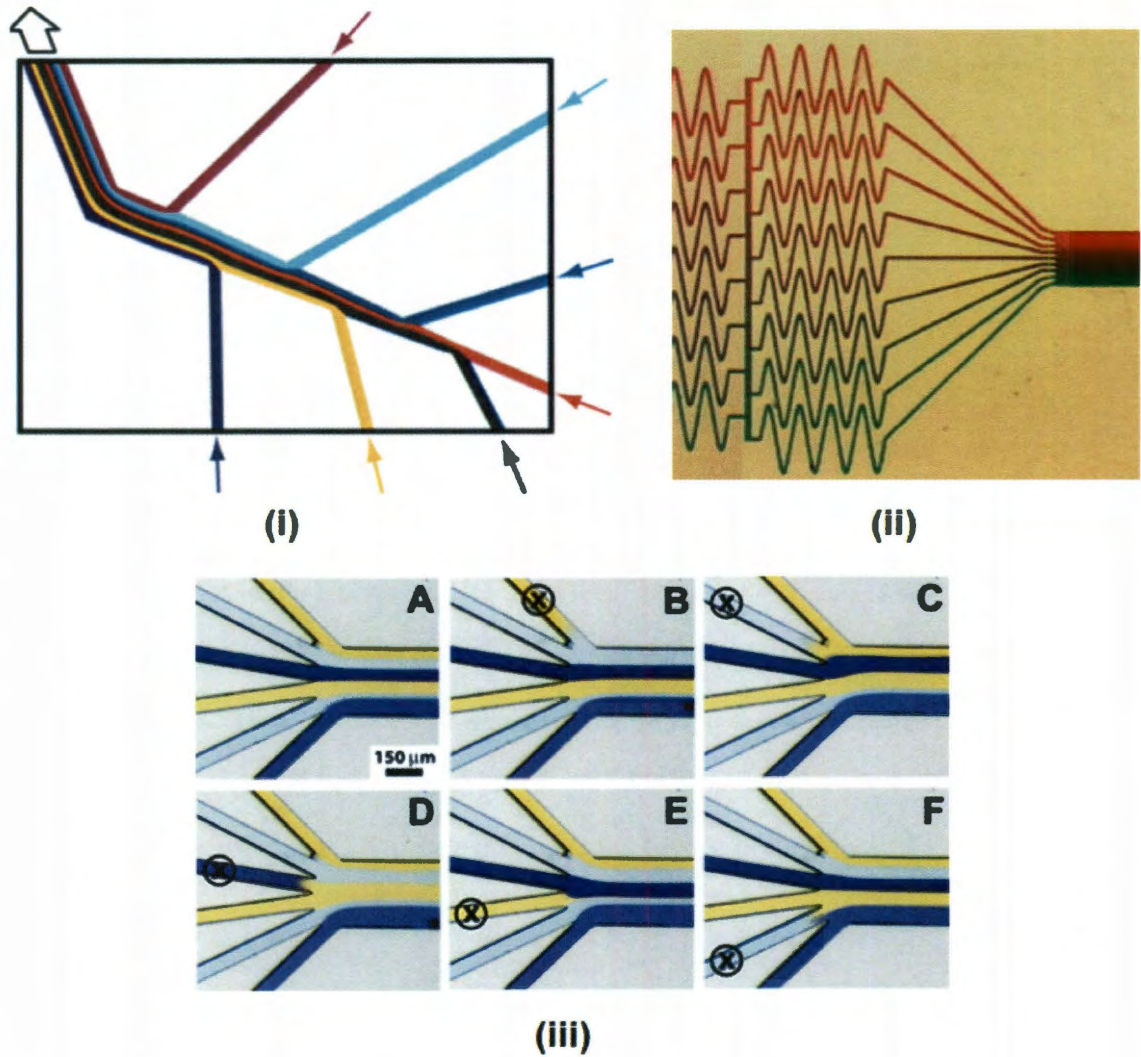


Figure 6.2: Illustrations of laminar flow behavior in microfluidic devices (i) Inlet channels with different colored dyes flow into the main channel at different points but remain exactly parallel to each other. (ii) Color gradient generator: Inlet streams (top to bottom) with colors varying from red to green and its intermediate mixtures, are introduced into the main channel. It can be seen that the color gradient is maintained even in the main channel due to laminar flow conditions. (iii) Effects of valve shut on and off: (A) Colored dye solutions flow through six inlet pipes to the main channel. The dyes flow as parallel streams in the main channel due to laminar conditions. Images (B – F) correspond to those wherein inlet streams are shut (one at a time, and counter clockwise for images B through F). Fluid is occupied by the stream entering at a higher pressure and mixing is still seen to be absent (Image Courtesy: Prof. G.M. Whitesides group website).

Assuming water to be the working fluid, typical velocities of 1 $\mu\text{m/s}$ – 1 cm/s and channel radii between 10–100 μm , N_{Re} is found to range in the order of 10^{-6} and 10. These low values of N_{Re} further confirm that viscous forces typically overwhelm inertial forces, and the resulting flows are linear (laminar). It is the essential dimensions of the microfluidic (10–100 μm) that provide this effect. Since inertia provides the nonlinearity that is responsible for numerous instabilities and turbulence, the loss in inertial nonlinearity accentuates physical phenomena that are less prominent on the macroscale (Fig. 6.2). The review by Squires and Quake provides further details on how laminar flow profiles in microfluidics can be systematically altered by increasing Reynolds number and geometry, thus providing the basis to designing microfluidic plumbing, mixing and actuation components.⁸

6.1.3 Péclet Number

High Reynolds numbers dominate most aspects of life, particularly when dealing with the macroscale through the dominance of inertia over viscous forces. The presence of eddies and turbulence in such conditions significantly lower the time scales of mixing. The situation differs in microfluidics, wherein laminar fluid flows that naturally arise in the low Reynolds number scenario, forces mixing to occur by diffusion alone. This behavior results in mixing times that can be unacceptably long and range in the order of minutes or more. It thereby becomes necessary to complement the Reynolds number with other dimensionless groups that quantify the “time scale” and thereby, the associated “path length” required for mixing to take place. This is captured by the Péclet number.

Consider the T junction geometry as shown in Fig. 6.3. Let two fluids (A and B) be injected to flow alongside each other upon entering the main channel with width “w”. It is well known that A and B initially mix at the interface, and hence, the next logical question would be to estimate the time (and corresponding distance z) when the two fluids become completely homogenized.

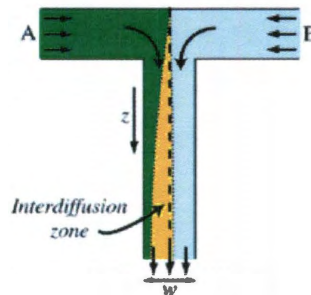


Figure 6.3: A microfluidic channel with T-junction geometry where two fluids A and B mix purely by diffusion. The Péclet number captures the time (and consequently channel length) required for complete mixing to take place (Figure adapted from Squires and Quake).

The time τ_D required for molecules to diffuse across the entire channel length is given by $\tau_D \sim w^2/D$, where D is the diffusion coefficient. In this time, the distance covered by the molecule down the channel would be, $z \sim vw^2/D$, where v is the fluid velocity. Consequently, the number of channel widths required for complete mixing to occur would be given by:

$$N_{Pe} = \frac{z}{w} = \frac{vw}{D} \quad (6-2)$$

The Péclet number (N_{Pe}) expresses the relative importance of convection to diffusion. In this example, the number of channel widths required for full mixing varies linearly with N_{Pe} . Thus, the reaction path length for complete mixing of a molecule (such as a protein, $D = 40 \mu\text{m}^2/\text{s}$) through a channel of $100 \mu\text{m}$ width and at a velocity of $100 \mu\text{m}/\text{s}$ would require approximately 250 channel widths (2.5 cm) and 4 minutes of mixing time. Thus, a characteristic feature of microfluidics is their typically large Péclet numbers.

Purely diffusive mixing can be advantageous or undesirable and depends purely on the application in hand. Often, microfluidic chemical reactors require different solutions to be brought together and mixed rapidly, allowing the dynamics of the reactions to be probed, rather than the diffusive dynamics of the molecules themselves. In this case, micropumps and micro rotary mixers have been devised to increase mixing by exploiting the parabolic flow profile nature in microchannels (Fig. 6.4).

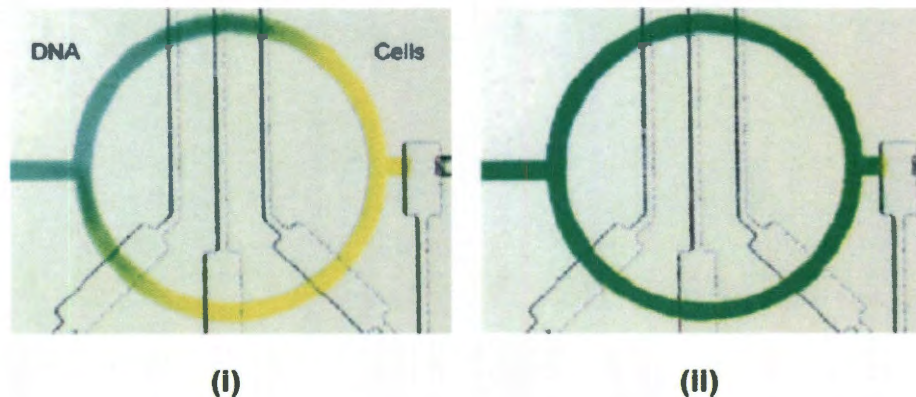


Figure 6.4: Rotary pumps have been utilized to rapidly mix solutions in microchannels (here DNA and cells). (i) DNA (green stream) and cells (yellow stream) before mixing. (ii) DNA and cell streams upon mixing (Figure adapted from Melin and Quake).

The opposite problem is faced, however, in sorting and analyzing the products of those same reactions: the faster the mixing, the harder the separation. Controlling dispersion in microfluidic devices, then, is often of paramount importance.

6.1.4 Capillary Number

For the case where fluid flows are immiscible, surface or interfacial tensions can affect the dynamics of the free surface. In this case, the capillary number (Ca) serves as an important dimensionless number that quantifies the competition between surface tension (γ) and viscous forces (μ).

$$Ca = \frac{\mu v}{\gamma} = \frac{\text{Viscous Stress}}{\text{Surface Tension Stress}} \quad (6-3)$$

Where: v = velocity of the fluid. Based on the capillary number, microfluidic geometries can be designed, both for low and high Reynolds Number flow to induce droplet and foam formation by inducing Rayleigh-Plateau instabilities.⁸ In the following section, we review recent work on gel formation in a microfluidic environment, which forms the basis to our work on ionically crosslinked gelation.

6.2 Microfluidic Formation of Ionically Cross-Linked Gels and Nanoparticle Assembled Capsules

6.2.1 Background

An active area of our research group has been on the use of self-assembly methods of NPs to form capsules. This method is a simple 2-step tandem-assembly approach in which a linear cationic polymer is mixed with a salt of a multivalent anion in the first

step, to form instantaneously a positively charged polymer-salt aggregate. These aggregates serve as colloidal templates to which, negatively charged NPs are added to in the second step to form Nanoparticle Assembled Capsules (NACs). In 2005, Rana *et al* demonstrated the 2-step tandem-assembly approach to form NACs using poly (L-lysine) (PLL) as the polymer and tetrasodium ethylenediamine tetraacetate (EDTA) as the multivalent anion, resulting in formation of positively charged colloidal aggregates of PLL crosslinked by EDTA (Fig. 6.5). These aggregates were unstable and grew in time. To stabilize the aggregates, NPs (such as silica) were added as a part of the second step, resulting in the formation of nanoparticle assembled capsules (NACs) where the shell boundary of the capsule was comprised of multiple layers of silica NPs (Fig. 6.5).¹

The governing synthesis parameter was the “*R* ratio”, defined as the total negative charge from the multivalent anion divided by the total positive charge from the polymer. Since the polymer/salt aggregates grow in time as metastable species (with growth rates a function of *R* ratio), the capsule sizes can be controlled by both growth time and *R* ratio. Larger silica NP capsules are prepared with polymer/salt aggregates aged for longer times than shorter times. The capsule material is essentially made of NPs and polymer in the shell, in which the polymer holds the oppositely charged NPs together. Interestingly, the NAC interior can contain either the polymer/salt aggregate or water, depending on the salt-type used. Thus polymer-filled or water-filled capsules can be generated in one pot, merely by changing the precursor.

Subsequent investigations have established the general nature of the tandem assembly method, wherein, a host of linear cationic polymers (poly(allylamine hydrochloride) or PAH) and multivalent salt variants (monosodium citrate, disodium

citrate, sodium acetate, trisodium citrate, sodium succinate, disodium sulfate tetrasodium ethylenediaminetetraacetate (EDTA) and disodium hydrogen phosphate (Na_2HPO_4)).² Besides SiO_2 NP capsules, capsules made of SnO_2 NPs, ZnO NPs, Fe_2O_3 NPs, Fe_3O_4 NPs, CdSe QDs, polymer, Al_2O_3 - SiO_2 NPs and SiO_2 NPs – silicic acid have been successfully synthesized.^{3-5, 17} In more recent developments, Murthy *et al* describe formation of patchy/multicompartment capsules using a blend of polymers (PAH and PLL), citric acid and SiO_2 NPs.⁶

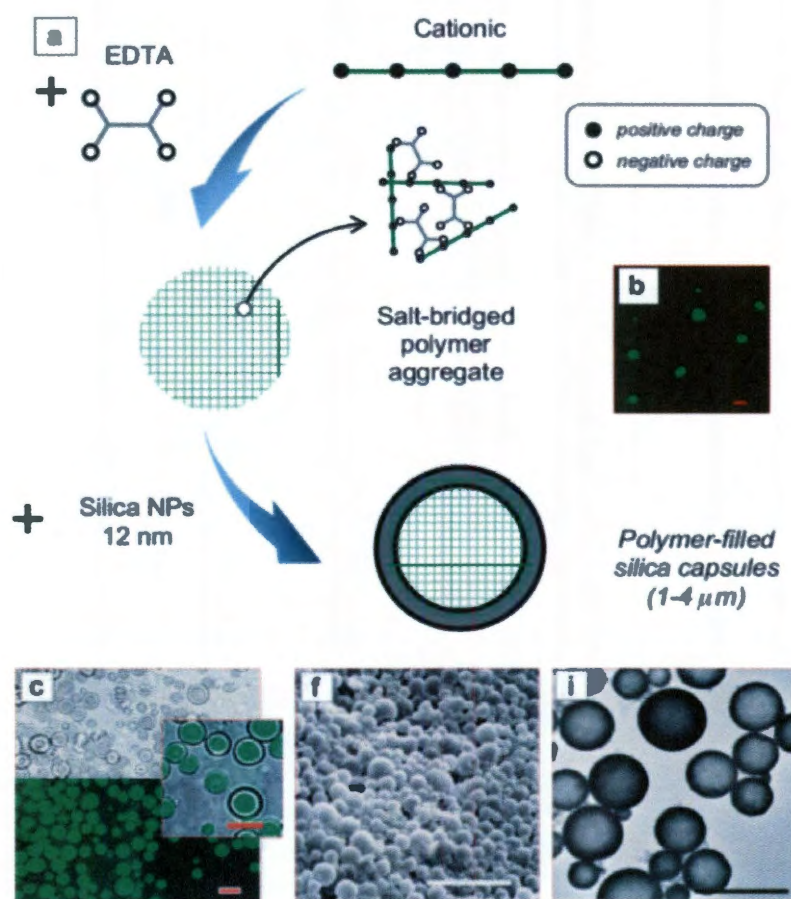


Figure 6.5: Schematic depicting tandem self-assembly of microcapsules. (a) Two-step formation of nanoparticle assembled capsules (NACs): In the first step, a positively charged linear cationic polymer (poly (L-lysine) (PLL) is reacted with a multivalent anion, tetrasodium ethylenediamine tetraacetate (EDTA) to form EDTA-bridged PLL aggregates. (b) Confocal microscopy image of EDTA-bridged PLL aggregates, where

PLL is partially conjugated by FITC fluorophores. (c) Bright field (top), confocal (bottom), and combined confocal/bright-field images (inset) of three different silica structures suspended in water. (f) SEM images of NACs. (g) TEM images of NACs (Scale Bars: 5 μm) (Figure adapted from Rana *et al*).

The unique selling proposition of the tandem-assembly process is its contribution to the field of green chemistry in obtaining closed shell colloidal structures through an environmental friendly route, as the entire synthesis is carried out in water, at near neutral pH and at room temperature. Further, the size of the colloidal template can be controlled by charge ratios of reactants that results in structures from sizes of 100 nm to 2 μm .¹⁸ To expand the scope of synthesizing NACs on a continuous mode basis and to form new types of NACs, it was envisaged that controlled flow conditions in a microfluidic could be beneficial. Further, with our understanding of transferring NPs to water phase using salty-micelles of surfactants, we could attempt the use of new NP types in forming the capsule shell boundary.

Fig. 6.6 shows the preliminary proposed schematic of forming NACs on a continuous mode basis. We planned to flow a linear cationic polymer (polyallylaminehydrochloride (PAH)) through the central stream and multivalent anions of citrate through the side streams to form citrate-bridged PAH aggregates. Farther down the channel, we proposed to add NPs so that NACs could be formed on a continuous mode basis. We also felt that adding NPs of two different types from the two side streams could result in the formation of “Janus” variants of capsules.

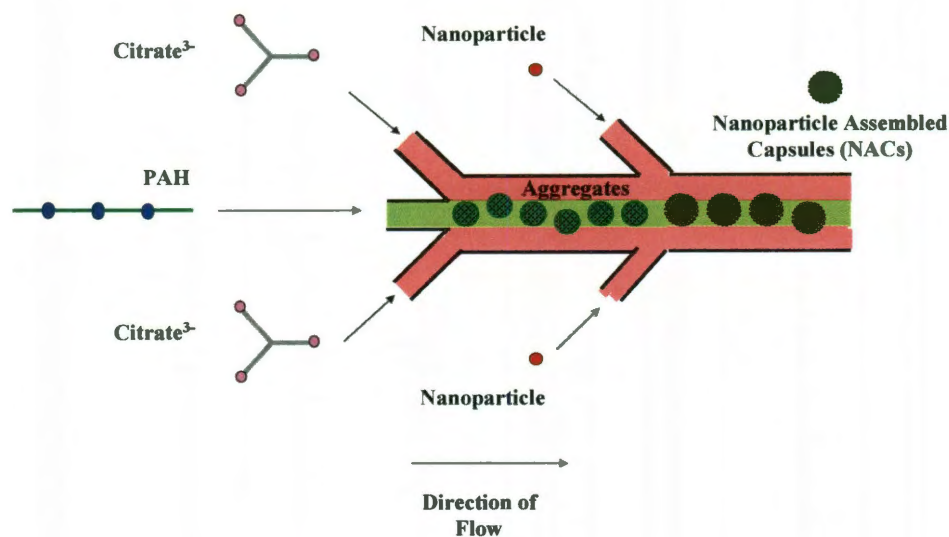


Figure 6.6: Preliminary schematic of forming nanoparticle assembled capsules (NACs) on a continuous mode basis and the possibility of forming new NAC types.

However, upon attempting the first step of flowing PAH through the central stream and citrate through the side streams of a three-inlet microfluidic channel, we found structures formed that were contrary to expectations. Fig. 6.7 shows the two contrasting scenarios of structures formed when PAH and citrate interact under bulk vortex-mixing conditions (top) and under laminar flow conditions in a microfluidic and under shear flow (bottom). We decided to re-visit the challenge of forming capsules at a later duration, upon characterizing and exploring this gelation phenomenon.

Thereby, to put into context the relevance of our work on gelation in microfluidics, we provide a brief literature overview of gel formation in microfluidics that constitutes the next section.

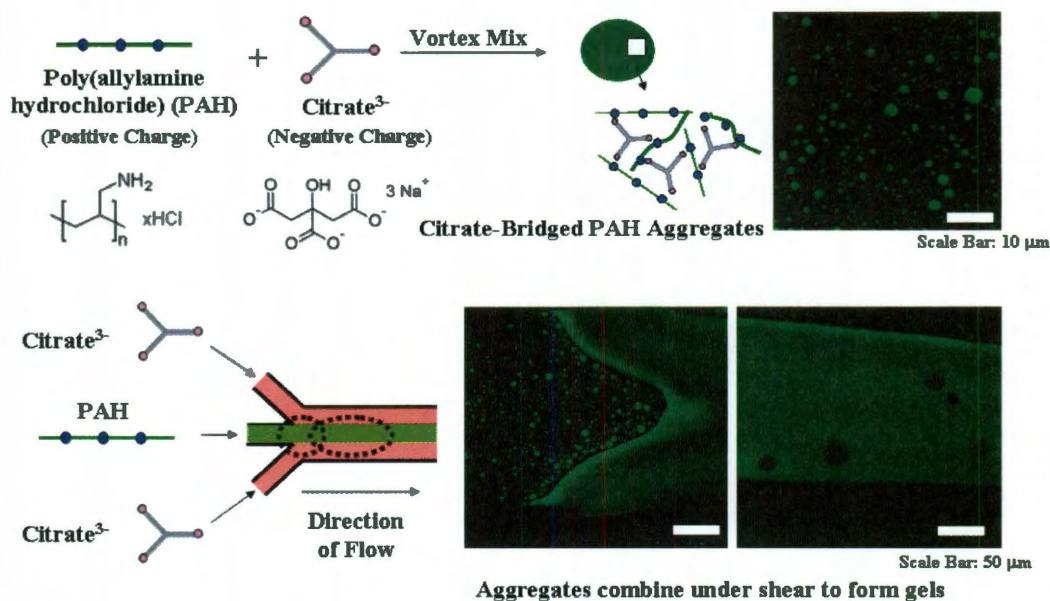


Figure 6.7: Polyallylamine hydrochloride (PAH) and citrate interactions in a bulk vortexing environment (top) gives rise to citrate-bridged PAH aggregates (fluorescence mode). In a microfluidic environment (bottom), new structures such as gels and droplets form, in addition to previously reported aggregates, when PAH and citrate flow under conditions of shear.

6.2.2 Gel Formation Strategies in Microfluidic Devices and their Applications

A recent focus area in microfluidic research has been on flow and formation of gels in microchannels.¹⁹⁻²⁶ Microfluidic devices allow for the confinement of reagents and precise control of the time of reaction.^{12, 27-33} Primary applications of gels in microfluidic devices are in forming components for flow control,^{21, 34-47} separations,⁴⁸⁻⁵² detection and sensing,^{41, 50} that are essential towards developing micro total analytical (μ TAS) systems. Recent μ TAS systems that use gel-based components include glucose and insulin detection devices,^{36, 41} enzymatic microreactors,⁵³ optical chemosensors⁵⁴ and nucleic acid separation systems.⁵⁵ Other applications of gels in microchannels include synthesis of advanced functional materials,^{25, 56-67} as encapsulation agents^{61-63, 67} and as adaptive liquid microlenses.⁶⁸

The principal advantage of using gels as functional components of (μ TAS) systems is that conventional microactuators (using electromagnetic, pneumatic, thermopneumatic or electrostatic principles for its functioning) require external power sources for their operation. Often, assembly lines and microcontrollers that constitute the power supply, far exceed the size of the miniaturized devices, thus restricting their use in portable/point-of-use applications from economical and practical standpoints.²¹ The use of gels that have functionalities responsive to thermal,³⁶⁻³⁹ photo^{40, 69} or chemical (ionic strength or pH) changes^{41, 42, 70} in the device environment has resulted in the development of a new class of non-mechanical microactuation systems, that do not require external power supply.^{37-40, 44} In response to external stimuli, gels undergo reversible or irreversible volume transitions from expanded to collapsed states, thus bypassing the requirements for external power supplies.^{34, 44, 45, 63, 66, 71}

An effective approach to incorporating gels within a microchannel is to form gel structures *in situ*.^{21, 46, 47, 72} *In situ* gel formation is an important route to fabricate gels at precise locations in a microchannel, which otherwise would require the use of multiple-steps of microfabrication.^{21, 22} To date, *in situ* gel formation in microfluidic channels has been based on polymerization reactions, in combination with additional steps like flow focusing, geometric confinement and UV/photolithography.^{21, 24, 46, 47, 57, 58, 60-64, 67, 73-79}

As an illustration, Beebe *et al* did pioneering work to fabricate active hydrogel components within microfluidic channels, by direct photo patterning of a liquid phase. This method allows for rapid, easy and *in situ* formation of stimuli-responsive flow components with exquisite high-definition designs (Fig. 6.8).²¹ An important feature of these hydrogels was their rapid response times (less than ten seconds) to changes in

external stimuli (pH). However, many of the hydrogels, particularly with high aspect ratios were found to be structurally weak and the use of prefabricated posts in microchannels was required to provide structural support and stability (Fig. 6.9).²¹ Similarly, Koh and Pishko incorporated biological grade polyethylene glycol (PEG) hydrogel microstructures into microchannels using photoreaction injection molding. Although a wide array of structures were achievable through this method, it required multiple steps of microfabrication and alignment (Fig. 6.10).²²

In some cases, charge-based cross-linking reactions have also been used to create gels and gel-based structures, such as those prepared from calcium chloride and sodium alginate.^{26, 33, 65} However, even such electrostatic cross-linking routes to gel formation require them to be carried out in a flow focusing geometry or with an additional polymerization step (Fig. 6.11).^{26, 57, 60, 65, 80, 81}

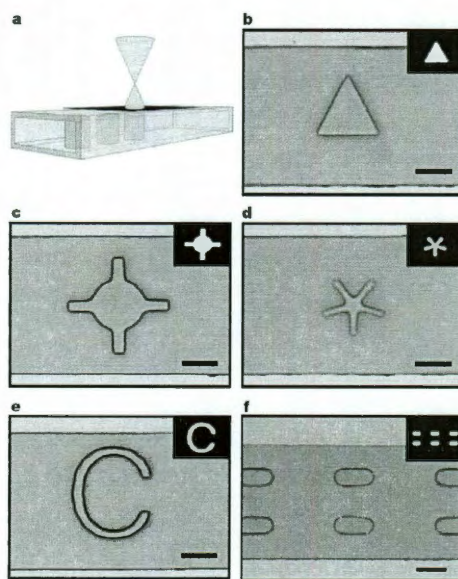


Figure 6.8: Rapid *in situ* formation of hydrogels in microchannels by direct photo patterning. (a) The fabrication procedure utilizes an online ultraviolet (UV) source and a photomask that transfers designs to the liquid phase with different shapes and patterns (b-

f). Note: The photomask containing respective designs are listed at the top right corner of each photograph in (b-e). (b) Triangle shape (c) Convex shaped pattern (d) Concave shaped pattern (e) High aspect ratio design shaped in the English alphabet “C” (f) Simultaneous polymerization of multiple structures with a single exposure of UV light. Scale bars: (b-e): 250 μm ; (f): 500 μm (Figure adapted from Beebe *et al*).

Bazargan and Stoeber recently reported on reversible gelation in microchannels from thermoresponsive pluronics with salt solutions of Na_3PO_4 . Gelation at room temperature was achieved, although it was found to occur within a limited range of pluronic and salt concentrations.^{23, 82}

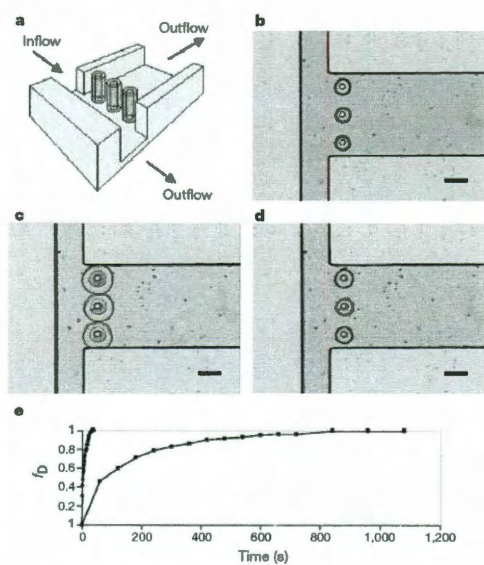


Figure 6.9: Prefabricated posts in a microchannel to provide structural support for hydrogels. (a) Diagram depicting hydrogel jackets around posts (b) Actual device after polymerization of hydrogels. (c) Hydrogel jackets block side channel branch in expanded states. (d) Contracted hydrogels allow fluid to flow down the side branch. (e) Improvement in time response of hydrogel jacket design (curve depicted by circles) versus alternate design using larger cylindrical structure but without hydrogel jacket (curve depicted by squares). f_D is the fractional change in diameter (scale bars: 300 μm) (Figure adapted from Beebe *et al*).

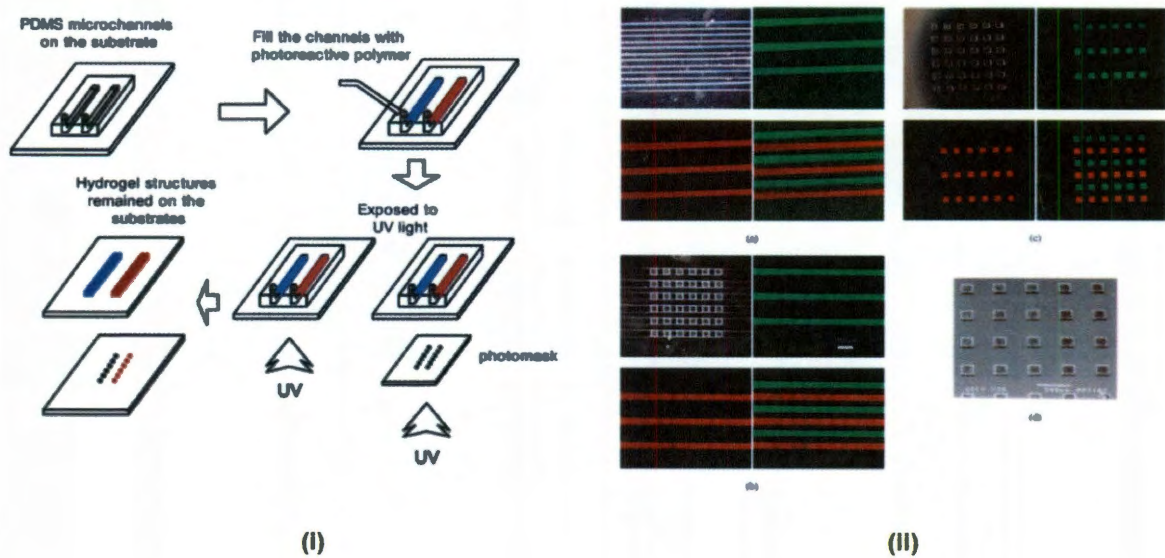


Figure 6.10: (i) Photoreaction injection molding procedure to incorporate hydrogel channels within PDMS microchannels (ii) Arrays of hydrogel microstructures containing different fluorophores. (Top Left or (a)) Six channels filled with precursor solutions containing Fluorescein Isothiocyanate (FITC) and Tetramethylrhodamine isothiocyanate (TRITC) alternatively. (Bottom Left or (b)) Hydrogel microstructures inside microchannels upon photopolymerization. (Top Right or (c)) Array of hydrogel microstructures obtained after removal of PDMS microchannels. (Bottom Right or (d)) Scanning electron microscope image of the hydrogel array. (Figures adapted from Koh and Pishko).

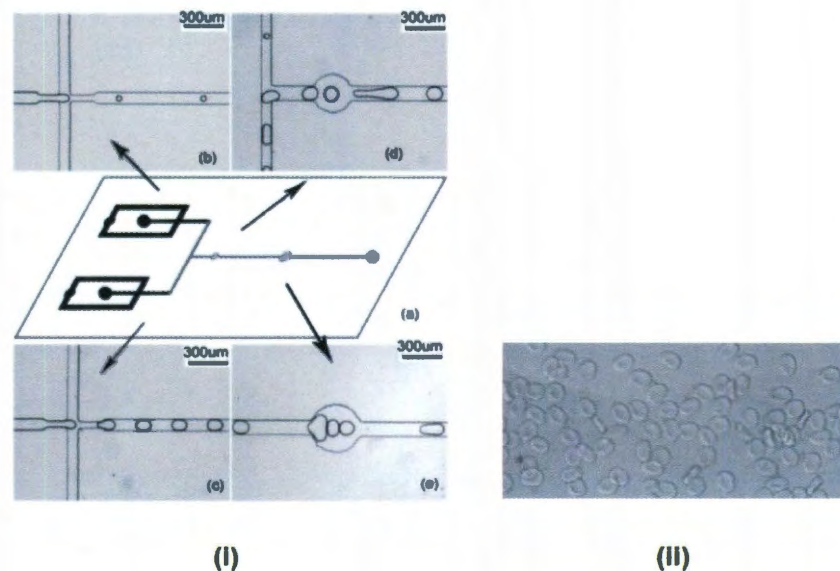


Figure 6.11: (i) (a) Schematic of microfluidic device used to prepare calcium alginate gels by cross-linking reactions of sodium alginate with calcium chloride, utilizing either

one (b, c) or two (d, e) flow-focusing step schemes. (b) One-flow focusing channel to generate sodium alginate droplets. (c) Another flow-focusing channel to generate CaCl_2 droplets. (d, e) Fusion channels with two circular expansion chambers where calcium alginate particles are formed, corresponding to two different conditions of volumetric flow rates. (ii) Optical microscopy images of calcium alginate particles (mean size of particle corresponds to $30\ \mu\text{m}$) (Figure adapted from Liu *et al*).

From the above discussion, it is apparent that a lot of progress has been made in gel formation in microfluidic channels that serve as active components in μTAS systems. Further, gel particles have additionally been synthesized that constitute a new class of advanced materials. However, the challenge to form gels *in situ* and without the requirement of microfabrication methods is yet to be realized. Furthermore, reversibility of gel thickness is controllable for the case of hydrogels, whereas gels formed via electrostatic reactions of calcium chloride and sodium alginate result in irreversible gels.

In the next section, we describe our contribution to the field of *in situ* gel formation in microfluidics. We have found that when a linear cationic polymer (poly(allylamine hydrochloride) (PAH)) reacts with a multivalent anion (trisodium citrate) under shear flow, polymer gelation can be achieved *in situ* and at room temperature. To the best of our knowledge, this is the first example of *in situ*, in-channel, room temperature polymer gel formation that is based on electrostatic interactions and does not require an immiscible phase or a flow focusing device. We find that the polyamine exhibits shear-thickening behavior while cross-linking with citrate to form viscoelastic gel phases, and that the gels remain stable and intact after cessation of flow.⁸³

6.2.3 Materials and Methods

6.2.3.1 Materials

Chemicals used in microfluidic template fabrication, channel fabrication and in PAH-citric acid interaction studies were procured from chemical suppliers and used without any further purification. Hydrogen peroxide (H_2O_2 , 30% (v/v)) and sulfuric acid (H_2SO_4) were procured from Fisher Scientific. A piranha solution used to clean silicon wafers, was prepared by mixing H_2O_2 and H_2SO_4 in volume ratios of 1:1. The piranha solution was effective in removing organic materials from the wafers. It is important to note that this solution is highly oxidative, corrosive and possibly explosive, and requires careful handling. SU-8 50 photoresist and SU-8 developer solutions were purchased from Microchem Corporation. Poly(dimethylsiloxane) (PDMS) used to make microfluidic channels was prepared from Sylgard 184[®] kits purchased from Dow Corning. The kit consists of a liquid silicone rubber elastomer base (vinyl-terminated PDMS) and a curing agent (mixture of a platinum complex and copolymers of methylhydrosiloxane and dimethylsiloxane) that was mixed in a weight ratio of 10:1 to result in liquid PDMS.

Poly(allylamine hydrochloride) (PAH, M_w : 70,000 g mol^{-1}) was obtained from Fisher Scientific and trisodium salt of citric acid (trisodium citrate or simply citrate) from Sigma-Aldrich. Unless specified otherwise, the pH of PAH and citrate solutions were maintained at their natural pH of preparation (pH of PAH was 4.38 and that of trisodium citrate was 8.38). Sodium hydroxide (1N NaOH) and hydrochloric acid (1N HCl) used in investigating the dependency of PAH-citric acid interactions on pH were purchased from Fischer Scientific. For fluorescence studies, charged dyes such as Fluorescein Isothiocyanate (FITC) and Rhodamine B isothiocyanate (RITC) were purchased from

Sigma-Aldrich. FITC and RITC dyes were conjugated to PAH for fluorescence studies using a membrane dialysis protocol described elsewhere wherein 1 % (w/v) of PAH was replaced by its conjugated variant.⁸⁴ Unless specified otherwise, all fluorescence studies utilized PAH conjugated with RITC (called PAH-RITC). A neutral fluorescent dye (dextran-tetramethylrhodamine or dextran-Rh) was procured from Invitrogen Corporation. Studies featuring the neutral dye were also performed at dye concentrations of 1% (w/v). All solutions were prepared using ultrapure grade water (18.2 M Ω -cm, Barnstead Nanopure Diamond System).

6.2.3.2 Microfluidic Master Template and Device Formation

Microfluidic channels used in this study have an architecture that consists of three inlet channels (width \times height, 50 $\mu\text{m} \times$ 50 μm) that merge to form the main channel (width \times height, 150 $\mu\text{m} \times$ 50 μm). The device was fabricated using standard replica molding techniques and photoresist processing guidelines.⁸⁵⁻⁸⁸ First, an inverse layout of the microchannel pattern was generated using conventional photolithography techniques in a Class 100 clean room facility (Rice University). Silicon wafers (University Wafers, 4-in. mechanical grade) were pre-cleaned in piranha and dehydrated at 200 °C. A layer of 50 μm thick negative UV photoresist (SU-8 50) was spun onto the wafer using a spin coater (Headway Research Inc., 2000 rpm for 30 seconds) and soft baked on a hot-plate at 95 °C for 20 minutes. Next, the device designed using AutoCAD and printed onto a chrome mask (Fineline Imaging), was transferred to the photoresist by a conventional contact aligner (SÜSS Mask Aligner MJB4). The photoresist was developed in SU-8 developer

solution to remove uncross-linked resist. This gave the master template with positive relief of the microchannels.

In fabricating the microfluidic device, liquid PDMS was poured onto the silicon master, degassed for 20 minutes and cured at 80 °C. Holes were punched into the cured PDMS channels which were then treated with UV/ozone environment (Novascan) and bound to glass slides. Tubings (SCI Scientific Commodities, 0.58 mm inner diameter) were inserted at inlet and outlet ports and the junctions were rendered air-tight using epoxy.

6.2.3.3 Monitoring Gel Formation

While imaging, the device was placed on the stage of an inverted microscope (Olympus) and reactants were flowed at controlled rates using either a syringe pump (Harvard Apparatus Pump 33) or a gas displacement pump (Fluigent MFCS 8C), as shown in Fig. 6.12. Unless specified otherwise, PAH was flowed through the central channel in all studies and citric acid was flown through the side channels. Events were monitored by video microscopy with a digital camera (Hamamatsu) at a rate of 10 frames/second using Simple PCI software. Structures resulting from PAH-citric acid interactions were characterized by optical microscopy (Olympus IX71) and confocal microscopy (Carl Zeiss LSM 510). In fluorescence studies, a laser excitation wavelength of 488 nm was chosen for FITC ($\lambda_{\text{Ex}} = 494.5 \text{ nm}$, $\lambda_{\text{Em}} = 519 \text{ nm}$) and an excitation wavelength of 543 nm was selected for both, RITC ($\lambda_{\text{Ex}} = 560 \text{ nm}$, $\lambda_{\text{Em}} = 580 \text{ nm}$) and dextran-Rh ($\lambda_{\text{Ex}} = 555 \text{ nm}$, $\lambda_{\text{Em}} = 580 \text{ nm}$). Image analysis and intensity profiling of fluorescing structures were carried out using Simple PCI and Image J (National Institutes of Health) softwares.

In studying PAH-citric acid interactions in microchannels, channels were first primed with PAH-RITC drawn through the central channel and ultrapure water through the side channels. After priming, the ultrapure water stream was replaced by citric acid buffer. Initial PAH concentration was 1 mg/mL and concentration of citric acid was adjusted so that charge ratio (R) of citric acid to PAH varied from 0.1 to 1 to 10 to 50. (Charge Ratio (R) is defined as the ratio of total negative charge of the added salt to the total positive charge of the polymer, $R = \frac{(\text{anion}) \times (z^-)}{(\text{cation}) \times (z^+)}$, where z^- is the negative charge per molecule of citric acid (3^-) and z^+ is the positive charge per PAH monomer (1^+). The base polymer concentration for calculations of citric acid at all specified an R ratio was 1 mg/mL).

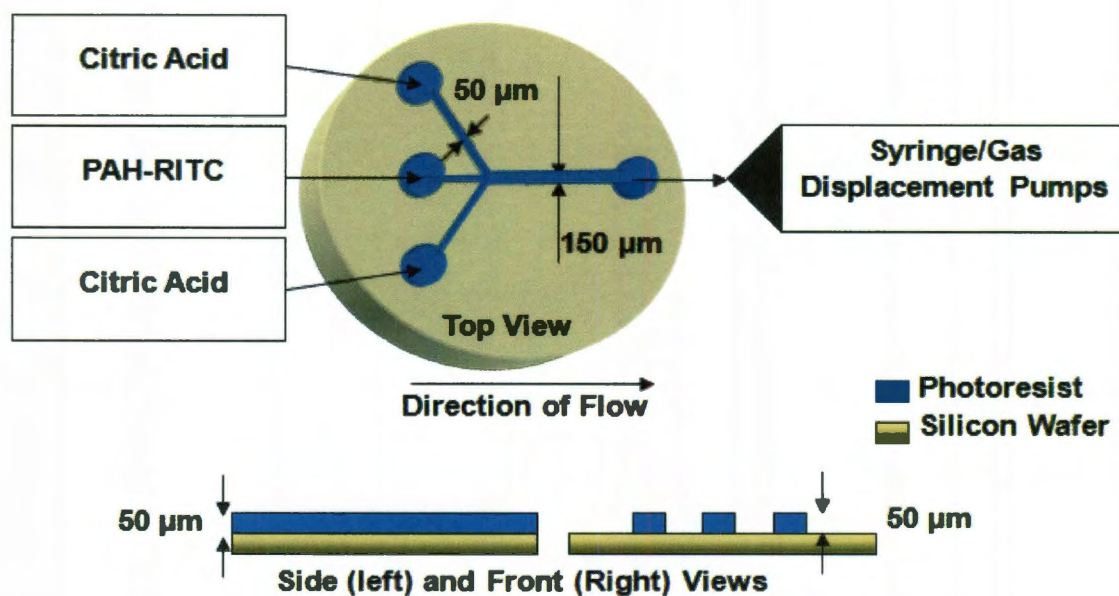


Figure 6.12: Schematic depicting experimental set-up of the microfluidic device and flow control systems used to study PAH-citrate interactions.

Flow of reactants was individually varied at volumetric flow rates of 25 μL/hr, 25 μL/min, 25 mL/hr and 25 mL/min (corresponding to flow rates from 0.025 to 1500

mL/hr). While it takes a minimum of 16 experiments to verify the resulting structures (for 4 R ratios and 4 flow rates), most data points were repeated a minimum of three times to ensure reproducibility of data and to obtain reliable statistics. For cases where flow rates were 25 $\mu\text{L/hr}$ or 25 $\mu\text{L/min}$, the experiments were repeated twice on account of the lengthy time duration of the experiment.

6.2.4. Results and Discussion

6.2.4.1 Nature of Structures formed in Microfluidic Channels

Predominantly, three types of structures (aggregates, gels and droplets) were seen to form. Co-existence of multiple structures was seen to occur in the microfluidic channel for several of the investigated conditions. Structures observed in the microfluidic device were plotted on a state diagram, shown in Fig. 6.13 as a function of R ratio and flow rate of reactants.

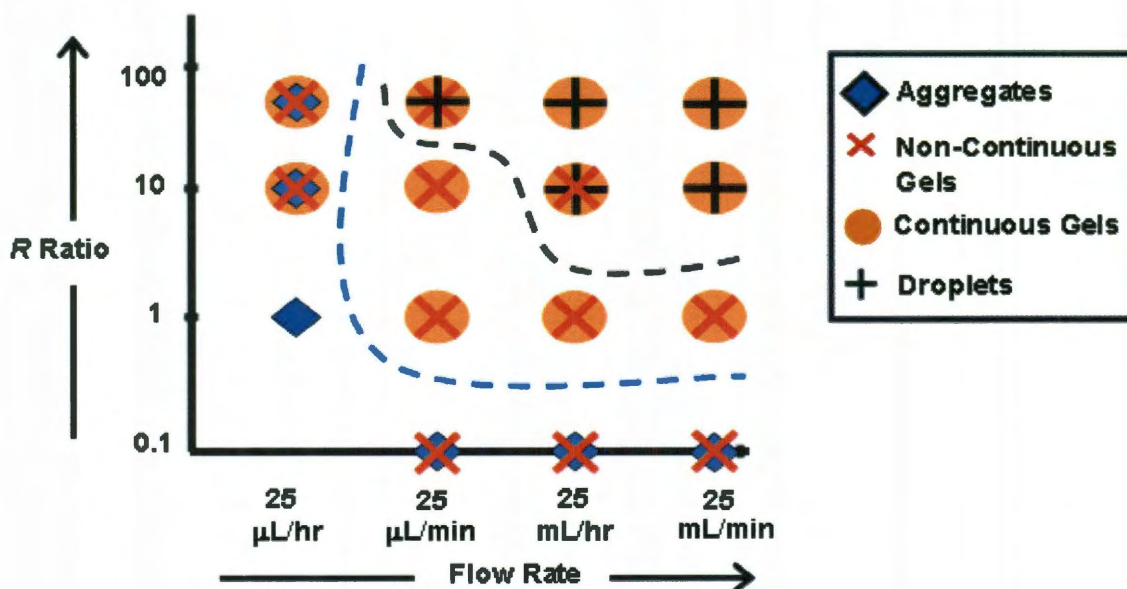


Figure 6.13: Nonequilibrium state diagram summarizing changes in state of PAH from PAH-citrate interactions. (Diagram constructed from changes observed in PAH stream

within the first five minutes of reacting flow. Initial inlet PAH concentration was fixed at 1 mg/mL for all cases). Regions west and south of dotted line demark the space where aggregates could be resolved under fluorescence microscopy and regions north and east of dashed line demark the space where droplets appeared.

These nonequilibrium structures correspond to those that emerged within a specific cut-off time interval. Eventually all conditions led to the formation of a gel phase. The cut-off time was fixed at 5 minutes, given that most structures formed within this time frame with the exception of a few cases of extreme R ratios or flow rates, where time required for structure formation spanned across several tens of hours. The cut-off time allowed us to probe the emerging structures and mechanism leading to gel formation.

(a) Citrate-bridged aggregates of PAH or PAH-citrate aggregates

The first structures that emerged were PAH-citrate aggregates that formed at the interface between the citric acid and PAH streams, as illustrated in Figs. 6.14 (a-c). These aggregates appeared as micron-sized spheres and as bright spherical spots under fluorescence mode, as shown in Fig. 6.14 (b). Upon cross linking, the fluorescence intensity of the PAH-citrate aggregates was seen to be significantly higher than the background fluorescence intensity of PAH-RITC. The aggregates formed were in Brownian motion and is consistent with earlier studies by Murthy *et al*, who reported formation of aggregates by vortex-mixing PAH and citrate in batch conditions.¹⁻⁵

(b) Gel networks of PAH

After aggregates formed, gel networks of PAH cross-linked by citrate appeared as non-continuous, irregularly shaped non-spherical networks. As with the aggregates, the

formation of the non-continuous gel phase, as shown in Figs. 6.14 (d-f) also began at the interface between the polymer and citrate streams. Eventually these non-continuous gel networks formed a continuous gel, as shown in Figs. 6.14 (g-i). Our microscopy studies also revealed that gelation occurred entirely within the PAH stream, indicating that the gel was very slow in diffusing into the citrate stream. As PAH got cross-linked by citrate, an increase in the fluorescence intensity was observed as the gel phase formed. Also, the viscosity of the PAH gel was significantly higher when compared to unreacted PAH and citrate streams.

(c) Droplets of Citrate

Once the gel phase was formed, aqueous droplets rich in citrate ions emerged within the gel, as shown in Figs. 6.14 (j-l). Most droplets formed at the junction of the PAH and citrate streams as illustrated in Figs. 6.14 (j) and 6.14 (l). A noteworthy feature of droplets that formed was their deformable nature wherein, they elongated to ellipsoids under shear flow. Droplets that emerged were found to be unstable in nature and after a sufficient number-density of droplets formed (at high R ratios and high flow rates), they grew to larger droplets and droplet networks as shown in Fig. 6.14 (k).

To establish that droplets were indeed citrate-rich aqueous regions, control experiments of two fluorescent dyes was performed. In the first experiment, PAH conjugated with FITC (PAH-FITC) was flowed through the central stream while a mixture of citrate and neutral dextran-Rh dye were flowed through the side streams, as shown in Fig. 6.15 (a). PAH conjugated with FITC was selected in this experiment over previously used PAH-RITC due to its appreciable difference in excitation wavelength

over dextran-Rh. Neutral dextran-Rh was selected to prevent electrostatic interactions of the dye with PAH. Upon droplet formation, reactant flow was stopped and the channel was imaged under a confocal microscope using FITC and Rhodamine filters. Fluorescence imaging revealed that droplets appeared dark under the FITC filter, thus indicating an absence of PAH in the droplets as shown in Fig. 6.15 (b). Droplets appeared bright under the Rhodamine filter, thereby indicating the presence of dextran-Rh inside the droplets, as shown in Fig. 6.15 (c). Intensity profiling across a magnified region of a representative droplet, as illustrated in Fig. 6.15 (e) and Fig. 6.15 (f) was carried out which confirmed the absence of PAH within the droplet and presence of dextran-Rh in regions within the droplet. A negative control experiment featured replacing citrate streams with a water-dextran-Rh stream upon onset of polymer gelation and droplet formation. It was seen that no droplets emerged, thereby establishing the requirement of citrate for droplet formation (Fig. 6.16). The citrate solution emerged as droplets only after completely cross-linking the PAH into a continuous gel. A plausible explanation for the emergence of citrate-rich droplets in completely gelled regions of PAH is that the gel remains permeable to the citrate solution. It is noteworthy that the driving force for citrate to diffuse into the PAH stream, even upon completely cross-linking PAH into a continuous gel, is predominantly from a concentration gradient, given that the concentration of citrate entering the side streams of the microfluidic channel was fixed. It is possible that the citrate ions exist as a separate phase in citrate-rich droplets, possibly to screen itself from the hydrophobic organic groups of cross-linked PAH. The presence of the neutral dextran-Rh dye specifically within the citrate-rich droplet phase and its absence from the gelled PAH region supports the concentration gradient driven

argument of citrate ion diffusion and the hydrophobic nature of the cross-linked PAH gel that results in the emergence of citrate-rich aqueous droplet phases.

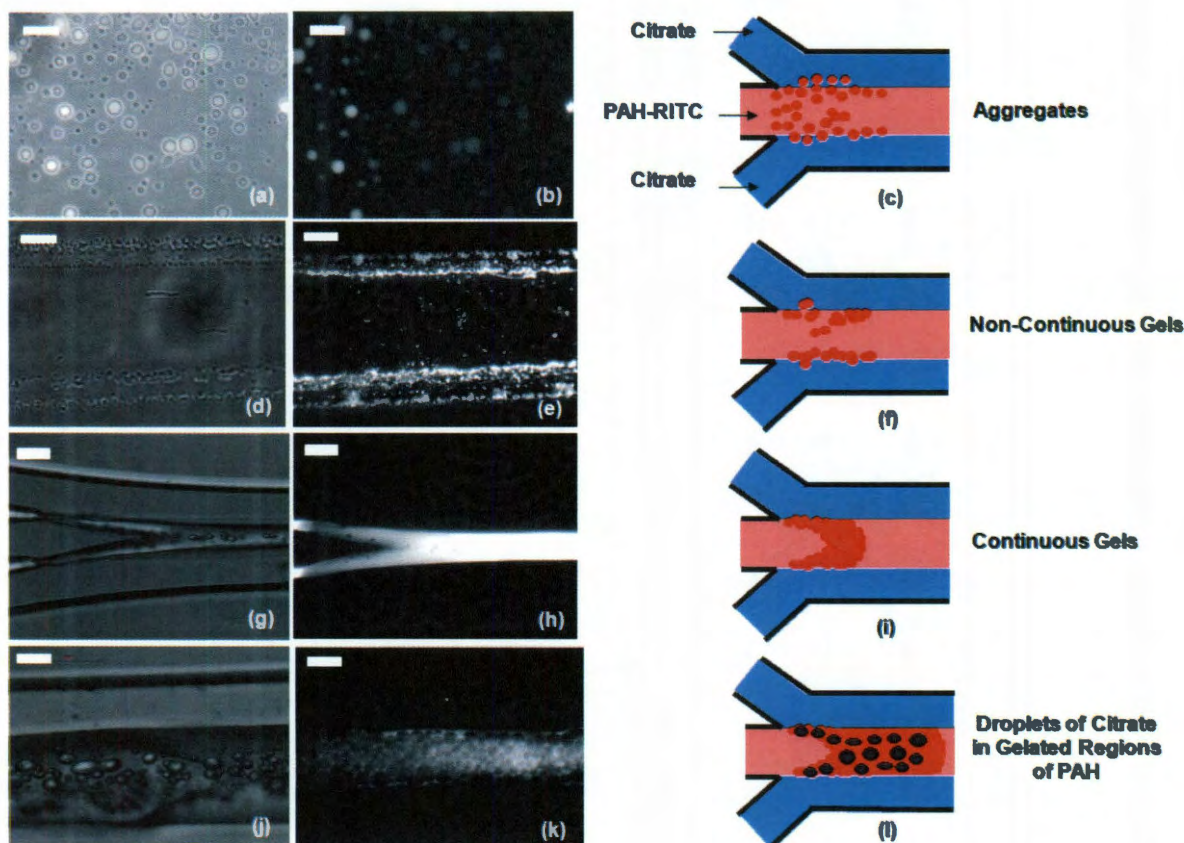


Figure 6.14: Optical and fluorescence microscopy images of structures formed in microfluidic channels from PAH-citrate interactions. (1) PAH-citrate aggregates (formation conditions: $R = 10$, PAH = 1 mg/mL, flow rate = 25 $\mu\text{L/h}$): (a) bright field and (b) fluorescence images and (c) schematic of region where aggregates formed in the microfluidic channel (scale bars - a, b: 10 μm). (2) PAH cross-linked incompletely to form noncontinuous gels (formation conditions: $R = 0.1$, PAH = 1 mg/mL, flow rate = 25 mL/h): (d) bright field and (e) fluorescent images and (f) schematic of the region in the microfluidic channel where discrete gels formed (scale bars-d, e: 10 μm). (3) PAH cross-linked completely to form continuous gels (formation conditions: $R = 50$, PAH = 1mg/mL, flow rate = 25 mL/h): (g) bright field and (h) fluorescent images and (i) schematic of the region in the microfluidic channel where continuous gels formed (scale bars - g, h: 50 μm). (4) Droplets rich in citrate ions (formation conditions: $R = 50$, PAH = 1mg/mL, flow rate = 25mL/min): (j) bright field and (k) fluorescent images of citrate droplets within the continuous gel stream of the microfluidic channel. (l) Schematic depicting droplet formation in the microfluidic channel. Droplets emanate from the junction of the microfluidic channel after reactant streams first interact and form

continuous gels. The droplets that formed flowed along the length of the channel. (scale bars - j, k: 25 μm)

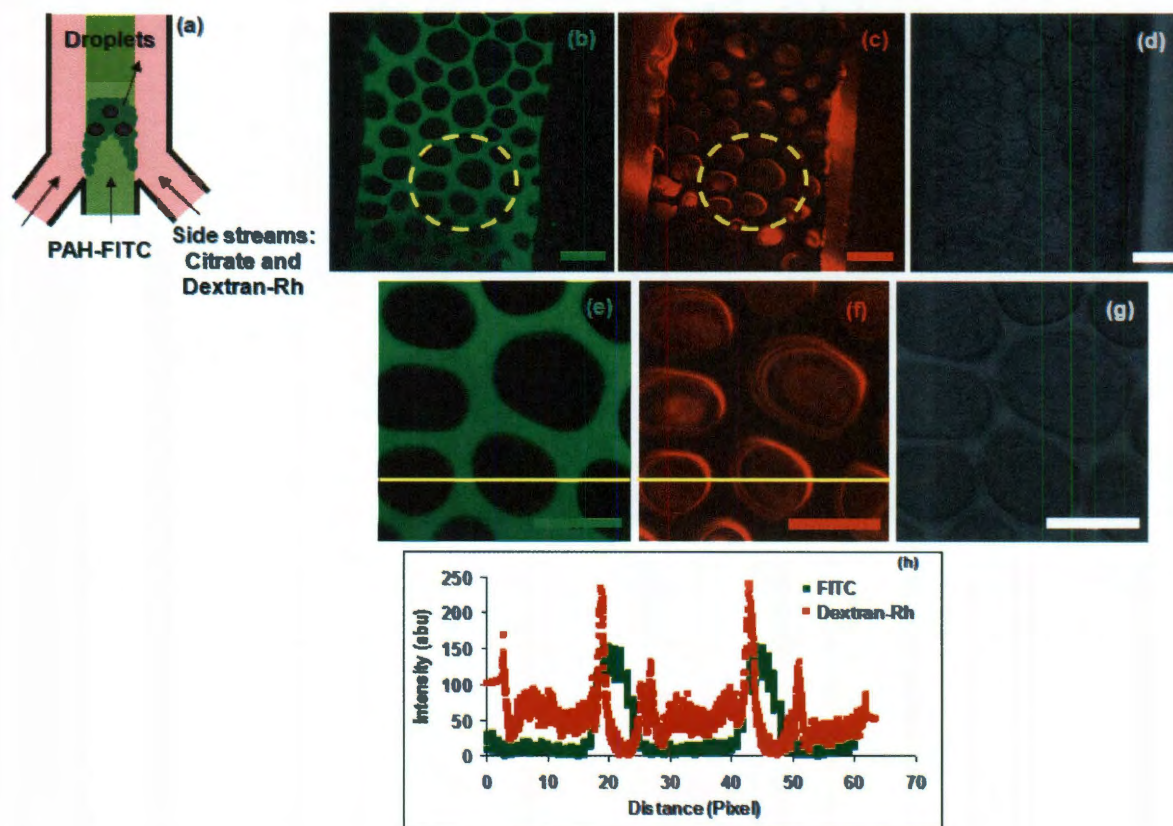


Figure 6.15: (a) Schematic to elucidate the nature of droplets. A neutral dye (dextran-tetramethylrhodamine) was added to the citrate stream and reacted with PAH-FITC under conditions of $R = 10$, PAH = 1 mg/mL, and flow rate = 25 mL/h. Upon droplet formation, the flow was stopped and the reactant streams were observed in fluorescence mode of a confocal microscope. (b) Confocal images of droplets observed under a FITC filter. (c) Confocal images of droplets observed under a rhodamine filter. (d) Differential interference contrast (DIC) image of droplets corresponding to images b and c. (e) Magnified region of a droplet observed through a FITC filter that corresponds to the circled region in image b. (f) Magnified region of a droplet observed through a rhodamine filter that corresponds to the circled region in image c. (g) DIC image of droplets corresponding to images e and f. (h) Intensity profiles of droplets in images e and f along regions marked with a white line establishes the absence of PAH in droplet and the diffusion of dextran dye into the interior of the droplet. (All scale bars are 20 μm)

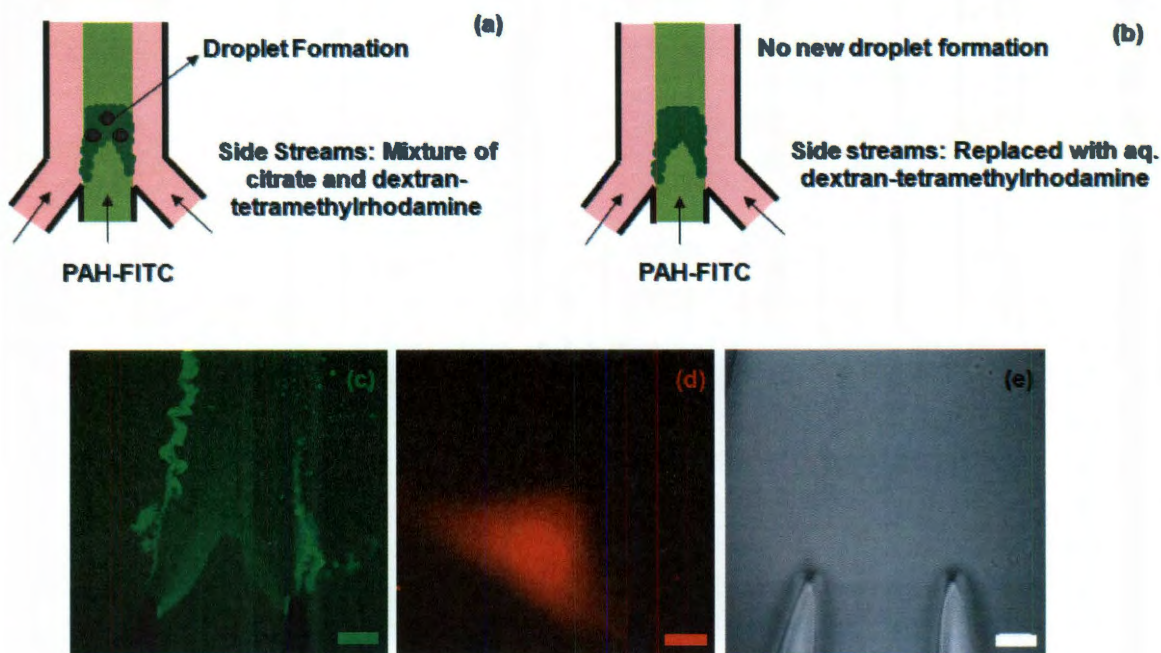


Figure 6.16: Negative control experiment to ascertain the requirement of citrate in forming droplets. Schematics (a, b) describe experiments that establish requirement of citrate to form droplets (Refer Figs. 6.12 and 6.14). Image (c) reveals that no new droplet formed when the citrate stream containing neutral dextran dye was replaced with an aqueous solution of neutral dextran dye. Images (d) and (e) are corresponding images under Rhodamine filter and in DIC mode respectively. (All scale bars: 20 μm)

6.2.4.2 Structural Changes in Microfluidic Channels

The previous section described the nature of structures from PAH-citrate interactions in microfluidic channels. From the nonequilibrium state diagram, it is evident that multiple structures co-exist across all R ratio-flow rate pairs. Fig. 6.17 is a representative confocal image of the microchannel that clearly illustrates co-existence of multiple structures. It can be seen from Figs. 6.13, 6.14 and 6.15 that the following trends emerge of structural evolution from PAH-citrate interaction:

- (1) PAH-citrate aggregates formed under conditions (a) R ratios ≥ 1 when flow rate was at 25 $\mu\text{L}/\text{hr}$. (b) R ratio = 0.1 for flow rates of 25 $\mu\text{L}/\text{min}$ or higher.

(2) Polymer gels emerged when (a) R ratios > 1 for flow rate of $25 \mu\text{L/hr}$ where non-continuous/continuous gels co-existed with aggregates but not droplets. (b) For R ratio of 0.1 and flow rates of $25 \mu\text{L/min}$ or higher, only non-continuous gels formed that co-existed with aggregates but not continuous gels or droplets.

(3) Droplets emerged for R ratios > 1 when flow rates were $25 \mu\text{L/min}$ or higher that co-existed with non-continuous/continuous gels. It is noteworthy that as the magnitude of flow rate increased, the R ratio at which droplets formed decreased ($R = 50$ for flow rate of $25 \mu\text{L/min}$ and $R = 10$ for flow rate of 25 mL/hr).

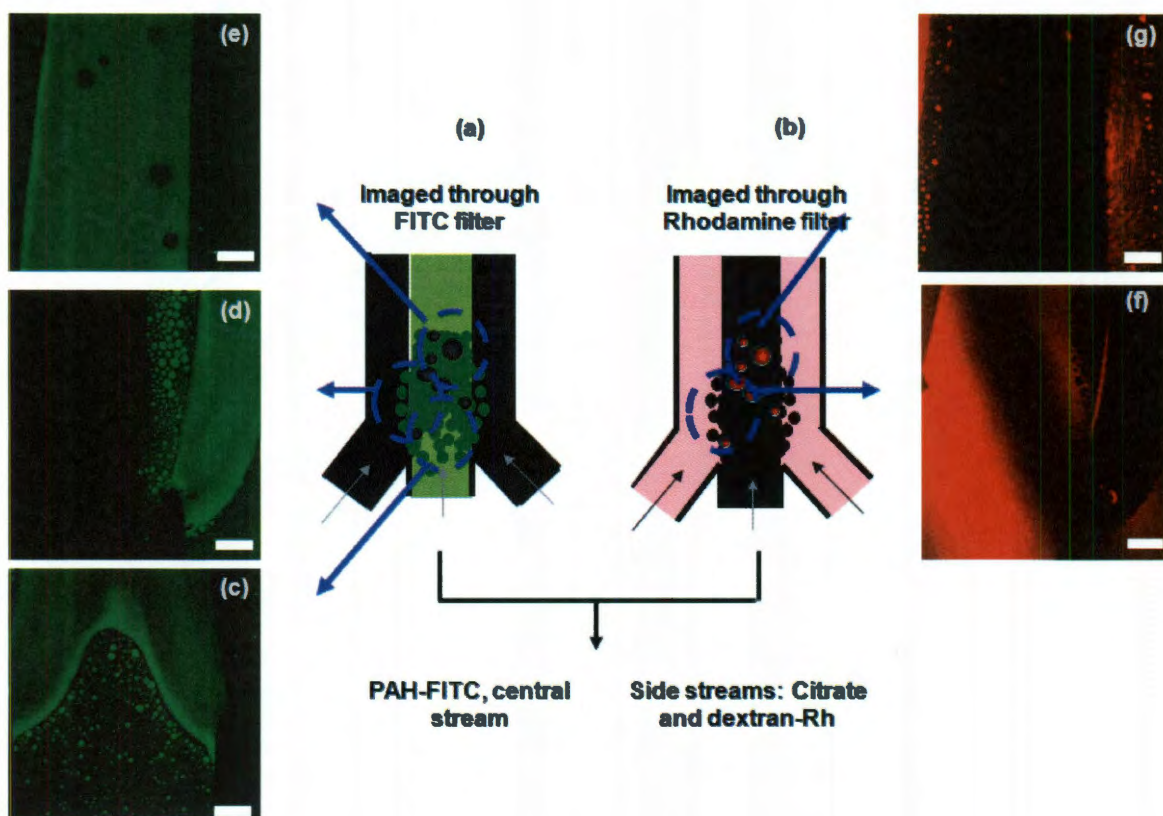


Figure 6.17: Schematic depicting the coexistence of structures in a microfluidic channel using confocal microscopy (conditions: $R = 10$, PAH = 1 mg/mL , and flow rate = 25 mL/h) when viewed under (a) a FITC filter and (b) a rhodamine filter. (c) Predominant existence of PAH-citrate aggregates (green spots) and gel (continuous green region). (d) PAH-citrate aggregates, gels, and citrate droplets (dark spots). (e) Citrate droplets present within the cross-linked polymer gel. (f) Complementary region to image d as viewed

through a rhodamine filter. PAH-citrate aggregates appear as dark spots. (g) Complementary region to image e as viewed through a rhodamine filter. The PAH gel appears dark, and droplets of citrate appear red because of the presence of dextran-Rh. (All scale bars are 20 μm)

The following sections explain the effects of charge ratio, flow rates and pH on structure formation.

6.2.4.3 Effects of R ratio and Flow Rates

The trends shown in Fig. 6.13 indicate that R ratio and flow rate of reactants affected the time required to form a PAH gel. For a given flow rate, an increase in R ratio provides a higher concentration of citrate ions into the microfluidic channel. The resulting effect was that aggregates appeared at $R = 1$ for a flow rate of 25 $\mu\text{L/hr}$, whereas for a higher R ratio of 50 and at the same flow rate, non-continuous and continuous gels formed along with aggregates. Given flow rates were equal, it is indicative that at higher R ratios, there was an increase in the rate of aggregate formation that resulted in faster gelation of PAH. This also explains the general trend of an increase in emergence of structures observed within the five minute time interval, as flow rates were increased for a given R ratio.

An increase in flow rate for a given R ratio has dual effects: Higher flow rates at a given R ratio increases the concentration of citrate ions in the channel from enhanced convection mediated transport. Higher flow rates also have an additional effect in that increased shear stresses promote gelation of PAH from combination of aggregates. It is important to note that simple diffusion of citrate in the absence of fluid flow did not promote gelation of PAH. To elaborate, when R ratio was fixed at 10, gelation of PAH occurred when reactants were flowed at 25 mL/min. However, when flow was halted by

equalizing pressure, no further gelation in PAH was observed downstream of the channel, although diffusion of citrate ions to the polymer stream continued from existing concentration gradients and electrostatic interactions (Fig. 6.18).

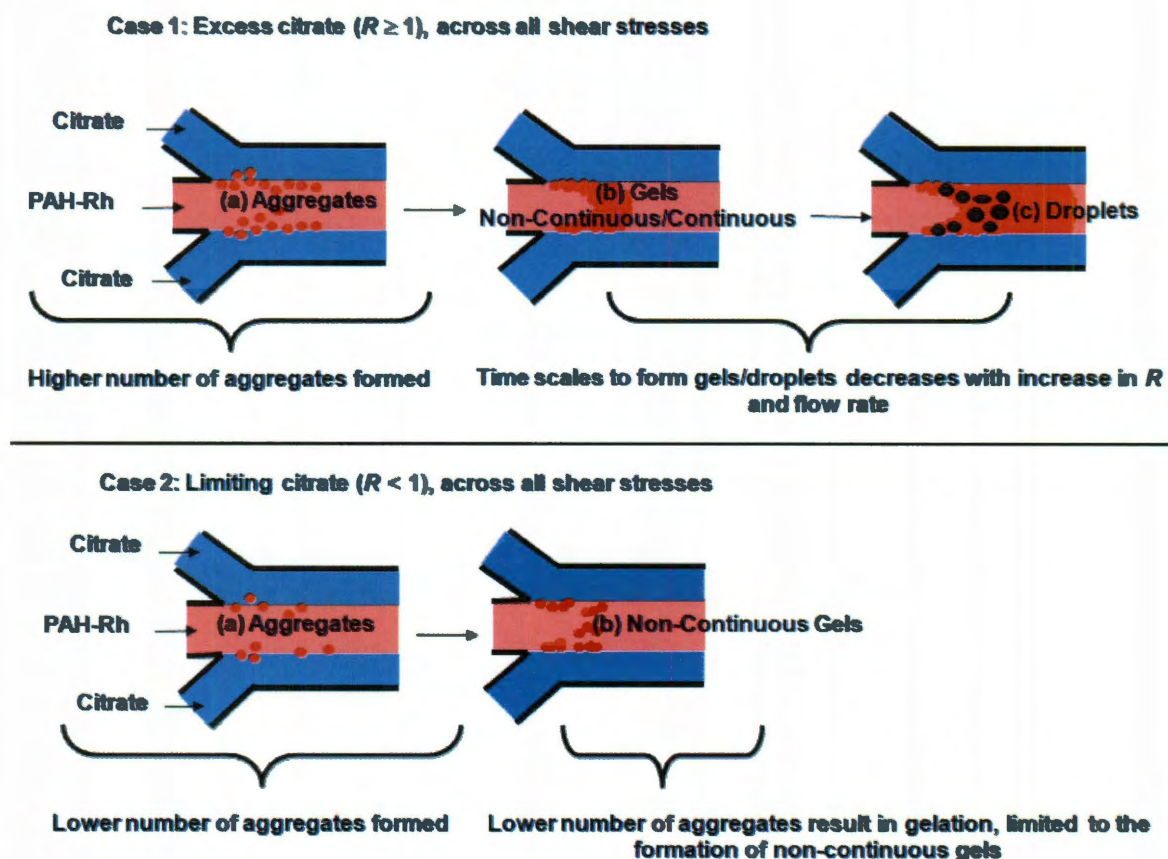


Figure 6.18: Schematic of structures from R ratio and flow dependent PAH-interactions in microchannels.

It can also be seen from Fig. 6.13 that in addition to shear stresses from flow rates, a threshold citrate concentration was required to form continuous gels from PAH-citrate aggregates. For the case where citrate ion concentration was limiting with respect to PAH at $R = 0.1$, cross-linking of PAH-citrate aggregates to form continuous gels did not occur, even several hours upon onset of reactant flow into the flow channels (Fig. 6.18). This

was true across the flow rates (and corresponding shear stresses) investigated ranging from 25 $\mu\text{L/hr}$ to 25 mL/min and may be attributed to an inadequate number of aggregates formed when citrate was limiting in concentration, thus rendering incomplete gelation of PAH across the range of flow rates (and shear stresses) investigated (Fig. 6.18).

6.2.4.4 Effect of Laminar Flow Conditions

A feature of our investigation on polymer gelation in microfluidic channels is that gelation and droplet formation were seen to occur specifically within the PAH stream of the microfluidic device. This may be rationalized from the laminar flow profiles prevalent in the microfluidic environment. It is known that the effective time t for diffusion of a species i across the length L in a channel is given by $t_i = \frac{L^2}{D_i}$, where D_i is the effective diffusivity of species i (sum of electrostatic and concentration gradient components). It is also known that the diffusivity of a polymer D_P (such as PAH, $M_w = 70$ kDa) is significantly smaller than that of a multivalent ion D_C (such as citrate, $M_w = 294$ Da). Hence, it follows that $t_P > t_C$, implying that the time required for citrate ions to diffuse into the PAH stream is much lower than that for the PAH to diffuse into the stream containing citrate ions. After the citrate ions diffuse into the PAH stream to cross-link the polymer, the viscosity of the resulting polymer gel stream increases and the diffusivity D_G of the gel becomes lower than both, the diffusivity of unreacted PAH and unreacted citrate ions ($D_G < D_P < D_C$). This further increase the time-scale for the polymer to diffuse through the gel matrix to the citrate stream, thus restricting gelation to occur mainly within the polymer stream. Thus, a laminar flow environment along with

differences in diffusivity of PAH and citrate restrict structure formation to within that of the polymer stream. To rule out geometrical effects, a control experiment was run where flow streams of reactants were switched (polymer in side streams and salt in central stream), which further confirmed that gels and droplets formed only within the polymer stream.

The trends from the state diagram and the discussions above suggest the following mechanism to explain gelation from PAH-citrate interactions in microchannels (Fig. 6.18). Under laminar flow, differences in diffusivity of PAH and citrate implies that structure formation starts at the interface between the citrate and PAH stream. Aggregates of PAH-citrate initially form when citrate ions diffuse into the PAH stream by salt-induced counter-ion condensation of the PAH backbone. Further, under shear flow, the aggregates combine to form an ionically cross-linked gel. Gelation increases with flow rates, from formation of higher numbers of aggregates by increased transport of citrate ions, and from combination of aggregates at higher shear. For the case where citrate ions exceed PAH in concentration ($R \geq 1$), gelation rates decrease with increase in R ratios and flow rates. Subsequent to continuous gel formation, excess citrate diffuses to gelled regions of PAH and exist as droplets that are rich in citrate, from saturation of available charge sites on PAH that are unavailable for cross-linking. For the case where citrate is limiting with respect to PAH, aggregates initially form which gelate PAH under shear. The extent of gelation however is limited to the formation of non-continuous gels, due to a lower number of aggregates initially formed. For this case, droplets of citric acid do not appear within the cut-off time scale, since cross-linking of PAH is incomplete.

6.2.4.5 Manipulating Electrostatic Interactions via pH

In this section, we report the effect of charge on gelation trends of PAH in a microfluidic channel. The charge on a multivalent citric acid and PAH can be manipulated using pH as a variable for respective solutions (citric acid has 3 pK_a values at 3.14, 4.77 and 6.39 and PAH has a single pK_a value at 8.5). Thereby, we show polymer gelation could be controlled using pH as a parameter.

Thus far, all studies of PAH-citrate interactions in the microchannel were carried out at a citric acid pH of 8.35 and a PAH pH of 4.38. In the following study, the pH of citric acid and PAH solutions were adjusted using 1N HCl and 1N NaOH solutions, outside of the microchannel, R ratio of a specific speciated form of citric acid to PAH was fixed at 50 (base concentration of PAH = 1 mg/mL) and flow rates of PAH and citric acid was fixed at 25 mL/hr.

We first discuss, gelation trends when PAH was positively charged (pH of PAH stream was fixed at 4.38) and the charge on citric acid was varied from trivalent to zerovalent states (See Table 6.1 for charged states of citric acid at different pH and Fig. 6.19 for corresponding gel profiles in the microchannel).

Gelation from cross-linking of PAH by the citric acid stream was seen to progressively decrease as charge on citric acid was lowered from its trivalent to zerovalent states. The PAH stream was completely cross-linked by citric acid when it was predominantly trivalent at pH 8.35 and also at its pK_a value of 6.39, where it coexisted equally as citrate³⁻ and citrate²⁻. The extent of PAH cross-linking however, reduced between the two pH levels, as citrate³⁻ progressively converted to the citrate²⁻ form.

Table 6.1: Characteristics of PAH gelation upon varying pH of citric acid (The pH of PAH was fixed at 4.38).

pH of Citric Acid Stream	Speciated States of Citric Acid	Gel Description
8.38	Citrate ³⁻ : (> 99%)	Fully cross-linked PAH stream (Figs. 6.19 (a, b))
6.39	Citrate ³⁻ : 50% Citrate ²⁻ : 50%	Fully cross-linked PAH stream (Figs. 6.19 (c, d))
5.56	Citrate ²⁻ : 77% Citrate ³⁻ : 11.5% Citrate ¹⁻ : 11.5%	Partially cross-linked PAH stream (Figs. 6.19 (e, f))
4.77	Citrate ²⁻ : 50% Citrate ¹⁻ : 50%	PAH cross-linking predominantly at the interface of PAH and citric acid streams (Figs. 6.19 (g, h))
4.0	Citrate ¹⁻ : 77% Citrate ²⁻ : 11.5% Citrate ⁰ : 11.5%	PAH cross-linking predominantly at the interface of PAH and citric acid streams (Figs. 6.19 (i, j))
3.14	Citrate ¹⁻ : 50% Citrate ⁰ : 50%	No cross-linking of PAH (Figs. 6.19 (k, l))
1.38	Citrate ⁰ : (> 99%)	No cross-linking of PAH (Figs. 6.19 (m, n))

When citric acid was primarily in its divalent state at pH 5.56, cross-linking of PAH was restricted to the interface of PAH and citric acid streams. Similar gelation trends were observed at the second pK_a of citric acid at pH of 4.77, where it coexisted equally as citrate²⁻ and citrate¹⁻ and at pH of 4.0, where citric acid was predominantly monovalent along with its divalent and uncharged forms. No gelation was observed at the first pK_a of

citric acid (pH = 3.14), where citric acid coexisted equally as citrate¹⁻ and citrate⁰) and at pH of 1.38, where the dominant species was zerovalent citrate (> 97%).

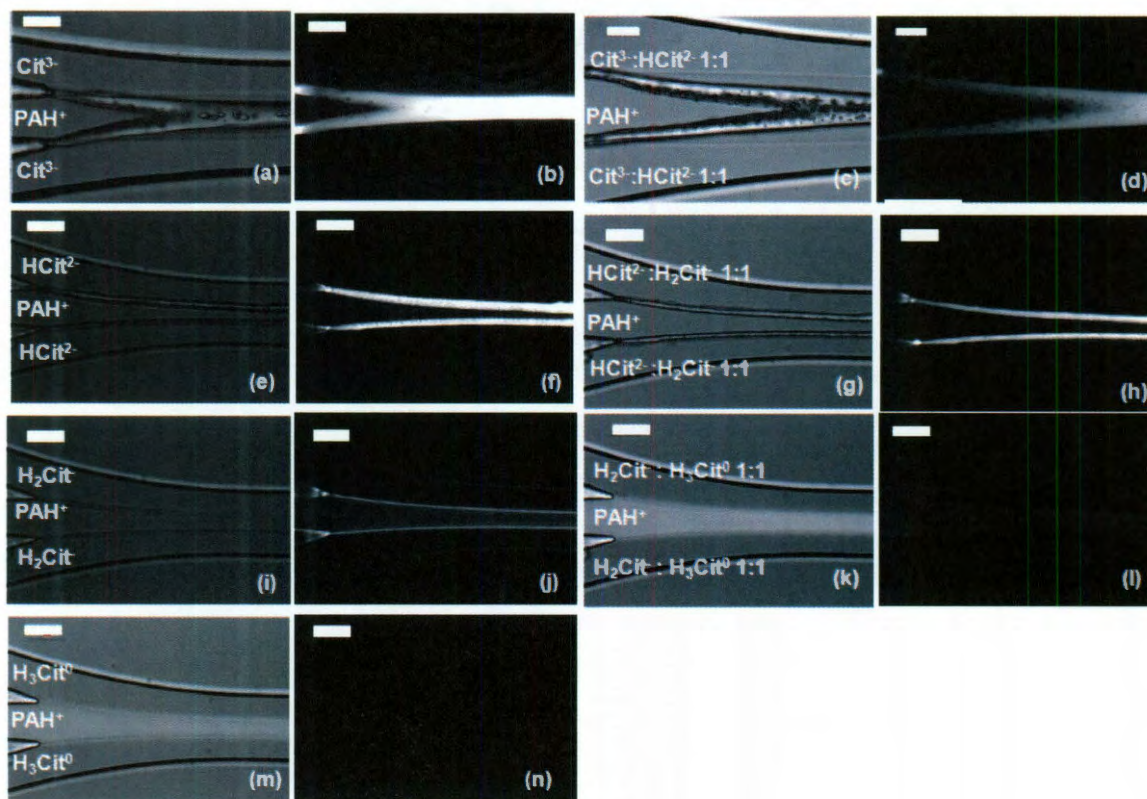


Figure 6.19: Gel profiles that emerge from interactions of PAH with citric acid. The pH of PAH was 4.38 and the pH of citric acid was varied to span its 3 pK_a values. R ratios of reactants were fixed at 50 and flow rate was maintained at 25 mL/hr. Bright Field (a) and Fluorescence images (b) when pH of citric acid stream was 8.38 (where it is predominantly in the trivalent (Cit^{3-}) state). Bright field (c) and Fluorescence (d) images when pH of citric acid stream was 6.39 (corresponds to pK_a value of citric acid where it co-exists as Cit^{3-} and HCit^{2-} in a 1:1 ratio). Bright field (e) and Fluorescence (f) images when pH of citric acid stream was 5.56 (where HCit^{2-} was at its highest theoretical level (77%)). Bright field (g) and Fluorescence (h) images when pH of citric acid stream was 4.77 (corresponds to pK_a value of citric acid where it coexists as HCit^{2-} and H_2Cit^- in a 1:1 ratio). Bright field (i) and Fluorescence (j) images when pH of citric acid stream was 4.0 (where H_2Cit^- is at its highest theoretical level (77%)). Bright field (k) and Fluorescence (l) images when pH of citric acid stream was 3.14 (pK_a value of citric acid where it coexists as $\text{H}_2\text{Cit}^{1-}$ and H_3Cit^0 in a 1:1 ratio). Bright field (m) Fluorescence (n) images when pH of citric acid stream was 1.38 (where citric acid exists predominantly in monovalent (H_3Cit^0 : > 97%) state). (All Scale Bars: 50 μm).

From the trends above, it emerges that divalent and trivalent citric acid induced cross-linking of PAH. Although gelation occurred at a pH of 4 where citric acid was predominantly monovalent, the presence of divalent citric acid species is proposed to have caused gelation. This can be inferred from an absence of gelation at pH of 3.14, where no divalent form of citric acid was present and was further confirmed by a control experiment wherein, gelation was observed upon adjusting the pH of citric acid to slightly above 3.14 (~ 3.17), where the divalent form of citrate first starts to emerge.

These observations are also consistent with our proposed mechanism of aggregates serving as precursors to gel formation under shear flow, as studies of PAH-citrate interactions in batch mode had previously established that for PAH-citrate aggregate formation to occur, it was necessary for citric acid to be in its di or trivalent forms.²

To elucidate the role of charge on PAH in gel formation, pH of PAH was adjusted to 10.25 (above its pK_a of 8.5) and pH of citric acid stream was maintained at 8.38. No gelation or droplet formation occurred when PAH was in its zerovalent form, thus further establishing the electrostatic basis of gel formation (Fig. 6.20).

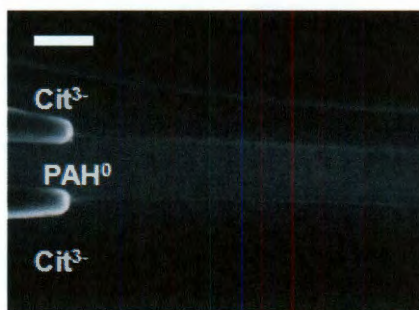


Figure 6.20: Fluorescence image when pH of PAH stream was adjusted to 10.25 (where it is uncharged: pK_a of PAH = 8.5) and the pH of citric acid was 8.38 (where it exists

predominantly as Cit^{3-}). R ratios of reactants were fixed at 50 and flow rate was maintained at 25 mL/hr. No reaction occurred of PAH and citrate under these conditions (Scale bar: 50 μm).

6.2.5 Conclusions

In this study, we describe the in situ gelation of poly(allylamine hydrochloride) (PAH) upon cross-linking by citrate anions under laminar flow conditions in a microfluidic channel. Gelation was seen to occur at room temperature, and parameters such as the charge ratio, shear stress from the reactant flow rate, and the pH of the reactant streams were seen to influence gel formation and morphology. Aggregates of PAH and citric acid initially formed by citrate-induced counter ion condensation of the PAH backbone from the diffusion of citric acid into the PAH stream. Under shear flow, aggregates combined to form noncontinuous gels across all flow rates when the charge ratio was limited in citrate. Continuous gels formed across all flow rates when the charge ratio favored citrate. Droplets of citric acid emerged in continuous gel regions where sites to cross-link PAH were saturated. The electrostatic basis of PAH-citrate interactions was shown by individually varying the pH of citric acid and PAH streams. The gelation of PAH took place only when PAH was charged and when citric acid was either in its divalent or trivalent state where aggregate formation first occurs. We believe that this is the first example of in situ, in-channel polymer gel formation that exhibits shear-thickening behavior leading to viscoelastic gels that remain stable and intact even upon cessation of flow. These gels are envisioned to have applications as nonmechanical flow regulators in microfluidic devices. Their formation could be engineered at room temperature, in situ, and at specified locations in a microchannel with the extent of flow regulation controllable by changing the reactant charge ratio and pH. Finally, we have shown that

these gels remain permeable to citrate droplets, which may enable us to encapsulate charged molecules of interest. Further studies into the stability of these droplets may lead to gels that serve as small-molecule carriers.

Returning to our original quest of forming NACs in capsules, we first decided to test if we can form NACs in the first place, based on our understanding of the state diagram. We know the flow conditions and R ratios under which aggregates appear. Based on such conditions, we formed aggregates in the microfluidic stream and upon its emergence, replaced the three streams with silica NPs (Fig. 6.21). We observed instantaneous formation of NACs in the microfluidic device, as analyzed by bright-field, fluorescence and scanning electron microscopy. While this served as further evidence of the existence of aggregates, a process modification will be required to make microfluidic formation of NACs, more tenable.

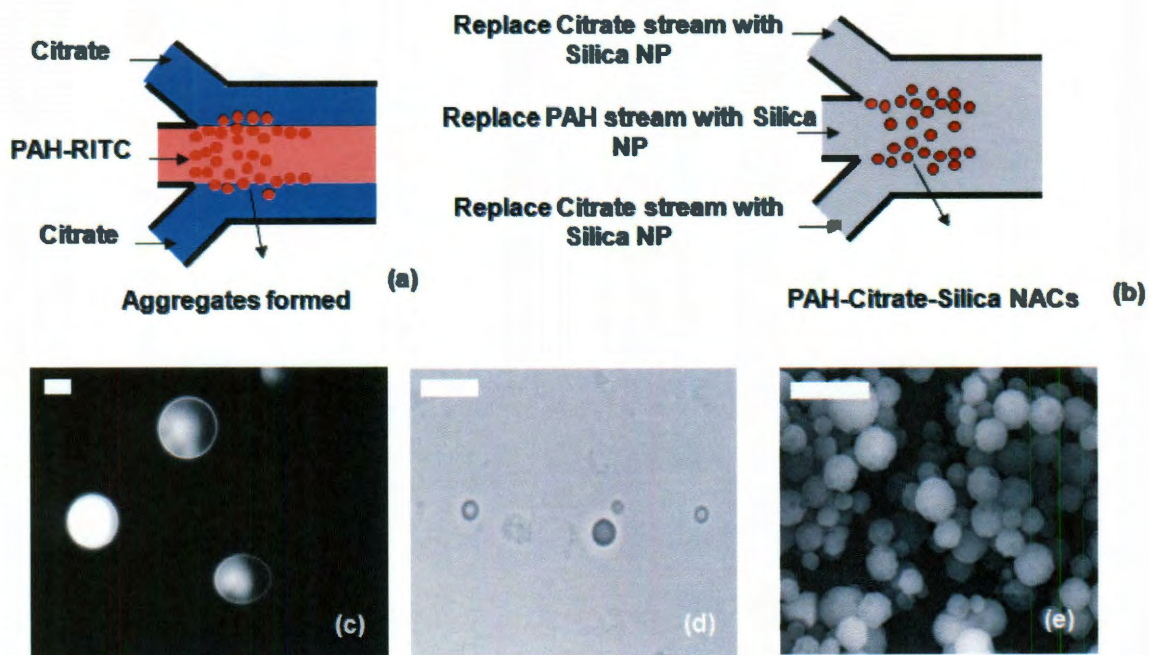


Figure 6.21: Experiment to show the formation of nanoparticle assembled capsules (NACs) in a microfluidic device. (i) PAH-RITC and citrate flowed based on conditions in

state diagram (Fig. 6.12) ($R = 10$, PAH = 1 mg/mL, flow rate = 25 μ L/hr) to form aggregate-like structures. (ii) All flow streams replaced by 20 wt.%, SiO₂ NP stream. If aggregates had indeed formed in schematic (i), reaction configuration in schematic (ii) should result in NAC formation. (iii) Fluorescence images of NAC-like structures formed in microfluidic environment. (iv) Bright field image of NAC-like structures analyzed outside of the microfluidic on a glass-slide. Characteristic NAC-like behavior observed in that, the structures were in Brownian motion (v) Scanning electron microscope (SEM) images of structures formed from schematic (ii) confirm formation of NACs. Hence, structures formed from schematic (i) were indeed aggregates of PAH-citrate.

6.3 References

1. Rana, R. K.; Murthy, V. S.; Yu, J.; Wong, M. S., Nanoparticle self-assembly of hierarchically ordered microcapsule structures. *Advanced Materials* **2005**, *17*, (9), 1145.
2. Murthy, V. S.; Rana, R. K.; Wong, M. S., Nanoparticle-assembled capsule synthesis: Formation of colloidal polyamine-salt intermediates. *Journal of Physical Chemistry B* **2006**, *110*, (51), 25619-25627.
3. Yu, J.; Murthy, V. S.; Rana, R. K.; Wong, M. S., Synthesis of nanoparticle-assembled tin oxide/polymer microcapsules. *Chemical Communications* **2006**, (10), 1097-1099.
4. Yu, J.; Yaseen, M. A.; Anvari, B.; Wong, M. S., Synthesis of near-infrared-absorbing nanoparticle-assembled capsules. *Chemistry of Materials* **2007**, *19*, (6), 1277-1284.
5. Kadali, S. B.; Soutanidis, N.; Wong, M. S., Assembling Colloidal Silica into Porous Hollow Microspheres. *Topics in Catalysis* **2008**, *49*, (3-4), 251-258.
6. Murthy, V. S.; Kadali, S. B.; Wong, M. S., Polyamine-Guided Synthesis of Anisotropic, Multicompartment Microparticles. *ACS Applied Materials & Interfaces* **2009**, *1*, (3), 590-596.
7. Whitesides, G. M., The origins and the future of microfluidics. *Nature* **2006**, *442*, (7101), 368-373.
8. Squires, T. M.; Quake, S. R., Microfluidics: Fluid physics at the nanoliter scale. *Reviews of Modern Physics* **2005**, *77*, (3), 977-1026.
9. Janasek, D.; Franzke, J.; Manz, A., Scaling and the design of miniaturized chemical-analysis systems. *Nature* **2006**, *442*, (7101), 374-380.
10. Psaltis, D.; Quake, S. R.; Yang, C. H., Developing optofluidic technology through the fusion of microfluidics and optics. *Nature* **2006**, *442*, (7101), 381-386.
11. Craighead, H., Future lab-on-a-chip technologies for interrogating individual molecules. *Nature* **2006**, *442*, (7101), 387-393.

12. deMello, A. J., Control and detection of chemical reactions in microfluidic systems. *Nature* **2006**, 442, (7101), 394-402.
13. El-Ali, J.; Sorger, P. K.; Jensen, K. F., Cells on chips. *Nature* **2006**, 442, (7101), 403-411.
14. Yager, P.; Edwards, T.; Fu, E.; Helton, K.; Nelson, K.; Tam, M. R.; Weigl, B. H., Microfluidic diagnostic technologies for global public health. *Nature* **2006**, 442, (7101), 412-418.
15. Beebe, D. J.; Mensing, G. A.; Walker, G. M., Physics and applications of microfluidics in biology. *Annual Review of Biomedical Engineering* **2002**, 4, 261-286.
16. Melin, J.; Quake, S. R., Microfluidic large-scale integration: The evolution of design rules for biological automation. *Annual Review of Biophysics and Biomolecular Structure* **2007**, 36, 213-231.
17. Bagaria, H. G.; Kadali, S. B.; Wong, M. S., Shell Thickness Control of Nanoparticle/polymer Composite Microcapsules. *Chemistry of Materials* **2009**, 23, (2), 301-308.
18. Kini, G. C.; Biswal, S. L.; Wong, M. S., Non-LBL Assembly and Encapsulation Uses of Nanoparticle-Shelled Hollow Spheres In *Advances in Polymer Sciences: Encapsulation (Modern Techniques for Nano- and Microreactors/-reactions)*, Caruso, F., Ed. Springer: 2010.
19. Roberts, M. T.; Mohraz, A.; Christensen, K. T.; Lewis, J. A., Direct flow visualization of colloidal gels in microfluidic channels. *Langmuir* **2007**, 23, (17), 8726-8731.
20. Conrad, J. C.; Lewis, J. A., Structure of colloidal gels during microchannel flow. *Langmuir* **2008**, 24, (15), 7628-7634.
21. Beebe, D. J.; Moore, J. S.; Bauer, J. M.; Yu, Q.; Liu, R. H.; Devadoss, C.; Jo, B. H., Functional hydrogel structures for autonomous flow control inside microfluidic channels. *Nature* **2000**, 404, (6778), 588.
22. Koh, W. G.; Pishko, M., Photoreaction injection molding of biomaterial microstructures. *Langmuir* **2003**, 19, (24), 10310-10316.

23. Bazargan, V.; Stoeber, B., Moving temporary wall in microfluidic devices. *Physical Review E* **2008**, 78, (6), 066303
24. De Geest, B. G.; Urbanski, J. P.; Thorsen, T.; Demeester, J.; De Smedt, S. C., Synthesis of monodisperse biodegradable microgels in microfluidic devices. *Langmuir* **2005**, 21, (23), 10275-10279.
25. Steinbacher, J. L.; McQuade, D. T., Polymer chemistry in flow: New polymers, beads, capsules, and fibers. *Journal of Polymer Science Part A-Polymer Chemistry* **2006**, 44, (22), 6505-6533.
26. Amici, E.; Tetradis-Meris, G.; de Torres, P.; Jousse, F., Alginate gelation in microfluidic channels. *Food Hydrocolloids* **2008**, 22, (1), 97-104.
27. Hernandez-Ortiz, J. P.; Ma, H. B.; Pablo, J. J.; Graham, M. D., Cross-stream-line migration in confined flowing polymer solutions: Theory and simulation. *Physics of Fluids* **2006**, 18, (12), 140602
28. Shestopalov, I.; Tice, J. D.; Ismagilov, R. F., Multi-step synthesis of nanoparticles performed on millisecond time scale in a microfluidic droplet-based system. *Lab on a Chip* **2004**, 4, (4), 316-321.
29. Caulum, M. M.; Henry, C. S., Measuring reaction rates on single particles in a microfluidic device. *Lab on a Chip* **2008**, 8, (6), 865-867.
30. Ahmed-Omer, B.; Brandt, J. C.; Wirth, T., Advanced organic synthesis using microreactor technology. *Organic & Biomolecular Chemistry* **2007**, 5, (5), 733-740.
31. Ristenpart, W. D.; Wan, J. D.; Stone, H. A., Enzymatic reactions in microfluidic devices: Michaelis-Menten kinetics. *Analytical Chemistry* **2008**, 80, (9), 3270-3276.
32. Serra, C. A.; Chang, Z. Q., Microfluidic-assisted synthesis of polymer particles. *Chemical Engineering & Technology* **2008**, 31, (8), 1099-1115.
33. Zhang, H.; Tumarkin, E.; Sullan, R. M. A.; Walker, G. C.; Kumacheva, E., Exploring microfluidic routes to microgels of biological polymers. *Macromolecular Rapid Communications* **2007**, 28, (5), 527-538.

34. Calvert, P., Gel sensors and actuators. *MRS Bulletin* **2008**, 33, (3), 207-212.
35. Zhang, C. S.; Xing, D.; Li, Y. Y., Micropumps, microvalves, and micromixers within PCR microfluidic chips: Advances and trends. *Biotechnology Advances* **2007**, 25, (5), 483-514.
36. Zhang, Y.; Kato, S.; Anazawa, T., A microchannel concentrator controlled by integral thermoresponsive valves. *Sensors and Actuators B-Chemical* **2008**, 129, (1), 481-486.
37. Yu, C.; Mutlu, S.; Selvaganapathy, P.; Mastrangelo, C. H.; Svec, F.; Frechett, J. M. J., Flow control valves for analytical microfluidic chips without mechanical parts based on thermally responsive monolithic polymers. *Analytical Chemistry* **2003**, 75, (8), 1958-1961.
38. Harmon, M. E.; Tang, M.; Frank, C. W., A microfluidic actuator based on thermoresponsive hydrogels. *Polymer* **2003**, 44, (16), 4547-4556.
39. Luo, Q. Z.; Mutlu, S.; Gianchandani, Y. B.; Svec, F.; Frechet, J. M. J., Monolithic valves for microfluidic chips based on thermoresponsive polymer gels. *Electrophoresis* **2003**, 24, (21), 3694-3702.
40. Sugiura, S.; Sumaru, K.; Ohi, K.; Hiroki, K.; Takagi, T.; Kanamori, T., Photoresponsive polymer gel microvalves controlled by local light irradiation. *Sensors and Actuators A-Physical* **2007**, 140, (2), 176-184.
41. Siegel, R. A.; Gu, Y. D.; Baldi, A.; Ziaie, B. In *Novel swelling/shrinking behaviors of glucose-binding hydrogels and their potential use in a microfluidic insulin delivery system*, Macromolecular Symposia, pp 249-256.
42. De, S. K.; Aluru, N. R.; Johnson, B.; Crone, W. C.; Beebe, D. J.; Moore, J., Equilibrium swelling and kinetics of pH-responsive hydrogels: Models, experiments, and simulations. *Journal of Microelectromechanical Systems* **2002**, 11, (5), 544-555.
43. De, S. K.; Aluru, N. R., A chemo-electro-mechanical mathematical model for simulation of pH sensitive hydrogels. *Mechanics of Materials* **2004**, 36, (5-6), 395-410.
44. Osada, Y.; Gong, J. P., Stimuli-Responsive Polymer Gels and their Application to Chemomechanical Systems. *Progress in Polymer Science* **1993**, 18, (2), 187-226.

45. Good, B. T.; Bowman, C. N.; Davis, R. H., Modeling and verification of fluid-responsive polymer pumps for microfluidic systems. *Chemical Engineering Science* **2004**, 59, (24), 5967-5974.
46. Kim, D.; Beebe, D. J., A bi-polymer micro one-way valve. *Sensors and Actuators A-Physical* **2007**, 136, (1), 426-433.
47. Kim, D.; Beebe, D. J., Hydrogel-based reconfigurable components for microfluidic devices. *Lab on a Chip* **2007**, 7, (2), 193-198.
48. Slater, G. W.; Guillouzie, S.; Gauthier, M. G.; Mercier, J. F.; Kenward, M.; McCormick, L. C.; Tessier, F., Theory of DNA electrophoresis (similar to 1999-2002(1)/(2)). *Electrophoresis* **2002**, 23, (22-23), 3791-3816.
49. Li, Y.; Buch, J. S.; Rosenberger, F.; DeVoe, D. L.; Lee, C. S., Integration of isoelectric focusing with parallel sodium dodecyl sulfate gel electrophoresis for multidimensional protein separations in a plastic microfluidic network. *Analytical Chemistry* **2004**, 76, (3), 742-748.
50. Vegvari, A.; Hjerten, S., A hybrid microdevice for electrophoresis and electrochromatography using UV detection. *Electrophoresis* **2002**, 23, (20), 3479-3486.
51. Viovy, J. L., Electrophoresis of DNA and other polyelectrolytes: Physical mechanisms. *Reviews of Modern Physics* **2000**, 72, (3), 813-872.
52. Chen, G.; Xu, X. J.; Lin, Y. H.; Wang, J., A sol-gel-modified poly(methyl methacrylate) electrophoresis microchip with a hydrophilic channel wall. *Chemistry-A European Journal* **2007**, 13, (22), 6461-6467.
53. Qu, H. Y.; Wang, H. T.; Huang, Y.; Zhong, W.; Lu, H. J.; Kong, J. L.; Yang, P. Y.; Liu, B. H., Stable microstructured network for protein patterning on a plastic microfluidic channel: Strategy and characterization of on-chip enzyme microreactors. *Analytical Chemistry* **2004**, 76, (21), 6426-6433.
54. Rudzinski, C. M.; Young, A. M.; Nocera, D. G., A supramolecular microfluidic optical chemosensor. *Journal of the American Chemical Society* **2002**, 124, (8), 1723-1727.

55. Chan, A.; Krull, U. J., Capillary electrophoresis for capture and concentrating of target nucleic acids by affinity gels modified to contain single-stranded nucleic acid probes. *Analytica Chimica Acta* **2006**, 578, (1), 31-42.
56. Wilms, D.; Klos, J.; Frey, H., Microstructured reactors for polymer synthesis: A renaissance of continuous flow processes for tailor-made macromolecules? *Macromolecular Chemistry and Physics* **2008**, 209, (4), 343-356.
57. Rondeau, E.; Cooper-White, J. J., Biopolymer microparticle and nanoparticle formation within a microfluidic device. *Langmuir* **2008**, 24, (13), 6937-6945.
58. Nie, Z. H.; Xu, S. Q.; Seo, M.; Lewis, P. C.; Kumacheva, E., Polymer particles with various shapes and morphologies produced in continuous microfluidic reactors. *Journal of the American Chemical Society* **2005**, 127, (22), 8058-8063.
59. Dendukuri, D.; Gu, S. S.; Pregibon, D. C.; Hatton, T. A.; Doyle, P. S., Stop-flow lithography in a microfluidic device. *Lab on a Chip* **2007**, 7, (7), 818-828.
60. Sauter, C.; Dhouib, K.; Lorber, B., From macrofluidics to microfluidics for the crystallization of biological macromolecules. *Crystal Growth and Design* **2007**, 7, (11), 2247-2250.
61. Oh, H. J.; Kim, S. H.; Baek, J. Y.; Seong, G. H.; Lee, S. H., Hydrodynamic micro-encapsulation of aqueous fluids and cells via 'on the fly' photopolymerization. *Journal of Micromechanics and Microengineering* **2006**, 16, (2), 285-291.
62. Chang, J. Y.; Yang, C. H.; Huang, K. S., Microfluidic assisted preparation of CdSe/ZnS nanocrystals encapsulated into poly(DL-lactide-co-glycolide) microcapsules. *Nanotechnology* **2007**, 18, (30).
63. Shah, R. K.; Kim, J. W.; Agresti, J. J.; Weitz, D. A.; Chu, L. Y., Fabrication of monodisperse thermosensitive microgels and gel capsules in microfluidic devices. *Soft Matter* **2008**, 4, (12), 2303-2309.
64. Kim, J. W.; Utada, A. S.; Fernandez-Nieves, A.; Hu, Z. B.; Weitz, D. A., Fabrication of monodisperse gel shells and functional microgels in microfluidic devices. *Angewandte Chemie-International Edition* **2007**, 46, (11), 1819-1822.

65. Liu, K.; Ding, H. J.; Liu, J.; Chen, Y.; Zhao, X. Z., Shape-controlled production of biodegradable calcium alginate gel microparticles using a novel microfluidic device. *Langmuir* **2006**, 22, (22), 9453-9457.
66. Kwon, H. J.; Gong, J. P., Negatively charged polyelectrolyte gels as bio-tissue model system and for biomedical application. *Current Opinion in Colloid & Interface Science* **2006**, 11, (6), 345-350.
67. Steinbacher, J. L.; Moy, R. W. Y.; Price, K. E.; Cummings, M. A.; Roychowdhury, C.; Buffy, J. J.; Olbricht, W. L.; Haaf, M.; McQuade, D. T., Rapid self-assembly of core-shell organosilicon microcapsules within a microfluidic device. *Journal of the American Chemical Society* **2006**, 128, (29), 9442-9447.
68. Dong, L.; Agarwal, A. K.; Beebe, D. J.; Jiang, H. R., Adaptive liquid microlenses activated by stimuli-responsive hydrogels. *Nature* **2006**, 442, (7102), 551-554.
69. Lo, C. T.; Throckmorton, D. J.; Singh, A. K.; Herr, A. E., Photopolymerized diffusion-defined polyacrylamide gradient gels for on-chip protein sizing. *Lab on a Chip* **2008**, 8, (8), 1273-1279.
70. Johnson, B. D.; Beebe, D. J.; Crone, W., Effects of swelling on the mechanical properties of a pH-sensitive hydrogel for use in microfluidic devices. *Materials Science & Engineering C-Biomimetic and Supramolecular Systems* **2004**, 24, (4), 575-581.
71. Yeghiazarian, L.; Mahajan, S.; Montemagno, C.; Cohen, C.; Wiesner, U., Directed motion and cargo transport through propagation of polymer-gel volume phase transitions. *Advanced Materials* **2005**, 17, (15), 1869.
72. Peterson, D. S., Solid supports for micro analytical systems. *Lab on a Chip* **2005**, 5, (2), 132-139.
73. Lewis, P. C.; Graham, R. R.; Nie, Z. H.; Xu, S. Q.; Seo, M.; Kumacheva, E., Continuous synthesis of copolymer particles in microfluidic reactors. *Macromolecules* **2005**, 38, (10), 4536-4538.
74. Bouquey, M.; Serra, C.; Berton, N.; Prat, L.; Hadziioannou, G., Microfluidic synthesis and assembly of reactive polymer beads to form new structured polymer materials. *Chemical Engineering Journal* **2008**, 135, S93-S98.

75. Randall, G. C.; Schultz, K. M.; Doyle, P. S., Methods to electrophoretically stretch DNA: microcontractions, gels, and hybrid gel-microcontraction devices. *Lab on a Chip* **2006**, 6, (4), 516-525.
76. Zourob, M.; Mohr, S.; Mayes, A. G.; Macaskill, A.; Perez-Moral, N.; Fielden, P. R.; Goddard, N. J., A micro-reactor for preparing uniform molecularly imprinted polymer beads. *Lab on a Chip* **2006**, 6, (2), 296-301.
77. Nisisako, T.; Torii, T., Formation of biphasic Janus droplets in a microfabricated channel for the synthesis of shape-controlled polymer microparticles. *Advanced Materials* **2007**, 19, (11), 1489.
78. Seo, M.; Nie, Z. H.; Xu, S. Q.; Lewis, P. C.; Kumacheva, E., Microfluidics: From dynamic lattices to periodic arrays of polymer disks. *Langmuir* **2005**, 21, (11), 4773-4775.
79. Nie, Z. H.; Li, W.; Seo, M.; Xu, S. Q.; Kumacheva, E., Janus and ternary particles generated by microfluidic synthesis: Design, synthesis, and self-assembly. *Journal of the American Chemical Society* **2006**, 128, (29), 9408-9412.
80. Zhang, H.; Tumarkin, E.; Peerani, R.; Nie, Z.; Sullan, R. M. A.; Walker, G. C.; Kumacheva, E., Microfluidic production of biopolymer microcapsules with controlled morphology. *Journal of the American Chemical Society* **2006**, 128, (37), 12205-12210.
81. Johann, R. M.; Renaud, P., Microfluidic patterning of alginate hydrogels. *Biointerphases* **2007**, 2, (2), 73-79.
82. Rubinstein, M.; Colby, R. H., *Polymer Physics*. Oxford University Press: New York, 2003.
83. Kini, G. C.; Lai, J.; Wong, M. S.; Biswal, S. L., Microfluidic Formation of Ionically Cross-Linked Polyamine Gels. *Langmuir* **2010**, 26, (9), 6650-6656.
84. Yoo, R. Assembling Nanoparticle-Assembled Capsules on a Planar Substrate. MS Thesis, Rice University, Houston, 2006.
85. Duffy, D. C.; McDonald, J. C.; Schueller, O. J. A.; Whitesides, G. M., Rapid prototyping of microfluidic systems in poly(dimethylsiloxane). *Analytical Chemistry* **1998**, 70, (23), 4974-4984.

86. Xia, Y. N.; Whitesides, G. M., Soft lithography. *Angewandte Chemie-International Edition* **1998**, 37, (5), 551-575.
87. Xia, Y. N.; Whitesides, G. M., Soft lithography. *Annual Review of Materials Science* **1998**, 28, 153-184.
88. McDonald, J. C.; Duffy, D. C.; Anderson, J. R.; Chiu, D. T.; Wu, H. K.; Schueller, O. J. A.; Whitesides, G. M., Fabrication of microfluidic systems in poly(dimethylsiloxane). *Electrophoresis* **2000**, 21, (1), 27-40.

Chapter 7

Summary and Recommendations for Future Work

7.1 Thesis Summary

The advent of a generic, economical, and facile approach to create stable NP aqueous suspensions was the motivation that led to this PhD thesis.¹⁻⁴ Since NPs synthesized in water often have high polydispersity, there is a need to effectively transfer monodisperse NPs synthesized in oil to water. The method of bilayer transfer is particularly useful and was originally pioneered by Brinker and coworkers. The transfer approach however had the following limitations (i) Transfer yields of NPs were low (45-55%) and NPs transferred as clusters or aggregates in bilayers (ii) A high surfactant concentration was required to formulate the initial microemulsion, which made the transfer process expensive while yet not giving the desired high transfer yields and single NP suspensions (iii) For medical applications where NP stability in high ionic strength buffers is essential (equivalent to 9 g-NaCl/L or higher), expensive and biocompatible phospholipids were used, making the process economically unviable.

An idea to address the above challenges motivated our efforts to develop a new and improved transfer process through an understanding of surfactant phase-behavior, as was described in Chapter 2. We found that through the addition of salt during the stage of emulsion formation, transfer yields of NPs increased dramatically to 90-100%. NPs in the new bilayer configuration of salty-micelles transferred as single particles. A lowering of surfactant solubility from salting-out effects along with counter-ion induced screening of head-group repulsions resulted in higher surfactant coverage on the NP surface. The latter effect also contributed to enhanced lateral compactness of salty-micelles, resulting in a bilayer environment with high non-polar nature that better conserved optical properties of

bare QDs. I showed the transfer scheme to be generic across different NP (CdSe QDs and tetrapods, Au, C₆₀, ZnO, Fe₂O₃, WO₃), surfactant (anionic - AOT, SDS, cationic - CTAB, nonionic - Neodol 91-7, hybrid anionic-nonionic - Avanel) and salt (NaCl, Na₂SO₄, Na₃Citrate, CaCl₂, AlCl₃) types.

In Chapter 3, the effect of salt-induced spontaneous emulsification of a blend of hydrocarbon/AOT/water was described. Implications of this effect on NP phase-transfer were secondary in that, the smaller sized hydrocarbon droplets resulted in a higher degree of NP phase-transfer post evaporation of the hydrocarbon. Salt was found to affect the nucleation of octane droplets by influencing the phase-behavior of AOT which in turn affected the initial droplet size and subsequent growth of nanoemulsion droplets that formed. The phase-behavior of AOT was the dominant factor over electrostatics in determining emulsion stability to coalescence. Beyond NP transfer yield, this result has important implications in areas of laundry and personal care, where the conventional approach to formulate emulsions with ionic surfactants is based on electrostatics-derived stability. Here we have learned the converse which leads to an alternate approach in formulating emulsions. Through the use of nonionic surfactants that rely on steric-stabilization over electrostatics, emulsions can be formed at lower concentrations where significant cost-benefits and water savings can be realized.

In Chapters 4 and 5, an application of NPs towards characterization of reservoirs was discussed. It was shown in Chapter 4 that by transferring NPs in bilayers of a nonionic surfactant Neodol 91-7, stability to aggregation was achieved even in high ionic strengths of 1M NaCl and 0.55M seawater. Temperature stability up to 70 °C was obtained by selecting the nonionic such that its cloud point was above the temperature of

application. Transport studies through crushed calcite columns in 1M NaCl and 0.55M seawater backgrounds and temperatures upto 70 °C showed QD/Neodol breakthrough was similar to that of an ideal tracer. Retardation coefficients evaluated were close to unity and overall QD recovery was >95%, thus making them ideal nanoreporters to carry and deliver oil-soluble tracers to oil-sites of a reservoir. Studies through quartz sand columns showed retardation of QD/Neodol at room temperature that increased significantly at higher temperatures. This was on account of a natural affinity of Neodol to quartz sand. In the oil industry, this behavior has prevented the use of nonionic alcohol ethoxylates in quartz sand and sandstone-type reservoir materials.

In Chapter 5, NP tolerance to aggregation in saline media was shown to increase up to 100 °C through the use of a hybrid surfactant Avel S150 CGN (Avel). The surfactant had nonionic and anionic functional groups on the same surfactant chain, with potential applications for quartz sand type reservoirs. The concerns of QD toxicity were addressed by synthesizing carbon-dot (C-Dot) nanoparticles and transferring them to bilayers of Avel as future nanoreporters for reservoir characterization.

In Chapter 6, findings on the tandem assembly process of PAH-citrate aggregates and nanoparticles in a microfluidic environment were discussed. In a laminar flow environment where mixing is limited by diffusion, instantaneous gelation of PAH-citrate aggregates was observed, where shear induced structural transformations from aggregates to non-continuous and continuous gels. Droplets of citric acid emerged in continuous gel regions where sites to cross-link PAH were saturated. The interactions leading to PAH-citrate crosslinking were electrostatic in nature - it was shown that the extent of gelation could be controlled by manipulating charge(s) on PAH and citric acid respectively, using

pH as the parameter. To form nanoparticle assembled capsules, flow-focusing microfluidic channel geometry is thus proposed.

7.2 Recommendations for Future Work

7.2.1 Electrostatic Self-Assembly of Nanoparticles to form Superlattices

In Chapter 2, we learned that the salty-micelle approach to NP phase-transfer resulted in aqueous suspensions of single NPs. Grzybowski and coworkers recently showed that single NPs with opposite charge could be self-assembled in aqueous media to form ordered superlattices with an open-type diamond-like structure (Fig. 7.1).¹¹⁻¹⁵

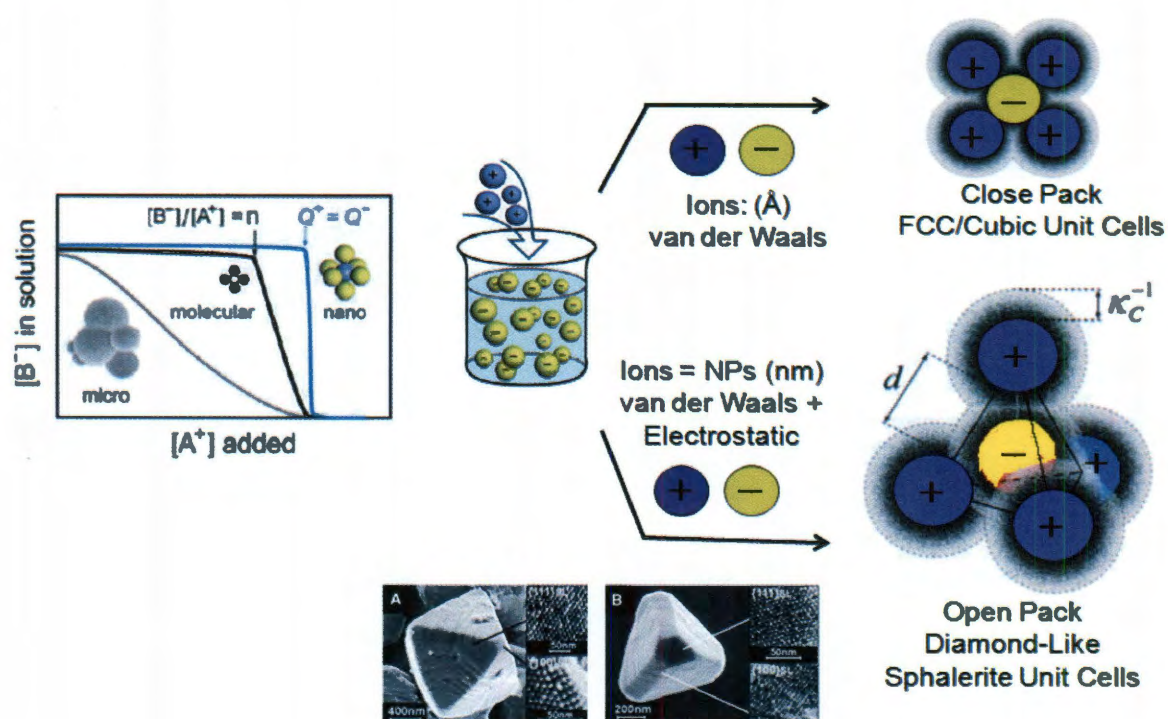


Figure 7.1: Electrostatic self-assembly (ESA) scheme to assemble oppositely charged nanoparticles into superlattices with open-pack diamond-like structure (Figure adapted from Kalsin *et al* and Kalsin and Grzybowski)

In their method, single NP suspensions were prepared by ligand exchange and the surfactants used were very expensive ($> \$1000/\text{g}$). Further, owing to the non-generic nature of ligand exchange, a limited number of NPs (namely Au and Ag) could be self-assembled to superlattices. The new NP transfer approach could address both the cost and non-generic issues of this method. Preliminary results showed that CdSe QDs could be assembled into superlattices (Fig. 7.2). This scheme could be extended to form binary and even ternary type superlattices, featuring two or more unique NP types. A foreseeable limitation of the new approach is the co-crystallization of salts and its subsequent separation. Recommended work for the future would be to formulate a robust approach to form single, binary, and ternary type superlattices in high yields. Furthermore, the flexibility of selecting surfactant types (anionic, cationic and nonionic) and chain lengths could lead to interesting new structures.

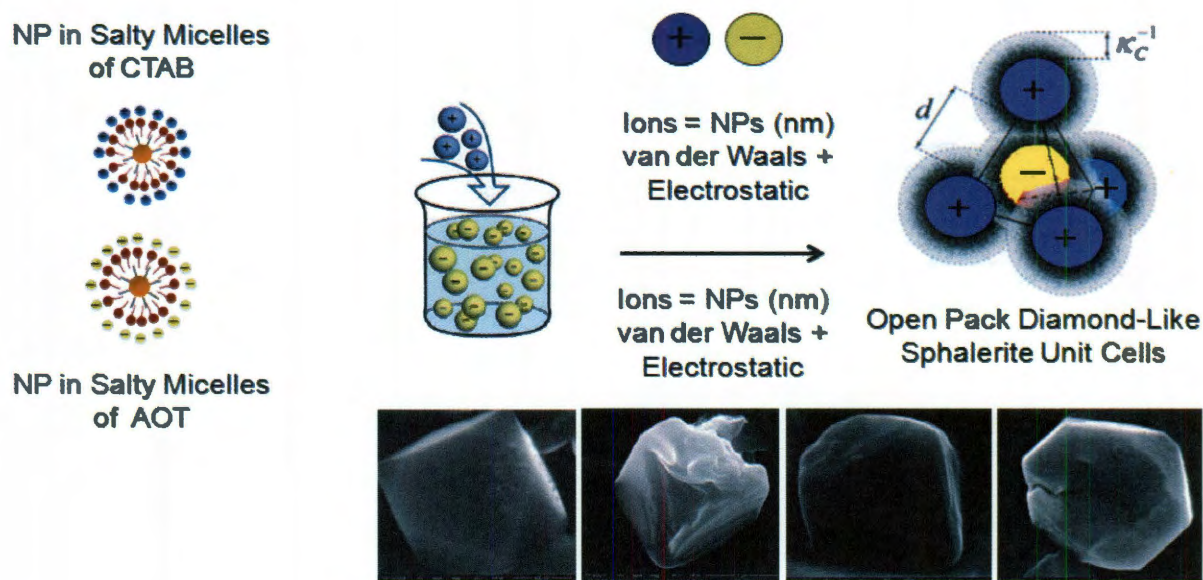


Figure 7.2: Electrostatic self-assembly (ESA) scheme to assemble oppositely charged nanoparticles using commercial surfactants (NP = CdSe QDs)

7.2.2 Nanoreporters with Oil-Detection Capabilities

In Chapters 4 and 5, it was shown that NPs formulated with nonionic and hybrid nonionic/anionic surfactants showed tolerance to aggregation in high salinity backgrounds and temperatures up to a 100 °C. In oil-free media, the NPs showed tracer-like breakthrough in various saline backgrounds and at temperatures upto 70 °C. As future work, these NPs can be used as nanoreporters towards the detection of oil in reservoirs.

In this regard, two classes of nanoreporters can be envisaged and are proposed as possible future forms of bilayer-based nanoreporters:

7.2.2.1 Nanoreporters where NPs function as Signaling or Contrast Agents

In the first category of nanoreporters, the NP in itself could selectively partition into oil domains in a reservoir. Fig. 7.3 show preliminary results of irreversible NP transfer to oil domains from seawater background into model oil such as isooctane. In this batch experiment, a suspension of QD/Neodol in 0.55M synthetic seawater background was contacted with an equal volume of isooctane. The system was heated in a paraffin oil bath to 90 °C (above the cloud point of Neodol) under conditions of gentle stirring such that the isooctane/seawater interface was not disturbed. In roughly two hours time, QDs were seen to migrate from the seawater phase to isooctane, as seen in the schematic. Upon transfer, when the system was cooled to room temperature, the QDs remained in the isooctane phase.

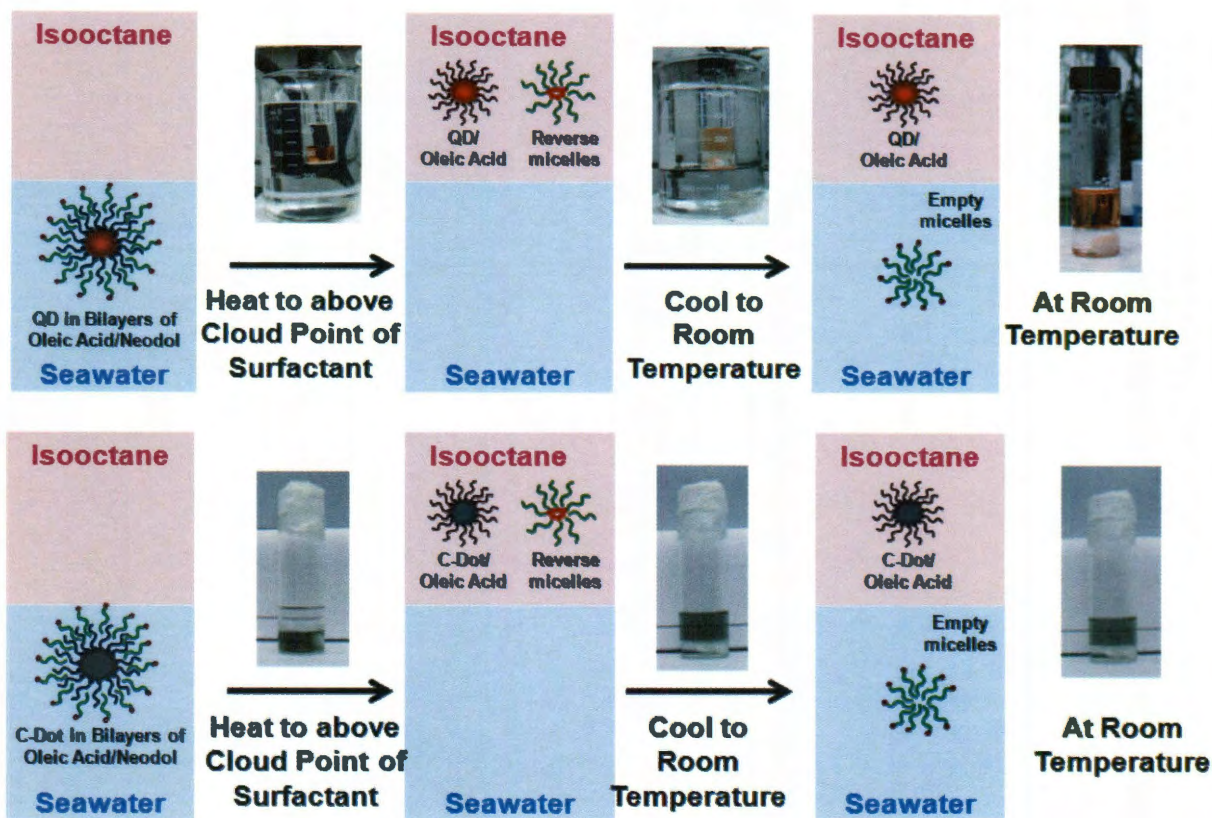


Figure 7.3: Irreversible migration of QDs (top panel) and C-Dots (bottom panel) from seawater to isooctane when the system is heated to 90 °C (above the cloud point of the surfactant Neodol 91-7) and cooled back to room temperature.

Such irreversible migration was also observed for a C-Dot/Neodol system, when heated to above the cloud point temperature of Neodol, C-Dots were found to irreversibly migrate to the isooctane phase showing the generality of the process. In the case of QDs, fluorescence could be a signal to demark oil domains from non-oil domains. Other NPs such as Fe_2O_3 , if transferred by this approach to an oil domain in a reservoir, could increase the signal response from an incoming seismic wavefront used to map a reservoir. These in turn could create better differentiation between oil and non-oil domains and improve the reliability of the detection process. Future work thus recommended is a systematic study of NP flow through calcite and quartz sand columns that are pre-

saturated with oil. Possible studies would also include imaging NPs entrapped in oil domains with fluorescence, seismic, or NMR-based techniques.

7.2.2.2 Nanoreporters where NPs function as Delivery Agents of Signaling Molecules

The second variant of proposed bilayer-based nanoreporters is depicted in Fig. 7.4. This variant was inspired from recent work published by Tour and coworkers.^{16, 17} In this scheme, the NPs serve as a carrier of a signaling molecule/tracer (such as radioactive tetrachlorobiphenyl (PCB) tracer or triheptylamine (THA) mass spectroscopy tracer) and delivers it selectively to oil-domains of a reservoir. Upon retrieving the NPs post transport through the reservoir column, NPs were analyzed for the amount of signaling molecules left behind and based on a mass balance, the quantity of signaling molecule delivered was estimated. Furthermore, studies were performed to quantify the dependency of oil-content in a reservoir with the amount of signaling molecule delivered. Thus with available calibration charts, the quantity of oil in a reservoir could be estimated using the signaling molecule left behind on the NP carrier.

The nanoreporters developed by Tour and coworkers were carbon-based (polyethylene glycol hydrophobic carbon clusters (PEG-HCC) and polyvinyl alcohol oxidized carbon black (PVA-OCB)) where a high molecular weight water-soluble polymer is covalently attached to the carbon-core.¹⁶ While the nanoreporter cargo has advantages of an inexpensive and non-toxic carbon source, the process of functionalizing the carbon-core with the PEG or PVA polymer involves multiple steps of synthesis and dialysis.

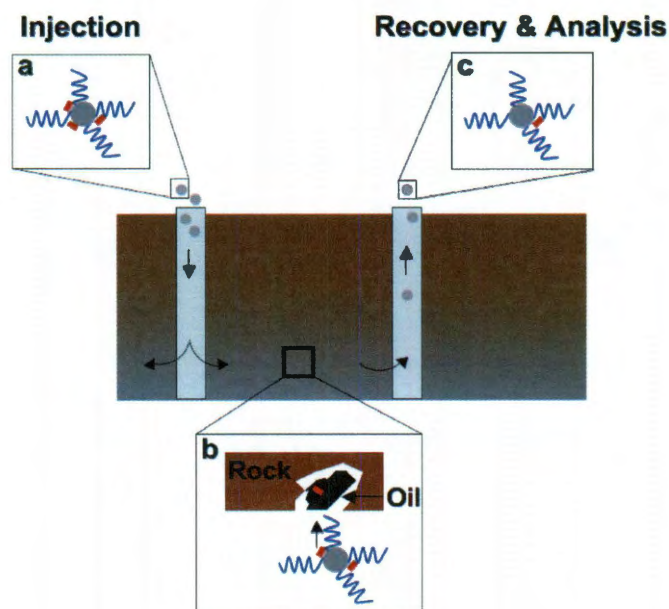


Figure 7.4: Schematic for delivery of signaling molecules loaded on a NP into oil domains within a reservoir (Figure adapted from Berlin *et al*).

An alternate approach to design a nanoreporter along the above lines would be to transfer the hydrophobic carbon core (carbon-black functionalized with oleic acid, called C-Dots) into bilayers of commercially available surfactants. A key difference of this new schematic is that the bilayer of oleic acid and surfactant is based on weak hydrophobic interactions, different from covalently attached PEG and PVA polymers onto HCC or OCBs. In the new schematic, the signaling molecule could be introduced into the hydrophobic bilayer domain and based on the type of surfactant used, breakthrough of bilayer C-Dot nanoreporters can be engineered to demonstrate tracer-like flow behavior in oil-free or oil-saturated porous media. Thus, the signaling molecule can be delivered selectively to oil-domains and used to estimate oil content in the column. This alternate configuration is scalable and can be made in large quantities and in an economical manner.

7.2.3 Polyamine Gels for Flow Control and Actuation

In Chapter 6, we had reviewed recent literature of gel formation approaches in microfluidics and its applications towards flow regulation and actuation.¹⁸ We saw that the challenge to form gels *in situ* and without the requirement of microfabrication methods is yet to be realized. In this regard, I believe that our discovery of the gelation phenomenon of PAH and citrate in a microfluidic environment has immense potential in applications of flow regulation.¹⁹ The outstanding features are *in situ* formation of gels at room temperature and at desired locations of a microchannel, without the requirements of microfabrication methods. Furthermore, gel thickness may be controlled by varying R ratios and the charge on the anion.

Figs. 7.5 (i) and (ii) represent preliminary data for thickness profiles of the PAH-citrate system, when carried through cycles of increase in pH followed by decrease and vice-versa. Although a hysteresis in gel thickness trends is observable between the two sequences of pH change, gelation trends did not change significantly and little differences were observed in resulting gel thickness.

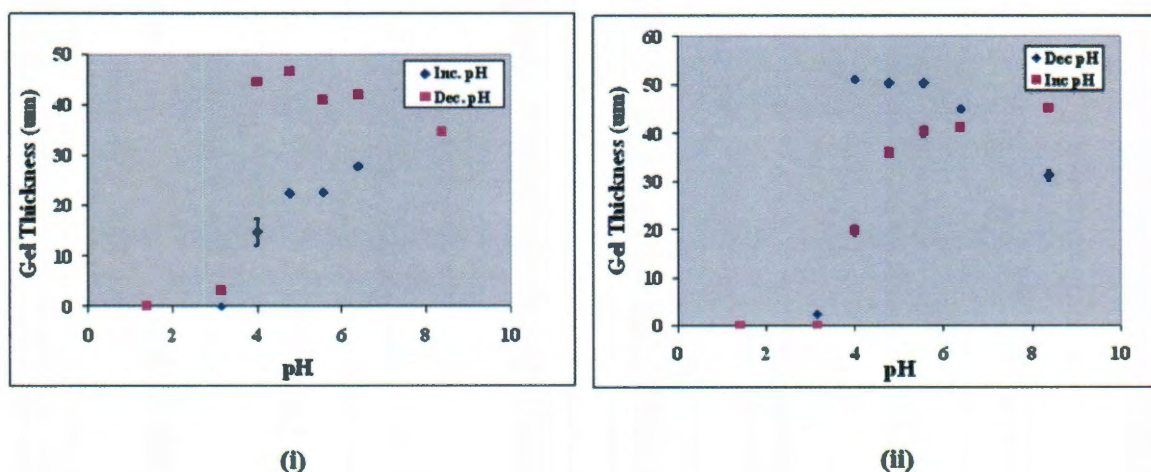


Figure 7.5: (i) Increase-decrease pH cycle – gel thickness profile and (ii) Decrease-

increase pH cycle – gel thickness profile for PAH-citrate gels formed, under conditions of R ratio = 50 (PAH = 1 mg/mL) and flow rate of 25 mL/hr.

It is proposed for future work that through the use of lithography and confocal microscopy, the gel thickness be monitored as a function of speciation on citric acid along the height of the microchannel so as to investigate possible applications of the gelation phenomenon in flow control and actuation.

7.2.4 Hybrid Polyamine/Glutaraldehyde Gels for Flow of Organic Solvents

Polyamine gels formed by ionic crosslinking of PAH and citric acid collapse when subjected to the environment of organic solvents. To design polyamine gels stable in organic solvents, a cross-linking reaction based on aldol condensation of polyamine gels with glutaraldehyde is proposed (Fig. 7.6 (i)).^{20, 21}

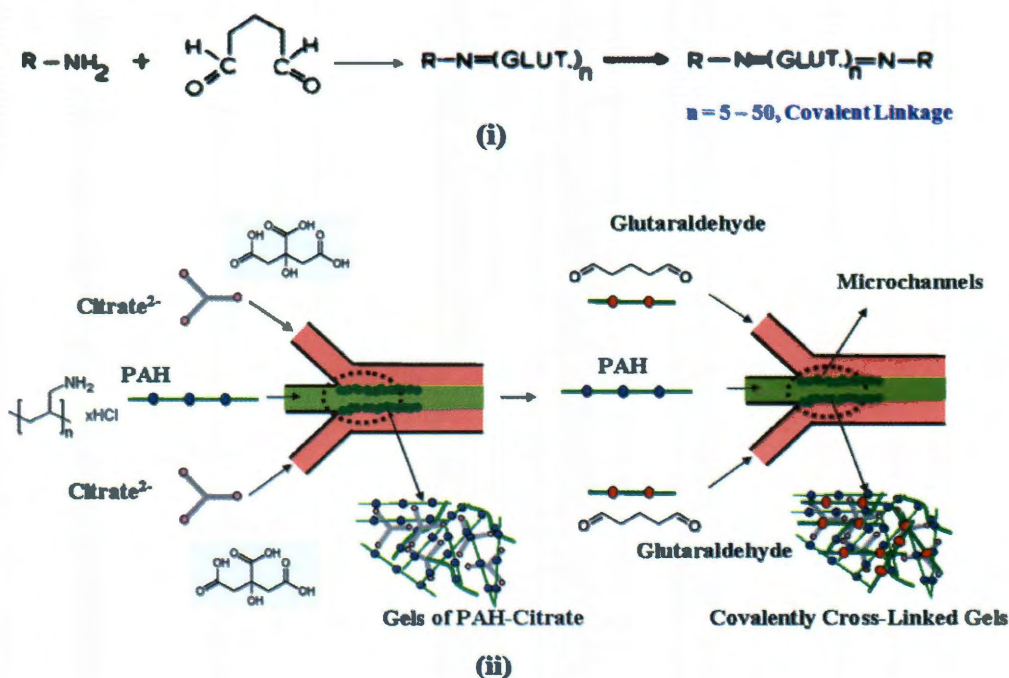


Figure 7.6: (i) Schematic of the aldol condensation reaction (ii) Schematic for forming hybrid polyamine-glutaraldehyde gels.

A proposed method to use the reaction in microchannels is given in Fig. 7.6 (ii). Preliminary results indicate that upon condensation with glutaraldehyde, the hybrid polyamine gels are stable in a paraffin oil environment (Fig. 7.7). It is thus proposed that through an optimization of R ratios, citric acid speciation and glutaraldehyde concentration, new variants of gels can be synthesized with compatibility to organic solvents.

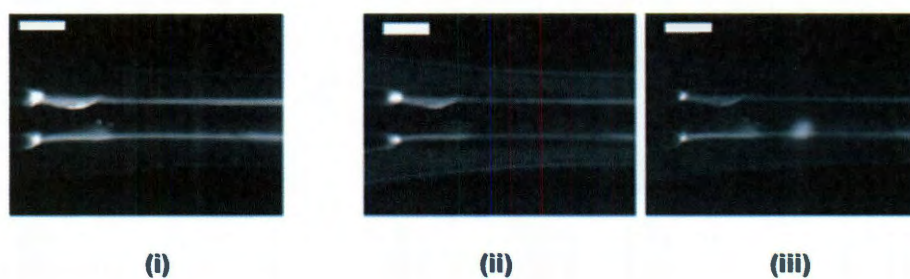


Figure 7.7: Stability of PAH-Citrate-Glutaraldehyde Gels (i) in environments of (ii) water and mineral oil (iii). All scale bars are 50 μm .

7.2.5 Flow Focusing Approaches for Microfluidic Synthesis of NACs

In Chapter 6, we demonstrated the feasibility of forming NACs in microchannels. However, NAC formation in the previous geometry was found to occur under highly specific conditions. Furthermore, the microchannel geometry in which tandem assembly was investigated was found to favor formation of gels over capsules. To make NAC synthesis more tenable while exploiting laminar conditions of a microchannel, I propose a modification to the existing device geometry by introducing an orifice or flow-focusing constriction. This in conjunction with an immiscible oil phase creates conditions of “pinch off” or “Rayleigh-Plateau instabilities”, making possible continuous-mode production of droplets of the polymer-salt aggregates. By introducing NPs downstream of the channel, NACs could be synthesized on a continuous mode basis. Preliminary results

suggest that NACs with tunable levels of surface coverage of NPs can be formed in microchannels based on reactant flow conditions and residence times of NPs (Fig. 7.8).

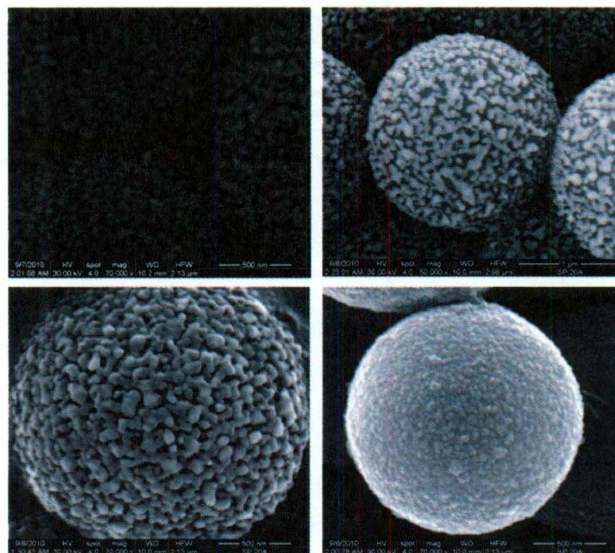


Figure 7.8: Nanoparticle assembled capsules (NACs) of PAH, citrate and silica NPs formed in a microchannel with flow-focusing geometry with varying levels of NP coverage.

Systematic investigation of reactant flow conditions, the spatial location where NPs are introduced along the channel length and the residence time of NPs in the channel could help control NP coverage of the resulting NACs and possibly pave the way to form new NAC variants with controllable surface morphology.

7.3 References

1. Fan, H. Y.; Yang, K.; Boye, D. M.; Sigmon, T.; Malloy, K. J.; Xu, H. F.; Lopez, G. P.; Brinker, C. J., Self-assembly of ordered, robust, three-dimensional gold nanocrystal/silica arrays. *Science* **2004**, 304, (5670), 567-571.
2. Bagaria, H. G.; Kini, G. C.; Wong, M. S., Electrolyte Solutions Improve Nanoparticle Transfer from Oil to Water. *Journal of Physical Chemistry C* **2010**, 114, (47), 19901-19907.
3. Kini, G. C. Bilayer Approaches for Nanoparticle Phase-Transfer. PhD Thesis, Rice University, Houston, 2011.
4. Kini, G. C.; Bagaria, H. G.; Ko, W.-Y.; Wong, M. S. Converting Nanoparticles in Oil to Aqueous Suspensions. 2009.
5. Fan, H. Y., Nanocrystal-micelle: synthesis, self-assembly and application. *Chemical Communications* **2008**, (12), 1383-1394.
6. Fan, H. Y.; Chen, Z.; Brinker, C. J.; Clawson, J.; Alam, T., Synthesis of organo-silane functionalized nanocrystal micelles and their self-assembly. *Journal of the American Chemical Society* **2005**, 127, (40), 13746-13747.
7. Fan, H. Y.; Leve, E.; Gabaldon, J.; Wright, A.; Haddad, R. E.; Brinker, C. J., Ordered two- and three-dimensional arrays self-assembled from water-soluble nanocrystal-micelles. *Advanced Materials* **2005**, 17, (21), 2587.
8. Fan, H. Y.; Lu, Y. F.; Stump, A.; Reed, S. T.; Baer, T.; Schunk, R.; Perez-Luna, V.; Lopez, G. P.; Brinker, C. J., Rapid prototyping of patterned functional nanostructures. *Nature* **2000**, 405, (6782), 56-60.
9. Brinker, C. J.; Lu, Y. F.; Sellinger, A.; Fan, H. Y., Evaporation-induced self-assembly: Nanostructures made easy. *Advanced Materials* **1999**, 11, (7), 579.
10. Fan, H. Y.; Leve, E. W.; Scullin, C.; Gabaldon, J.; Tallant, D.; Bunge, S.; Boyle, T.; Wilson, M. C.; Brinker, C. J., Surfactant-assisted synthesis of water-soluble and biocompatible semiconductor quantum dot micelles. *Nano Letters* **2005**, 5, (4), 645-648.

11. Kalsin, A. M.; Fialkowski, M.; Paszewski, M.; Smoukov, S. K.; Bishop, K. J. M.; Grzybowski, B. A., Electrostatic self-assembly of binary nanoparticle crystals with a diamond-like lattice. *Science* **2006**, 312, (5772), 420-424.
12. Kalsin, A. M.; Grzybowski, B. A., Controlling the growth of "ionic" nanoparticle supracrystals. *Nano Letters* **2007**, 7, (4), 1018-1021.
13. Bishop, K. J. M.; Grzybowski, B. A., "Nanoions": Fundamental properties and analytical applications of charged nanoparticles. *Chemphyschem* **2007**, 8, (15), 2171-2176.
14. Bishop, K. J. M.; Kowalczyk, B.; Grzybowski, B. A., Precipitation of Oppositely Charged Nanoparticles by Dilution and/or Temperature Increase. *Journal of Physical Chemistry B* **2009**, 113, (5), 1413-1417.
15. Bishop, K. J. M.; Wilmer, C. E.; Soh, S.; Grzybowski, B. A., Nanoscale Forces and Their Uses in Self-Assembly. *Small* **2009**, 5, (14), 1600-1630.
16. Berlin, J. M.; Yu, J.; Lu, W.; Walsh, E. E.; Zhang, L. L.; Zhang, P.; Chen, W.; Kan, A. T.; Wong, M. S.; Tomson, M. B.; Tour, J. M., Engineered nanoparticles for hydrocarbon detection in oil-field rocks. *Energy & Environmental Science* **2010**, 4, (2), 505-509.
17. Yu, J.; Berlin, J. M.; Lu, W.; Zhang, L. L.; Kan, A. T.; Zhang, P.; Walsh, E. E.; Work, S. N.; Chen, W.; Tour, J. M.; Wong, M. S.; Tomson, M. B., Transport Study of Nanoparticles for Oilfield Application. In *SPE International Conference on Oilfield Scale*, Aberdeen, U.K., 2010.
18. Calvert, P., Gel sensors and actuators. *MRS Bulletin* **2008**, 33, (3), 207-212.
19. Kini, G. C.; Lai, J.; Wong, M. S.; Biswal, S. L., Microfluidic Formation of Ionically Cross-Linked Polyamine Gels. *Langmuir* **2010**, 26, (9), 6650-6656.
20. Cheung, D. T.; Nimni, M. E., Mechanism of crosslinking of proteins by glutaraldehyde. 1. Reaction with model compounds. *Connective Tissue Research* **1982**, 10, (2), 187-199.

21. Cheung, D. T.; Nimni, M. E., Mechanism of crosslinking of proteins by glutaraldehyde. 2. Reaction with monomeric and polymeric collagen. *Connective Tissue Research* **1982**, 10, (2), 201-216.

Appendix A

Section A1: Photoluminescence Studies

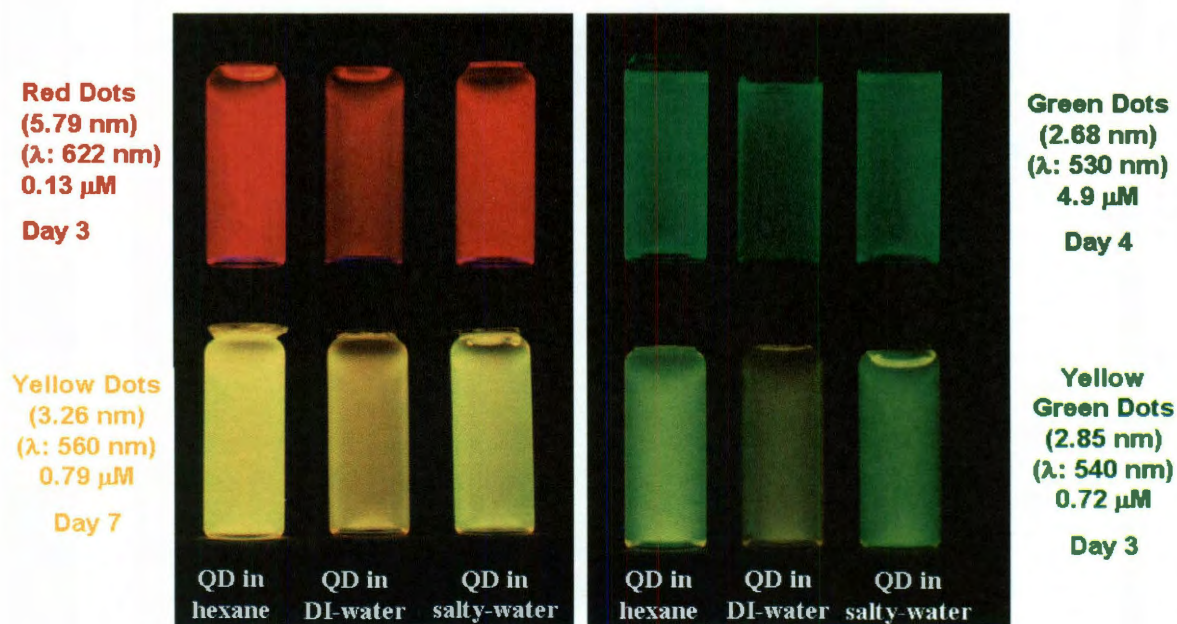


Figure A1: Dark-field digital images of CdSe QD fluorescence in three different environments upon excitation by a UV-lamp source. In each set comprising a triad, the left sample is QDs in hexane, the middle sample is QDs in plain/deionized (DI)-water micelles of AOT and the right sample is QDs in salty-water micelles of AOT. CdSe QD Types: Clockwise from Left – Red dots (5.79 nm), Green dots (2.68 nm), Yellow-Green dots (2.85 nm) and Yellow dots (3.26 nm). The measured quantum yields for the yellow-green dots (from left to right) are 14%, 3% and 5% respectively.

Section A2: Thermogravimetric Analysis (TGA)

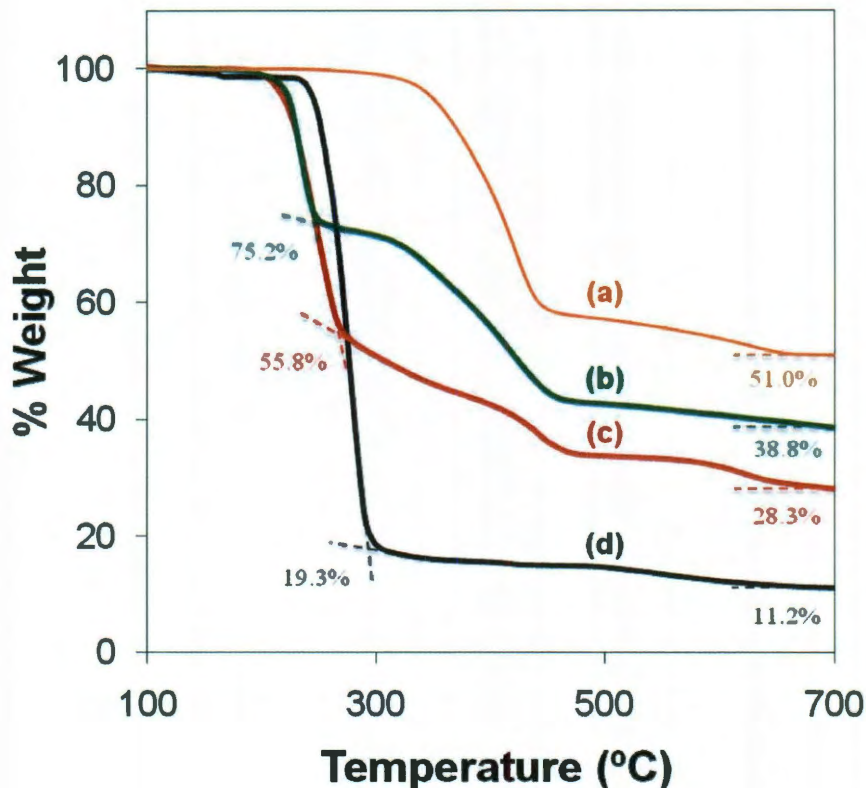


Figure A2: Results from thermogravimetric analysis of (a) CdSe+OA from hexane (b) CdSe+OA+AOT from 'no-salt' water, (c) CdSe+OA+AOT from 'salty' water and (d) AOT only. ('OA' refers to oleic acid).

Loss profile of AOT only (curve 'd') indicates major weight loss of 80.7% (100-19.3) around 295 °C followed by a gradual loss of up to 88.8% (100-11.2) at 700 °C. This data is helpful in identifying the weight fraction of AOT when CdSe+Oleic acid (OA) is present in the sample. For example, in the weight loss profile of CdSe+OA+AOT from 'salty' water (curve 'c'), the initial weight loss of 44.2% (100-55.8) at around 270 °C is attributed to AOT alone as no such peak is present in CdSe+OA (curve 'a'). Then the contribution of AOT in curve (c) at 700 °C is given by $44.2 \times 88.8/80.7 = 48.6\%$. Similarly, the contribution of AOT in curve (b) corresponding to CdSe+OA+AOT in 'no-

salt'water at 700 °C is given by $(100-75.2) \times 88.8/80.7 = 27.3\%$. The presence of 48.6% and 27.3% AOT in samples from 'salty' and 'no-salt' water, respectively, indicates that the remaining weight loss at 700°C of 23.1% ($100-28.3-48.6$) and 33.9% ($100-38.8-27.3$) is from CdSe+OA. Based on these values, the AOT:'CdSe+OA' ratio for samples from 'salty' and 'no-salt' water are calculated to be 2.1 ($48.6/23.1$) and 0.81 ($27.3/33.9$). These results point to a 2.62 fold higher amount of AOT in the 'salty' water sample compared to the 'no-salt' sample.

Section A3: Nile Red Studies

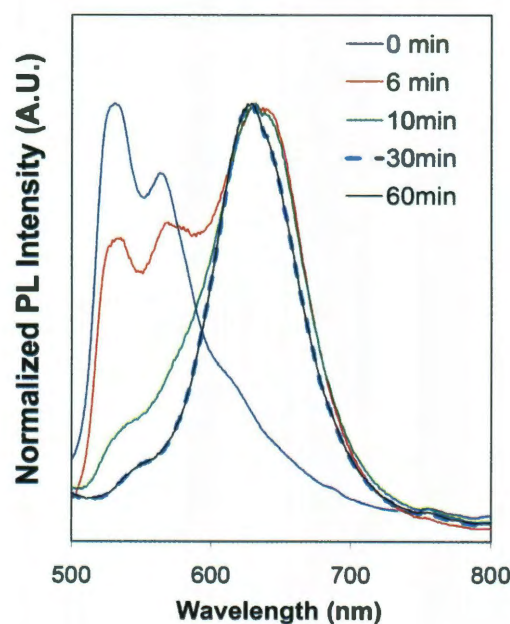


Figure A3: Nile red PL spectra at various stages of the phase transfer process (up to 60 minutes).

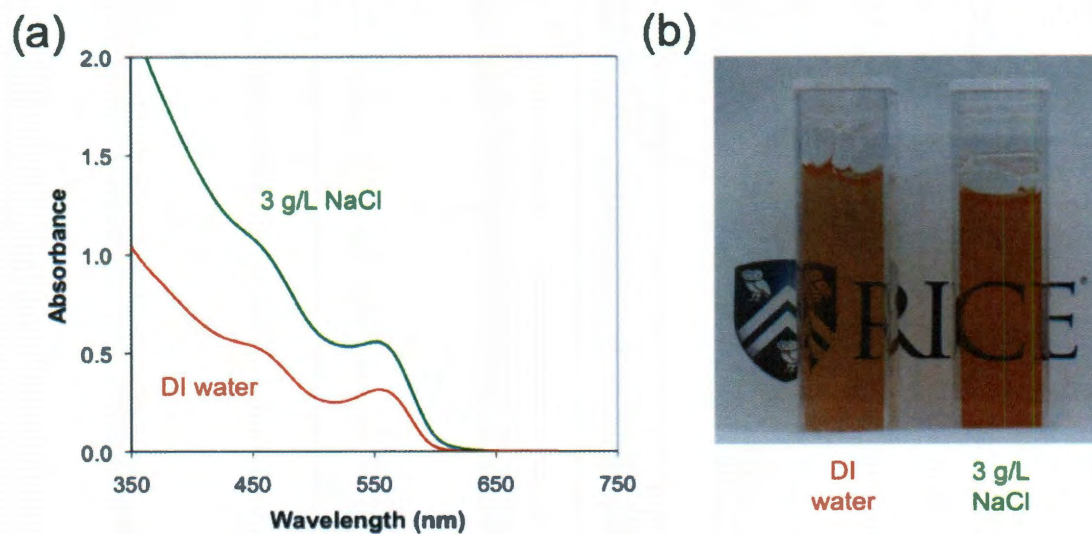
Section A4: Phase-Transfer of CdSe QDs using CTAB

Figure A4: (a) UV-Vis spectra and (b) photograph of CdSe QDs phase transferred in DI water and 3 g/L NaCl solution with CTAB as the phase transfer agent.

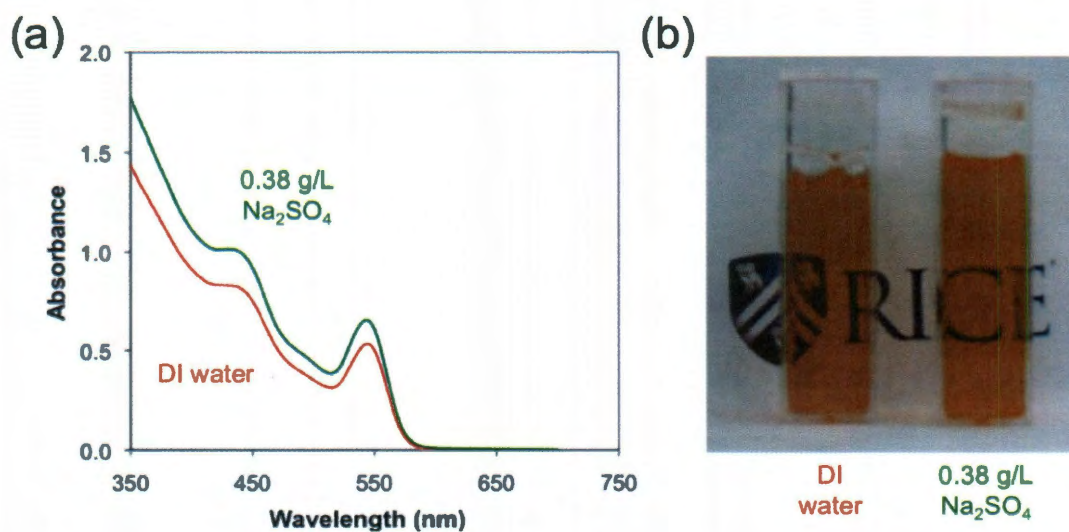
Section A5: Phase-Transfer of CdSe QDs in Na₂SO₄

Figure A5: (a) UV-Vis spectra and (b) photograph of CdSe QDs phase transferred in DI water and (b) 0.38 g/L Na₂SO₄ solution with AOT as the phase transfer agent.

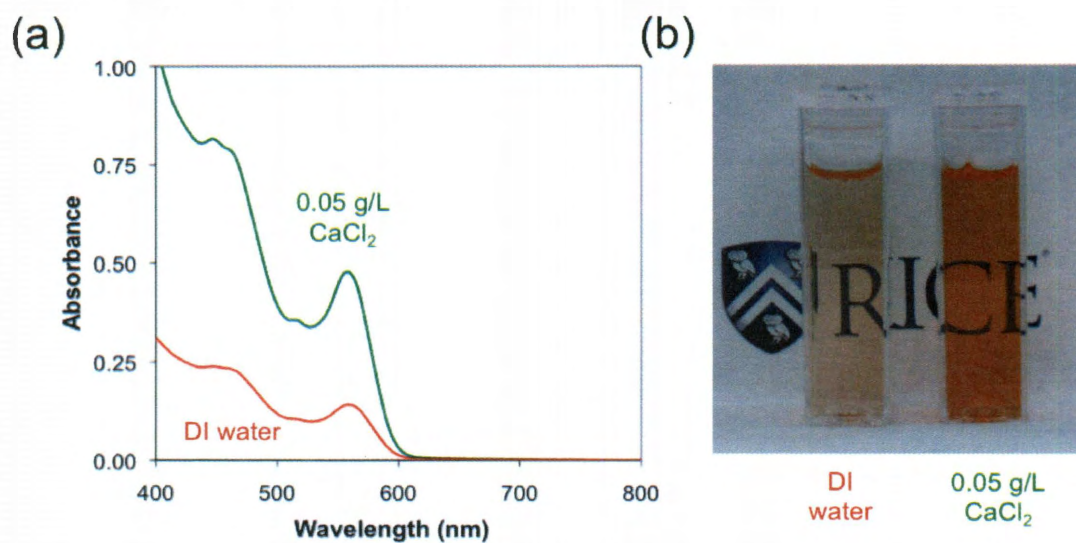
Section A6: Phase-Transfer of CdSe QDs in CaCl_2 

Figure A6: (a) UV-Vis spectra and (b) photograph of CdSe QDs phase transferred in DI water and (b) 0.05 g/L CaCl_2 solution with AOT as the phase transfer agent.

Appendix B

Section B1: Time-dependent Droplet Size of Nanoemulsions formed by Diluting 60/30/10 and 80/10/10 W/O Microemulsions in Excess Brine.

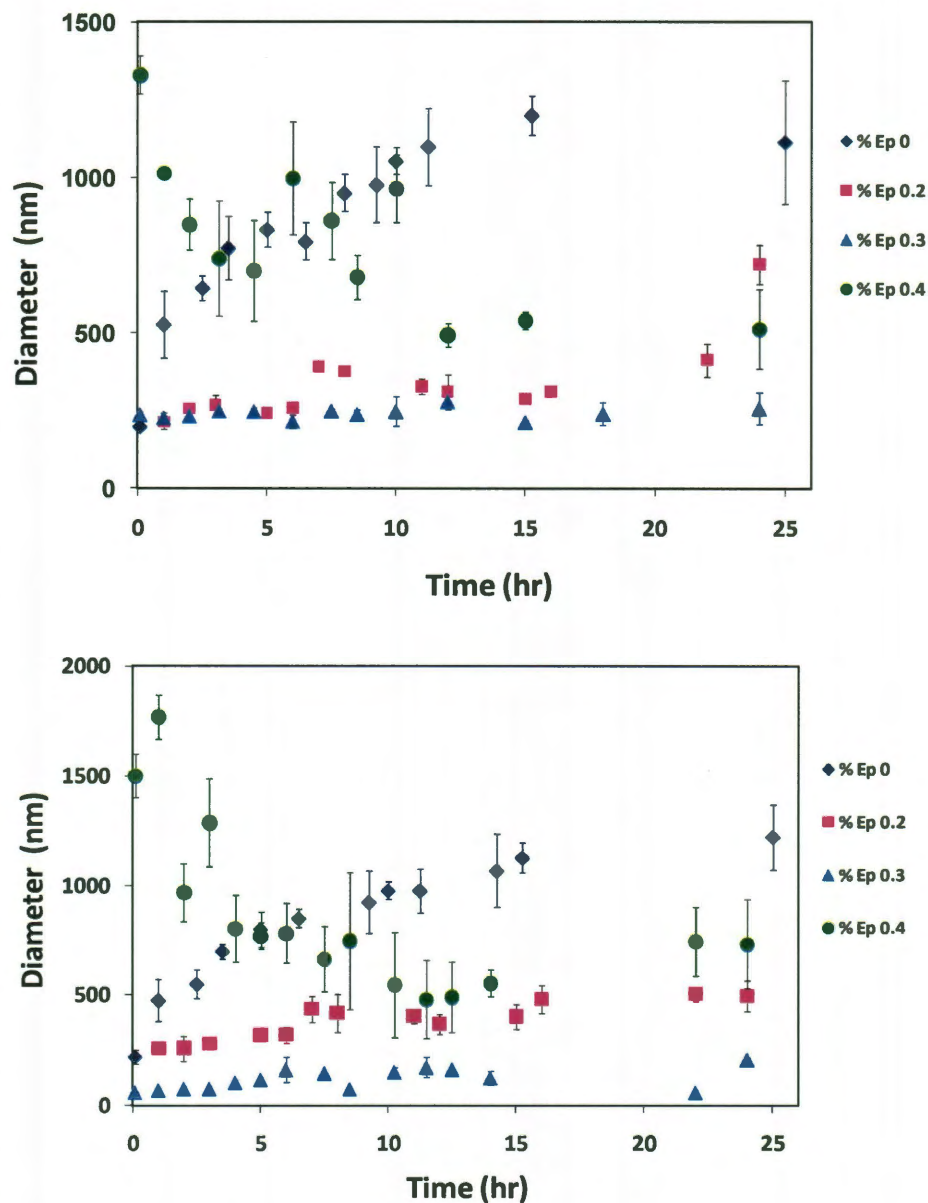


Figure B1: Octane drop size study with respect to time in Octane/Brine nanoemulsions obtained by diluting 60/30/10 (top) and 80/10/10 (bottom) Octane/AOT/Water microemulsions in different levels of excess brine (AOT = 1.5 g/L).

Section B2: Time-dependent Droplet Size of Nanoemulsions formed by diluting 70/20/10 B/O Microemulsions with Different Internal Salinities in Excess Brine.

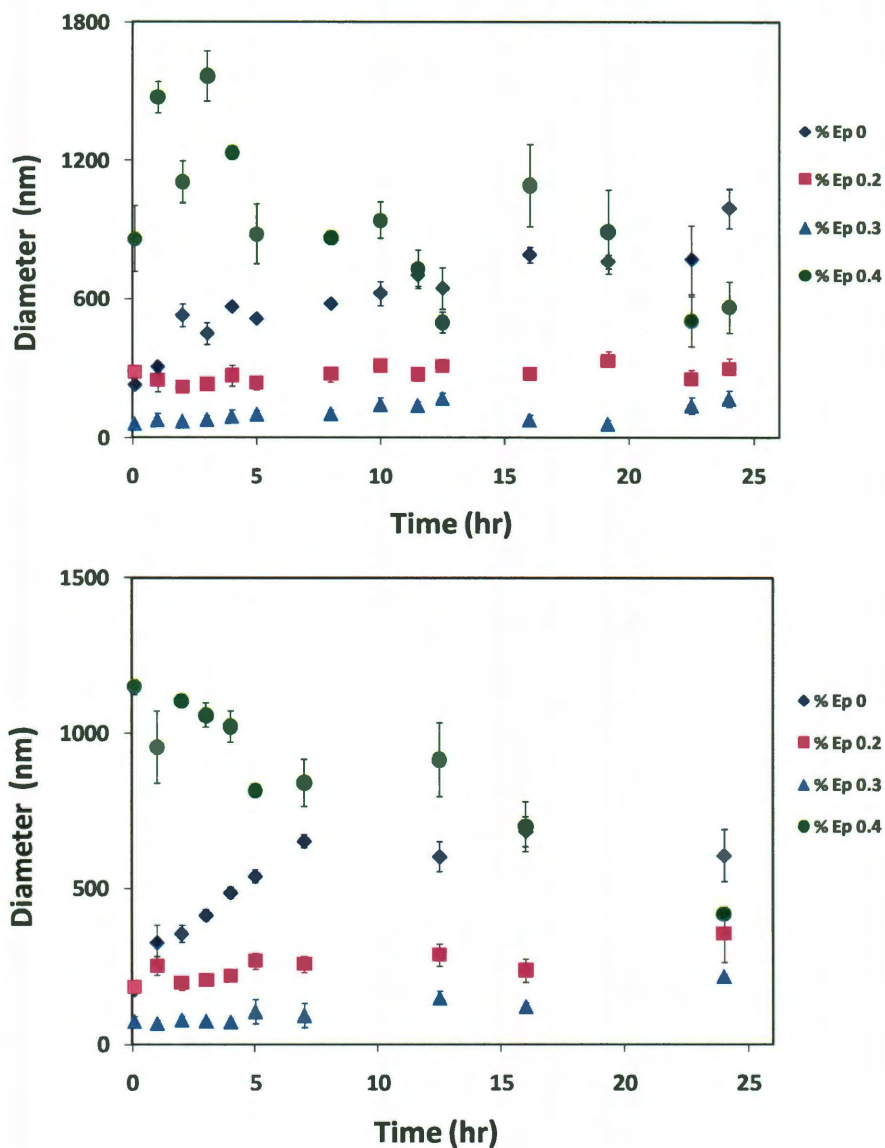


Figure B2: Octane drop size study with respect to time in Octane/Brine nanoemulsions obtained by diluting 70/20/10 Octane/AOT/Brine ($\% \varepsilon = 0.2$) (top) and 70/20/10 Octane/AOT/Brine ($\% \varepsilon = 0.4$) (bottom) microemulsions in different levels of excess brine (AOT = 1.5 g/L).

Section B3: Time-dependent Zeta Potential on Octane Drops of Nanoemulsions formed by diluting 60/30/10 and 80/10/10 W/O Microemulsions in Excess Brine.

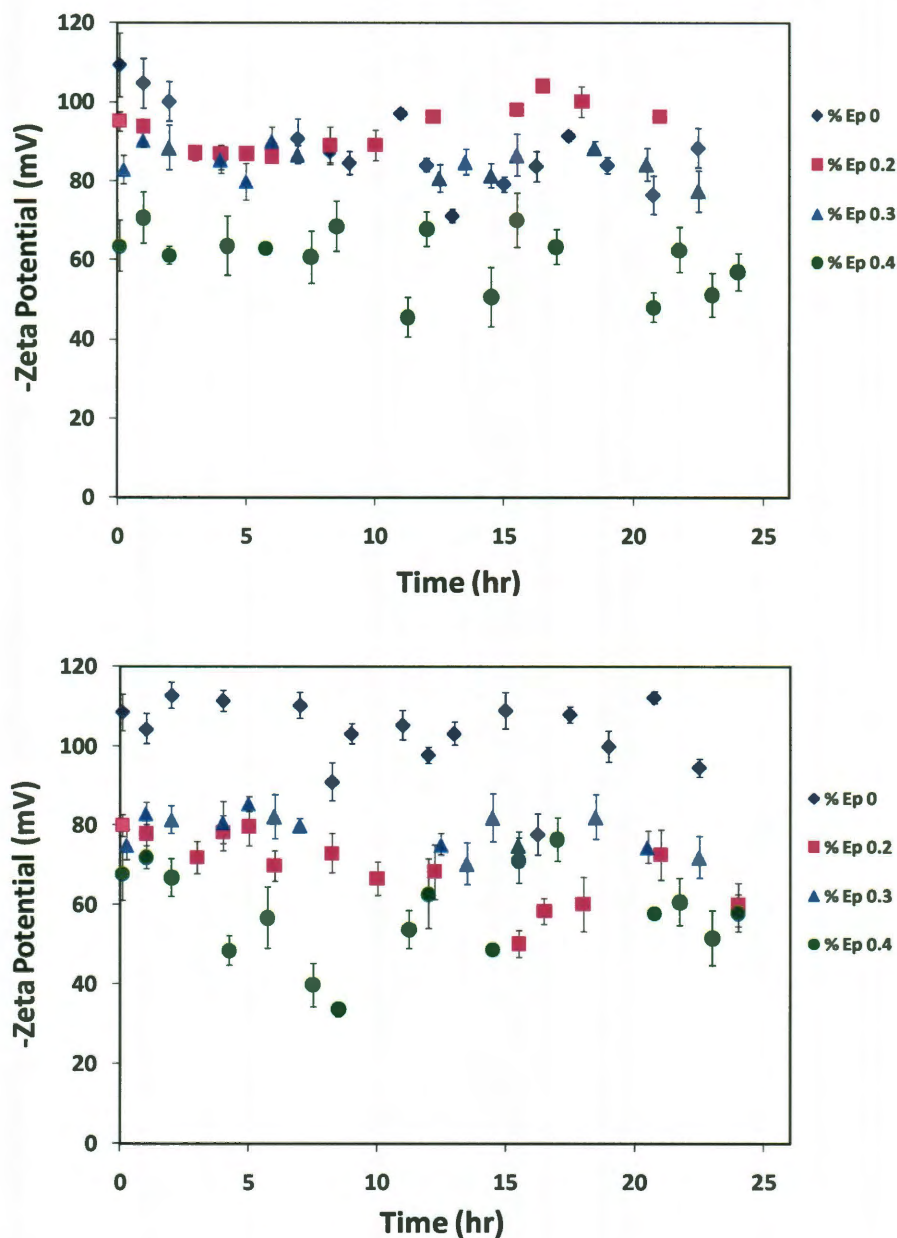


Figure B3: Zeta potential of Octane/Brine nanoemulsions obtained by diluting 60/30/10 (top) and 80/10/10 (bottom) Octane/AOT/Water microemulsions in different levels of excess brine (AOT = 1.5 g/L).

Section B4: Plots of R^3 vs. t of Nanoemulsion Drops formed by diluting B/O Microemulsions in Winsor I ($\% \epsilon = 0$).

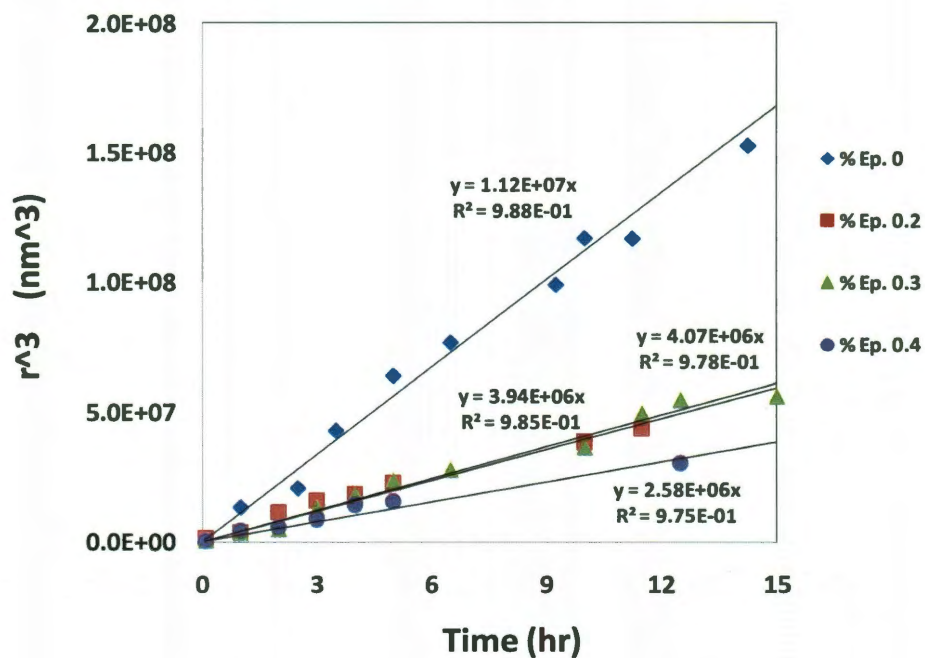


Figure B4: Plots of R^3 vs. t for nanoemulsions prepared by diluting 70/20/10 Octane/AOT/Brine microemulsions with different levels of internal salinity ($\% \epsilon = 0, 0.2, 0.3$ and 0.4) in excess water ($\% \epsilon = 0$, Winsor I). AOT = 1.5 g/L).

Appendix C

Section C1: Details of Curve Fitting by the CXTFIT Routine

The transport equation of NPs moving through porous media can be represented by a 1-dimensional advective-dispersion equation given by Eq. 4.13 in the main text. For the case when NPs show 100% breakthrough, or when they are not taken up by the column material, the term $\gamma \sim 0$. Eq. 4.13 thus takes the form:

$$R \frac{\partial C}{\partial t} = D \frac{\partial^2 C}{\partial x^2} - v \frac{\partial C}{\partial x} \quad (\text{C4.1})$$

Eq. C4.1 is a partial differential equation that is subject to the following initial and boundary conditions and thus bears an analytical solution:

The initial condition of Eq. C4.1 is:

$$C(x,0) = 0, \text{ for } t = 0 \quad (\text{C4.2})$$

The boundary conditions of Eq. C4.1, for $t > 0$ are:

$$C(0,t) = C_0 \quad (\text{C4.3})$$

$$vC_0 = vC - D \left. \frac{\partial C}{\partial x} \right|_{x=0} \quad (\text{C4.4})$$

The analytical solution for Eq. C4.1 has been described by van Genuchten and Alves and is given by Eq. C4.5.

$$C(x,t) = C + (C_0 - C)A(x,t) + B(x,t) \quad (\text{C4.5a})$$

and

$$C(x,t) = C + (C_0 - C)A(x,t) + B(x,t) - CA(x,t - t_0) \quad (\text{C4.5b})$$

Eq. C4.5a is valid for the time interval, $0 < t < t_0$, where t_0 represents the time till which the NPs are pumped to the column. Eq. C4.5b is valid for the time interval $t > t_0$, i.e after NPs enter the column. A and B are defined as follows:

$$A = \frac{1}{2} \operatorname{erfc} \left[\frac{Rx - vt}{2\sqrt{DRt}} \right] + \left(\frac{v^2 t}{\pi DR} \right) \exp \left[-\frac{(Rx - vt)^2}{4DRt} \right] - \frac{1}{2} \left(1 + \frac{vx}{D} + \frac{v^2 t}{DR} \right) \exp \left(\frac{vx}{D} \right) \operatorname{erfc} \left[\frac{Rx + vt}{2\sqrt{DRt}} \right]$$

(C4.6)

and

$$B = \frac{\gamma}{R} \left\{ t + \left(\frac{Rx}{2v} - \frac{t}{2} + \frac{DR}{2v^2} \right) \operatorname{erfc} \left[\frac{Rx - vt}{2\sqrt{DRt}} \right] - \left(\frac{t}{4\pi\tau D} \right)^{1/2} \left(Rx + vt + \frac{2DR}{v} \right) \exp \left[-\frac{(Rx - vt)^2}{4DRt} \right] + \left(\frac{t}{2} - \frac{DR}{2v^2} + \frac{(Rx + vt)^2}{4DRt} \right) \exp \left(\frac{vx}{D} \right) \operatorname{erfc} \left[\frac{Rx + vt}{2\sqrt{DRt}} \right] \right\}$$

(C4.7)

The analytical solution was used to fit the experimental breakthrough profiles (without the washout portion) in cases where C/C_0 does not exceed 100% using the method of least squares with R, D and γ as fitting parameters.^{62, 66}

Section C2: Breakthrough Profile of Tracer through Calcite

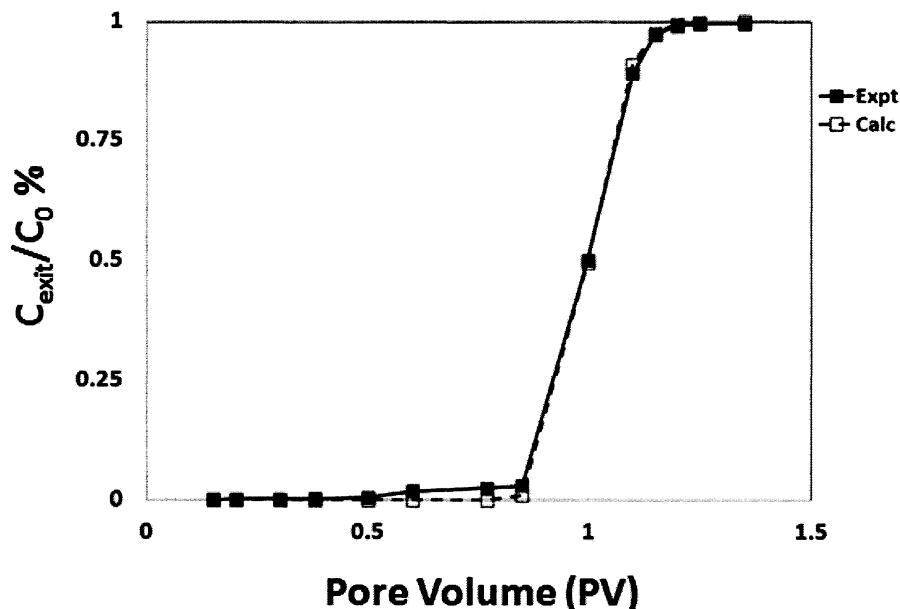


Figure C1: Experimental and fitted results for $^3\text{H}_2\text{O}$ transport through calcite, 0.55M Synthetic seawater background, 25 °C. R and D values were estimated at 1 and 0.012 $\text{cm}^2 \text{min}^{-1}$ respectively.

Section C3: Transport and Breakthrough of QD/Neodol through Quartz Sand

The natural affinity of alkyl ethoxylate nonionics to sand is well known in surfactant literature⁷⁵ and their use in sandstone reservoirs is not practiced in areas of enhanced oil recovery.⁷⁶ In this section, we investigate the transport and breakthrough of QD/Neodol through quartz sand and evaluate if the high natural affinity of the Neodol coating impacts QD breakthrough and recovery. Table C1 summarizes the parameters used for QD/Neodol breakthrough experiments through quartz sand (Fischer, 99.9999%).

A 0.54M synthetic seawater suspension of QD/Neodol was passed through the quartz sand packed column at different temperatures (Fig. C2). Breakthrough of 50% occurred at 1.1 PV for the room temperature case and was delayed to between 1.2-1.4

PVs at higher temperatures. At higher temperatures, complete breakthrough occurred with C_{exit}/C_0 seen to exceed 100% that indicated adsorption.

Table C1: Parameters used for QD/Neodol breakthrough experiments in quartz sand.

Parameter	Value	Remarks
Column Length (L)	11 cm	--
Column Inner Diameter (d)	1 cm	--
Pore Volume (PV)	3.6 mL	PV estimated from tritiated water breakthrough experiments ⁶²⁻⁶⁵
Porosity (ϵ)	0.41	Eq. 4.10
Soil particle radius (a_c)	152-402 μm	--
Particle density (ρ_p)	2.52 g/cc	--
Bulk density (ρ_b)	1.48 g/cc	Eq. 4.11
Volumetric flow rate (Q)	8 mL/hr	
Darcy velocity (v_d)	2.44 m/d	Eq. 4.12
Linear pore velocity	5.86 m/d	Eq. 4.12
Background salinity	1M NaCl and 0.54M synthetic seawater	
Temperature	25, 50 and 70 °C	

The breakthrough profiles further indicates delays to result from effects of retardation over dispersion. This was different from the transport behavior observed in the case of calcite in seawater background, where QD adsorption was not observed and dispersion effects from temperature were prevalent. This shows NP transport through porous media is dependent on both, the type of saline environments as well as the material constituting the medium.

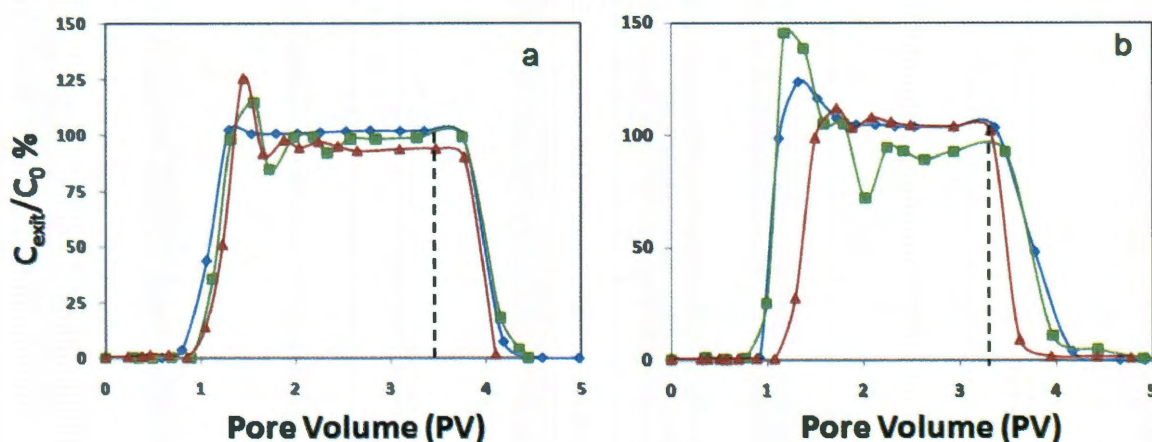


Figure C2: Breakthrough profiles of QD/Neodol in (a) 0.54M synthetic seawater (b) 1M NaCl. At PV \sim 3.0-3.5, the inlet QD/Neodol formulations were replaced by solutions with respective background salinities. The error bar on C_{exit}/C_0 was $\pm 2\%$.

That QD adsorption was through Neodol-sand interactions is also evident from the release of QDs after more inlet solution flowed into the column. QD release followed a plug-like behavior, suggesting rapid substitution of QDs adsorbed onto sand via Neodol with empty Neodol micelles that existed in the influent solution. Overall QD recovery across all temperatures was $> 92\%$, indicating that NPs, although partially adsorbed onto sand, was recovered through the course of the experimental run (Table C2). Thus in the scope of NP transport, the use of nonionics, atleast for packed-sand columns did not result in significant retention of QDs.

Table C2: Percent recovery of QDs from quartz packed columns at different temperatures.

Carrier Fluid	25 °C	50 °C	70 °C
0.54M synthetic seawater	94	93	92
1M NaCl	95	99	90

Section C4: Sensitivity Analysis of 1D Advection-Dispersion Equation

Sensitivity Analysis of the 1D advection-dispersion equation was performed by individually varying one of the three parameters of (R, D and γ) of Eq. 4.13 while keeping the other two constant.

Fig. C3 represents the scenario where R was varied from 1 (no partitioning of NP onto column surface: for calcite, k_d at R = 1 is 0 mL g⁻¹) to 5 (significant partitioning of NP onto column surface: for calcite, k_d at R = 1 is 1.093 mL g⁻¹) while keeping D (0.001 cm² min⁻¹) and γ (0 min⁻¹) constant. The implication of increasing R was reflected by the delay at which NP breakthrough occurred. For R = 1, breakthrough was seen to occur at 1 PV and this increased to 5 PV's for R = 5.

Fig. C4 represents the alternate scenario where D was varied from 0.00001 cm² min⁻¹ to 0.1 cm² min⁻¹ while keeping R and γ fixed at 1 and 0 min⁻¹ respectively. The first trend that emerged was that the PV at which breakthrough occurred did not shift (breakthrough took place at 1PV). At low values of D (0.00001 cm² min⁻¹ and 0.0001 cm² min⁻¹), concentration variation of NPs with PV was seen to occur in a manner akin to a step change. This implies that in the absence of dispersion, NPs would breakthrough as a pulse. When D was increased progressively, breakthrough of NPs was

seen to shift from a pulse to a gradual spread, but about the same PV where 50% breakthrough first occurred. This highlights effects brought about by column porosity which results in non-ideal flow patterns different from ideal plug flow.

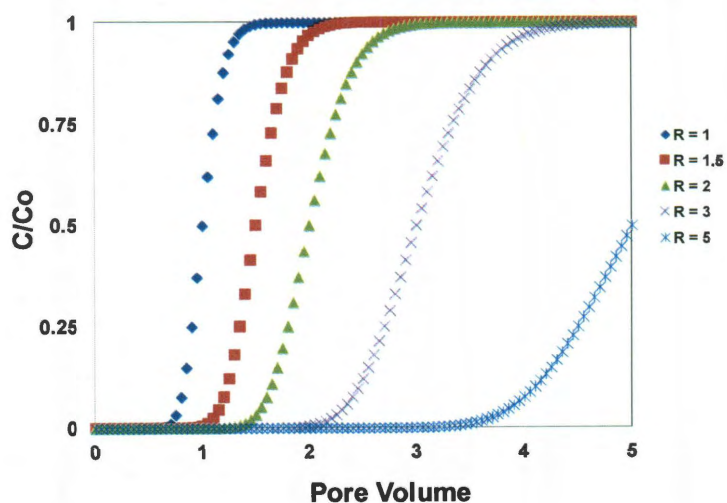


Figure C3: Sensitivity analysis of 1D advection-dispersion equation by varying R while keeping D and γ constant.

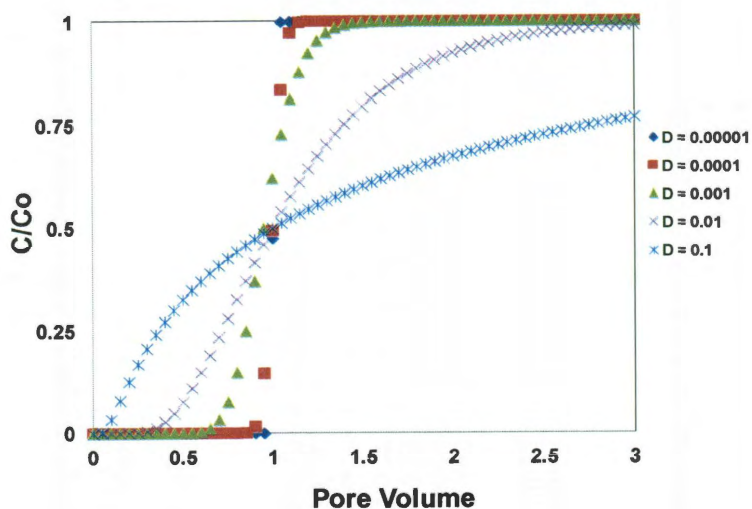


Figure C4: Sensitivity analysis of 1D advection-dispersion equation by varying D while keeping R and γ constant.

Fig. C5 represents the third scenario where γ was varied from 0.00001 min^{-1} to 0.1 min^{-1} while keeping R and D fixed at 1 and $0.001 \text{ cm}^2 \text{ min}^{-1}$ respectively. While the concentration-PV profile was similar to that in Fig. C3, the outlet concentration reduced progressively from 100% to lower values indicating permanent retention of NPs by column material.

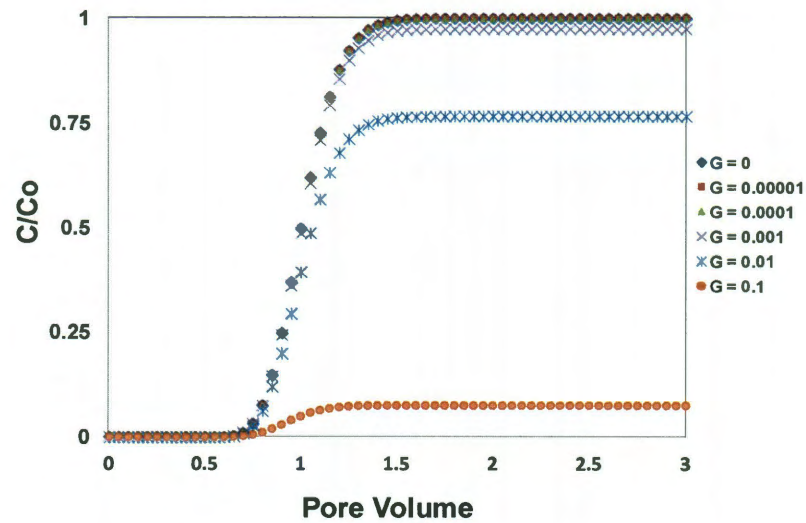


Figure C5: Sensitivity analysis of 1D advection-dispersion equation by varying γ while keeping R and D constant.